

CLARKSON UNIVERSITY

**AERODYNAMIC FLOW CONTROL OF A HIGH LIFT SYSTEM
WITH DUAL SYNTHETIC JET ARRAYS**

A Dissertation

By

**Robert Bruce Alstrom, B.Eng (Aero), M.Eng (Aero), M.A.Sc
Aerospace Engineer**

Department of Mechanical and Aeronautical Engineering

Submitted in partial fulfillment of the requirements

for the degree of

Doctor of Philosophy, Mechanical Engineering

July 26, 2013

Accepted by the Graduate School

_____, _____
Date, Dean of the Graduate School

The undersigned have examined the thesis entitled ‘**Aerodynamic Flow Control of a High Lift System with Dual Synthetic Jet Arrays**’ presented by **Robert Bruce Alstrom**, a candidate for the degree of **Doctor of Philosophy (Mechanical Engineering)** and hereby certify that it is worthy of acceptance.

Date

Dr. Pier Marzocca, Advisor

Date

Dr. Erik Bollt, Co-Advisor

Date

Dr. G. Ahmadi, Co-Advisor

Date

Dr. Daniel Valentine

Date

Dr. Ronald LaFleur

Destiny is no matter of chance. It is a matter of choice. It is not a thing to be waited for, it is a thing to be achieved.

~ William Jennings Bryan



Space Shuttle Discovery (OV-103) during STS-114

ABSTRACT

Implementing flow control systems will mitigate the vibration and aeroacoustic issues associated with weapons bays; enhance the performance of the latest generation aircraft by reducing their fuel consumption and improving their high angle-of-attack handling qualities; facilitate steep climb out profiles for military transport aircraft. Experimental research is performed on a NACA 0015 airfoil with a simple flap at angle of attack of 16° in both clean and high lift configurations. The results of the active control phase of the project will be discussed. Three different experiments were conducted; they are Amplitude Modulated Dual Location Open Loop Control, Adaptive Control with Amplitude Modulation using Direct Sensor Feedback and Adaptive Control with Amplitude Modulation using Extremum Seeking Control. All the closed loop experiments are dual location. The analysis presented uses the spatial variation of the root mean square pressure fluctuations, power spectral density estimates, Fast Fourier Transforms (FFTs), and time frequency analysis which consists of the application of the Morlet and Mexican Hat wavelets. Additionally, during the course of high speed testing in the wind tunnel, some aeroacoustic phenomena were uncovered; those results will also be presented. A cross section of the results shows that the shape of the RMS pressure distributions is sensitive to forcing frequency. The application of broadband excitation in the case adaptive control causes the flow to *select* a frequency to lock in to. Additionally, open loop control results in global synchronization via switching between two stable states and closed loop control inhibits the switching phenomena, but rather synchronizes the flow about multiple stable shedding frequencies.

ACKNOWLEDGMENTS

I would like to acknowledge the Air Force Office of Scientific Research and Clarkson University, for without their financial support, the completion of this work would not be possible.

Drs. Ahmadi, Marzocca, Bollt and Dr. LaFleur, I have very much enjoyed our interactions. It is through these interactions that I was able to see your generosity and benefit from your wisdom and encouragement throughout this endeavor. Professor Valentine, I have learned so much from our many discussions about science and life, and I really appreciated your humor.

To Doug Leonard, your continued support, design advice, creativity and imagination were invaluable during the course of this research. To my lab mates in Room 287, past and present, I consider myself fortunate to have met you all and I feel privileged to have had the opportunity to learn from you and to share my passion for aerospace science and engineering with you.

To Dr. Kuxhaus, Jen Clarke, Ellen Weil, Stephen Pedersen, Bang-Guel Han, Alex and Andreas, Steve and Mary and to the rest of our Clarkson-Potsdam group of friends, you have all been a blessing to me and my life is much richer because of you!!

To Eve LaCourtüre, Very simply, I love you.

TABLE OF CONTENTS

ABSTRACT	iv
ACKNOWLEDGMENTS	v
TABLE OF CONTENTS	vi
TABLE OF FIGURES	vii
CHAPTER 1.0: INTRODUCTION.....	1
1.1 OVERVIEW	1
1.2 MOTIVATION.....	4
1.3 BACKGROUND	5
1.3.1 DEVELOPMENTS IN SYNTHETIC JET ACTUATOR TECHNOLOGY.....	5
1.3.2 CONTROL OF FLOW SEPARATION	16
1.3.3 FLOW CONTROL APPLICATIONS IN AEROSPACE.....	26
1.4 RESEARCH OBJECTIVES.....	30
1.5 TECHNICAL APPROACH	30
1.6 OUTLINE OF THE DISSERTATION.....	31
CHAPTER 2.0: MODELING, SIMULATION AND CONTROL THEORY FOR ACTIVE FLOW CONTROL.....	32
2.1 INTRODUCTION	32
2.2 SYNCHRONIZATION AND ACTIVE FLOW CONTROL.....	32
2.2.1 THE EFFECT OF FORCING AMPLITUDE ON SYNCHRONIZATION	38
2.2.2 THE EFFECT OF THE CLOSED LOOP FORCING FREQUENCY ON SYNCHRONIZATION	46
2.2.3 TIME FREQUENCY ANALYSIS	47
2.3 SIMULATION OF AN ADAPTIVE PID (PROPORTIONAL) CONTROL & EXTREMUM SEEKING FEEDBACK FOR EXPERIMENTAL ACTIVE FLOW CONTROL	51
2.4 DISCUSSION.....	61
CHAPTER 3.0: EXPERIMENTAL HARDWARE AND INSTRUMENTATION.....	63
3.1 THE HIGH SPEED WIND TUNNEL.....	63
3.2 NACA 0015 AIRFOIL	64
3.3 AEROLAB SIX AXIS FORCE BALANCE	67
3.4 SENSORS.....	68
3.5 DIRECTED SYNTHETIC JET ACTUATORS	69
3.6 REAL TIME CONTROL HARWARE AND SOFTWARE (dSPACE™)	75
4.1 INTRODUCTION	82
4.2 DATA ANALYSIS METHODS	84
4.3 FLOW INDUCED NOISE SOURCES	87
4.4 UN-ACTUATED FLOW PHYSICS	96
CHAPTER 5.0: ACTIVE CONTROL RESULTS (OPEN & CLOSED LOOP)	114
5.1 INTRODUCTION	114
5.2 DUAL LOCATION OPEN LOOP CONTROL	114
5.3 ADAPTIVE CONTROL WITH AMPLITUDE MODULATION	132
USING DIRECT SENSOR FEEDBACK (DUAL LOCATION)	132
5.4 ADAPTIVE CONTROL WITH AMPLITUDE MODULATION	143
USING EXTREMUM FEEDBACK CONTROL (DUAL LOCATION)	143
CHAPTER 6.0: CONCLUSIONS AND FUTURE WORK.....	181
6.1 CONCLUSIONS	181
6.2 FUTURE WORK	182
REFERENCES.....	184

TABLE OF FIGURES

Figure 1.1: Strike Aircraft Test Directorate F-14 A/B Tomcat;	1
Figure 1.2: F-111 Aardvark	1
Figure 1.3: Categories of Synthetic Jet Actuators [5]	5
Figure 1.4: Typical ZNMF devices, three different types of excitation mechanisms [7] ...	7
Figure 1.5: Orifice geometry. A) Axisymmetric, B) Rectangular (or 2D) [7].....	7
Figure 1.6: Optimization Study Results [10]	8
Figure 1.7: Dual cavity SJA with Frequency Response [11].....	9
Figure 1.8: Piston Based SJA [12]	9
Figure 1.9: Frequency Response of Piston Based SJA [12]	10
Figure 1.10: Piston Based SJA with curved slot [13]	11
Figure 1.11: Second generation slot [13].....	11
Figure 1.12: Velocity vs. Frequency Diagram [13]	12
Figure 1.13: Bell XV-15 Tiltrotor Aircraft [14]	13
Figure 1.14: Actuator Module Flight Hardware [14].....	13
Figure 1.15: XV-15 Integrated Flow Control Actuator [14].....	14
Figure 1.16: Different Flow Regions in Slot/Orifice [7]	15
Figure 1.17: Frequency Scales in separated flows [8]	18
Figure 2.1: System and Control Law [17]	36
Figure 2.2: Open Loop Dynamics of the Rossler Oscillator.....	37
Figure 2.3: Rossler Oscillator: Open Loop Spectra	37
Figure 2.4: Closed Loop control of Rossler oscillator [$k=0.01, f_F=0.3417$ Hz]	39
Figure 2.5: Closed Loop FFT [$k=0.01, f_F=0.3417$ Hz]	39
Figure 2.6: Closed Loop control of Rossler oscillator [$k=0.05, f_F=0.3417$ Hz]	41
Figure 2.7: Closed Loop FFT [$k=0.05, f_F=0.3417$ Hz]	41
Figure 2.8: Closed Loop control of Rossler oscillator [$k=0.1, f_F=0.3417$ Hz]	42
Figure 2.9: Closed Loop FFT [$k=0.1, f_F=0.3417$ Hz]	42
Figure 2.10: Closed Loop control of Rossler oscillator [$k=0.2, f_F=0.3417$ Hz]	43
Figure 2.11: Exposed limit cycle [$k=0.2, f_F=0.3417$ Hz].....	43
Figure 2.12: Closed Loop FFT [$k=0.2, f_F=0.3417$ Hz].....	44
Figure 2.13: Closed Loop control of Rossler oscillator [$k=0.4, f_F=0.3417$ Hz]	45
Figure 2.14: Exposed limit cycle [$k=0.4, f_F=0.3417$ Hz].....	45
Figure 2.15: Closed Loop FFT [$k=0.4, f_F=0.3417$ Hz].....	46
Figure 2.16: Effect of Variation of Closed Loop Forcing Frequency.....	47
Figure 2.17: Open Loop Spectrogram of the Rossler attractor	49
Figure 2.18: Spectrogram for controlled Rossler attractor	50
Figure 2.19: Schematic of closed loop control for backward facing step [49]	52
Figure 2.20: Adaptive Proportional controller configuration	54
Figure 2.21: Schematic of the Time Varying Proportional Gain.....	54
Figure 2.22: Time histories: Control Force, Gain and Phase Plane plot.....	54
Figure 2.23: Average Control Gain vs. Frequency	55
Figure 2.24: Frequency Spectra comparison (Adaptive PID).....	56
Figure 2.25: General schematic of Extremum Seeking Controller [54]	57
Figure 2.26: Extremum Seeking Controller in Simulink	58

Figure 2.27: Fixed Gain-Time Varying Forcing Frequency configuration	58
Figure 2.28: Control Force and Time Varying forcing frequency.....	59
Figure 2.29: Rossler Closed Loop Time Histories.....	60
Figure 2.30: Frequency Spectra Comparison (Extremum Seeking)	61
Figure 3.1: Wind Tunnel Test and Test Section	63
Figure 3.2: Partial Wing Assembly.....	64
Figure 3.3: Flap segments with pin holes	65
Figure 3.4: Wing Schematic	65
Figure 3.5: Strut with wire harnesses.....	66
Figure 3.6: False walls in test section	66
Figure 3.7: Wing mounted on Force Balance	67
Figure 3.8: Pressure transducer locations	68
Figure 3.9: Directed synthetic jet.....	69
Figure 3.10: Two dimensional diffuser [90]	70
Figure 3.11: Diffuser flow regimes [90]	71
Figure 3.12: Area Ratio vs. Non-dimensional Diffuser Length [Cocanower].....	71
Figure 3.13: Cavity and diffuser-slot.....	72
Figure 3.14: Compression Ring Assembly	73
Figure 3.15: Transfer Function: LE SJA.....	74
Figure 3.16: Transfer Function: TE SJA.....	75
Figure 3.17: Schematic of Experimental Setup	76
Figure 3.18: Data Acquisition block diagram.....	77
Figure 3.19: Real Time Signal/System monitoring	78
Figure 3.20: Real Time Control Work Station.....	78
Figure 3.21: Open Loop Control Block Diagram	80
Figure 3.22: Closed Loop Control Schematic for adaptive control.....	81
Figure 4.1: Low Reynolds number flow without reattachment [100]	83
Figure 4.2: Low Reynolds number flow with reattachment [100].....	84
Figure 4.3: Morlet Wavelet.....	86
Figure 4.4: Mexican Hat Wavelet.....	86
Figure 4.5: Spectra 0-4 degrees AoA.....	88
Figure 4.6: Spectra 6-10 degrees AoA.....	89
Figure 4.7: Spectra 12-16 degrees AoA.....	90
Figure 4.8: Spectra 18-20 degrees AoA.....	91
Figure 4.9: Spectra at 4 degrees AoA, Slots Closed.....	92
Figure 4.10: Spectra 6-8 degrees AoA, Slots Covered	92
Figure 4.11: Flat Plate Cascade [104].....	92
Figure 4.12: Test Section Configuration.....	94
Figure 4.13: Parker Mode Variation with Angle of Attack	95
Figure 4.14: RMS Pressure vs. Chordwise Position	98
Figure 4.15: Pressure Sensor time series	99
Figure 4.16: Chordwise Power spectra, $\alpha = 16^\circ, \delta_f = 0^\circ, U = 5 \text{ m/s}$	100
Figure 4.17: Wavelet Map, $x/c=0.1826, \alpha = 16^\circ, \delta_f = 0^\circ, U = 5 \text{ m/s}$	101
Figure 4.18: Wavelet Map, $x/c=0.2293, \alpha = 16^\circ, \delta_f = 0^\circ, U = 5 \text{ m/s}$	102
Figure 4.19: Wavelet Map, $x/c=0.2660, \alpha = 16^\circ, \delta_f = 0^\circ, U = 5 \text{ m/s}$	103
Figure 4.20: Wavelet Maps, $x/c=0.3026, \alpha = 16^\circ, \delta_f = 0^\circ, U = 5 \text{ m/s}$	104

Figure 4.21: Wavelet Maps, $x/c=0.3393$, $\alpha = 16^\circ$, $\delta_f = 0^\circ$, $U = 5 \text{ m/s}$	106
Figure 4.22: Wavelet Maps, $x/c=0.3760$, $\alpha = 16^\circ$, $\delta_f = 0^\circ$, $U = 5 \text{ m/s}$	106
Figure 4.23: Wavelet Maps, $x/c=0.4126$, $\alpha = 16^\circ$, $\delta_f = 0^\circ$, $U = 5 \text{ m/s}$	107
Figure 4.24: Wavelet Maps, $x/c=0.4493$, $\alpha = 16^\circ$, $\delta_f = 0^\circ$, $U = 5 \text{ m/s}$	107
Figure 4.25: Wavelet Maps, $x/c= 0.7483$, $\alpha = 16^\circ$, $\delta_f = 0^\circ$, $U = 5 \text{ m/s}$	108
Figure 4.26: Wavelet Maps, $x/c= 0.7846$, $\alpha = 16^\circ$, $\delta_f = 0^\circ$, $U = 5 \text{ m/s}$	108
Figure 4.27: Wavelet Maps, $x/c= 0.8120$, $\alpha = 16^\circ$, $\delta_f = 0^\circ$, $U = 5 \text{ m/s}$	109
Figure 4.28: Chordwise Variation of Frequency	110
Figure 4.29: Chordwise Power spectra, $\alpha = 16^\circ$, $\delta_f = 20^\circ$, $U = 5 \text{ m/s}$	111
Figure 4.30: Comparison of RMS Pressure distributions	113
Figure 5.1: RMS Pressure Distributions- Clean Wing Configuration (Frequency Sweep)	117
Figure 5.2: RMS Pressure Distributions- High-Lift Wing Configuration (Frequency Sweep).....	119
Figure 5.3: Un-Actuated Flow Frequency Spectra (FFT).....	120
Figure 5.4 Actuated Flow Spectra (FFT): Clean Wing Configuration (Open Loop)	121
Figure 5.5: Enhanced FFT, Stations 1 to 3 (Open Loop).....	122
Figure 5.6: Enhanced FFT, Stations 4 to 6 (Open Loop).....	123
Figure 5.7: Enhanced FFT, Stations 7 to 9 (Open Loop).....	124
Figure 5.8: Enhanced FFT, Stations 10 & 11(Open Loop).....	125
Figure 5.9: Actuated Flow Spectra (FFT): High Lift Configuration	126
Figure 5.10: Variation of Normal Force with Forcing Frequency.....	127
Figure 5.11: Wavelet Map Panel: High Lift Configuration Part 1 ($f_m=100 \text{ Hz}$)	130
Figure 5.12: Wavelet Map Panel: High Lift Configuration Part 2 ($f_m=100 \text{ Hz}$)	131
Figure 5.13: Direct Sensor Feedback Adaptive Control.....	133
Figure 5.14: RMS Pressure Distribution, Clean Wing configuration ($x/c=0.4126$)	134
Figure 5.15: Displacement of Fluctuation Level at Sensor Station 3	135
Figure 5.16: RMS Pressure Distribution, Clean Wing configuration ($x/c=0.7846$)	136
Figure 5.17: RMS Pressure Distribution, High Lift configuration ($x/c=0.4126$)	137
Figure 5.18: RMS Pressure Distribution, High Lift configuration ($x/c=0.7846$)	137
Figure 5.19: Closed Loop Frequency Spectra, Direct Feedback, $\phi= 180^\circ$	139
Figure 5.20: Wavelet Map Panel, Clean Wing configuration (DFB Control, $\phi= 180^\circ$) ..	140
Figure 5.21: Wavelet Map Part 2, $x/c=0.3026$	141
Figure 5.22: Wavelet Map Part 2, $x/c=0.2660$	141
Figure 5.23: Experimental Extremum Seeking Control Loop Configuration.....	144
Figure 5.24: Extremum Seeking Controller Gain, K versus Velocity	146
Figure 5.25: Frequency Domain Response of Extremum Seeking Control signal	148
Figure 5.26: Variation of Control Signal Amplitude at ES Control Forcing Frequency	149
Figure 5.27: Time Series of Extremum Seeking control signals	150
Figure 5.28: RMS pressure distribution for wing under Extremum Seeking Control	152
Figure 5.29: Extremum Seeking Control Times Series, Clean Wing configuration	154
Figure 5.30: Enhanced FFT, Stations 1 to 3 (Extremum Seeking).....	155
Figure 5.31: Enhanced FFT, Stations 4 to 6 (Extremum Seeking).....	156
Figure 5.32: Enhanced FFT, Stations 7 to 9 (Extremum Seeking).....	157
Figure 5.33: Enhanced FFT, Stations 1 to 3 (Extremum Seeking).....	158

Figure 5.34: Wavelet Map Panel, Clean Wing configuration (Extremum Seeking)	160
Figure 5.35: Wavelet Map Part 2, Clean Wing configuration (Extremum Seeking).....	161
Figure 5.36: Wavelet Map Part 2 ($x/c=0.2660$), $\delta_f = 0^\circ$ (Extremum Seeking)	162
Figure 5.37: RMS Pressure Distribution, High Lift Configuration (Extremum Seeking)	164
Figure 5.38: Time Series, High Lift configuration (Extremum Seeking).....	165
Figure 5.39: Enhanced FFT, Stations 1 to 3 (High Lift, Extremum Seeking).....	167
Figure 5.40: Enhanced FFT, Stations 4 to 6 (High Lift, Extremum Seeking).....	168
Figure 5.41: Enhanced FFT, Stations 7 to 9 (High Lift, Extremum Seeking).....	169
Figure 5.42: Enhanced FFT, Stations 10 to 11 (High Lift, Extremum Seeking).....	170
Figure 5.43: Wavelet Map Panel Part 1, High Lift configuration (Extremum Seeking)	173
Figure 5.44: Wavelet Map Panel Part 2, High Lift configuration (Extremum Seeking)	174
Figure 5.45: Comparison of RMS Pressure Distributions	176
Figure 5.46: Closed Loop Frequency Spectra (Clean, Extremum Seeking).....	177
Figure 5.47: Closed Loop Frequency Spectra, Magnified (Clean, Extremum Seeking)	178
Figure 5.48: Comparison of adaptive controllers (Clean configuration).....	179
Figure 5.49: Comparison of adaptive controllers (High Lift configuration)	180

CHAPTER 1.0: INTRODUCTION

1.1 OVERVIEW

Over the past century, commercial and military aircraft design has emerged through compromises between design tradeoffs. The vehicle configuration must be able to accommodate a wide range of operational flight conditions with a fixed geometry. The optimal geometry for takeoff conditions is significantly different from the optimal geometry for high speed cruise conditions. To address the wide variation in operation conditions, traditional flow control technologies were designed. For example, the Northrup Grumman F-14 (Figure 1.1) and the General Dynamics F-111 Aardvark (Figure 1.2) and EF-111 Raven (the electronic warfare variant) employed swing wing technology that permitted the optimal planform shape under different flight conditions.



Figure 1.1: Strike Aircraft Test Directorate F-14 A/B Tomcat;

Figure 1.2: F-111 Aardvark

The multi-element high-lift system, typically employed for the takeoff and landing segments of a mission profile are often ‘morphed’ into a single element for cruise conditions. This is a passive type of flow control. In recent years, NASA, various military organizations (DARPA and AFOSR) and the major aircraft manufacturers have been engaged in the development of active flow control research programs with the goal of achieving improvements in aero and hydrodynamic performance and maneuvering compared with conventional passive approaches. Within the field of active flow control, the control of separated flows has been identified as one of the more important flow control tasks as it has a significant impact on the operational capability of an atmospheric flight vehicle and so it is not surprising that this well known phenomena has received considerable attention from both aerodynamicists and the practitioners of controls and dynamical systems theory. Flow separation is generally understood to be the detachment of a fluid from a solid surface. This detachment is accompanied by a severe adverse pressure gradient and a noted thickening in the region of rotational flow adjacent to the solid surface; in addition to this effect, there is also an increase in the velocity component normal to the surface. Flow separation incurs a loss of lift with increased drag and poor pressure recovery on primary flight surfaces and aero-propulsion components such as diffusers. For example, fighter aircraft are equipped with different types of short range infrared guided munitions and positioning technologies for optimal firing solutions; as a result we have seen the development of vectored thrust aircraft that are capable of super-maneuverability. Such aggressive flight conditions result in unsteady separation on the airframe as a whole. Operating in a prolonged high-alpha condition will produce buffeting on wings and tail planes, fore body separation as well as degraded handling

qualities. Military transports often operate at forward operating bases or carry out humanitarian missions and must land on less than ideal runways in length due to the situation in the theater of operation, hence today's fixed wing military transport aircraft are required to be capable of extreme short take off and land (EXSTOL). Active flow control programs envision the development and use of actuators, sensors and controllers for use on elements of an aerospace system that can significantly affect operational capabilities such as aircraft wings and tail configurations (such as twin tailed high performance fighter aircraft), engine nacelles, internal ducts (like the serpentine inlets fitted to the B-2 Stealth Bomber), nozzles, projectiles and weapons bays. The benefits of flow control include reductions in weight and reduced fuel consumption and noise. Previous attempts at active flow control have involved steady suction and blowing, and although successful, this method required a lot of input energy to gain a meaningful lift increase or drag reduction. Periodic excitation was introduced by Schubauer and Skramstad [1]; specifically, perturbations in a laminar boundary layer were used to initiate Tollmien-Schlichting waves. This discovery became the primary tool for studying instabilities in fluid flows; specifically, periodic excitation accelerates and regulates the generation of large coherent structures (LCS), especially when the mean flow is unstable, the instability in the mean field allows high momentum fluid to be transferred across the mixing layer. Periodic excitation was also used in controlling laminar separation and transition. Subsequently separation control via periodic excitation (both acoustic and hydrodynamic) have been demonstrated on a wide variety of simple configurations, such as flow over backward facing steps and ramps [2,3], sharp leading edges, various airfoils, delta wing and cylinders in cross flow. It is primarily because of the above mentioned

reasons that periodic or unsteady excitation is often used in the control of aerodynamic flows. Thus it is the challenge of this research to use spanwise arrays of ZNMF devices combined with periodic excitation and advanced control algorithms to control the separation of aerodynamic flow from a single element high lift system.

1.2 MOTIVATION

Under the Flow Control portfolio, the U.S. Air Force seeks to advance the fundamental understanding of complex time-dependent flows, their interactions and control, by creatively integrating theoretical, numerical, and experimental analysis techniques to develop physically based predictive models and innovative concepts [4]. Specifically, the interests' lies in understanding the basic issues associated with vortex and shear layer flow and the closed-loop control of such phenomena. Implementing flow control systems will mitigate the vibration and aeroacoustic issues associated with weapons bays; enhance the performance of high performance aircraft and the allow for the reduction in fuel consumption and improved high angle of attack handling qualities for fighter aircraft and facilitate steep climb out profiles for military transport aircraft. To date only the XV-15 Tiltrotor aircraft and the F-16 aircraft have been flight tested with a full active flow control system, thus there is still the need to understand the issues of mechanization of flow control systems in order to take such systems from the wind tunnel to a fully operational active flow control system. To that end, the goal of this research is to explore the physical insights of a single element high lift airfoil under open and closed loop periodic control using specially designed flow control devices.

1.3 BACKGROUND

1.3.1 DEVELOPMENTS IN SYNTHETIC JET ACTUATOR TECHNOLOGY

The last two decades has seen significant design, development and testing of both open and closed loop flow control systems. At the heart of these active flow control systems is the synthetic jet actuator (SJA). There are four different categories of synthetic jet actuator (Figure 1.3); those categories are fluidic, moving object/surface, plasma and electromagnetic. The most common of these is the fluidic device which uses the mechanism of fluid injection and suction in a periodic manner. Of the fluidic devices, the zero-net-mass-flux (ZNMF) devices are the most prevalent in the literature on active flow control. The terms ZNMF device and synthetic jet actuator are used interchangeably. The ZNMF device will be the fluidic device applied in this experimental research project.

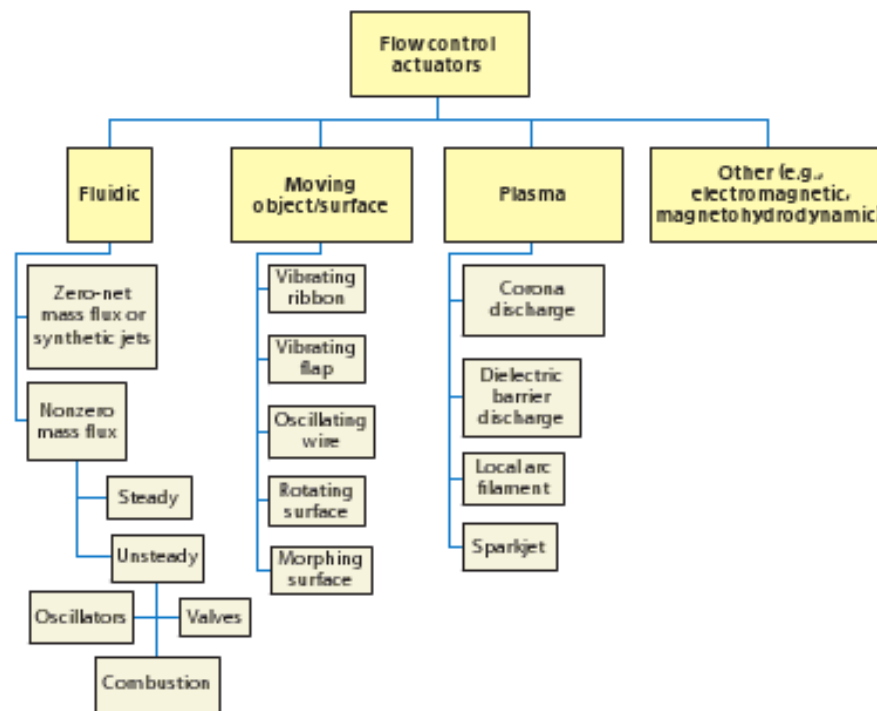


Figure 1.3: Categories of Synthetic Jet Actuators [5]

A typical synthetic jet actuator contains three components: an oscillatory driver/transducer (there are different types and will be discussed below), a cavity and an orifice or a slot. The purpose of the oscillating driver is to compress and expand the fluid in the cavity by periodically (or aperiodically) changing the cavity volume at the excitation frequency f that will create pressure oscillations (Figure 1.4). As the cavity volume is decreased, the fluid in the cavity is compressed and discharges some fluid from the orifice. In a similar way, as the cavity volume is increased, the fluid expands in the cavity creating a localized negative pressure gradient causing fluid to be ingested into the cavity via the orifice. Typical orifice geometries include an axisymmetric hole (height h , diameter d) and rectangular slot (height h , depth d and width w) as shown schematically in Figure 1.5. Note here that the orifice walls are straight. A jet is then formed from the entrained fluid and results in vortices being shed when the driver or transducer reaches and exceeds critical amplitude. Specifically, jet formation is defined as the appearance of a time averaged outward velocity along the jet axis and corresponds to the generation and subsequent convection or escape of a vortex ring [6]. In Figure 1.4, we see that there are three kinds of drivers/transducers that are commonly used in the design of synthetic jet actuators:

- A piezoelectric wafer bonded to a metallic shim and driven by an ac voltage
- A piston driven by a shaker or crankshaft
- A loudspeaker housed in a cavity and driven by an electrodynamic voice coil

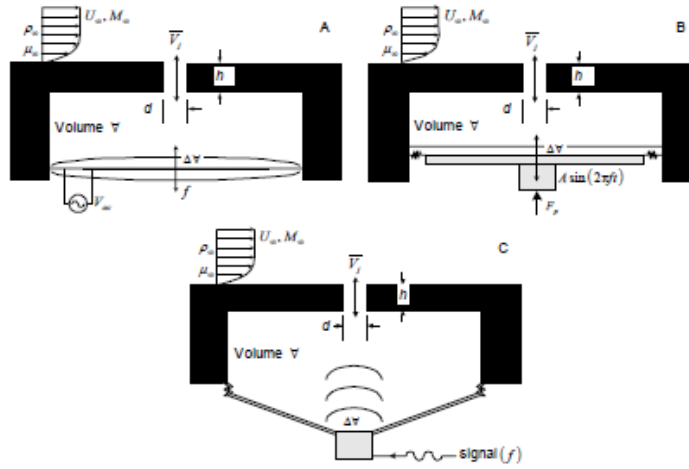


Figure 1.4: Typical ZNMF devices, three different types of excitation mechanisms [7]

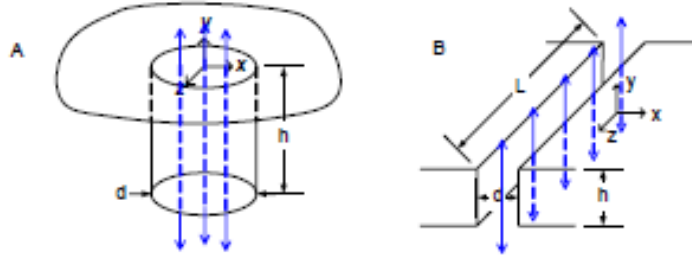


Figure 1.5: Orifice geometry. A) Axisymmetric, B) Rectangular (or 2D) [7]

Each of these SJA configurations has its particular frequency response characteristics; current thinking suggests that a wide bandwidth is required in order to force the low frequency modes present in external flows [8]. A piezo-based SJA has a transfer function that contains peaks and troughs indicating the strong nonlinear nature that results from the combined effects of the driver/cavity and orifice. These types of actuators can also have a single peak which results in a narrow bandwidth. To address this issue, design optimization studies have been performed by Gallas [9] and Oyarzun [10]; yet a wide flat frequency response has not been achieved thus far. One might resolve this design limitation by increasing the diameter of the piezo-disc bender, this however may be acceptable for bench top jet test articles but will not be acceptable for integration into

aerodynamic test platforms where are space constraints to consider. Below in Figure 1.6 are some results of a slot optimization for an input voltage of $100 V_{pp}$. Note that the maximum velocity and gain-bandwidth objective functions yielded identical designs; but more importantly note the single dominant peak and narrow bandwidth.

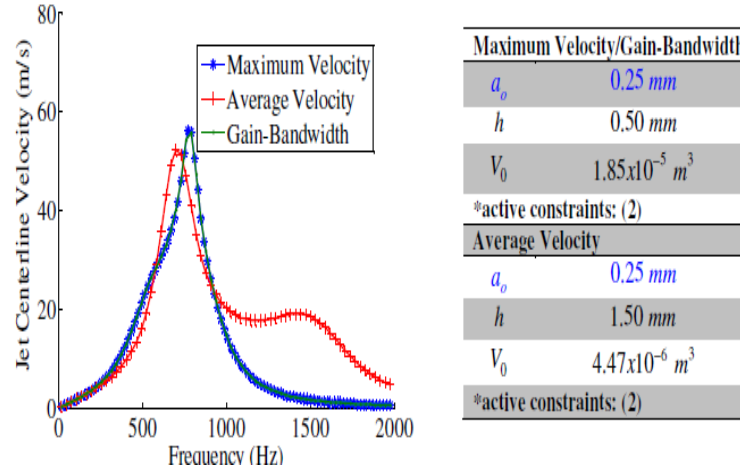


Figure 1.6: Optimization Study Results [10]

The single peak in the transfer function is important because it determines how this specific ZNMF device is excited. Specifically, the narrow bandwidth precludes one from using a pure sinusoidal excitation signal as the actuator will not produce any significant velocity when a single frequency is used, as such nonlinear forcing methods must be employed in order to excite the low frequency wake instability and promote coupling between the frequencies scales present in an external flow.

Although a bench top test article, a dual cavity actuator (Figure 1.7) provides a more favorable result in terms of the actuator broadband characteristics as compared to the single unimorph actuators.

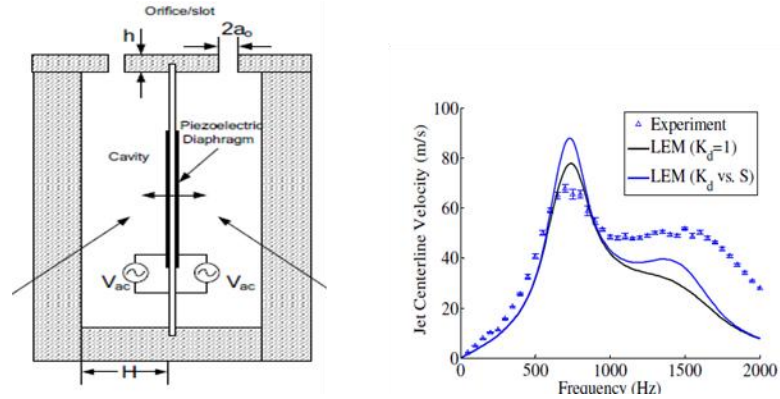


Figure 1.7: Dual cavity SJA with Frequency Response [11]

For an SJA fitted with a piston, such as the one shown below in Figure 1.7, note here that the bandwidth is acceptable in the sense that it is wide enough and has sufficient low end frequencies in order force an external aerodynamic flow (Figure 1.8); the peak velocity is not large enough for high speed wind tunnel testing of active flow control systems. However this may be addressed by some optimization of this configuration.

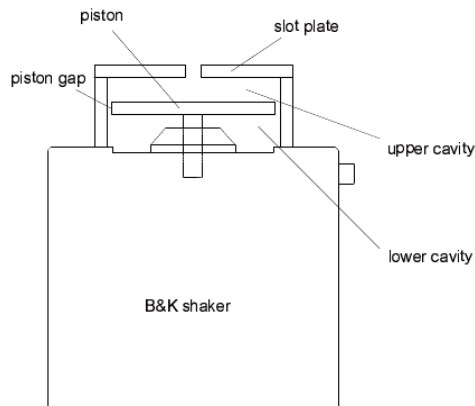


Figure 1.8: Piston Based SJA [12]

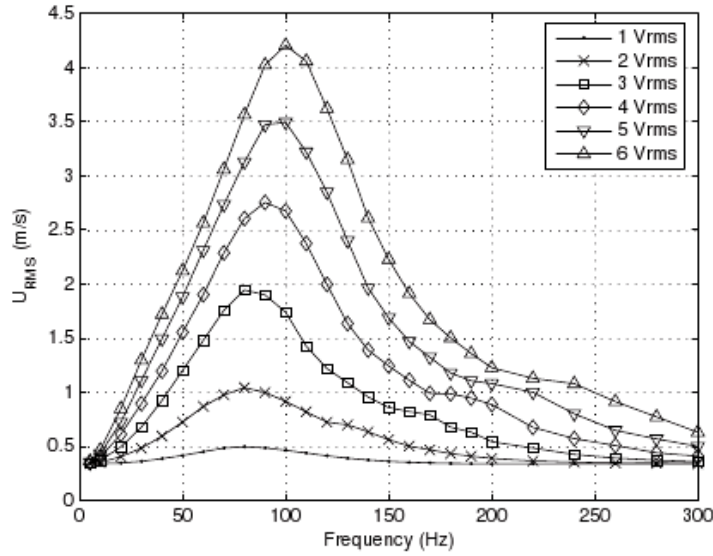


Figure 1.9: Frequency Response of Piston Based SJA [12]

The application of the piston driven ZNMF device is promising in that it is possible to achieve high exit velocities at low frequencies. Once such example in the literature is the work of Gilarranz et al [13]. In this work, Gilarranz presents work on the design and development of a high powered synthetic jet actuator. The operating principle is that of the actuator is that of a crankshaft piston driven engine (Figure 1.10). There are two versions of this actuator (Figure 1.11), one with a fixed slot width and the other is adjustable via a cam. Gilarranz would eventually integrate these devices into a NACA 0015 airfoil. The actuators with the fixed slots were tested at 0.8 mm and 1.6 mm slot widths. For the actuator configuration of 0.8 mm at 200 Hz, the maximum exit velocity was 80 m/s and for the 1.6 mm slot configuration at 200 Hz yielded a maximum velocity of 60 m/s. Experimental evaluation of the adjustable slot actuator revealed that it is capable of 124 m/s at 100 Hz for a 0.4 mm slot width.

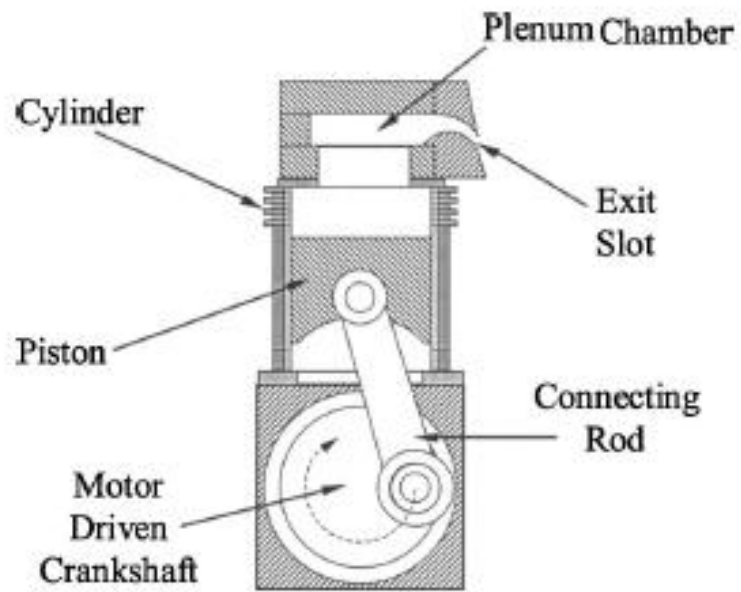


Figure 1.10: Piston Based SJA with curved slot [13]

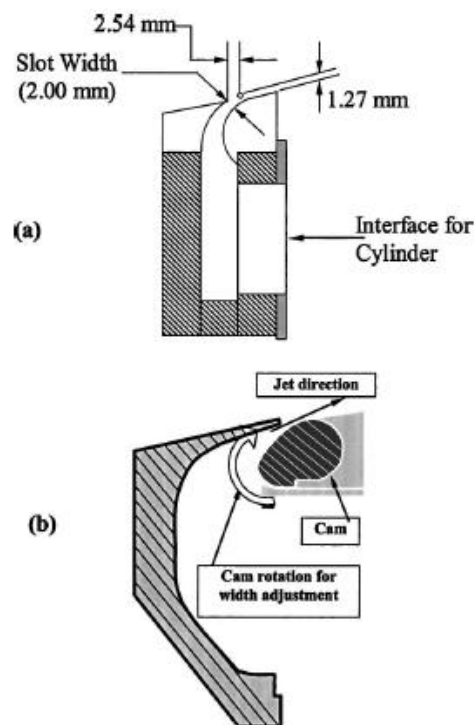


Figure 1.11: Second generation slot [13]

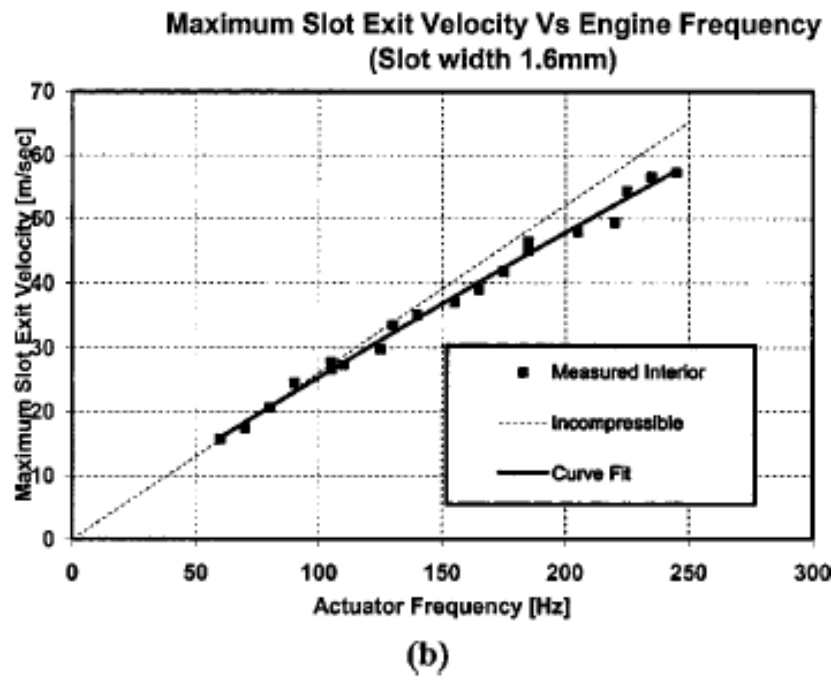
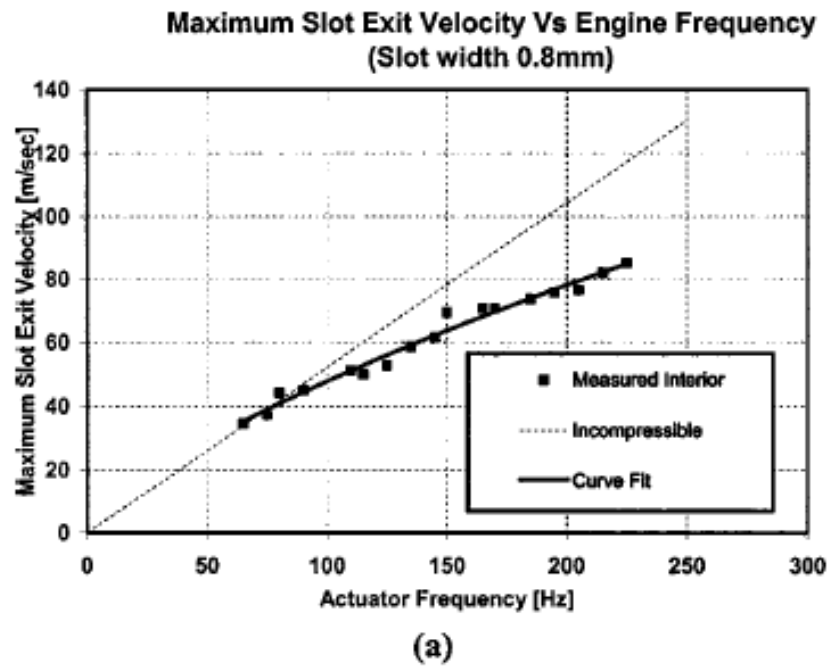


Figure 1.12: Velocity vs. Frequency Diagram [13]

A research program funded by DARPA under the Micro-Adaptive Flow Control program culminated in a successful full scale flight technology demonstration of active flow control on the Bell XV-15 Tiltrotor aircraft (Figure 1.13) [14].



Figure 1.13: Bell XV-15 Tiltrotor Aircraft [14]

The actuators used in the flight test program were designed by Boeing, University of Arizona and IIT. The actuator modules are voice coil based and are designed to produce high exit velocities over a wide frequency range without requiring cooling. The actuator modules themselves are square frames designed to fit in a linear array below specially designed slotted cover plates (Figure 1.14)



Figure 1.14: Actuator Module Flight Hardware [14]

As mentioned above the modules are fitted to slotted plates. In Figure 1.15, note that the slot is two dimensional and curved. The curved slot facilitates the jet leaving the slot at a tangent to the curvature of the trailing edge flap. Note also the application of a curved slot in Gillaraz's work.

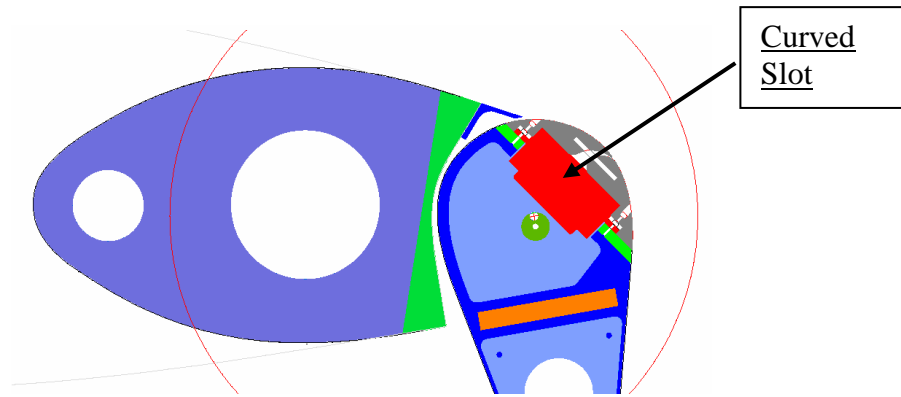


Figure 1.15: XV-15 Integrated Flow Control Actuator [14]

No significant explanation is given in the works of Gilarranz and Nagib as to why curved slots are used in design of the synthetic jet; from schematics it becomes clear that physically it is necessary to develop the cavity-slot geometry to meet the space constraints associated with flight surfaces like the one shown in Figure 1.16. How does this curvilinear slot profile affect the performance of the synthetic jet actuator? This question is best answered by discussing the flow physics in a slot with parallel walls. The flow inside an SJA orifice is naturally unsteady and complex. One of the sources of complexity in orifice flows are the mechanical losses associated with the orifice, namely separation of the flow from the walls on both the in-stroke and out-stroke of the SJA. Separation can cause significant blockage there by reducing the flow in the 'gas path'. This reduction of effective flow is referred to as the *vena contracta*. Orifice flow can be described as having three distinct regions of flow as shown schematically in Figure 1.16.

The first region is predominately entrance flow, followed by a fully-developed region and then an exit region. These flow regions are valid for one half of the total period; by making the assumption that the flow in the orifice is symmetric one can then conclude that the flow will develop in a similar manner when the flow reverses. The first case corresponds to the stroke length being much smaller than the orifice height ($L \ll h$); for this condition it is expected that the internal flow can easily reach a fully developed state with losses of the linear viscous type. The nonlinear, weaker losses are associated with the entrance and exit regions. The second condition occurs when the stroke length is much larger than the orifice height ($L \gg h$). For this condition, the losses are predominantly the nonlinear losses that can be attributed to the entrance and exit effects. The entrance region extends throughout the entire length of the orifice. The last case is where the stroke length and orifice height are of approximately the same order magnitude; the implication is that the losses associated with the fully developed region should nearly equal to those of the nonlinear losses from the entrance and exit effects.

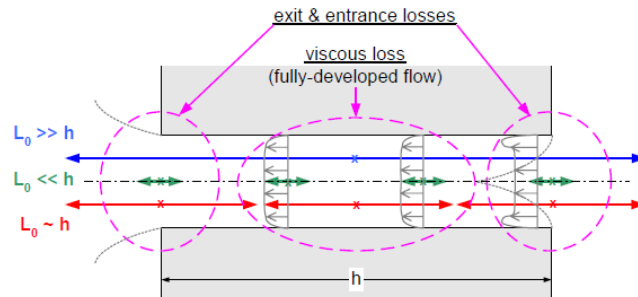


Figure 1.16: Different Flow Regions in Slot/Orifice [7]

The losses mentioned above due to the lack of pressure recovery (slot loss) on the cavity side of the orifice on the in-stroke of the actuator and jet dump loss. To mitigate these losses, it is possible to use a curved neck angled toward the downstream direction. In this manner, the boundary layer flowing over the slot is energized by ingesting low

momentum fluid on the in-stroke and re-accelerate the fluid in the slot on the out-stroke and hence injecting the boundary layer with high-momentum fluid upstream of the slot making the boundary layer more resistant to separation. The details of this design will be covered in the discussion on the design of the synthetic jet actuator.

1.3.2 CONTROL OF FLOW SEPARATION

Active control can be subdivided into two categories: open loop and closed loop control. Closed loop control can be further classified into quasi static and dynamic; for quasi-static closed loop control works on the time scale of the mean flow and dynamic closed loop control works on the scale of the flow dynamics. Active control means that energy is added to the flow via steady suction and blowing or periodic excitation. Open loop separation control studies provide the foundational understanding needed to pursue the development of closed loop flow control systems design and development. Specifically, periodic excitation has been shown to encourage the regulation of large coherent structures in the flow field [15], this is largely due to the fact that fluid flows are nonlinear and contain multiple frequency scales; these frequency scales can be targeted so as to enhance the nonlinear interactions between the separation bubble, shear layer and wake (vortex shedding) frequencies. Open loop flow physics studies, both computational and experimental have revealed that there are parameters that are significant for the flow control task; these parameters are actuation frequency, excitation amplitude, modulation signals, actuation or slot location and orientation, and the effects of Reynolds number and compressibility. For the purposes demonstrating the link between the flow physics and control system development we will concentrate on the first three parameters only.

- **Actuation Frequency**

From Figure 1.17 we see that embedded in a lifting surface aerodynamic flow over are the shear layer instability (f_{SL}) and the global wake instability (with vortex shedding frequency, f_{wake}). These two instabilities interact in a nonlinear manner. The nonlinear interaction referred to here is similar in nature to the phenomena of internal resonance that is found in nonlinear mechanical systems. In Part B of Figure 1.17, we see that there is a closed separation bubble that is at some distance aft of the leading edge; the frequency scale associated with separation is designated, f_{sep} . It is possible that as the flow begins to separate, that all the frequency scales may be present in the flow. In the fully separated region and post stall flow (Part C, Figure 1.17), it is shown that there is a leading edge shear layer rollup and the global instability present. The vortex shedding and shear layer frequency is common to all three fluid flow conditions. When periodic excitation is introduced, one or more of these modes in the flow can be excited. Periodic excitation enhances the weak nonlinear coupling already present in the flow. As a result, the controlled flow becomes more ordered versus broadband and turbulent; this new flow state leads to an increased average lift coefficient. Periodic excitation when viewed from a nonlinear dynamical system point of view encourages synchronization; this is when a nonlinear system that is capable of chaotic behavior, locks on to the frequency of the driving input and for a time results in periodic equilibrium state. It stands to reason then, that the application of closed loop control would extend the region of synchronization. Narayanan and Banaszuk (2003) [16] demonstrated that multi-tonal excitation was successful in the control of separation on planar diffuser.

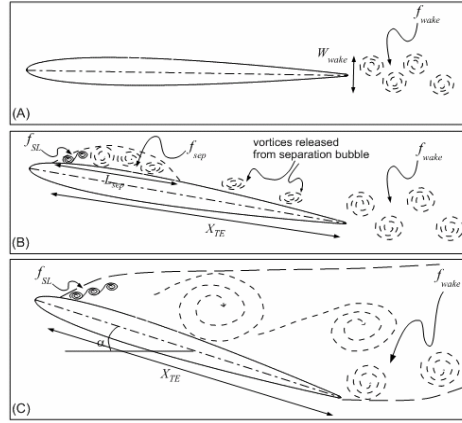


Figure 1.17: Frequency Scales in separated flows [8]

- **Excitation Voltage**

One of the other important parameters for a ZNMF device is the excitation voltage which essentially corresponds to the jet velocity. The excitation voltage will not change as it is predetermined but the output of the ZNMF device will be affected by the change in flow velocity; in fact control authority changes monotonically with flow velocity. It is possible then, for a synthetic jet actuator to become saturated. For a ZNMF flux device to be efficient, small perturbations from the actuator is preferable for controlling a flow; this is consistent with the finding of Pyragas [17] in the sense the small or low level control effort is all that is needed to confine a highly coupled nonlinear system to a periodic orbit or equilibrium limit cycle.

- **Modulation of Input Signals**

Piezo-based actuators as indicated have narrow band frequency responses, even after a design optimization has been performed [9]. Specifically, the Helmholtz frequency of the actuator is typically not located the frequency region of receptivity. To address this design limitation, [18], introduced amplitude modulation method. Since a

piezobased ZNMF device is resonant driven with a periodic signal, it is possible to provide a harmonic wave train $e(t)$, which is amplitude modulated to the actuator:

$$e(t) = [1 + \varepsilon \sin(\omega_m t + \phi_m)] A_r \sin(\omega_c t) \quad (1.1)$$

where A_r is the amplitude of the carrier signal, ω_c is the mechanical frequency of the actuator and ε is the modulation amplitude ($0 \leq \varepsilon \leq 1$), ω_m is the modulation frequency which is set at the desired frequency of receptivity of the fluid system. If one applies trigonometric identities, it becomes apparent the wave train contains frequency components at ω_c , ω_m and at $\omega_c \pm \omega_m$.

Many of the experimental flow control studies present in the literature are open loop control for fixed wing separation control applications. Initially, closed loop flow control studies were focused on the control of aeromechanical (or compressor) instabilities in jet engines and combustion instabilities. The increase in the level of sophistication in the control algorithms applied to aerodynamic flow control problems has been evidenced in the research work conducted on active control of cavity flows mainly by [19, 20]. Before describing some of these relevant works, it is important to understand some of the issues that face the development of appropriate and effective closed-loop control strategies. The successful application of closed-loop control is dependent upon the availability of a mathematical model that accurately represents the phenomena of interest; this is in fact the case for modern control theory. The difficulty with such models for flow control is that reduced order models (ROM) tend to be high dimensional and highly nonlinear. It should be stated that not every feature of a turbulent flow for example needs to be modeled and controlled; it is sufficient to capture only the dominant instabilities or large coherent structures [21] and in turn the model is computationally tractable. One of the

main shortcomings of model reduction is the when a controller is applied to such a reduced order model; the result may not be realistic since the controlled result may have driven the model beyond its mathematical validity. Also it is difficult to accurately capture the transient growth of stable modes for a given flow problem. For example Joshi pointed out that in their application of a PI controller to transitional channel flow; it was observed that the control action induced an unobservable transient response that could trigger turbulence. In other words, the control action should not induce instabilities. This is holds true for controllers designed in the frequency domain. Controllers designed based on modern control theory are more suited to handling transient effects via eigenmode non-normality. However it may be more efficient in model based controllers to utilize robust control theory because these design methods have robustness properties embedded in them that not only account for external disturbances, but also model uncertainties and errors. Error and uncertainties arise from the manner in which the models are formulated. Several mathematical methods are presented in the flow control literature and they are as follows: Proper Orthogonal Decomposition, the Galerkin Projection Method and Balanced truncation. The reader is directed to Rowley and Batten [21] for further details on each of these methods of model reduction. For completeness, there are computational approaches such as LES and DNS but are not necessarily appropriate for real time high speed computations associated with experimental active flow control. The issues discussed here are by no means exhaustive; for a more through survey of the multidisciplinary issues associated with active flow control the reader is directed to [22 and 23]. Now let us revisit the discussion on cavity flows. Why are cavity flows important? The flow over open cavities is relevant in many aerospace, automotive and

naval applications. The freestream condition under which cavity flow are induced can vary from low speed incompressible flow to highly compressible supersonic flow. The flow conditions produce physical phenomena that have intense pressure fluctuations inside the cavity which are generally undesirable. The flow field characteristics and the intense aero-acoustic environment are driven by the interaction of the shear layer with the aft wall of the cavity. This interaction of the flow with the cavity wall setup a resonance characterized by tones in the unsteady pressure spectra. These tones are often accompanied by large amplitude broadband pressure levels that detrimental to the contents of the cavity and the vehicle itself; one such example is airframe structural fatigue in weapons bay cavities caused by the resonance [24]. In the context of the research task at Clarkson University, we will focus on some of the closed loop control algorithms applied to the cavity flow control problem.

Debiasi and Samimy [25] present results of an experimental investigation for controlling shallow cavity flow in the Mach number range of 0.25-0.5. The flow exhibits the staging characteristics that were predicted by semi-empirical Rossiter formula with multiple modes for the Mach number range of 0.32-0.38 and a single strong mode at other Mach numbers. It was found that forcing the flow at M0.3 demonstrated that the actuator had good authority over a large range of frequencies; to that end logic based controller was implemented to search the frequency space for the optimal forcing frequency. The logic based controller is based the application of three if statements related to the maximum sound pressure level and frequency. The controller operates in a closed loop fashion by using feedback information from the flow until it has found the satisfying forcing frequency, once the frequency is found it reverts back to an open loop scheme. The

controller was embedded in an outer loop that continuously monitored the flow and triggered a new search if there was an increase in spectral intensity or change in flow Mach number. The results generally showed a marked reduction in the frequency peaks associated with the baseline cavity flow. This controller did not require the use of a mathematical model. In the experimental work of Caraballo et al [26], a reduced order model was developed from PIV images and combined with stochastic estimation based on six sensors. This model was then used in designing an optimal controller with the Linear Quadratic Regulator (LQR) theory. The experimental results show that for a flow Mach number of 0.3, the LQR based controller significantly reduced the amplitude of the stable limit cycle. Kegerise et al conducted a two part cavity flow control experiment in which a fixed gain and adaptive controller were applied to the cavity flow-resonance problem. In Part One of the experiment, a generalized predictive control (GPC) algorithm was formulated. The control algorithm demonstrated it could suppress multiple Rossiter modes at a fixed Mach numbers ranging from 0.275-0.38. The controller performance was evaluated with output disturbance rejection and an input sensitivity transfer function. In Part Two of the experiment, an adaptive version of the controller was applied; The control algorithm utilizes a gradient decent approach (the basis for the least mean square (LMS) adaptive filter) to update the GPC coefficients at each step. The past input-output data and an estimate of the open loop response are used to implement the algorithm at fixed Mach numbers. The results show that the adaptive controller was able to suppress multiple frequency peaks at various Mach numbers and was also capable of sustained suppression from M0.275 to M0.29, beyond this range; the controller is limited by spill over induced by the fixed plant model used in the adaptive control algorithm. Here are

but a few examples of the application of closed loop dynamic controllers to the specific flow control problem of open cavities; a thorough treatment of these activities can be found in [27]. It should be noted here that regardless of the controller design the resulting control signal must be incorporated into a harmonic voltage input signal to the actuator. As such, the parameters that can be adjusted by the designed control signal are the amplitude and the frequency. The criterion for selection of which parameter to use is most likely determined by the sensitivity of the flow system and the control task. However such design information is not often given explicitly in the research works on active flow control unless it is clearly stated. For the logic based controller example in which a harmonically driven compression driver-diaphragm fitted with a converging nozzle was used, it was the frequency that was adjusted based on the changes in the flow condition. For the LQR example, it is not clear how the control signal was incorporated into the harmonic voltage input to the actuator. Mapping the control signal is an important detail when considering the design and implementation of control algorithms in a real time environment. We will now turn our attention to the application of adaptive and extremum seeking control algorithms to lifting surface, channel and flat plate flow control problems.

Wu and Breuer [28] present experimental work on the control turbulent boundary layers in a water channel facility. The control scheme used in this experiment is called the Filtered-X-LMS algorithm (FXLMS). The FXLMS algorithm is based on the finite impulse response (FIR) version of the LMS adaptive filter. FIR filters are used because they do not induce phase distortion due to its inherent linear phase response and they computed without recursion and are always stable. For further details on the LMS

algorithm and the properties of FIR filters, refer to Haykin [29]. Rathnasingham and Breuer [30] found however the LMS approach was computationally intensive and was susceptible to changes in the flow system, actuator performance and sensor drift. Hence the application of the FXLMS filter. The FXLMS filter differs from the LMS filter in that the feedforward path contains an additional filter which essentially estimates any changes that may arise in the system dynamics and negates the effect of any phase delays. Note that there are different versions of the FXLMS algorithm. The results show that the FXLMS algorithm was able to integrate inputs from multiple sensors and isolate coherent structures and reject spurious small scale noise. The controller was also able to maintain control in the presence of large phase delays between reference and feedback sensors and the actuators. The FXLMS algorithm also performs well in the presence of nonlinearities. The FXLMS algorithm readily implementable in practical flow control applications and is not model based.

At TU Berlin, a technique for controlling Tollmien-Schlichting (TS) Waves was successfully implemented in low speed wind tunnel experiments to cancel TS-Waves in a two-dimensional laminar boundary layer of an unswept modified NACA 0008 wing. Naturally occurring TS waves were attenuated by active control down to 10 % of the wing chord. The control scheme used in this instance was again the FXLMS algorithm typically used in active noise control applications.

Tian and Cattafesta present experimental results performed on a NACA 0025 airfoil [31]. An adaptive closed-loop controller (can be classified as system identification and disturbance rejection algorithm) is used to optimize the lift to drag ratio of post stall

separated. A more detailed description of this work is given Tian's doctoral thesis [32]. The input to the actuators used multiple amplitude modulated (AM) or burst modulated (BM) signals that covered 33% of the airfoil span. A simplex optimization approach was applied to the lift and drag measured by a strain gauge balance for feedback and for searches for the optimal AM or BM actuation in the closed loop configuration. An energy penalty function based on electrical power consumption of the actuators was added to the cost function to study the tradeoff between the aerodynamic performance and the power required for closed loop control. In the initial assessment of the aerodynamic characterization of the airfoil, it was observed that a convective instability was present in the separated shear layer and vortex shedding in the wake. The application of the closed loop control increased the lift-to-drag ratio by a factor of 3 due to small amplitude forcing (both AM and BM) of the nonlinear interactions between the convective instability and the vortex shedding global instability.

A control system design that has been particularly successful in recent flow control experiments is extremum seeking control [33, 34, 35, 36, and 37]. Extremum seeking control does not require any model of the fluid system and has been shown experimentally to be very robust. This method measures signals and uses the information to maximize or minimize some quantity (e.g. minimize drag), and adjusts the value of a control system parameter in order to facilitate the extremization of this quantity. The tuning is performed by the superposition of small variations on the control parameter; the change in the control parameter depends on whether the quantity to be extremized is in phase or out of phase with the variations of the control parameter. The extremum seeking controller can be classified as a quasi-static control scheme. This section served to

introduce the some of the challenges associated with active flow control; however a more in-depth discussion on the control theory and physical concepts related to controlling flow separation will be presented in Chapter 2.

1.3.3 FLOW CONTROL APPLICATIONS IN AEROSPACE

There are a significant number of fixed wing flow control studies in the literature, however in this subsection, only those flow control experiments pertinent to the work at Clarkson University presented. Lovato [38] conducted experimental work on a NACA 0015 airfoil using acoustic excitation for flow control. The experiment was conducted for both a static and a dynamically pitching airfoil. Only the static airfoil results are relevant to the work at Clarkson. For the static airfoil, Lovato determined that the frequency, at which the free shear layer is most receptive to active control, is equal to four times the calculated vortex shedding frequency of the NACA 0015 airfoil studied in her experiment. The fundamental frequency researches a constant after the separation point arrives at the leading edge and the airfoil has stalled. Forcing at the fundamental frequency inhibits vortex pairing which prevents shear layer growth; the implication is that the separated region is then reduced as a result. Control or forcing the flow at the corresponding sub-harmonics enhances vortex pairing which causes the shear layer to grow. The overall result from this experiment is that a 36% increase in the upper surface pressure coefficient was witnessed when airfoil was actuated in an open loop control configuration. Active flow control wind tunnel experiments were conducted at NASA Langley's Low Turbulence Pressure Tunnel (LTPT) using a two-dimensional supercritical high-lift airfoil (Energy Efficient Transport) with a 15% chord hinged leading edge flap and a 25% chord trailing edge flap [39]. The focus of this work is the

application of ZNMF devices near the trailing edge flap shoulder at $M0.1$ and a chord Reynolds numbers 1.2×10^6 to 9×10^6 with leading and trailing edge and trailing edge flap deflections of -25 degrees and 30 degrees, respectively. Active flow control was applied both upstream of the trailing edge flap and immediately downstream of the trailing edge flap should and the effects of Reynolds number, excitation frequency and amplitude are demonstrated. The excitations around the trailing edge flap are then combined to control trailing edge flap separation. The combination of two closely spaced actuators around the trailing edge flap knee was shown to increase the lift produced by an individual actuator. Phase sensitivity between two closely spaced actuators seen at low Reynolds numbers is confirmed at higher Reynolds numbers. It was found that the momentum input to completely control flow separation on the configuration required significant control power, more than the actuators were capable of providing. Greenblatt [40] used a NACA 0015 semispan airfoil with a chordwise split flap to demonstrate dual location separation control. The ZNMF perturbations were introduced first at the leading edge, the shoulder of the deflected flap separately and then in both locations simultaneously. Leading edge periodic excitation mimic the effect of a leading edge device and the flap shoulder excitations simulate additional flap deflection and have the effect of reducing drag. The simultaneous excitations at post stall angles of attack produce an increase in the wings lift that exceeds each of the jet locations individual contribution. When the excitation frequencies are the same, lift is strongly dependant on the phase difference between the two excitation locations. An optimum phase difference is reached when the suction stroke of the flap-shoulder control coincides with the minimum shear layer proximity to the flap surface. At the optimum phase difference,

increases in lift are observed over the entire semispan wing, resulting in the wing maximum lift coefficient between 0.24 and 0.44 depending on the flap deflection configuration and angle. Flap-shoulder control effectiveness does not diminish at the extremities of the finite inboard flap; neither inboard in the vicinity of the junction vortex nor outboard in proximity to the flap edge vortex. For large flap deflections across the entire span, flap-shoulder control excitations generate a powerful tip vortex that can be exploited for lift enhancement on low aspect ratio wings. The sensitivity to excitation phase difference is however decreased significantly as one moves toward the wing tip.

An extensive series of wind tunnel tests were performed at the Illinois Institute of Technology's large wind tunnel facility to examine effects of active flow control on an advanced high lift airfoil with a simple flap [41]. These tests were conducted under the auspices of the Boeing/DARPA/NASA/AFRL sponsored Adaptive flow control Vehicle INtegrated Technologies (ADVINT) program. The goal of the test program was to gain further insight into the mechanisms that govern active flow control for flow states with large separated regions and its effects on separation control versus circulation control. Steady blowing was used extensively in conjunction with a surface tangent downstream facing slot located immediately upstream of the flap on the trailing edge of the main element. Amplitude sweeps were carried out for several flap configurations and freestream velocities over a wide range of angles of attack. Nagib et al state in their conclusions, that improvements in the sectional lift coefficient do not necessarily imply that the separation region is being fully eliminated; but perhaps the circulation is being enhanced, hence the improvement in lift. They also state that controlling separation and circulation are coupled together.

Melton et al [42] present results on a NACA 0015 airfoil with 30% chord trailing edge flap tested at deflection angles of 0, 20 and 40 degrees. The primary objective this experiment was to compare force and moment data obtained from integrating the surface pressures to data obtained from a 5-component strain gage balance in preparation for further three dimensional testing of the model. Active flow control (unsteady excitation) was applied at an angle of 6 degrees where published results indicate that oscillatory momentum coefficients exceeding 1% are required to delay aerodynamic separation. Periodic excitation with an oscillatory momentum coefficient of 1.5% and a reduced frequency of 0.71 caused a significant delay of separation on the airfoil with a flap deflection of 20 degrees. Higher momentum coefficients at the same reduced frequency were required to achieve the same level of flow attachment on the airfoil with a flap deflection of 40 degrees. There was a favorable comparison between the balance and integrated pressure force and moment results. The experiment conducted by Melton et al [42] and Greenblatt [40] are very relevant to the research being conducted at Clarkson in that the results presented give researchers insight into the open loop actuated wing performance for various model configurations .

1.4 RESEARCH OBJECTIVES

1. Understand the open loop behavior of a NACA 0015 high-lift system and thenature of the flow physics of this system without control;
2. To infer about the merits of selected control laws by representing the flow physics with a highly nonlinear dynamical system in order to understand the mechanism of synchronization as it relates to active flow control; from this evaluation select the appropriate control law(s);
3. Demonstrate closed loop control experimentally and hence synchronization by implementing suitable control laws;
4. Validate numerical investigations (using a chaotic attractor) with experiments, and analyze the experimental results using linear and nonlinear signal processing analysis which will expose the nonlinearities in the flow and help visualize the mechanism of synchronization.

1.5 TECHNICAL APPROACH

The closed loop separation research task is first initiated with the design and fabrication of synthetic jet actuators that are specially designed to fit inside a NACA 0015 airfoil with a simple flap. This is followed by the installation of an instrumentation package that consists of pressure transducers, a force balance strain gauge wire harness and an accelerometer. The data acquisition and control will be executed using hardware in the loop equipment. We will begin the experimental study with a wind tunnel test of the un-actuated wing for the purpose of flow physics characterization and data analysis. From

the analysis, specific wing configurations and test conditions will be selected for open and closed loop control studies. This activity will be then followed by an assessment of the open and closed loop results. In parallel with this experimental activity, modeling and simulation of a dynamical system will be used to select the control scheme to be used in the closed loop control of separated flows on the experimental test wing here at Clarkson University.

1.6 OUTLINE OF THE DISSERTATION

In the first Chapter a brief state-of-the-art on active flow control is presented. Chapter 2 begins with the presentation of the theoretical background on the applicable control and dynamical systems theory followed by the simulation and modeling of a dynamical system under closed loop control and the data analysis methods to be used in this research. Chapter 3 describes the experimental design and the control system hardware and software configuration that will be used in this research. Chapter 4 will discuss the results obtained from the system identification wind tunnel tests on the un-actuated NACA 0015 single element high lift system followed by preliminary aeroacoustic assessment of the configured wind tunnel test section. In Chapter 5, the results of the open and closed loop control experiments are given and discussed. Lastly, Chapter 6 will consist of a summary and follow-on research directions.

CHAPTER 2.0: MODELING, SIMULATION AND CONTROL THEORY FOR ACTIVE FLOW CONTROL

2.1 INTRODUCTION

In this chapter we attempt to understand why the presence of unsteady periodic forcing of boundary layer causes the phenomena of boundary layer (BL) separation to be delayed or a separated wake to reattach itself to a lifting surface. Using a chaotic attractor as an analogy for a turbulent BL, we present simulation results that provide some preliminary insight into the mechanism of synchronization which allows periodic closed loop control to be effective is the suppression flow instabilities and the reattachment of separated flows. Two candidate control laws based on Pyragas and Extremum Seeking Control are evaluated followed by an Adaptive PID controller.

2.2 SYNCHRONIZATION AND ACTIVE FLOW CONTROL

Synchronization is a basic nonlinear phenomenon in physics, uncovered by Huygens; specifically, Huygens found that two weakly coupled pendulum clocks (hanging on the same beam) became synchronized in phase [43]. There are many different types of synchronization such as complete synchronization, lag synchronization, generalized synchronization, phase and imperfect synchronization. With respect to active flow control we are interested in phase synchronization or frequency locking. Self-sustained oscillators that are external driven by a periodic forcing function exhibit frequency locking. Similarly, a *fluid system* is a weakly coupled nonlinear system that when forced by a periodic or unsteady excitation results in a re-organization of the flow structures present in the fluid systems hence the relevance of synchronization to active flow control. A typical boundary layer attached to a lifting surface possesses frequency scales or

modes. These frequency scales (or instabilities/frequency receptivity) can be exploited to affect the manipulation of the boundary layer. Experimental work has shown aerodynamic fluid flow to be sensitive to the magnitude of forcing and the input frequency. Seifert and his colleagues [44] point out the following:

A fundamental mechanism that is often identified in SJ (synthetic jet) based separation control is the formation of large coherent structures in the separated shear layer due to oscillatory forcing. These structures entrain outer high momentum fluid into the boundary layer; thereby delaying separation. However, the effectiveness of this mechanism relies on the receptivity of the mean flow to the imposed oscillations which in turn depends on the stability characteristics of the separated flow. Thus to be effective, the perturbations have to be of appropriate frequency and sufficient amplitude and be introduced at the right location in the boundary layer.

Lovato (1992) [38] conducted active acoustic control experiments on a NACA 0015 airfoil, for which tangential pulsed air was employed. The following conclusions were drawn:

1. The fundamental frequency for a NACA 0015 airfoil is a function of angle of attack and freestream velocity prior to stall. This frequency is an integral multiple of the wake frequency. Post stall the frequency remains constant as the angle of attack increases and is a function of the freestream velocity only.
2. Acoustic and pulsed air active control at the fundamental frequencies is successful in inhibiting the pairing of the vortical structures in the separating boundary layer. Active control at the sub-harmonics of the fundamental frequency enhances vortex structure pairing.
3. Active control at frequencies corresponding to the fundamental frequencies of the NACA 0015 airfoil and its sub-harmonics reduces the size of the post stall

separation region over the airfoil and results in increased surface pressure coefficient magnitudes.

Experiments for the both static and dynamic airfoils cases, but only the static airfoils results are applicable to the AFOSR project at Clarkson University. Joe et al [45] performed numerical simulations on a flat plate at $Re=300$ at high angles of attack with leading and trailing edge actuation. Their objective was the control of vortex shedding. The results demonstrated that vortex shedding was amplified when forced at this frequency resulting in larger lift oscillations; it was also noted that there was a sensitivity to phase angle (between the input and lift coefficient) at high angles of attack. A feedback controller was designed to generate stable phase locked limit cycles for a larger range of forcing frequencies. This provides the capability to have a sustained high lift condition. For the same flat plate configuration, Taira and Rowley [46] applied the extremum seeking control algorithm in order to track and obtain the optimal forcing frequency in a continuous time manner. Preliminary results indicate that separated flows can lock on to such optimal forcing frequencies to maximize lift. From these few references one can see clearly that the mechanism that these researchers are attempting to exploit is synchronization. It is pointed out by Pyragas and others that there exists an infinite number of unstable periodic orbits (UPOs) that are embedded in a strange attractor. These UPOs can be stabilized by small perturbations. When we attempt to control the flow over a lifting surface with unsteady excitation we are in fact targeting these unstable periodic orbits in the flow; we know them as coherent structures. A coherent structure for example is a pair of counter rotating vortices that tend to remain stationary and have more or less the same size [47]. The best way to understand the concept of

synchronization is to perform a simple numerical experiment. To facilitate this we will now introduce the well-known Rossler oscillator. The Rossler oscillator is the simplest chaotic system with continuous time, because it has a single second order nonlinear term, zx in its equations. The Rossler oscillator also exhibits strong phase coherence. The Rossler oscillator equations are given as follows:

$$\begin{aligned}\dot{x} &= -\Omega y - z + F(t) \\ \dot{y} &= \Omega x + ay + F(t) \\ \dot{z} &= b + z(x - c) + F(t)\end{aligned}\tag{2.1a, b, c}$$

Where $\Omega = 1, a = b = 0.2$ and $c = 5.7$. These parameters yield a Rossler oscillator in a chaotic regime. In the physics literature there are two main methods for inducing synchronization; they are external forcing via a coupling with another nonlinear dynamical system and open loop periodic forcing. Since we are interested in the effects of closed loop excitation of fluid systems, we will use a simple method given by Pyragas. Pyragas presents work on time continuous self controllers [17]. The results show that for a relatively small feedback gain, stabilization of an unstable periodic orbit can be achieved. Pyragas makes reference to a ‘periodic external force of special form’. The special form that Pyragas discusses is of the form:

$$F(t) = k[y_i(t) - y(t)]\tag{2.2}$$

The term $y_i(t)$ is the desired periodic orbit and the constant k is known in the dynamical systems literature as a coupling constant and in the control systems community it is a proportional gain. The second term $y(t)$, is a state from the system that is feedback. Schematically the system is as follows:

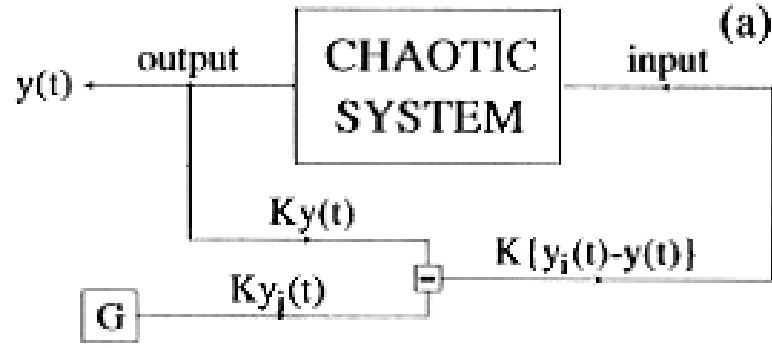


Figure 2.1: System and Control Law [17]

The specific control law for this numerical experiment will be of the form given in Equation 2.2 and can be written as follows:

$$F(t) = k[\sin(2\pi f_F t) - y] \quad (2.3)$$

From Equation 2.3, we can see that there are two parameters, the proportional gain and the forcing frequency. The numerical experiment will be conducted in two parts; the first part will evaluate the influence of the forcing amplitude governed by the parameter, k , and the forcing frequency will be held constant at twice the fundamental frequency of 0.17 Hz. The second part will involve fixing the forcing amplitude $k=1$ and varying the forcing frequency at even multiples of the fundamental frequency. Before we present the closed loop results, the open loop dynamics of the Rossler oscillator are presented in Figure 2.2 and Figure 2.3.

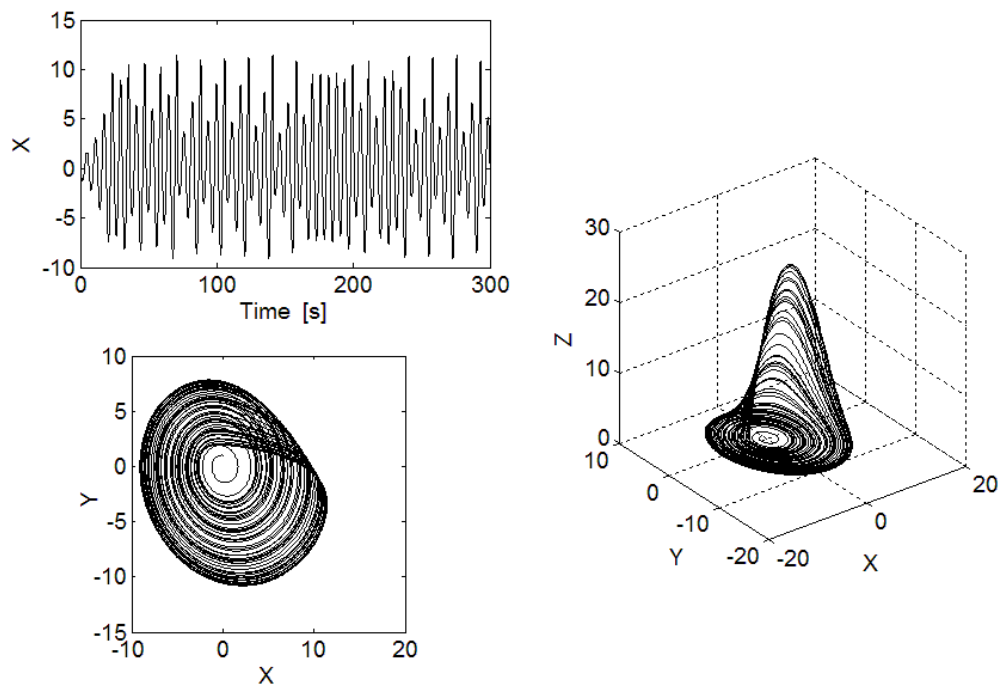


Figure 2.2: Open Loop Dynamics of the Rossler Oscillator

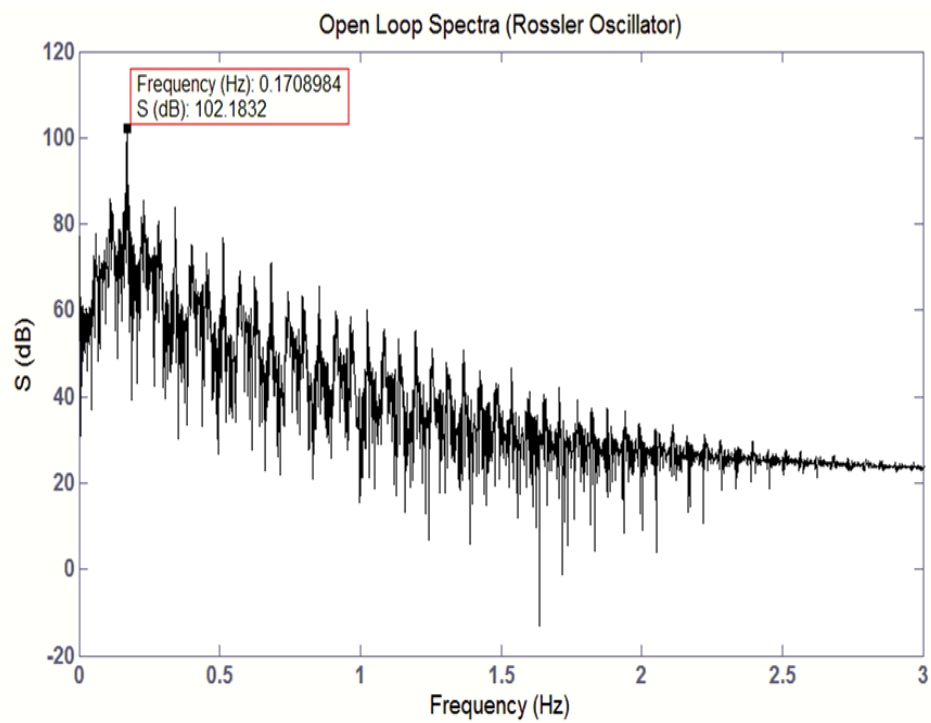


Figure 2.3: Rossler Oscillator: Open Loop Spectra

The Fourier spectrum of the Rossler oscillator is in general broadband and is characteristic of low dimensional chaotic systems i.e. one to three dimensions. The reader will note that there is an arrangement of distinct peaks; these peaks correspond to the Rossler bands seen in phase plane of .The results are presented in the sections to follow consist of a 2 by 2 plot matrix. The first plot is the time history of the state X , followed by the phase plane (X, Y), the time series of the control signal, U , and then phase plane (U, X) which is called a Lissajous curve.

2.2.1 THE EFFECT OF FORCING AMPLITUDE ON SYNCHRONIZATION

For $k=0.01$ (Figure 2.4) we see that the interior Rossler bands appear to be squeezed together. This happens because certain frequencies are suppressed although still in a chaotic regime. The attractor still exhibits strong phase coherence. It should be pointed out that the forcing amplitude is very small yet we see significant changes to the features in the phase plane. Note that in the frequency spectra (Figure 2.5) we see that the largest peak associated with the natural dynamics of the system is moving toward 0.17 Hz. To the right of the largest peak we see that there are peaks missing as compared to Figure 2.3; as mentioned previous these peaks are suppressed and this is how they present in the frequency spectra. For $k=0.05$, the influence of the forcing frequency is more pronounced. In the phase plane (X, Y) (Figure 2.6) we see that the Rossler bands collapse onto each other. Like the phase plane plot, the Lissajous curve (U, X) also shows the bands collapsing onto each other as expected. The frequency spectra (Figure 2.7) shows that there is a peak at 0.1129 Hz that is completely suppressed as are other modes to the left of the 0.168 Hz peak.

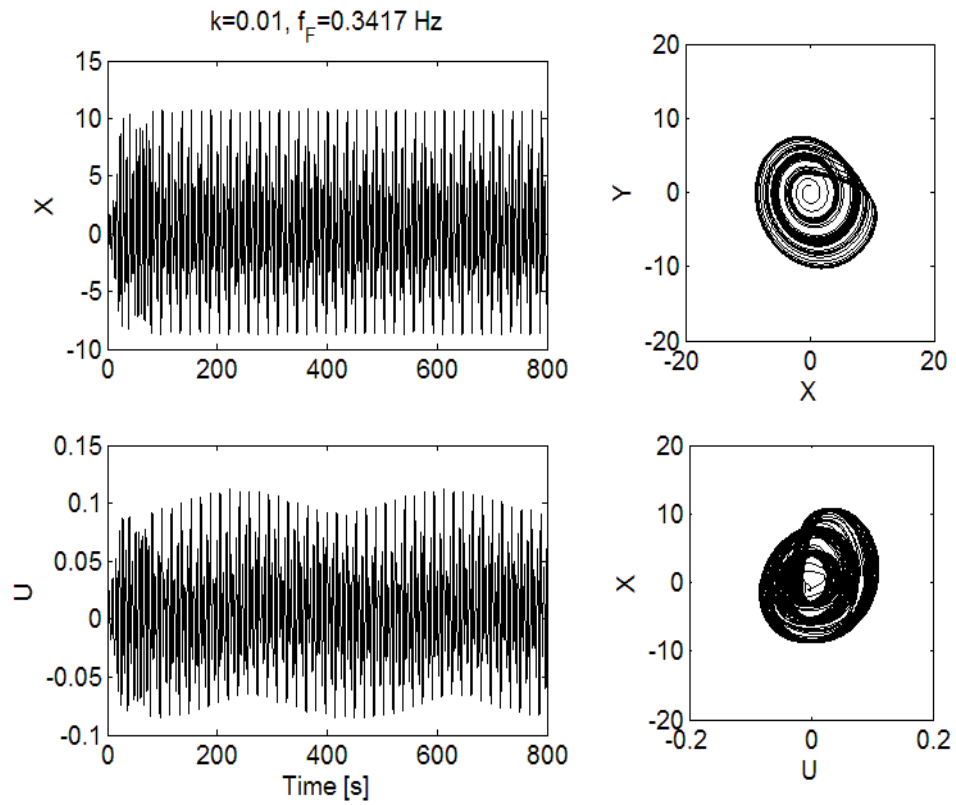


Figure 2.4: Closed Loop control of Rossler oscillator [$k=0.01, f_F=0.3417 \text{ Hz}$]

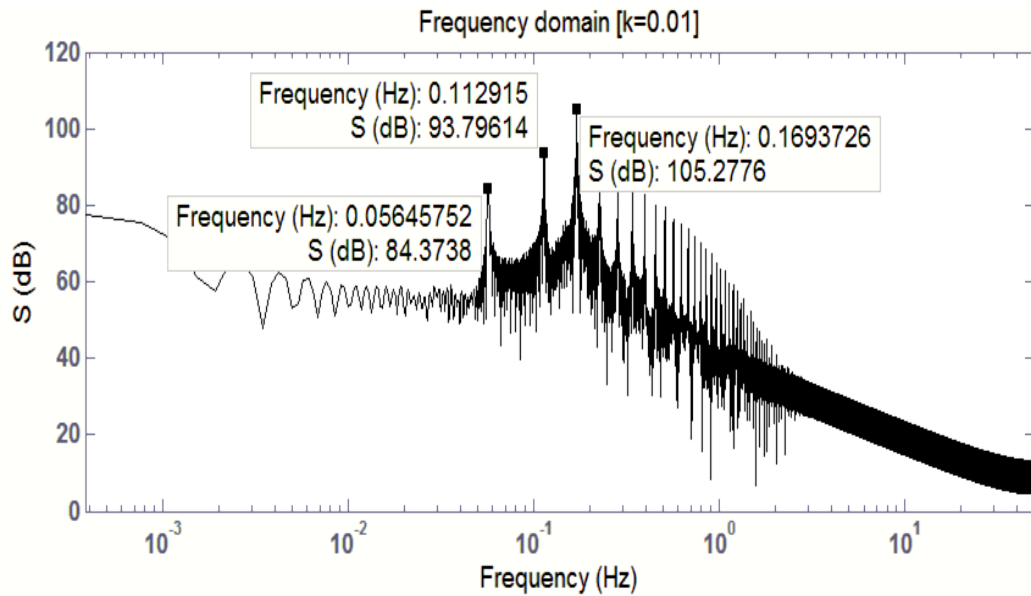


Figure 2.5: Closed Loop FFT [$k=0.01, f_F=0.3417 \text{ Hz}$]

The peak located at 0.168 Hz will eventually pass through 0.17 Hz and keep increasing to the right with increasing feedback gain until the frequency of 0.34 Hz is reached; at this point we say that the system is synchronized. When the feedback gain is less than 0.2, we see that the eyelet expands (Figure 2.8) and converges to a tight band that encircles a spiral. The frequency spectra (Figure 2.9) shows that the region to the left of the 0.168 Hz peak now has no peaks, indicating that all low frequency modes have been completely suppressed.

In general, when the feedback gain is increased, the closed loop system under goes a bifurcation; this bifurcation can be characterized by either a Lyapunov exponent or a parametric plot that consists of the feedback gain, k on the horizontal axis and the state, say X on the vertical axis. When this is done it was found that a gain equal to 0.2 (Figure 2.10) resulted in the collapse of the eyelet in the phase plane (X , Y). This collapse or shrinking of the eyelet means that the phase coherence is being destroyed; beyond this value of feedback gain the Rossler attractor is then frequency locked.

Removal of the transient reveals a rotated elliptical double limit cycle, in both the phase plane (X , Y) and the Lissajous curve (U , X). The coupled limit cycle indicate that there are two frequencies present. This observation is supported by Figure 2.12 where we see two frequency peaks. This 0.1716 Hz peak will migrate toward the prescribed forcing frequency of 0.34 Hz also seen in Figure 2.12.

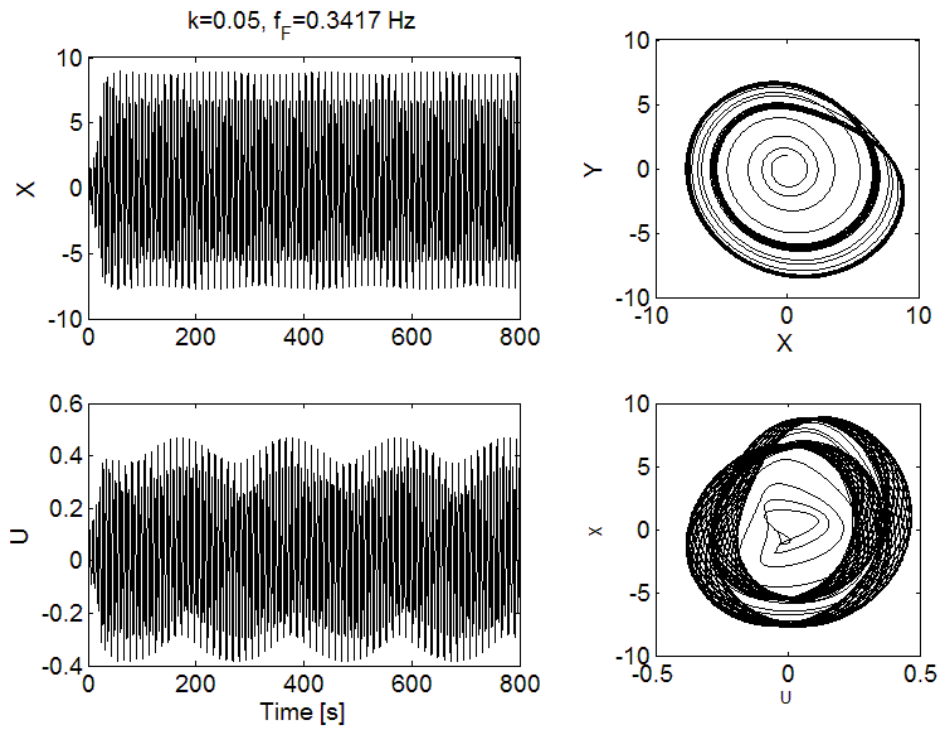


Figure 2.6: Closed Loop control of Rossler oscillator [$k=0.05, f_F=0.3417 \text{ Hz}$]

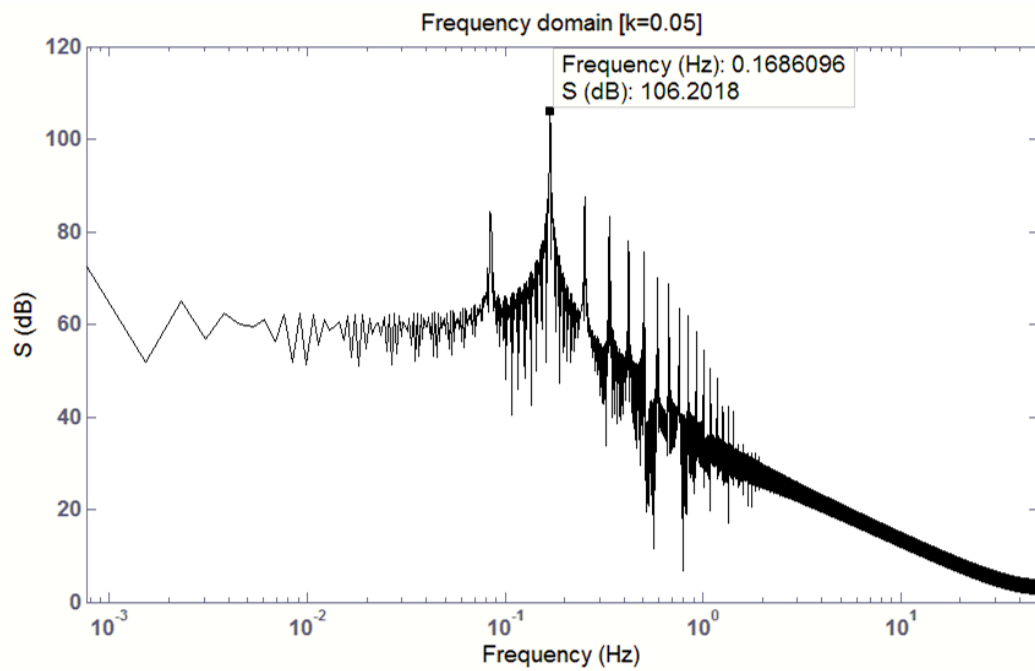


Figure 2.7: Closed Loop FFT [$k=0.05, f_F=0.3417 \text{ Hz}$]

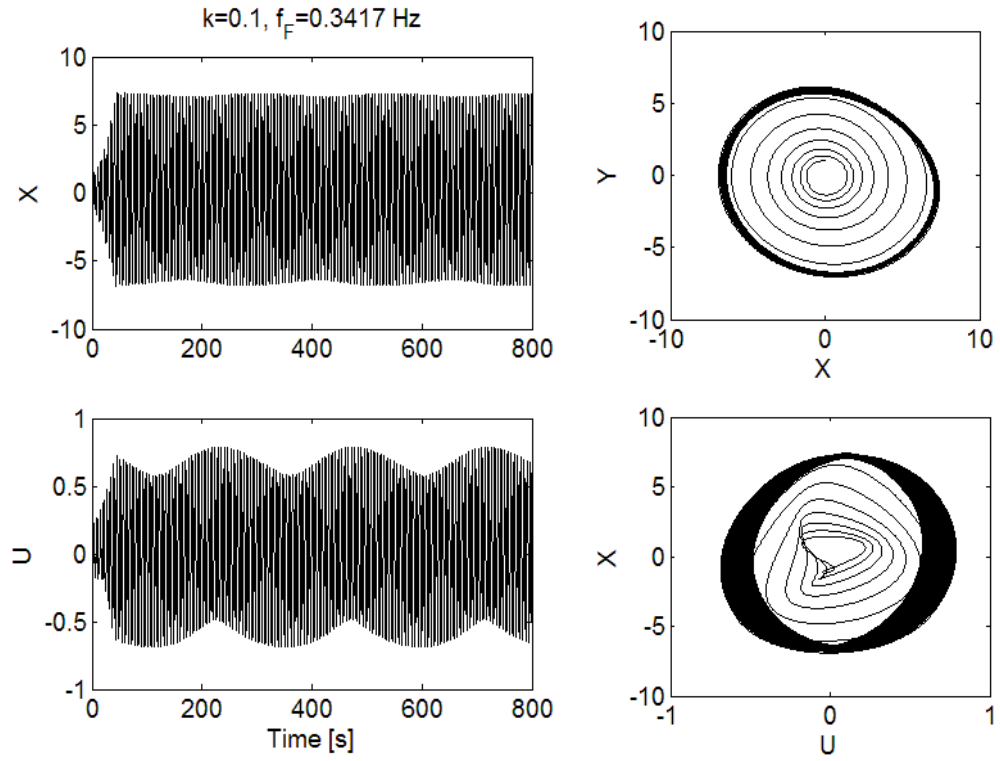


Figure 2.8: Closed Loop control of Rossler oscillator [$k=0.1, f_F=0.3417 \text{ Hz}$]

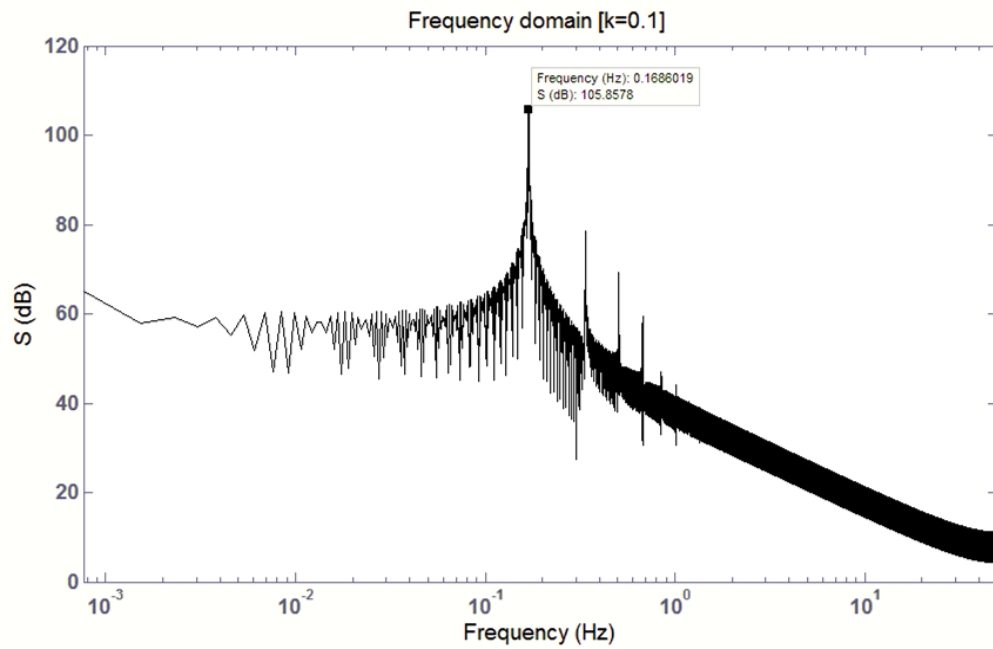


Figure 2.9: Closed Loop FFT [$k=0.1, f_F=0.3417 \text{ Hz}$]

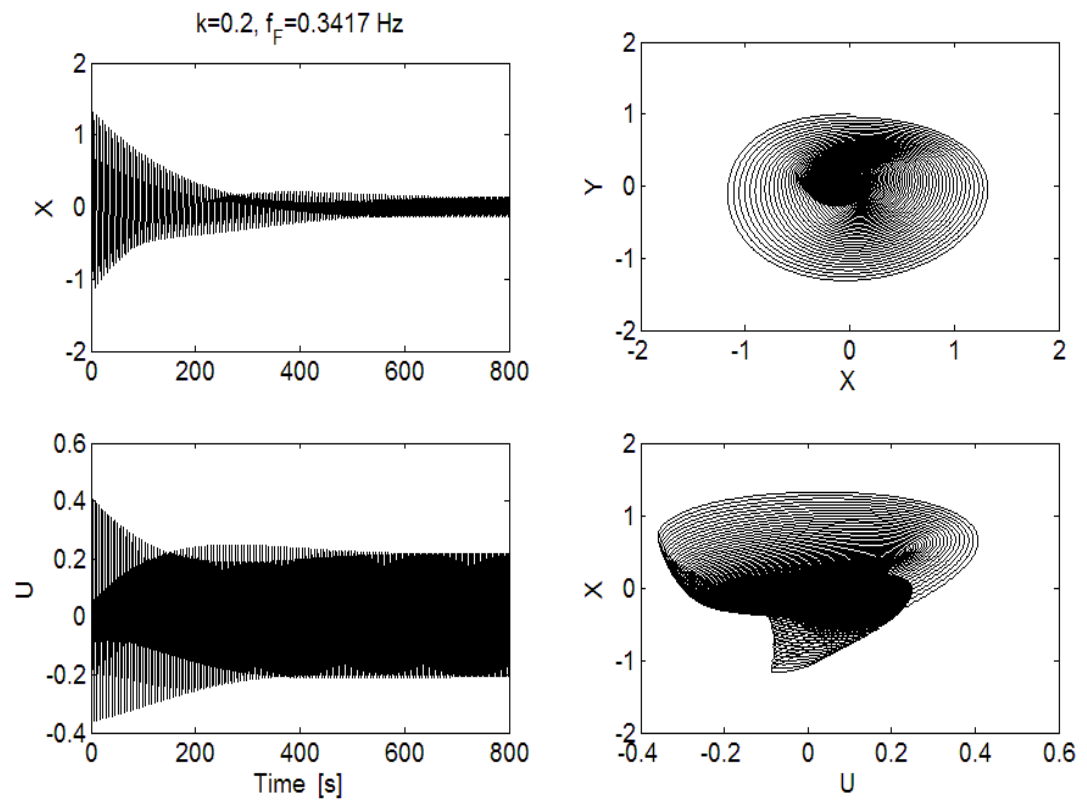


Figure 2.10: Closed Loop control of Rossler oscillator [$k=0.2$, $f_F=0.3417$ Hz]

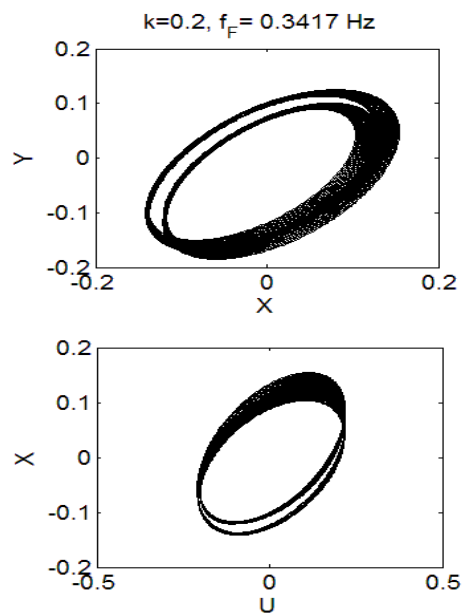


Figure 2.11: Exposed limit cycle [$k=0.2$, $f_F=0.3417$ Hz]

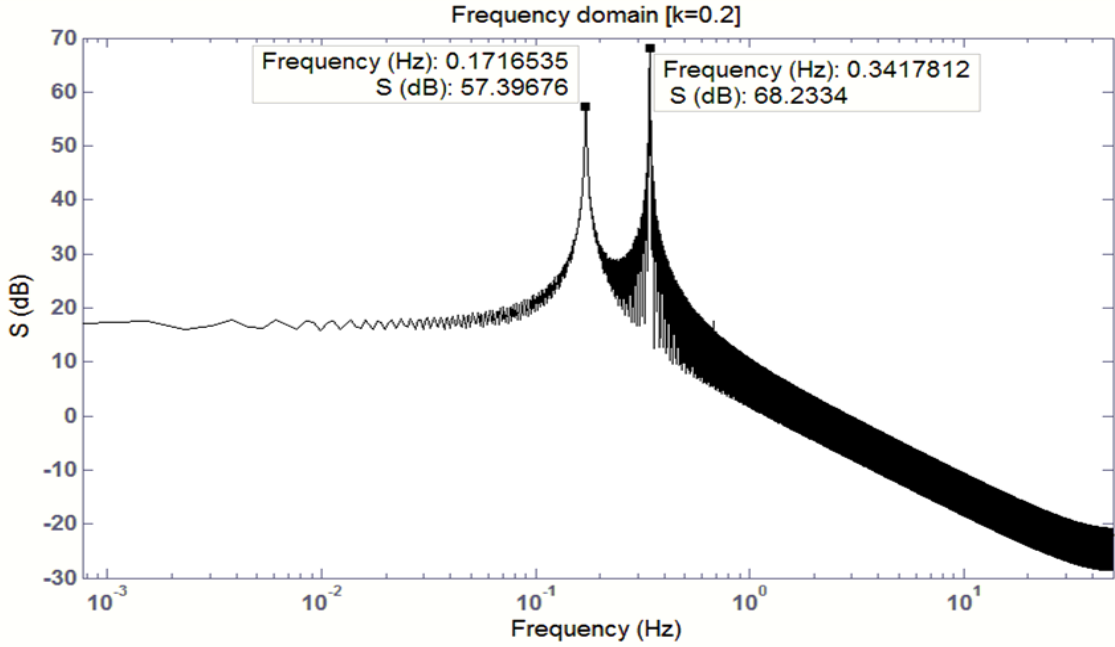


Figure 2.12: Closed Loop FFT [k=0.2, $f_F=0.3417$ Hz]

A further increase in feedback gain to 0.4 reveals that the period of time over which the initial transient response takes place is reduced as shown in the inlay of Figure 2.13. At the center of both phase planes we see a limit cycle [(X, Y), (U, X)]. Again if one removes the transient, a period one orbit is exposed (Figure 2.14) indicating that there is now only one frequency associated with this closed loop system. The frequency spectrum again supports this finding (Figure 2.15). The next section will discuss the effect of forcing frequency on the mechanism of synchronization.

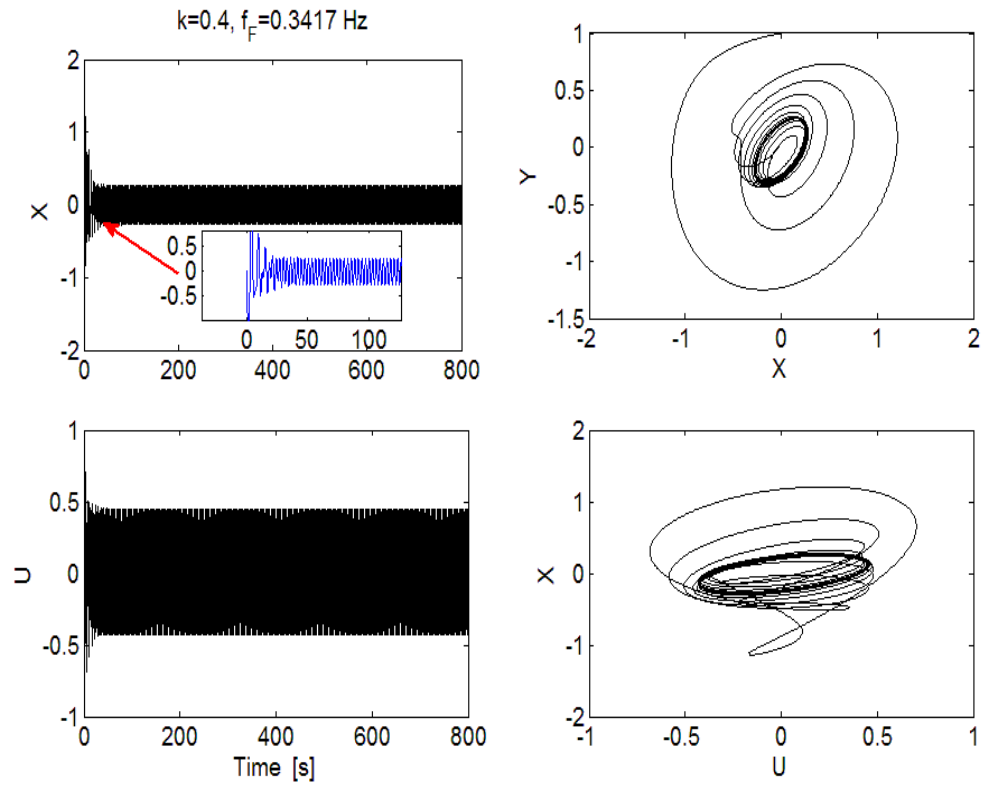


Figure 2.13: Closed Loop control of Rossler oscillator [$k=0.4$, $f_F=0.3417$ Hz]

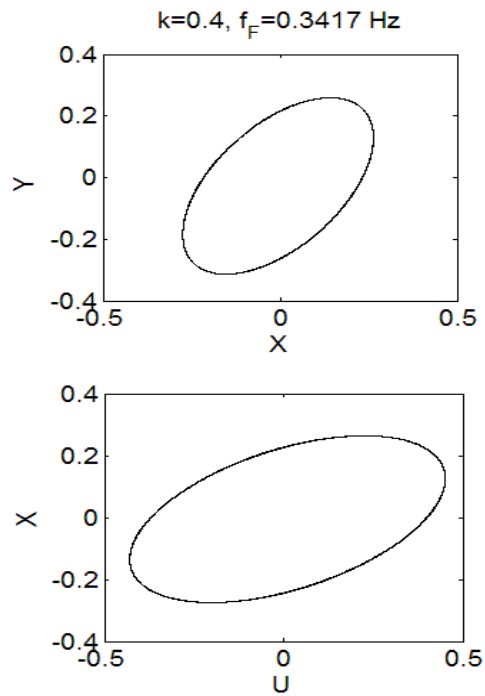


Figure 2.14: Exposed limit cycle [$k=0.4$, $f_F=0.3417$ Hz]

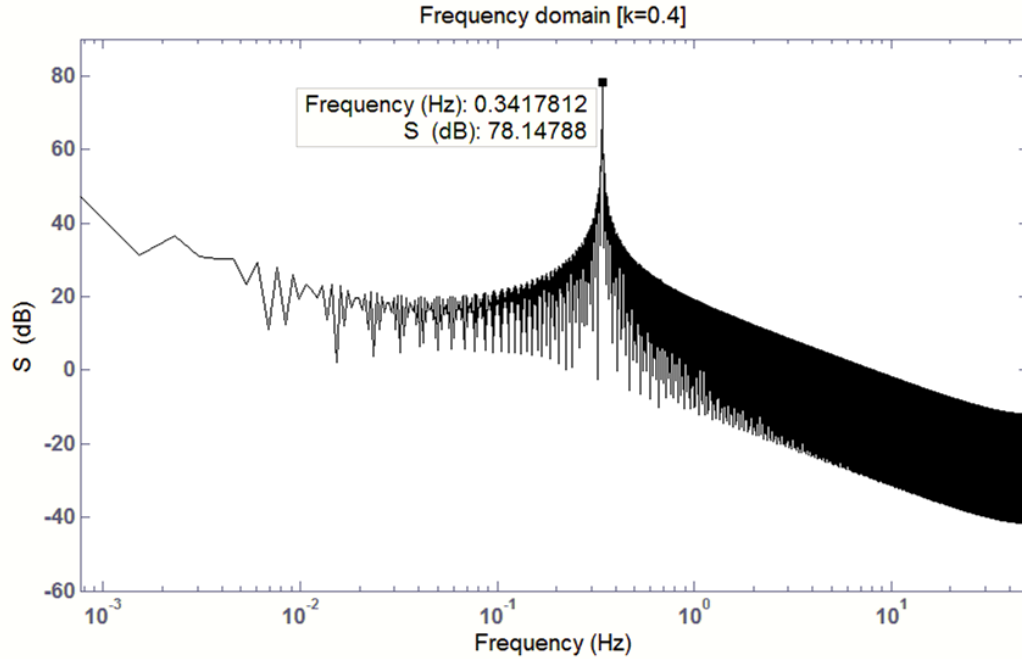


Figure 2.15: Closed Loop FFT [k=0.4, $f_F=0.3417$ Hz]

2.2.2 THE EFFECT OF THE CLOSED LOOP FORCING FREQUENCY ON SYNCHRONIZATION

For this part of the numerical study, the feedback gain, k is set equal to unity and the forcing frequency is varied. In Figure 2.16, it can be observed that closed loop forcing at the fundamental frequency of 0.17 Hz causes a significant reduction in the amplitude of the time history as compared to the open loop time history. For the frequency spectra corresponding to 0.17 Hz we see that there is a single peak at 0.17 Hz, but reduced in amplitude. When the forcing frequency is increased to twice the fundamental or 0.34 Hz, it is observed that the amplitude of the time series further reduces in magnitude; this corresponds to what is seen in the spectra. Specifically, we see that there is a rounded peak at 0.17 Hz, indicating that the natural dynamics of the chaotic Rossler attractor is suppressed. The secondary peak to the right is located at 0.34 Hz the prescribed forcing

frequency. The Rossler attractor, when forced at 2 times its fundamental is frequency locked; this indicated by the fact that we see only one very sharp peak at 0.34 Hz.

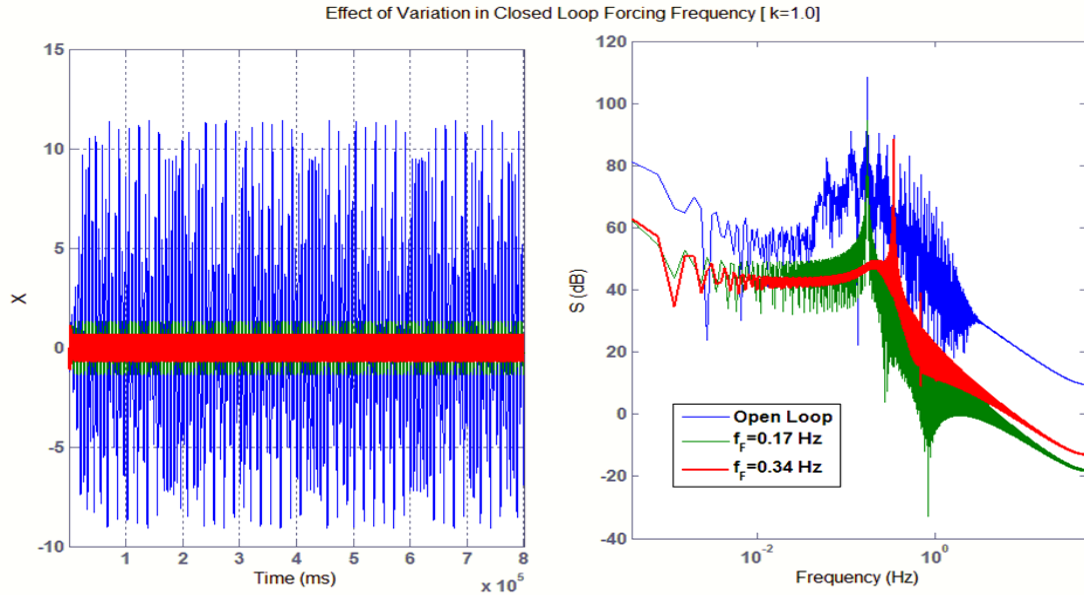


Figure 2.16: Effect of Variation of Closed Loop Forcing Frequency

2.2.3 TIME FREQUENCY ANALYSIS

The mechanism of synchronization allows one to manipulate the frequencies in a system as well as their amplitudes, modes shapes and degree of regularity. The application of closed loop control enhances frequency manipulation. In Lovato's dissertation, one of the recommendations given was that wavelet transforms are to be used to help determine flow frequencies in both time and space; to that end a wavelet transform is one of many time-frequency analysis methods by which one may evaluate events and nonstationary processes in aerodynamic, aeromechanical and acoustic signals. In general, the main use of a time frequency approach for studying time series (that could be nonstationary) is to analyze the time variation of the spectral quantities. It stands to reason that one can then visualize the time-frequency variation of the modes in both the open and closed loop

Rosler attractor. A time frequency distribution that is commonly employed is the Wigner-Ville distribution (WVD). In general the WVD is a measure of the signal at a past time with the same signal at a future time point [48]. The drawback is that this creates cross terms (interferences) which tend to show up as highly oscillating terms that result from the superposition of spate spectral components of the signal; sometimes these cross terms make it difficult to interpret the spectrogram or time-frequency map. Depending on the application, one can remove these interferences by averaging but this will reduce the resolution. By definition the WVD is the Fourier transform of the central covariance function. For any time series $X(t)$, we can define the central covariance function as:

$$C_c(\tau, t) = X(t - \frac{1}{2}\tau)X^*(t + \frac{1}{2}\tau) \quad (2.4)$$

Then the Wigner-Ville distribution is:

$$V(\omega, t) = \int_{-\infty}^{\infty} C_c(\tau, t) e^{-i\omega\tau} d\tau \quad (2.5)$$

Using the Time Frequency Toolbox, it is possible to change the colour map to contours making the cross terms more visible and use the cross terms help in task of interpreting the results. Figure 2.17 shows the spectrogram for the open loop Rosler oscillator. In this time-frequency map we can observe the following things; we see that there are several frequency components that do not vary with time. There are what appear to be smeared spectral elements below the constant frequency of 0.05 Hz. There is a strong constant frequency line at 0.17 Hz, the fundamental frequency of the un-controlled attractor. These lines of constant frequency correspond to what is found in the FFT of the same signal. This open loop spectrogram also shows the strong phase coherence of the Rosler attractor. When closed loop control (Figure 2.18) is applied to the Rosler attractor at

$k=0.2$, we find that following changes are observed in the time-frequency map; the mode contours below 0.05 Hz show what appears to be an exponential-like decay with time over duration of 100s. The space above the low frequency modes does not have any cross terms which means that the controller causes a time frequency variation. We can observe a line of cross terms about a constant frequency about 0.08 Hz and above that we also note that there no cross terms. The remaining modes located normally found in between the major spectral peaks, have been pulled toward the spectral element located at approximately 0.1716 Hz. It is interesting to note that the fixed forcing frequency of 0.34 Hz or twice the fundamental frequency does not show up in the time frequency map were as it is visible in the FFT for this case.

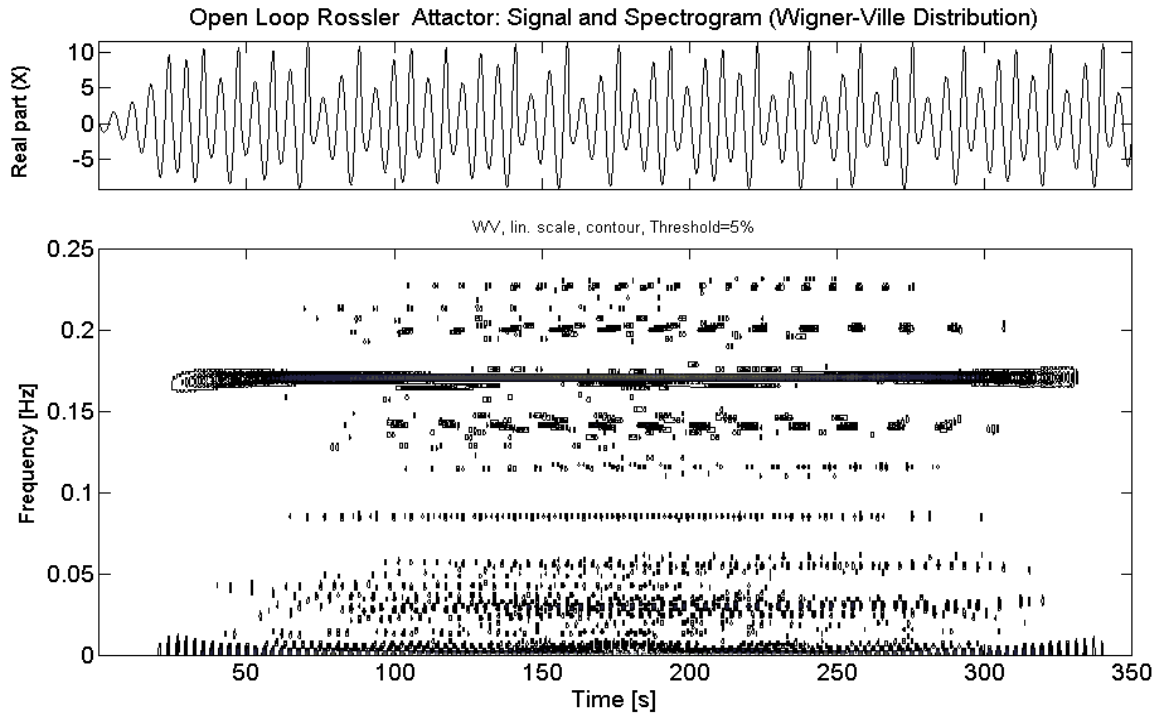


Figure 2.17: Open Loop Spectrogram of the Rossler attractor

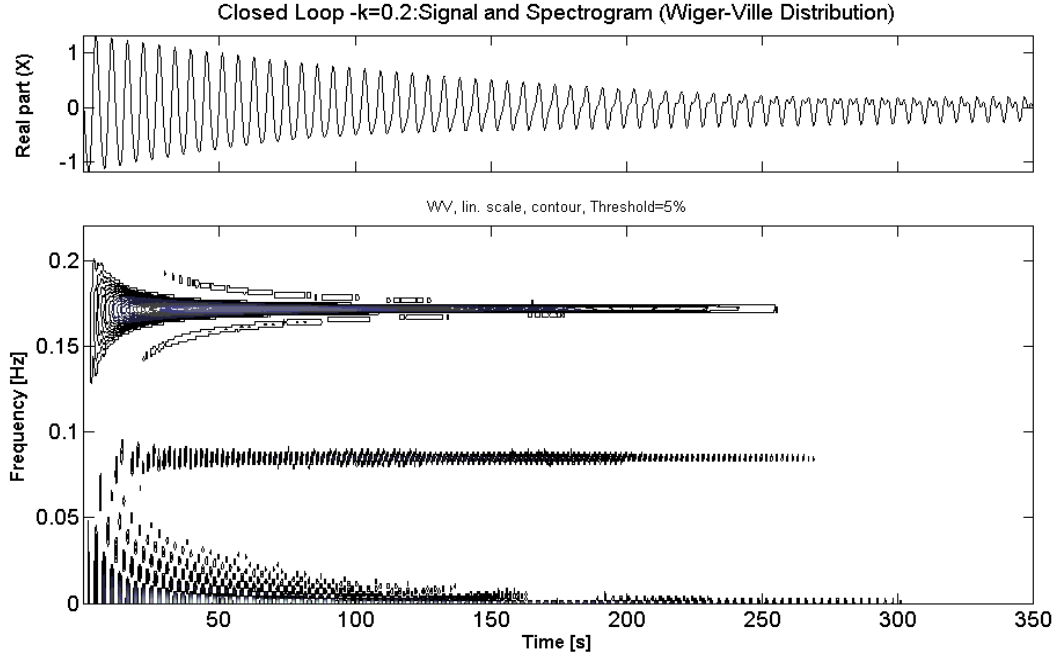


Figure 2.18: Spectrogram for controlled Rossler attractor

In this section we have seen the difference between the two routes to synchronization, mainly phase/frequency locking and suppression. Suppression in the context of synchronization does not mean a full collapse of the resulting limit cycle as would expected the control problem one of regulation, but suppression here means the reduction in amplitude of the limit cycle. Phase/frequency locking and suppression manifests themselves in both the phase space and the frequency spectra. For phase/frequency locking, in the phase space, when a control parameter is increased, a critical value will be approached such that a limit cycle is born and will reach finite amplitude if persistent excitation used as a control signal. In the spectra, the peak associated with the natural dynamics of the system moves to coincide with the prescribed forcing frequency. For suppression, the limit cycle seen in the phase space shrinks to become a stable limit cycle and in the spectra, the peak associated with the natural dynamics of the system no longer

moves but, the amplitude becomes smaller and will eventually vanish, leaving only the peak associated with the control signal. Earlier in the chapter some pertinent results from Lovato's research indicated that there was indeed as sensitivity when forcing the flow at fundamental frequencies; for example the post stall region was reduced in size and mainly active control at the fundamental inhibits vortex pairing. In this numerical study we have seen that when forcing a nonlinear system at particular frequencies that certain modes are inhibited in a similar manner to that reported by Lovato. The next section will detail some the data analysis methods that will be used on the data collected from the aerodynamic system identification and real time control experiments.

2.3 SIMULATION OF AN ADAPTIVE PID (PROPORTIONAL) CONTROL & EXTREMUM SEEKING FEEDBACK FOR EXPERIMENTAL ACTIVE FLOW CONTROL

It has been stated in Section 2.2 of this chapter that aerodynamic flows are nonlinear in nature. Rigorous mathematical modeling yields the well-known Navier-Stokes equations (nonlinear PDEs) for which attempts have been made to develop controllers for these equations. However the controllers developed are not readily applicable for real time experimental implementation. Earlier in the chapter we have seen that a simple controller with carefully selected parameters yield a stable synchronized nonlinear plant. But the controller is a fixed gain-fixed frequency controller and cannot adapt to changing plant characteristics. This will be the case for aerodynamic flows which are time varying and non-stationary in nature. Garwon et al [49] demonstrated that combined adaptive PI and extremum seeking controllers (Figure 2.19) could successfully decrease the size of the recirculation region on a backward facing step. The inner loop was formed by the PI controller that was tuned based on an ISTE tuning rule and the outer loop was formed by

the extremum seeking feedback used to estimate the optimal forcing frequency. This the first only instance (as far as the author is aware) of an adaptive PID controller being applied to experimental active flow control research. Extremum seeking control by itself was used by Taira [46] for the inclined flat plate in low Reynolds number flow (computational), UTRC for the asymmetric diffuser [33] and a high lift system [36]. For further details on the application of extremum seeking control the reader is referred to Chapter 1, page 25. In this section, we will explore what happens to a nonlinear system i.e. the Rossler attractor when it is subjected to and adaptive PID controller (*time varying gain-fixed forcing frequency*) and extremum seeking feedback (*fixed gain- time varying forcing frequency*) using the controller structure previously defined by Pyragas (See Equations 2.2 and 2.3). Further, addition of a time varying feedback gain and extremum seeking feedback will extend the methods of Pyragas.

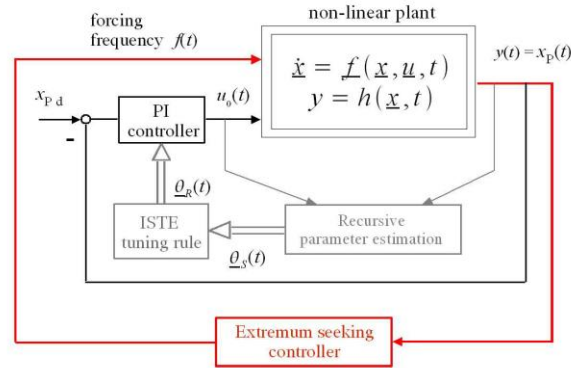


Figure 2.19: Schematic of closed loop control for backward facing step [49]

Recall that:

$$F(t) = k[y_i(t) - y(t)] \quad (2.9)$$

Suppose that the feedback gain, k is derived from the following adaptive tuning rule:

$$\dot{k} = \gamma[y_i(t) - y(t)]^2 - \sigma k \quad (2.10)$$

The second term is to account for any unmodeled dynamics; this term is called the σ -modification term and γ is the adaptation parameter. Let $E(t) = y_i(t) - y(t)$, then Equation 2.10 can be rewritten as:

$$\dot{k} + \sigma k = \gamma[E(t)]^2 \quad (2.11)$$

Let $u=[E(t)]^2$ then:

$$\dot{k} + \sigma k = \gamma u \quad (2.12)$$

Using the Laplace transform $\frac{1}{s+a}$, we arrive at the following:

$$k(s) = \frac{\gamma}{s+\sigma} u(s) \quad (2.13)$$

In the time domain, $k(s)$ becomes:

$$k(t) = \gamma e^{-\sigma t} u(t) \mapsto \gamma e^{-\sigma t} [y_i(t) - y(t)]^2 \quad (2.14)$$

So that control force can be rewritten as follows:

$$F(t) = \{\gamma e^{-\sigma t} [y_i(t) - y(t)]^2\} [y_i(t) - y(t)] \quad (2.15)$$

The complete closed loop system is show below in Figure 2.20. The Simulink block labeled ‘Adaptive Proportional Gain’ contains the time varying gain and is schematically depicted below in Figure 2.21.

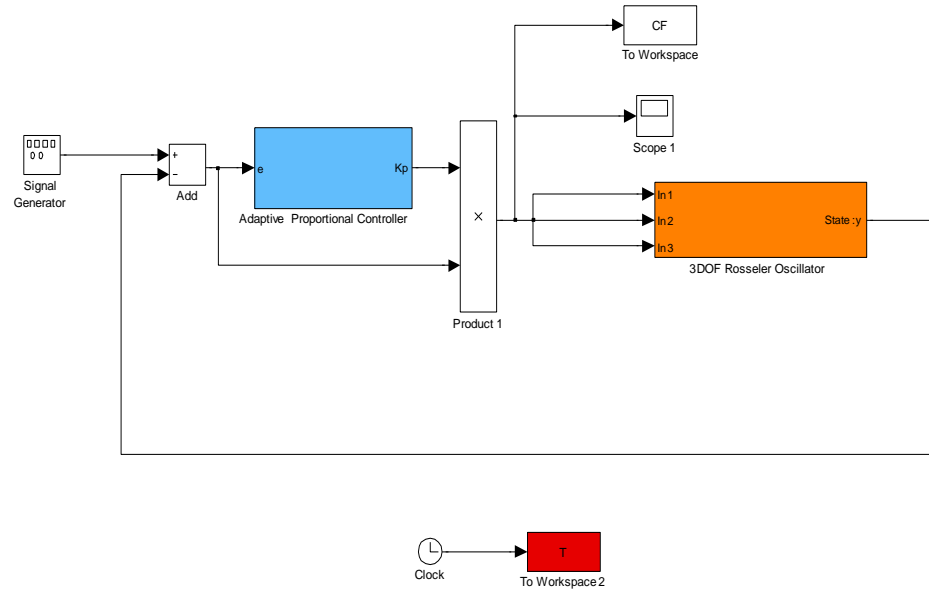


Figure 2.20: Adaptive Proportional controller configuration

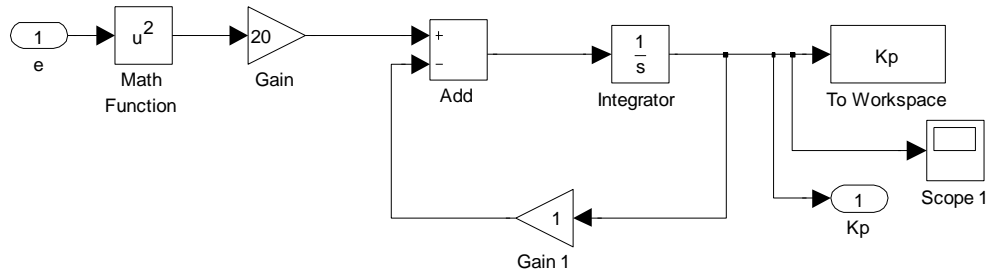


Figure 2.21: Schematic of the Time Varying Proportional Gain

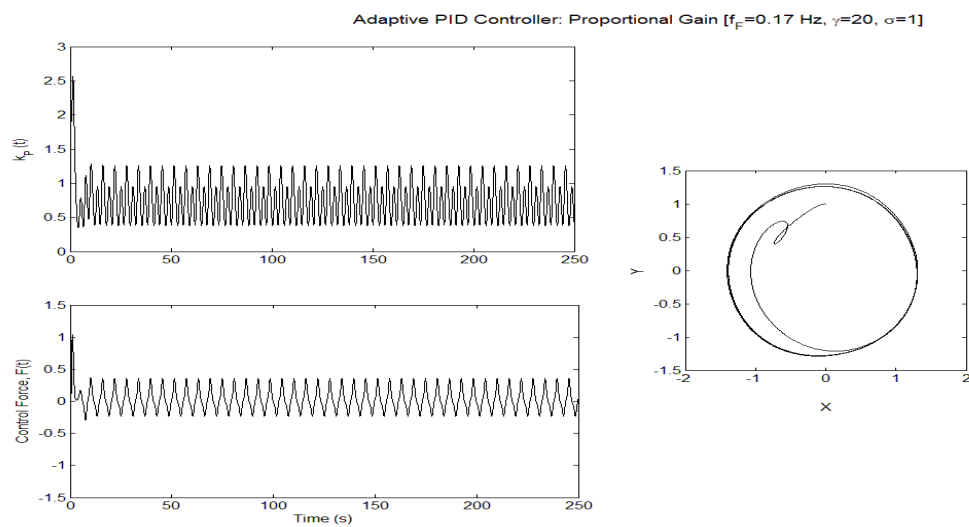


Figure 2.22: Time histories: Control Force, Gain and Phase Plane plot

For the adaptive proportional gain application the results show that the time varying proportional gain settles into a limit cycle as does the control force at a fixed frequency of 0.17 Hz. The time varying gain with adaptation parameter, $\gamma = 20$ and $\sigma = 1$ result in an average gain of 0.7521. The adaptive proportional gain allows for rapid synchronization of the Rossler attractor with the forcing frequency of 0.17 Hz as is indicated by the period 1 limit cycle in also in Figure 2.22.

If the forcing frequency is increased, the magnitude of the average feedback gain increases in a nonlinear manner (Figure 2.23). This indicates that increased control power is required to decrease the diameter of the limit cycle; in fact the orbit shown in Figure 2.22 becomes a rotated ellipse as a result of the increased control power. The slope of the curve starts to flatten out at 0.34 Hz indicated the sensitivity/receptivity of the attractor to this forcing frequency.

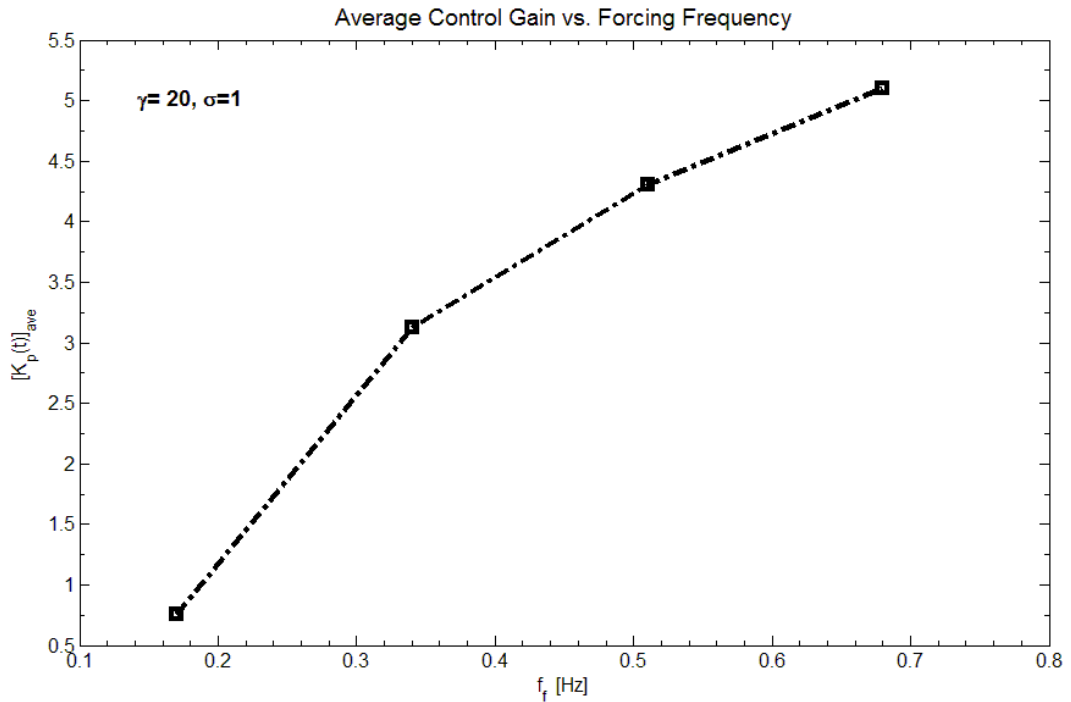


Figure 2.23: Average Control Gain vs. Frequency

By now the reader is familiar with the open loop response of the Rossler attractor (Figure 2.3). In comparison to the closed loop frequency response, it can be observed that there is a 10 dB reduction in magnitude at 0.17 Hz. Also note that all other modes have been suppressed with exception of the higher harmonics of the fundamental frequency. The adaptive PID controller in this simulation has encourages synchronization in a nonlinear plant and responds quickly to the time dependant changes in the nonlinear plant, similar results were obtained by Lin et al [50]. Based on the initial results presented, it is felt that this controller is appropriate for experimental implementation in the upcoming closed loop flow control experiments.

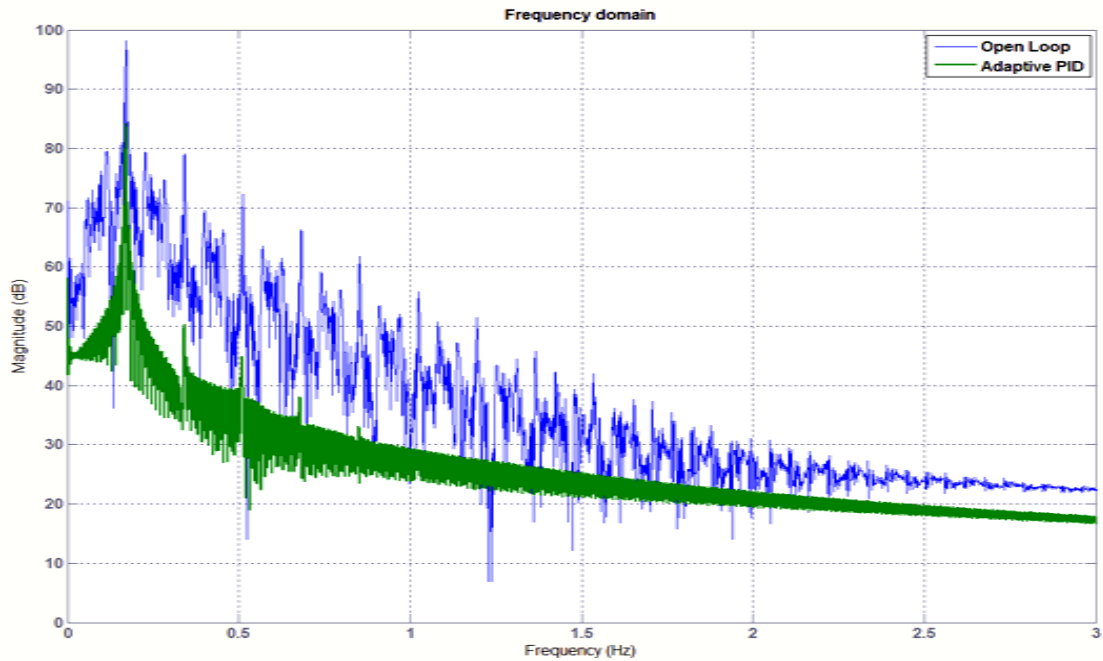


Figure 2.24: Frequency Spectra comparison (Adaptive PID)

The next simulation is of a fixed gain-time varying forcing frequency controller, where the frequency is changed by an extremum seeking feedback loop. The extremum seeking controller (Figure 2.25) consists of two filters, a low pass filter and a high pass filter, an

integrator and a signal generator which provides the controller with periodic persistent excitation. The output signal, y passes through the high pass filter. The high pass filter removes the mean value but not the perturbation frequency, ω . The product of the filtered output and the zero mean sine signal leads to a zero mean signal as long as the maximum is not obtained. This signal is then passed through a low pass filter to extract the new mean value. Change of $\hat{\theta}$ due to integration is the result until the output, θ converges towards the optimal one. The choice of gain, cut-off frequencies, amplitude and frequency of the sine signal determines the speed of convergence. The reader is directed to Krstic and Wang [51] as they have provided a rigorous first proof of stability for general nonlinear systems. When implementing a time varying frequency using the extremum seeking controller, initial simulation runs reveal that the frequency signal sometimes becomes negative; negative frequencies have no physical meaning. Therefore an absolute value block must be used to ensure the correct physical interpretation.

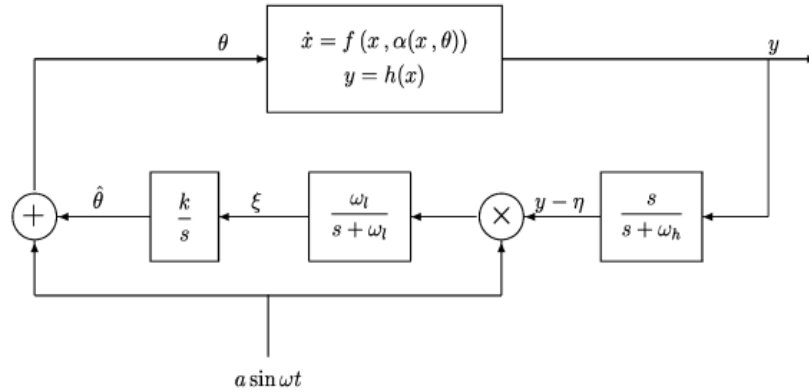


Figure 2.25: General schematic of Extremum Seeking Controller [54]

The control signal of a similar structure but with a forcing frequency that varies with time and a fixed gain. The control force is written in the following manner:

$$F(t) = k[\sin 2\pi f(t)t - y(t)] \quad (2.16)$$

The Simulink realization of the extremum seeking controller on the inner loop is shown below in Figure 2.27.

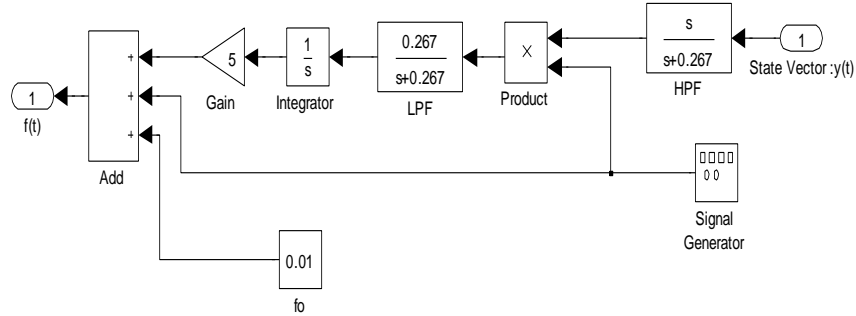


Figure 2.26: Extremum Seeking Controller in Simulink

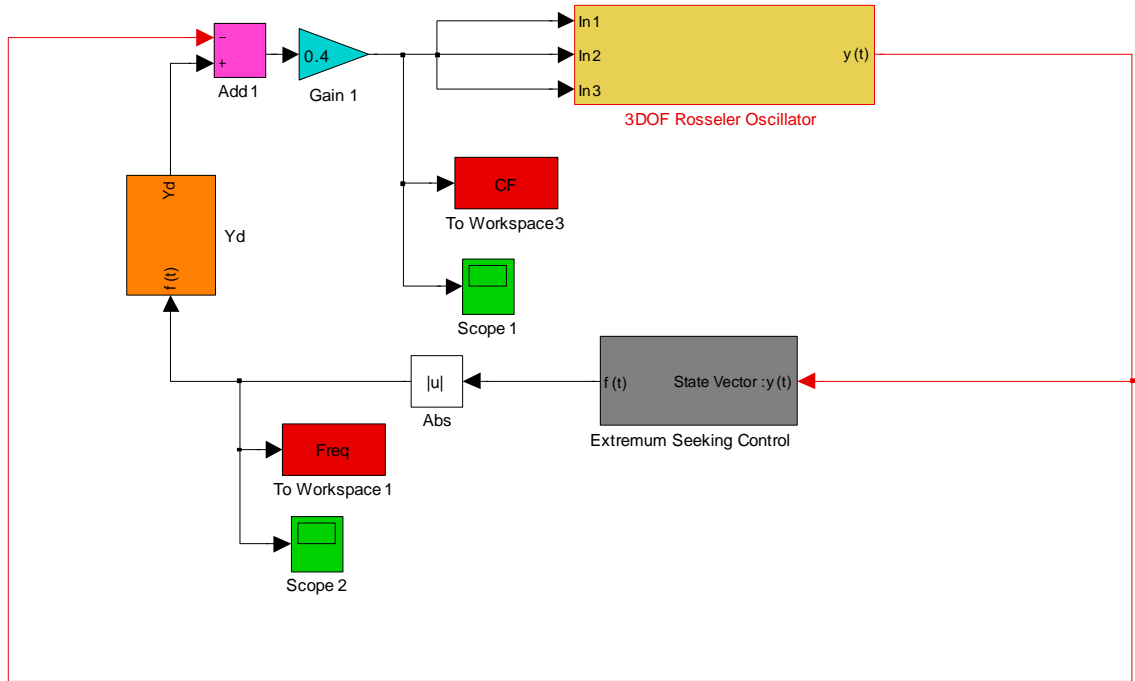


Figure 2.27: Fixed Gain-Time Varying Forcing Frequency configuration

The extremum seeking tuning criteria used in the simulation are as follows:

Fundamental of Rossler Attactor $f_0 = 0.17 \text{ Hz} > \text{Perturbation}, \omega$

$> \text{Filter frequencies}, \omega_l, \omega_h$

The low and high pass filter cut-off frequencies are to 0.0424 Hz and the perturbation frequency set to 0.0849 Hz with amplitude $a= 0.1$. The fixed gain, k , is set equal to 0.4. The control force is irregular because of the time varying frequency, but provides broadband persistent excitation. This attribute is ideal if one is to sufficiently promote coupling between modes in a weak nonlinear system such a fluid flow.

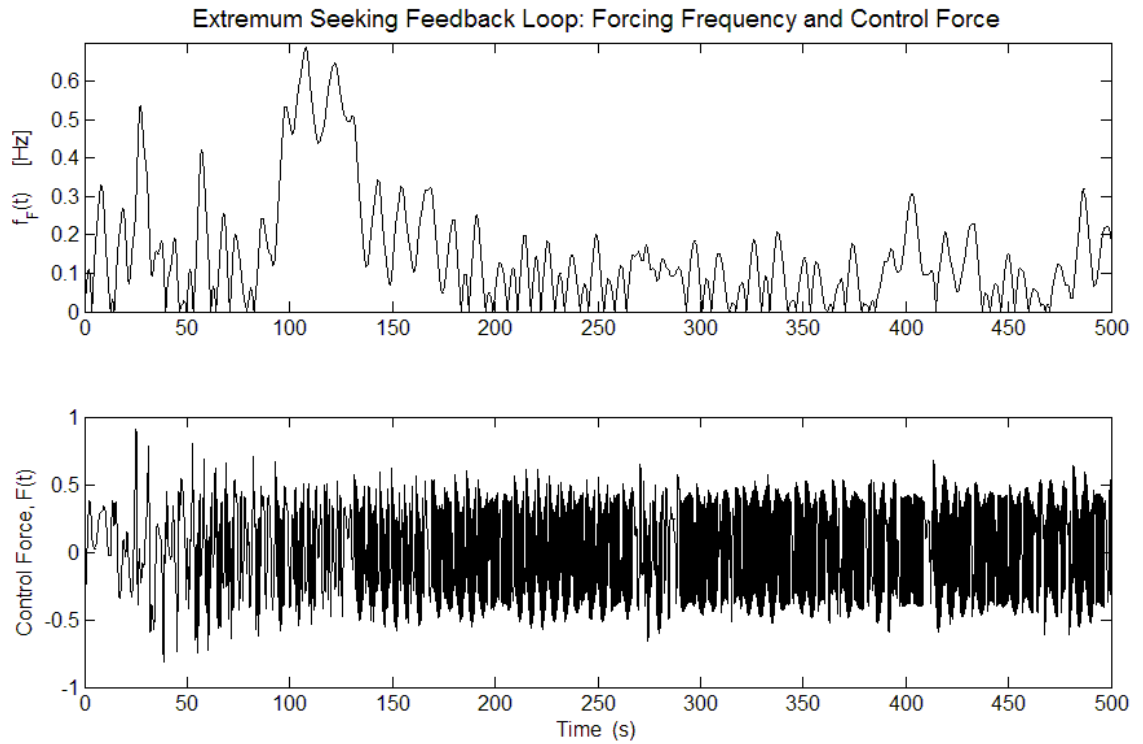


Figure 2.28: Control Force and Time Varying forcing frequency

Further inspection of the frequency time history reveals that there is an event that occurs between say 80 s and terminates at about 150s. During this time interval, the forcing frequency climbs to 0.7 Hz, nearly four times larger than the fundamental (0.17 Hz); it is also noted that the amplitude of oscillation recorded from the Rossler oscillator output starts to decrease shortly after 50 s (Figure 2.29). The mean of forcing frequency time history is about 0.17 Hz, the natural dynamics of the Rossler attractor. It is possible that because the feedback gain is fixed, the time varying frequency compensates in order to reduce the amplitude. More signal processing is required to verify this.

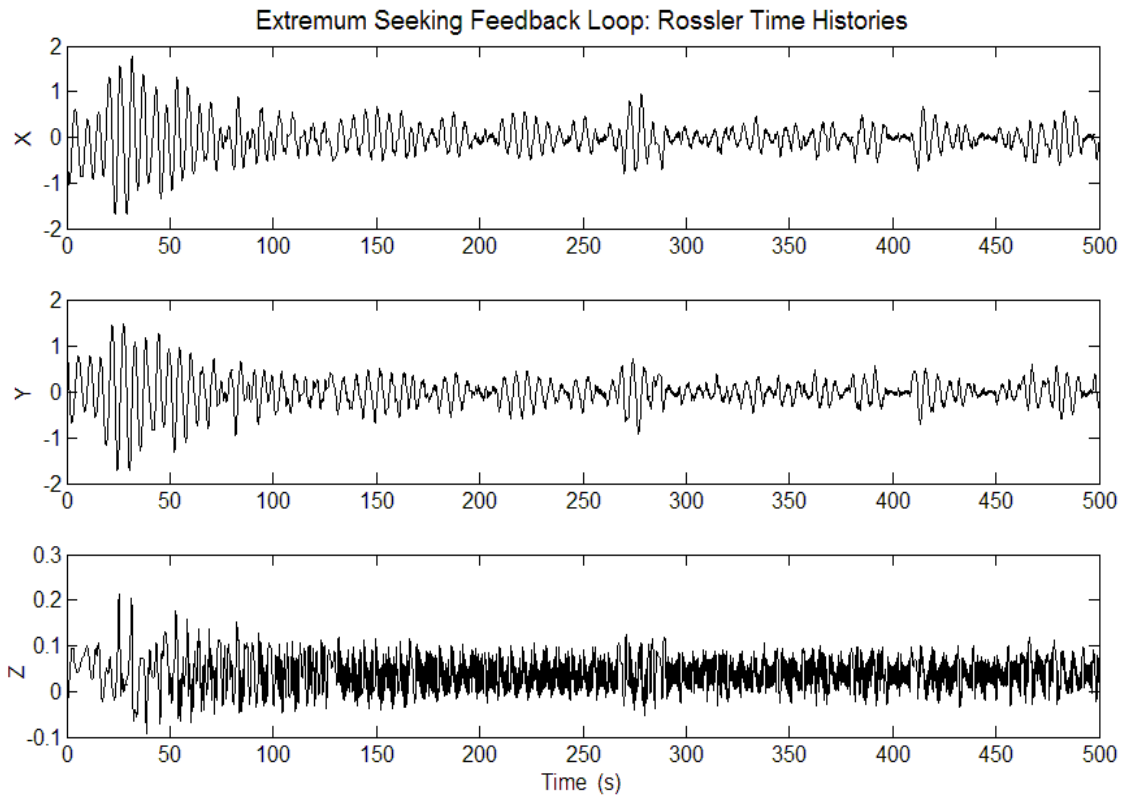


Figure 2.29: Rossler Closed Loop Time Histories

For the same value of feedback gain, in the fixed gain-fixed frequency case (See Figure 2.14), the closed loop response is period one orbit, but time varying frequency causes the

orbit to decrease, ultimately collapsing what left of the Rossler eyelet. In the frequency domain (Figure 2.30), there is broadband attenuation of all modes, unlike the resulting closed loop spectra for the adaptive PID controller (Figure 2.24) and a 31dB attenuation of the natural dynamics of the Rossler attractor.

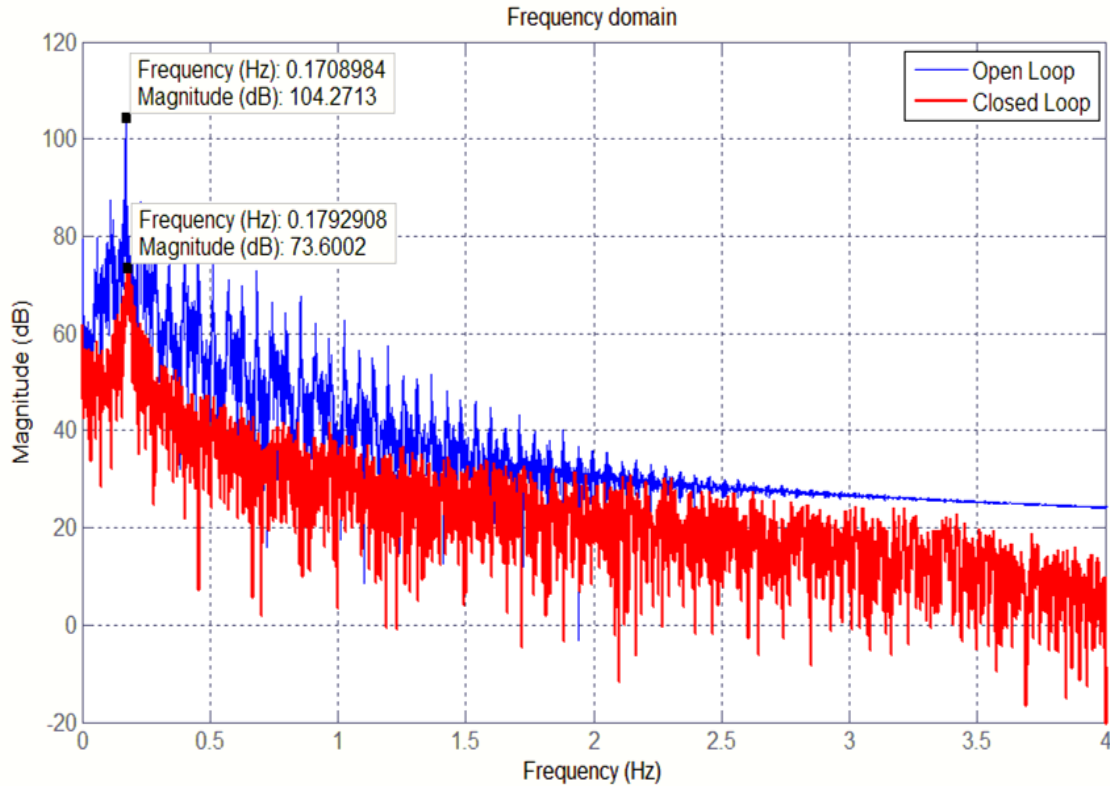


Figure 2.30: Frequency Spectra Comparison (Extremum Seeking)

2.4 DISCUSSION

In this section it has been demonstrated via simulation that both of these controllers extend the methods of Pyragas and promote good synchronization between the control force and the nonlinear plant. For the extremum seeking controller, the optimal forcing frequency based on the power spectra 0.1792 Hz, and 4.9% higher than the fundamental frequency of 0.17 Hz. These controllers are simple yet very effective and can be

implemented with little difficulty experimentally as demonstrated by the various research teams. In simulation the adaptive PID controller is able to suppress the chaotic behavior of the Rossler system; however experimental implementation might prove to be challenging because of the voltage constraint on the synthetic jet actuators. Specifically, the adaptive PID controller works because the gain magnitude changes with time and it must *not* be restricted in any way or else it will not be able to deliver the control authority demonstrated in simulation. The voltage constraint may remove the very property that makes the adaptive PID effective. The extremum seeking controller is designed specifically for dealing with nonlinear plants like the chaotic Rossler system or an experimental aerodynamic flow system. The extremum seeking controller is effective because after a few cycles, the controller is able to lock into unstable periodic orbits or optimal vortex shedding frequencies for which the flow is receptive under challenging plant conditions; for the experiment this means flow conditions at the post stall angle of attack. What these controllers have in common is the application of broadband excitation. The implication here is that a nonlinear system either contrived or experimental, selects from a range of frequency scale(s) to lock into. The closed loop controller configuration forces the system to remain frequency locked. In this way both controllers are effective. However practically speaking, the extremum seeking controller is more experimentally appropriate given some of the hardware limitations.

CHAPTER 3.0: EXPERIMENTAL HARDWARE AND INSTRUMENTATION

This chapter provides a brief discussion on the fabrication and assembly of the experimental hardware and instrumentation required to execute and complete the given research objectives.

3.1 THE HIGH SPEED WIND TUNNEL

The Clarkson University wind tunnel (Figure 3.1) is an open circuit wind tunnel equipped with a Howden Buffalo 179 HP AXIVANE Fan. The tunnel is capable of producing 70 m/s (M0.205 at sea level under standard day conditions). The test section is 121.92 cm x 91.44 cm x 152.4 cm. The test section floor and ceiling are made of medium density fiber wood; the removable floor and ceiling make it possible to modify the test section for specific aerospace and automotive research testing. The side walls of the test section are made of clear plexiglass for optical access. For turbulence reduction there are two conditioning screens and settling chamber up stream of the test section. The wind tunnel is not treated acoustically.



Figure 3.1: Wind Tunnel Test and Test Section

3.2 NACA 0015 AIRFOIL

The model used for this research is a NACA 0015 airfoil fitted with a simple trailing edge flap. The chord is 30 cm and the span is 40 cm with a maximum thickness of 4.5 cm at 30 % of the chord. The model is made of 6061 Aluminum. This material was selected because its manufacturability and light weight. The wing is designed to accommodate two arrays of synthetic jet actuators and instrumentation; specifically the wing has a cavity which provides access to the model instrumentation .There are eleven holes of 1 mm diameter; eight on the main element and three on the trailing edge flap. These holes are for the pressure transducers (See Section 3.4). The wing assembly is modular, it is comprised of 6 pieces in the spanwise direction that are fastened

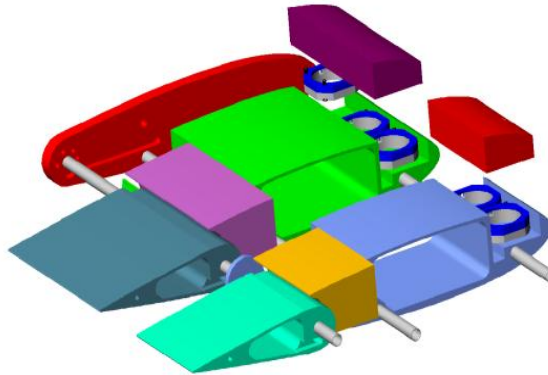


Figure 3.2: Partial Wing Assembly

together by three brass tubes and held together by three corresponding threaded compression rods (Figure 3.2). The flap is located at 75% of the chord; this flap location was selected because is recommended in McCormick [52] that the optimal flap chord ratio is 0.25. The trailing edge flap is connected to the main element via one the brass tubes and threaded compression rod. To ensure that the flap angle is the same throughout the span of the wing, the flap segments are held in place with pins (Figure 3.3). The brass

tube and compression rod is located at the center of the leading edge of the flap serves as the hinge line for the trailing edge flap. The flap is manufactured with holes that allow researcher to set specific flap angles. These flap angles are 0, 5, 10, 20, 40 degrees (Figure 3.4). The flap has a wire channel on the right side which allows for a wire harness access from the main element cavity to the cavity inside the flap.

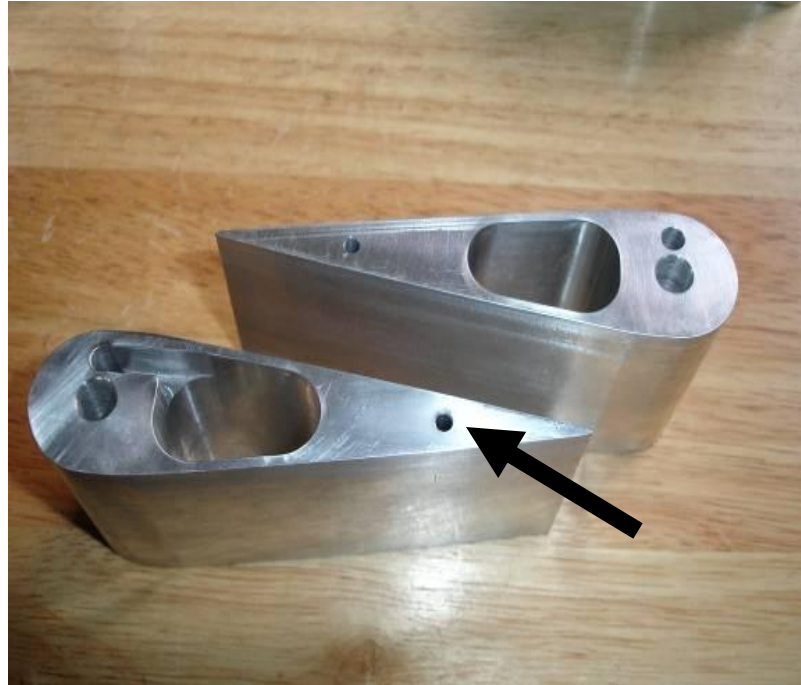


Figure 3.3: Flap segments with pin holes

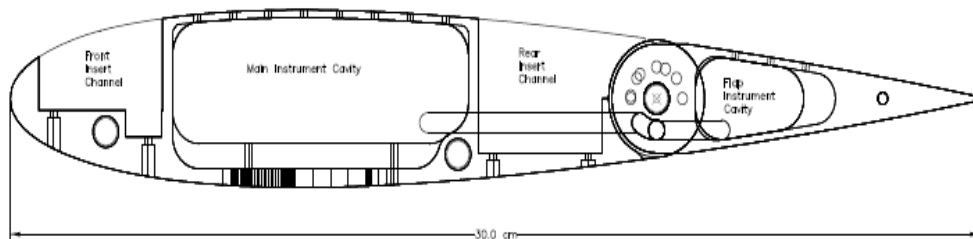


Figure 3.4: Wing Schematic

The wing is mounted to the six axis force balance by a strut made from aerodynamic tubing. The strut is attached to a support plate that fastened to the pressure side of the airfoil. The strut also accommodates wire harnesses for the synthetic jet actuators and the

pressure transducers that are embedded inside the wing. In order to ensure two dimensional flow about the wing, false walls are installed in the test section. One of the walls is made of plexiglass for optical access for PIV image capture and the other is made of plywood. The inside of the plywood wall is painted black as is the wing in order to prevent any reflection during the flow visualization process.



Figure 3.5: Strut with wire harnesses

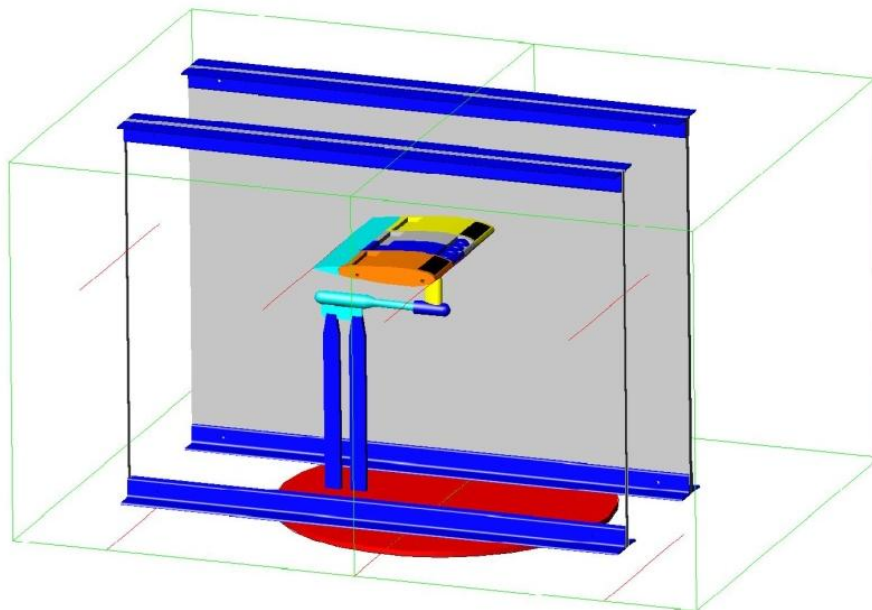


Figure 3.6: False walls in test section

3.3 AEROLAB SIX AXIS FORCE BALANCE

A six axis internal force balance systems is used to obtain force and moment measurements on the airfoil and control pitch (angle of attack) and yaw of the airfoil model. The force balance system includes a specially machined load cell fitted with strain gauges.

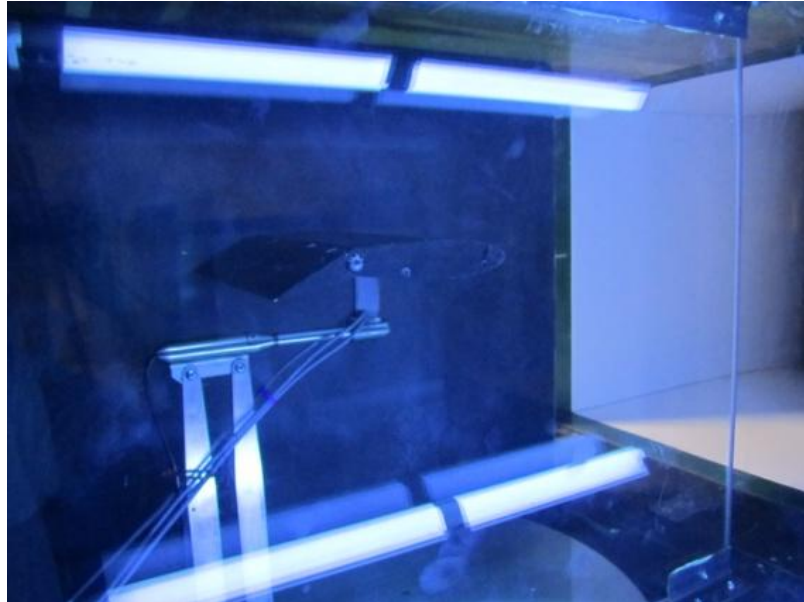


Figure 3.7: Wing mounted on Force Balance

The tip of the sting is located at exactly the center of the test section. The motion of the force balance is computer controlled via Labview codes. The calibration of the force balance is accomplished by applying weight to a calibration bar and measuring the output voltages. A calibration matrix aids in the conversion of voltages. The force balance is rated at 444 N in the normal direction, 111 N in the axial or drag direction and maximum side force of 333 N. The pitch, yaw and rolling moments are rated at 22.5 Nm, 16.9 Nm and 16.9 Nm respectively. In Figure 3.5, the reader will notice that the wing and strut are welded to a socket designed to accommodate the sting. The wing is kept upright and parallel to the tunnel floor by locking screws that are tightened with an Allan key.

3.4 SENSORS

The wing is instrumented with eleven equally spaced PCB 103B01 pressure transducers placed in series along the chord of the wing. There are eight transducers located on the main element of the airfoil and three transducers located in the flap. The locations are indicated in Figure 3.8. The pressure transducers are signal conditioned and powered by three 4 channel PCB Model 482 C Series Signal Conditioners. Each transducer comes with a calibration chart and a sensitivity value.

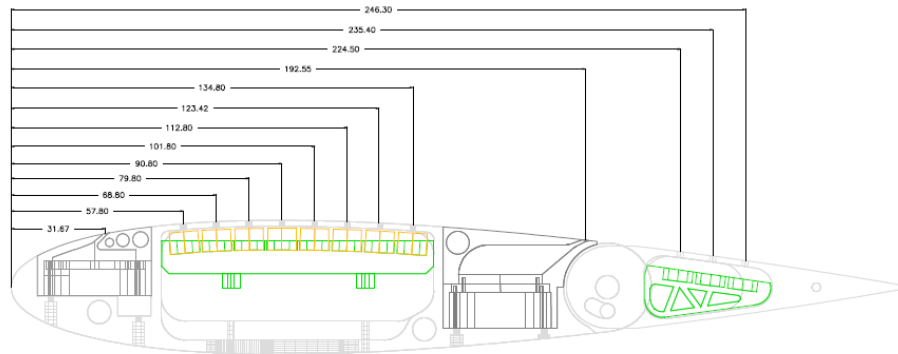


Figure 3.8: Pressure transducer locations

The pressure transducers have a resonant frequency of 13 kHz; the data is sampled at 8 kHz. In addition to the pressure sensors, an accelerometer will be added to the instrumentation package in order to assist in the investigation of flow induced vibration caused by bluff body vortex shedding at high angle of attack as well as providing the means to obtain the true angle attack in the ‘wind on’ condition; this is needed because it has been observed that the sting deflects when loaded with the wing and airload combined. The accelerometer is a PCB 352A56 with a frequency range of 0.5 Hz to 10 kHz and a resonant frequency of 45 kHz. The accelerometer will be mounted close to the centerline of the strut.

3.5 DIRECTED SYNTHETIC JET ACTUATORS

The synthetic jet actuators are designed to be integrated into a NACA 0015 airfoil. The directed synthetic jet (DSJ) design is primarily based on the work of McCormick [55]. The study of DSJs began is an investigation into candidate solutions for separation control for helicopter rotor systems, in particular the suppression of retreating blade stall. A DSJ is equipped with a tangential slot as shown below in Figure 3.9.

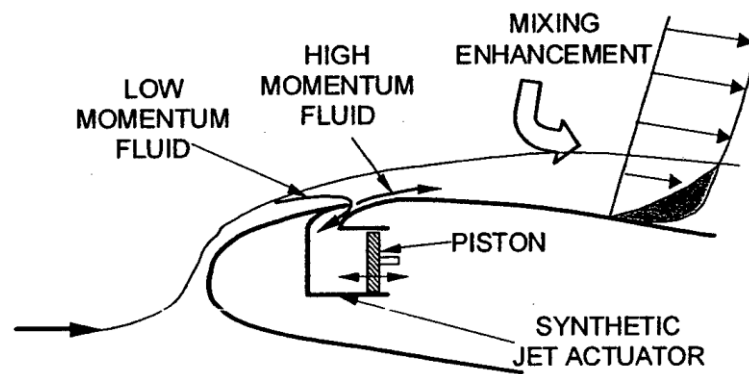
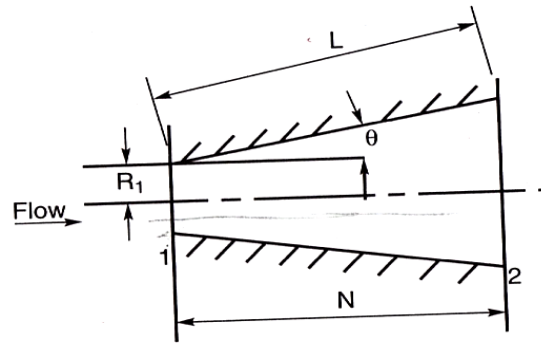


Figure 3.9: Directed synthetic jet [52]

During the ingestion part of the cycle, the jet draws low momentum fluid in from the near wall region which brings the higher momentum fluid closer to the surface of the airfoil. On the exhaust stroke, the actuator injects high momentum flow into the flow at an angle. It has been recommended that this injection angle be less than 45 degrees [53]; the angle of injection was chosen to be 30 degrees for this project due to the curvature of the NACA 0015 airfoil at the leading edge and the manufacturing constraints imposed by an angle less than 30 degrees. The synthetic jets designed by Gilarranz [13] are piston driven and no explicit reason is given for the particular design of the slot except for the purpose of turning the flow. The overall design does however consider the space constraints inside the wing. In the work of Nagib [14], the drivers are voice coils shrouded by a 2

dimensional curved slot designed by CFD methods; space constraints were also considered in this design to the extent that the synthetic jet was placed in the trailing edge flap. The Clarkson actuators are piezo- based and are comprised of circular unimorph from Omega Piezo, a stereo lithographed support structure and a clamping ring to enforce the boundary conditions at the periphery of the unimorph. McCormick pointed out that one of the loss mechanisms in synthetic jets is the dump loss caused by the vena contracta at the mouth of the orifice on the cavity side; it is also the source of distortion of the harmonic velocity signal. To mitigate the loss mechanism, the 2D slot is shaped like a diffuser and thus it allows for the application fluid machinery design principles discussed in Cocanower [54]. This approach was not taken with the other designs. The 2D slot is treated as a 2D diffuser shown in Figure 3.10. Note the equation describing the geometry is given also.



$$A_R = \frac{A_2}{A_1} = 1 + \frac{2N}{W_1} \tan \theta$$

Figure 3.10: Two dimensional diffuser [55]

When the slot is treated as a diffuser, the designer can control the pressure recovery. The following design charts were used to obtain the geometry of the diffuser-slot:

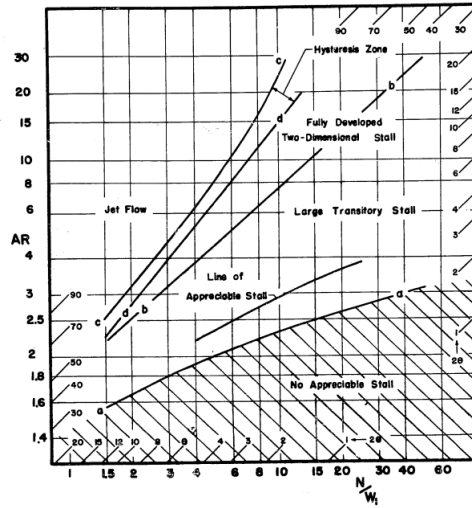


Figure 3.11: Diffuser flow regimes [55]

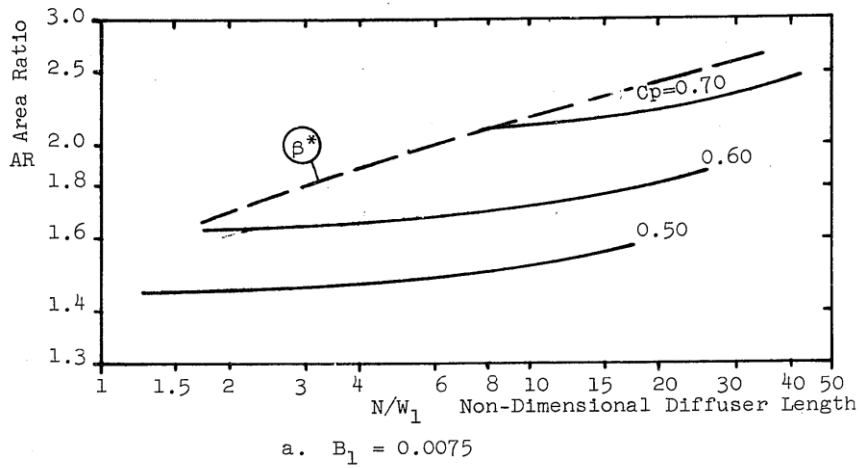


Figure 3.12: Area Ratio vs. Non-dimensional Diffuser Length [54]

It is however more efficient and accurate to utilize the following relationships in the design of the diffuser-slot:

$$A_R = 1 + 2 \left(\frac{N}{W_1} \right) \tan \theta \text{ and } C_{p_i} = 1 - \frac{1}{A_R^2} \quad (3.1)$$

Using these relationships one can now obtain the final diffuser parameters to be used for engineering drawings and manufacture. The parameters are given below:

$$C_{p_i} = 0.6; A_R = 1.6; R_o = 0.79mm; R_l = 0.5mm$$

$$N = 4.75mm; L = 4.75mm; 2\Theta = 7^\circ, \Theta = 3.5^\circ$$

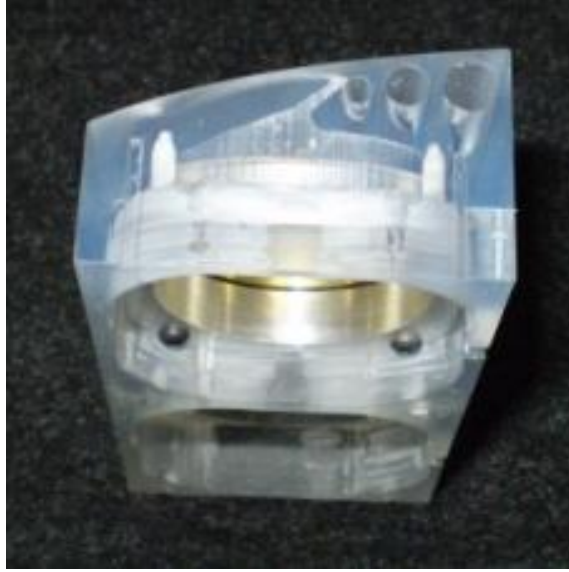


Figure 3.13: Cavity and diffuser-slot

It was noted in Ausseur's dissertation, that the synthetic jet arrays, when tested did not register the same frequency for each jet. One possible source of these differences is the degree of clamping. Upon further inspection of the NACA 4412 arrays it was found that the unimorph was attached to the actuator housing on one side only. The literature on synthetic jet actuators provided a possible solution to this boundary condition issue; Mossi [56] demonstrated experimentally that there is a relationship between clamping pressure and diaphragm deflection and hence natural frequency. For this experiment, the synthetic jet arrays are designed such that the practitioner can tune the natural frequency of the individual jets in the arrays. To accomplish this support structure is designed to accommodate an aluminum compression ring and neoprene o-rings held in by screws (Figure 3.14)



Figure 3.14: Compression Ring Assembly

During, the assembly process it was discovered that plastic stereolithographed support structure cannot support more than 20 in-oz of torque as such these test articles are acceptable to move ahead with basic characterization. Initial analysis was performed using a MATLAB code developed by the University of Florida based on the work of Gallas [7, 57]. The characterization of the synthetic jet actuators is completed using a Polytech PVS-400 laser vibrometer in order to tune the peizo-membranes. The velocity measurements were obtained using a TSI IFA- 100 hotwire anemometer with a single hotwire probe operating in constant temperature mode. The transfer functions of the leading and trailing edge actuators are shown below in Figure 3.15 and Figure 3.16. The leading edge synthetic jet has a peak velocity of 13.9 m/s at 1100 Hz and a secondary velocity of 1.4 m/s at 1800 Hz. The trailing edge jet has a peak velocity of 19.74 m/s at 1000 Hz. It should be noted that both of these fluidic devices have a dominant narrow band characteristics which indicate the nonlinear nature of piezo-driven synthetic jets. From a control systems stand point, the energy of the aerodynamic flow for both low and

high speed cases is below 500 Hz. The frequency of the both jets are well above 500 Hz, therefore a nonlinear forcing function maybe required to excite the flow in its frequency region of receptivity. From past experiments documented in the literature on active flow control, we know that the flow is sensitive to dual location excitation. Further, the flow also responds to the phasing of the actuator arrays.

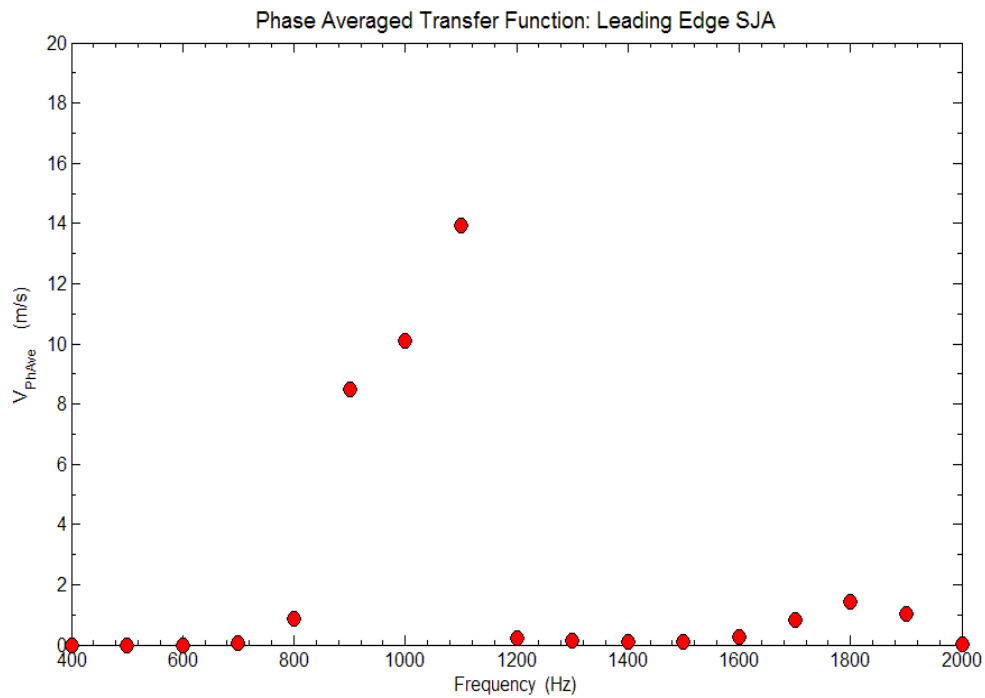


Figure 3.15: Transfer Function: LE SJA

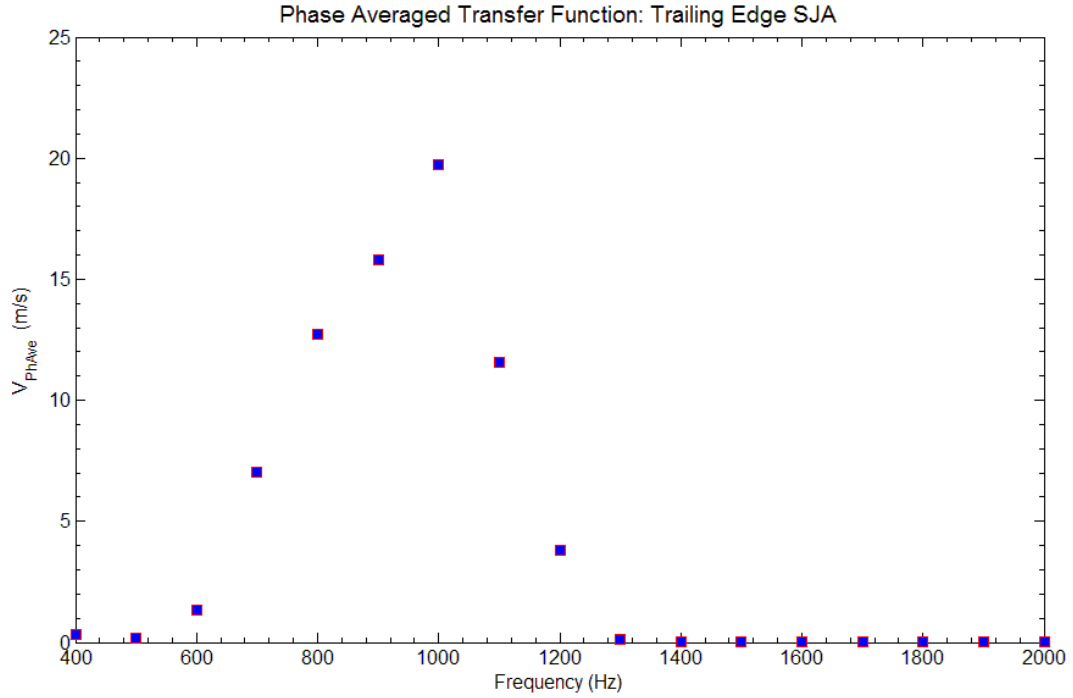


Figure 3.16: Transfer Function: TE SJA

3.6 REAL TIME CONTROL HARDWARE AND SOFTWARE (dSPACE™)

The DS1103 PPC Controller Board is specially designed for the development of highspeed multivariable digital controllers and real time simulation. It is a real time control system based on a Power PC processor. The dSPACE 1103 ACE Kit provides a means by which researchers can rapidly develop controller and implement control system designs and assess their performance. dSPACE has been used extensively in closed loop active flow control. The DS1103 board has a bus frequency of 133 MHz. It also has 16 muxed channels equipped with 4 sample and hold analogue to digital conversion (ADC) with 16 bit resolution and 4 channels each equipped with one sample and hold ADC. The schematic below shows (Figure 3.17) the integrated system used in the experiment. Included in the instrumentation package is a wire harness from the AEROLAB Force

balance which allows the author to obtain time series from the force balance strain gauges. What allows researcher to develop controllers and collect data simultaneously is the supporting software called Control Desk. For example, the data for the aerodynamic system identification experiments is collected via a Simulink block system that is constructed to read the pressure transducer and force balance signals (Figure 3.18)

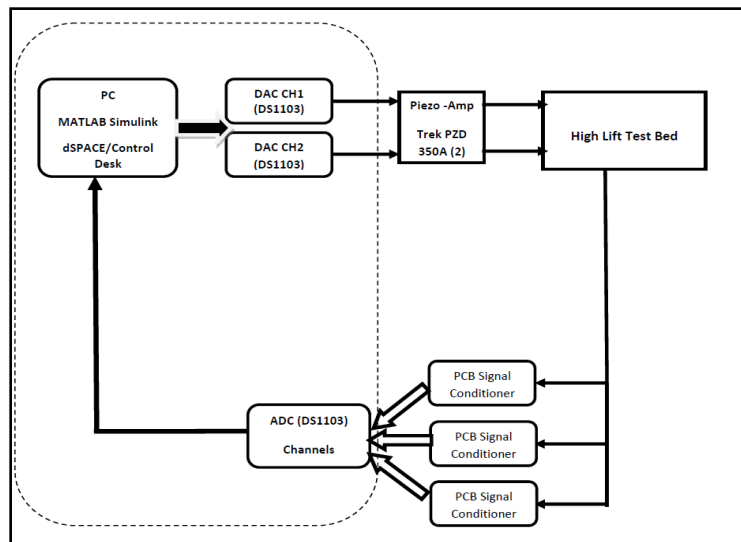


Figure 3.17: Schematic of Experimental Setup

On the left hand side, the three MUX-ADC blocks are a special dSPACE block set in the Simulink library. These blocks contain the channels which the transducers and force balance (on the right hand side in red) signals are plugged into. These blocks perform the analogue to digital conversion; this makes it possible for engineers to collect the data or have the signals operated on mathematically as if you were running a simulation. Once in the Control Desk environment, you will have the options for displaying the real time signals (Figure 3.19) and data acquisition configurations.

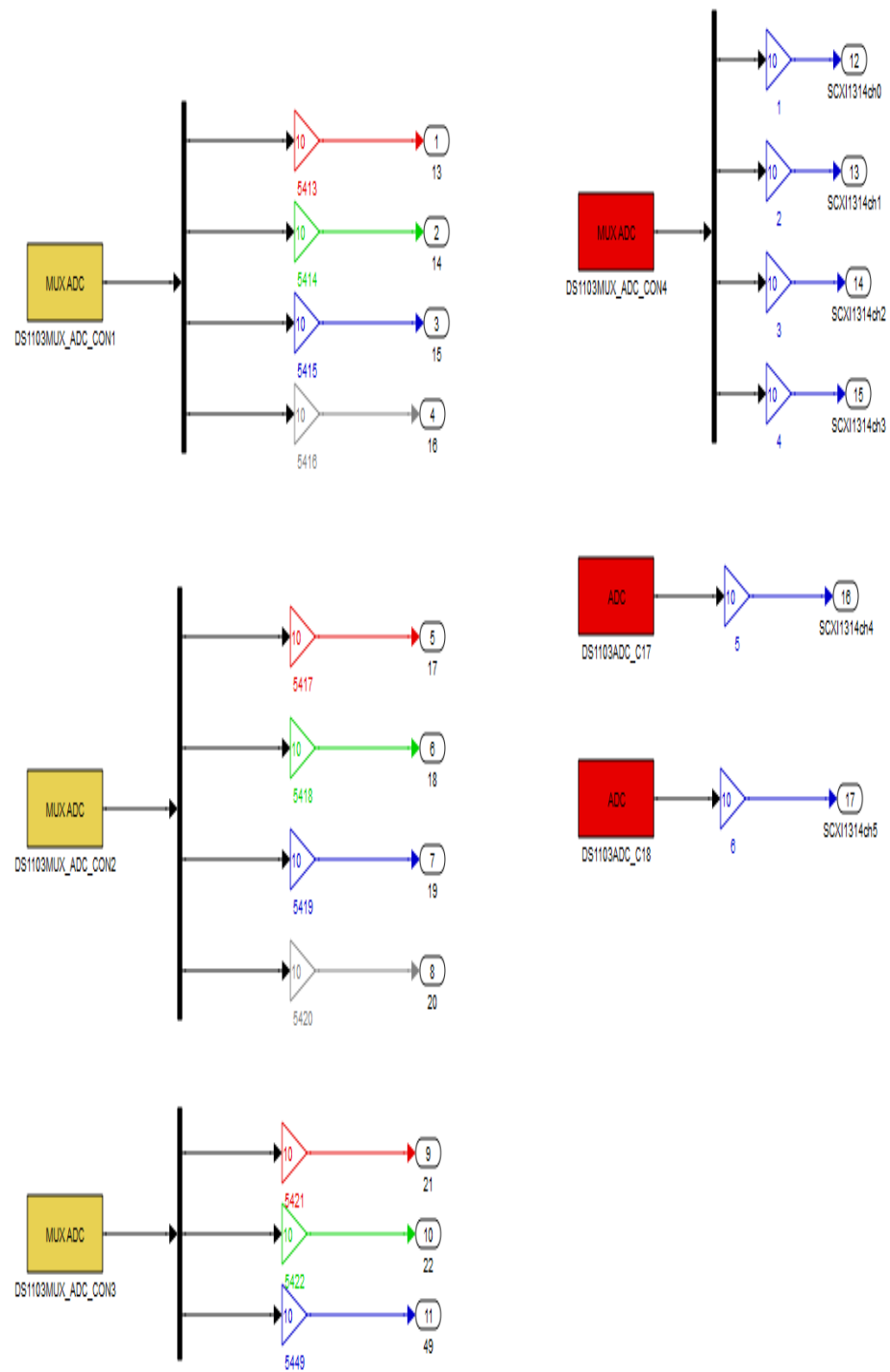


Figure 3.18: Data Acquisition block diagram

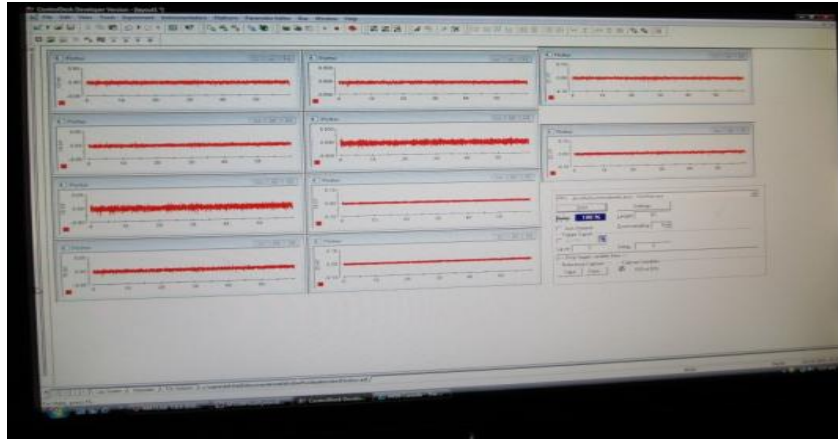


Figure 3.19: Real Time Signal/System monitoring



Figure 3.20: Real Time Control Work Station

Figure 3.21 shows how the open loop feedforward control was implemented in the Simulink environment. Specifically, the reader will note that there are two carrier function generators; their purpose is to drive the piezo-discs at their natural frequency while the secondary sinewave generators provide a common modulating frequency to both channels. There is a constant with a value of 1 and block names 'SAFE', this allow the operator in the dSPACE Control Desk environment to be able to shut off the

feedforward control via a virtual push button. In this way the operator control the when the control voltage is turned on without interfering with the data acquisition function. This schematic corresponds to Equation 1. Starting in the upper left corner of Figure 3.22, the reader will note the red dSPACE Simulink blocks; these blocks facilitate the acquisition of data from the six axis force balance. Below in the red box (dashed outline) there are three pulse/sinewave generators. The first two are assigned to Channels A and B, front and rear synthetic jet arrays respectively. These generators provide the closed loop control voltage to the hardware. The third is a test sinewave generator which allows the practitioner to perform a diagnostic and calibration procedure before supplying power to the arrays. This accomplished by attaching a B & C cable from the DS1103 board to a storage oscilloscope; using a T-junction, tap from this signal and route it to the input side of the Trek amplifier. Next, attach a multimeter to the output side of the Trek amplifier and read the voltage. By completing this procedure, one can check the voltage and the waveform before supplying power to the arrays. There are two manual switches to the left of the red box (dashed outline) located in the red circles; these manual switches allow you to command only the test generator and terminate the closed loop command voltages. Inside the solid blue box is the plant/wing. The virtual wing is configured such that the data acquisition function happens simultaneously with closed loop control once a feedback switch is closed and the power is on. The reader will note that each of the three sensor clusters has a common constant (orange block) with a value of zero. When you wish to select a particular pressure transducer feedback signal, the state of the switch can be manually changes. In the off position the signal is routed to the zero constant, this effective terminates the signal. In the one position, the signal is routed or passed to a

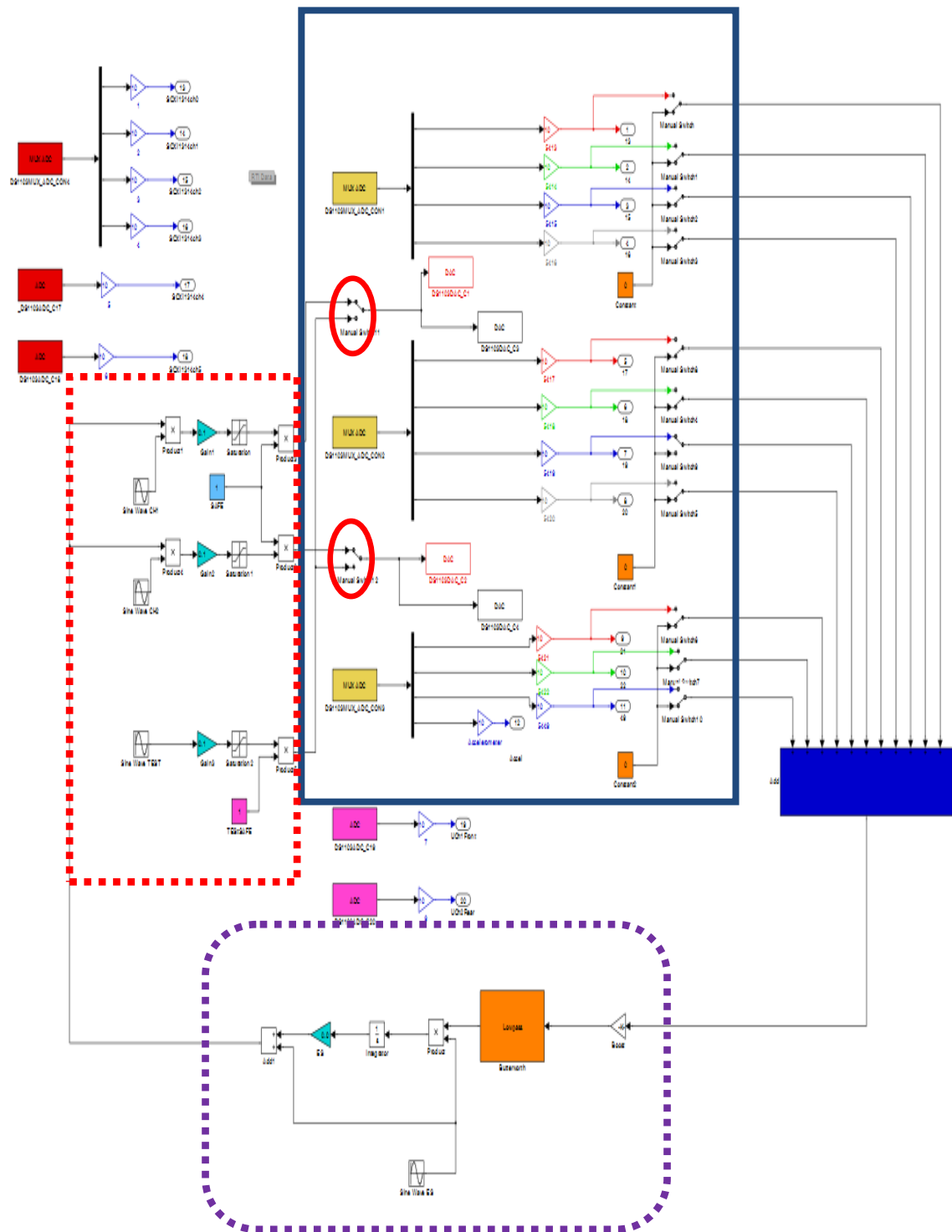


Figure 3.22: Closed Loop Control Schematic for adaptive control

CHAPTER 4.0: ANALYSIS OF UNSTEADY SEPERATED FLOW USING SURFACE PRESSURE MEASUREMENTS & AEROACOUSTICS

4.1 INTRODUCTION

In Chapter 1, the research objective stated that there is a requirement to characterize fully the aerodynamics and the aero-mechanical response of a NACA 0015 based single element high lift system. The current chapter aims to satisfy, at least in part the stated research objective given in Chapter 1, Section 1.4. Insight into the flow physics occurring in an airfoil boundary layer is particularly instructive for the purposes of modeling, simulation and the implementation of both open and closed loop control. Specifically, the purpose of the baseline test is to obtain insight into the aerodynamic characteristics of the un-actuated NACA 0015 airfoil in both cruise and high lift configurations. Specifically we are looking to identify the natural frequencies (or frequency scales) present in the flow over the wing especially those at the stall onset, stall and post stall conditions for the purposes of real time control applications. For Reynolds numbers less than 500,000, laminar separation occurs. In this flow regime, when the boundary layer on the upper surface of the airfoil separates and forms a separated shear layer. In some instances, the separated shear layer fails to reattach, forming a wide wake as shown in Figure 4.1. At higher Reynolds numbers, a turbulent separated shear layer *may* reattach, resulting a laminar separation bubble (Figure 4.2). A change between these two flow regimes is generally unsteady in nature and occurs over a finite range of Reynolds numbers for a given angle of attack. Huang and Lin [58] conducted experiments on a cantilevered NACA 0012 airfoil. The results show that the evolution of the vortex shedding behind the airfoil at low angle of attack is closed related to the behavior of the shear layer

instabilities. At high angles of attack, the low frequency vortex shedding is superimposed by the high frequency shear layer instabilities; this is so because the vortex shedding frequency decreases with increasing angle of attack. Huang and Lin also pointed out in the Reynolds number/angle of attack domain i.e. parameter space there are four characteristic modes associated with vortex shedding; they are laminar, subcritical, transitional and supercritical modes. At significantly high angles of attack (i.e. $\alpha \geq 18^\circ$ is considered to be deep stall [59]) the wing experiences bluff body shedding which is the dominant characteristic of the flow. For our experiment, deep stall is 16° . Huang and Lin indicated that for the bluff body effect there is no unique wave frequency, however, it is not clear to the author whether no unique wave frequency means the vortex shedding frequency or the shear layer frequency. It has been shown by Tian experimentally that a wide wake has a shear layer frequency; this has also been demonstrated computationally by Mittal et al [8]. Perhaps Huang and Lin's statement in [58] might be indicating indirectly (as they did not generate any frequency spectra) that the bluff body effect yields a broadband frequency domain response.

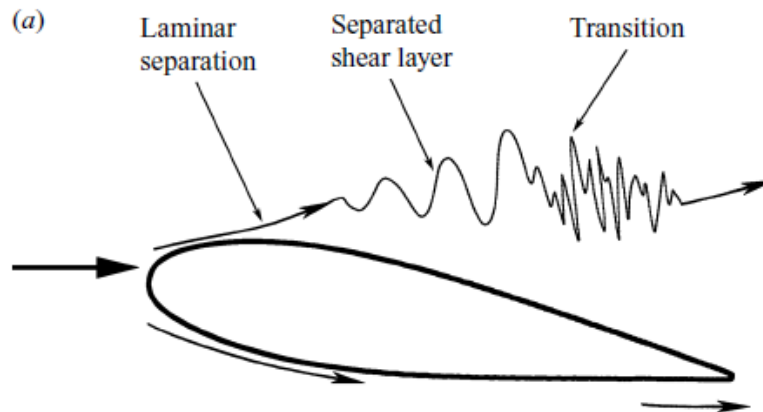


Figure 4.1: Low Reynolds number flow without reattachment [60]

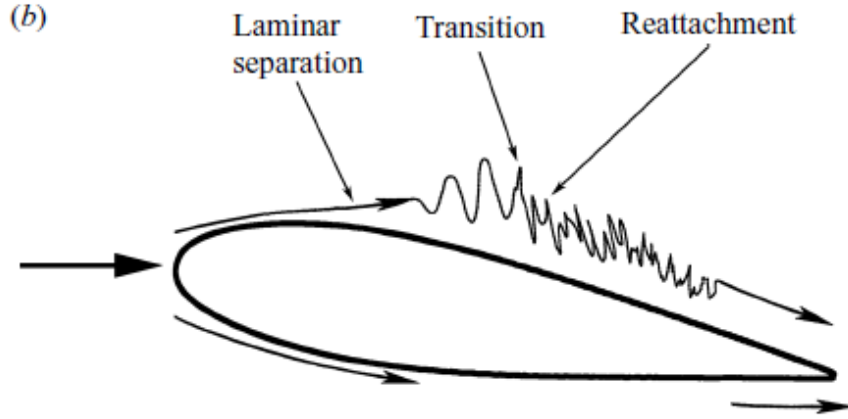


Figure 4.2: Low Reynolds number flow with reattachment [60]

4.2 DATA ANALYSIS METHODS

The pressure signals are generally noisy. In order to remove the noise from the signal in a holistic manner, the signal was truncated and then averaged; it was found that other methods of filtering might introduce spectral artifacts when performing signal processing. For these experiments, all the data records are 30 s in length and sampled at 8 kHz for the aeroacoustic study (Section 4.3) and 9 kHz for all other experiments. When the data record (with time) is time averaged, the resulting number of samples is 40,000. The frequency resolution at 9 kHz is 0.225 Hz for 40,000 samples. The frequency resolution at 8 kHz is 0.2 Hz also for 40,000 samples. The experimental technique for collecting the data involves waiting at least one minute after changing the angle of attack, tunnel speed (for closed loop control) or the forcing/modulation frequency (for open loop control) before recording the data. For a description of the experiments see Chapter 5. The results are presented using the RMS pressure distribution (or RMS pressure versus sensor location). The RMS pressure is calculated in the following way:

$$P_{RMS} = \left[\frac{1}{T} \int_0^T [P_i(t)] dt \right]^{0.5} \quad (4.1)$$

where i is from 1 to 11 indicating the number of transducers and the pressure time series is time averaged as described above. The RMS pressure is non-dimensionalized by dynamic pressure, $q = \frac{1}{2}\rho_o U^2$. The reader will note the use of power spectral density estimates (PSDs) and Fast Fourier Transforms (FFTs) throughout the thesis. Power spectral density estimates involve windowing; and one must select an appropriate window length and window i.e. like a Hanning window to arrive at a meaningful frequency resolution. The problem with using a windowed PSD is that the selection of certain windows can smear out frequency scales that might otherwise aid an engineering analysis. To address this problem, time averaged FFTs are used. The time averaged FFT offers spectra with good frequency resolution and a clean or low noise presentation of the stationary frequency components contained in the signal. In Chapter 2, the use of the Wigner-Ville time frequency distribution was presented. This is made possible by using the Matlab based Time Frequency Toolbox (TFTB). The TFTB works well with signals that are either generated from simulations with short time durations or longer simulation times with low sampling frequencies; this is not appropriate for application to experimental signal processing because it results in computer memory error issues when the sampling frequency is very high. From a practical implementation standpoint, it made sense to use wavelet scalograms which circumvented the computer memory issue and accommodated the kHz range sampling frequencies associated with this experimental work while providing the time frequency analysis capability. From a research standpoint, wavelets are well suited for analyzing multiscale signals with intermittency. Continuous wavelets provide better frequency resolution and the transform itself is a band-pass filter. For this research, we have decided to use the Morlet and Mexican Hat wavelets. The

Morlet wavelet (Figure 4.3) is best suited to the analysis of locally periodic signals. The Mexican Hat wavelet (Figure 4.4) is best suited to analyze individual extrema. In addition, the Mexican Hat wavelet is closely related to a normalized Gaussian Filter.

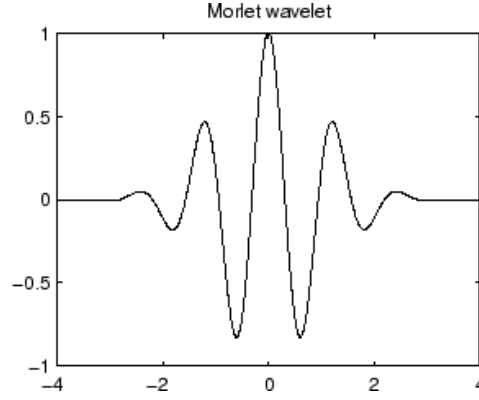


Figure 4.3: Morlet Wavelet

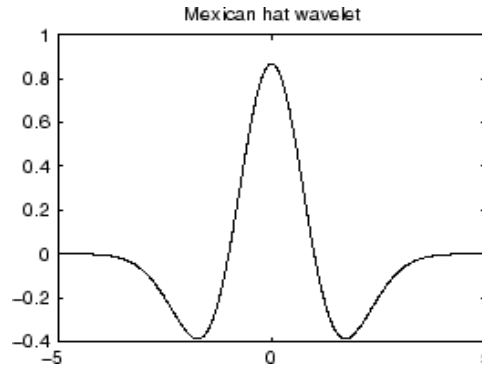


Figure 4.4: Mexican Hat Wavelet

The mathematical definitions for each of the wavelet are provided below:

$$\text{Morlet: } \psi_M(t, \omega) = \frac{\omega}{\sqrt{c_\psi}} \left(e^{2i\pi t\omega} - e^{\frac{z_0^2}{2}} \right) e^{-2\pi^2(t\omega)/z_0^2} \quad (4.2)$$

$$\text{Mexican Hat : } \psi_2(\sigma, t) = \sigma \left(\frac{t^2}{4\sigma^2} - \frac{2}{\sigma} \right) \left(\frac{1}{2\sqrt{\pi}\sigma} e^{\frac{-t^2}{4\sigma}} \right) \quad (4.3)$$

The implementation of the wavelet transforms (scalogram) is facilitated by a Matlab toolbox developed by Professor Jacques Lewalle of Syracuse University.

4.3 FLOW INDUCED NOISE SOURCES

Initially the experiment was conducted with the synthetic jet actuator slots open. This however produced an acoustic disturbance that became very pronounced at 4, 6 and 8 degrees angle-of-attack. This is evident from the foremost transducer $x/c=0.1826$, located downstream the SJA slot. The reader will note that there is a frequency peak that fluctuates about 423 Hz in all of the power spectra plots; this will be discussed later in the text. At 4 degrees three very round distinct frequency peaks equally spaced at 825.5 Hz, 1238 Hz, and 2100 Hz appear (Figure 4.5). At 6 degrees, the 825.5 Hz peak decrease in amplitude and peak at 590.5 Hz appears; the peak at 1238 Hz shifts to 1014 Hz and is considerably more pronounced. It is also observed that 1438 Hz appears and the rounded 2.1 kHz remains. At 8 degrees, the author believes that the 590.5 Hz shift to 715.5 Hz and is very sharp; the other modes seem to be suppressed with the increase in angle of attack (Figure 4.6). Typically, a cavity that is exposed to a fast moving boundary layer will develop resonant modes. As the velocity increases these modes establish a standing wave pattern similar to that which is developed in open cavities. Beyond the critical velocity, the frequency peaks will lose their sharpness. In this case, the velocity was held constant and the angle-of-attack was changed; increasing the angle-of-attack had the same effect as velocity in that the peaks at 4 degrees rounded and at 8 degrees, certain peaks sharpen and increase in amplitude. As with cavity flows, once the resonant modes reach the equilibrium limit cycle state often indicated by a large amplitude frequency peak, there are reflections that take place inside the cavity and spill out into the shear layer; spill over results in the propagation of the acoustic disturbance downstream of the open SJA slots. All the frequency peaks to the right of the 423 Hz are due to the open slots, this is

confirmed by the fact that at 10 degrees all that remains is the frequency peak about 423 Hz (Figure 4.6). Note that as the angle-of-attack increases, spectrum becomes increasingly more broadband. The broadband response is an indication that the flow over the wing is turbulent and the pressure gradient is becoming more severe with the increase in angle of attack.

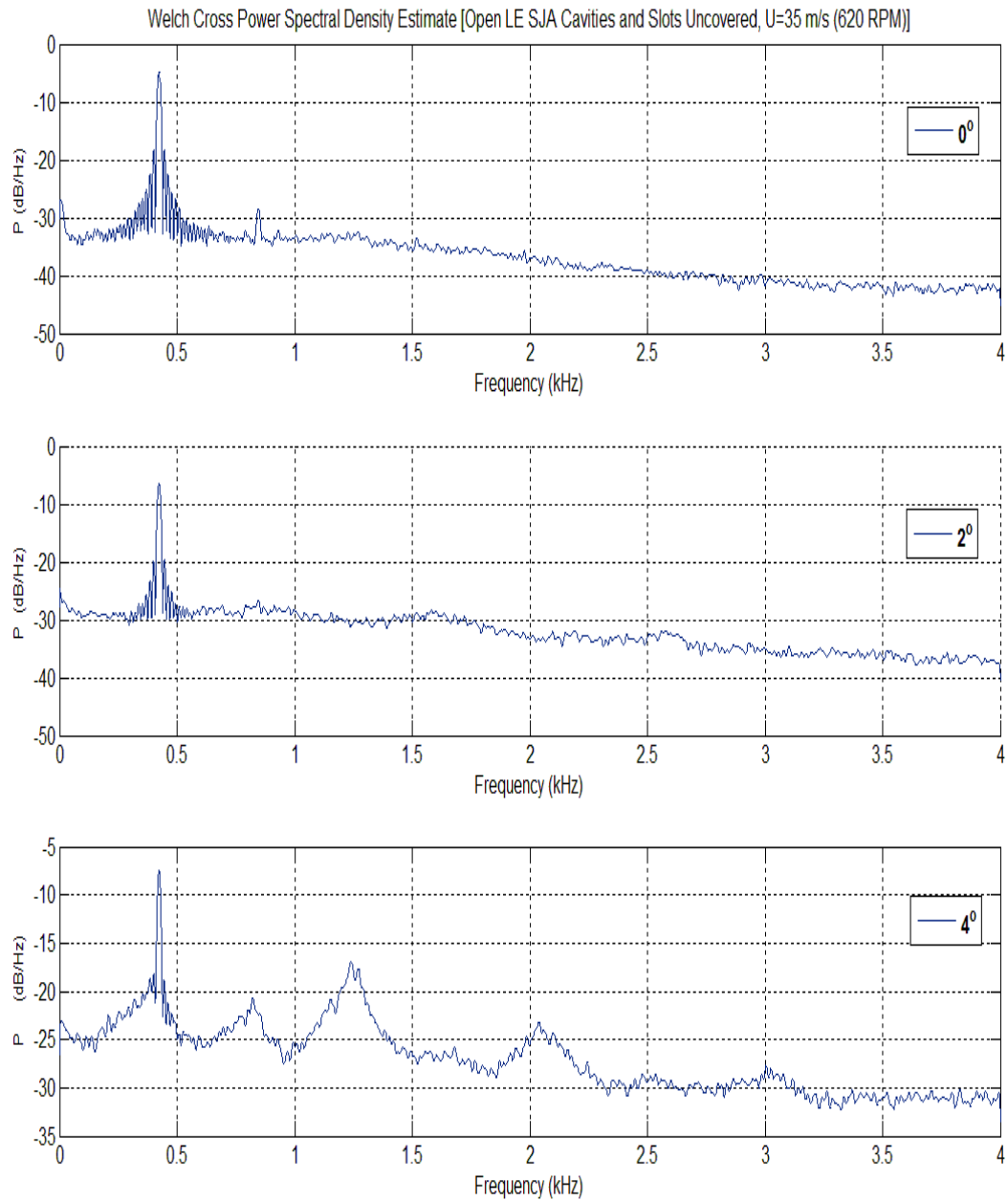


Figure 4.5: Spectra 0-4 degrees AoA

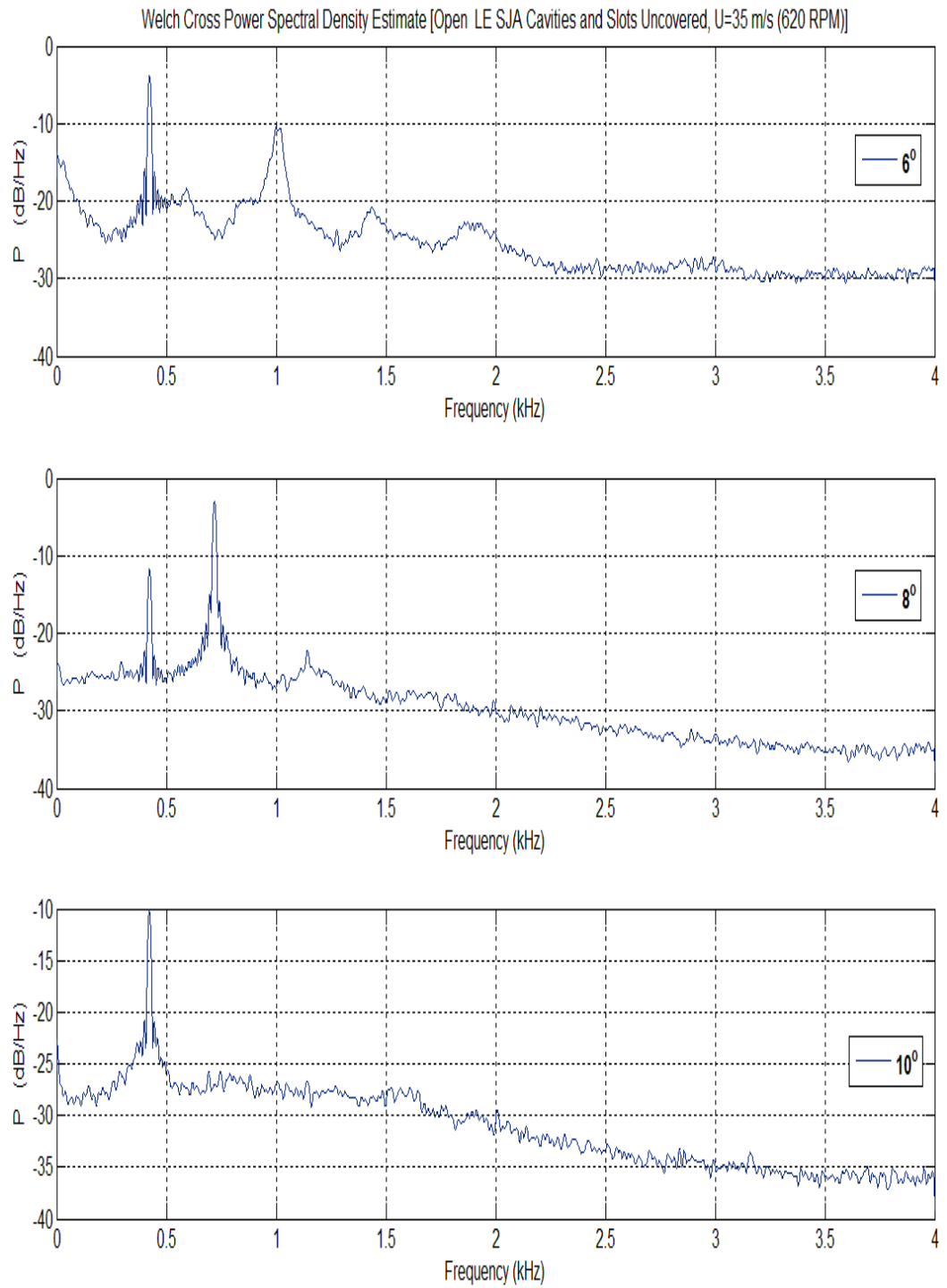


Figure 4.6: Spectra 6-10 degrees AoA

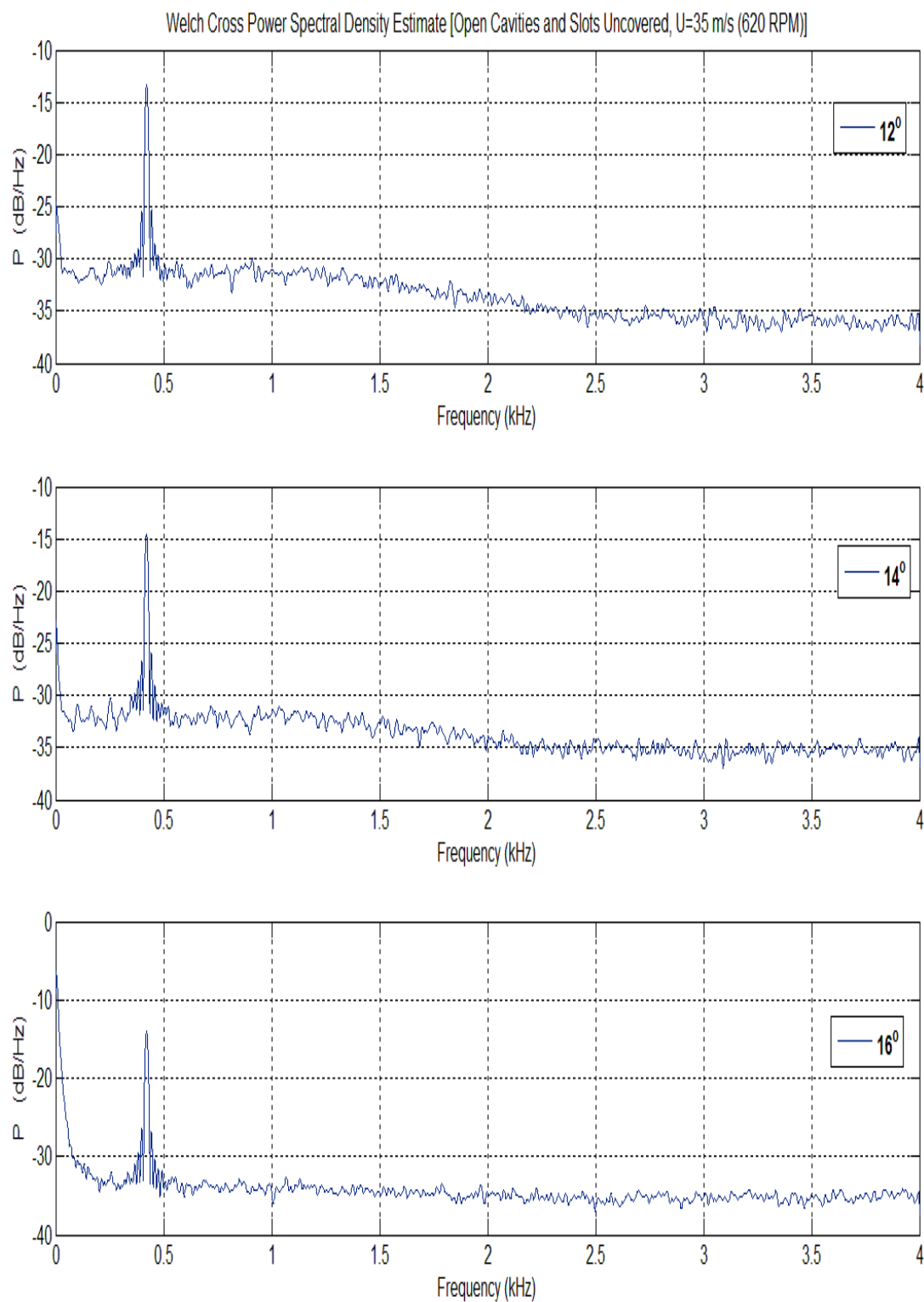


Figure 4.7: Spectra 12-16 degrees AoA

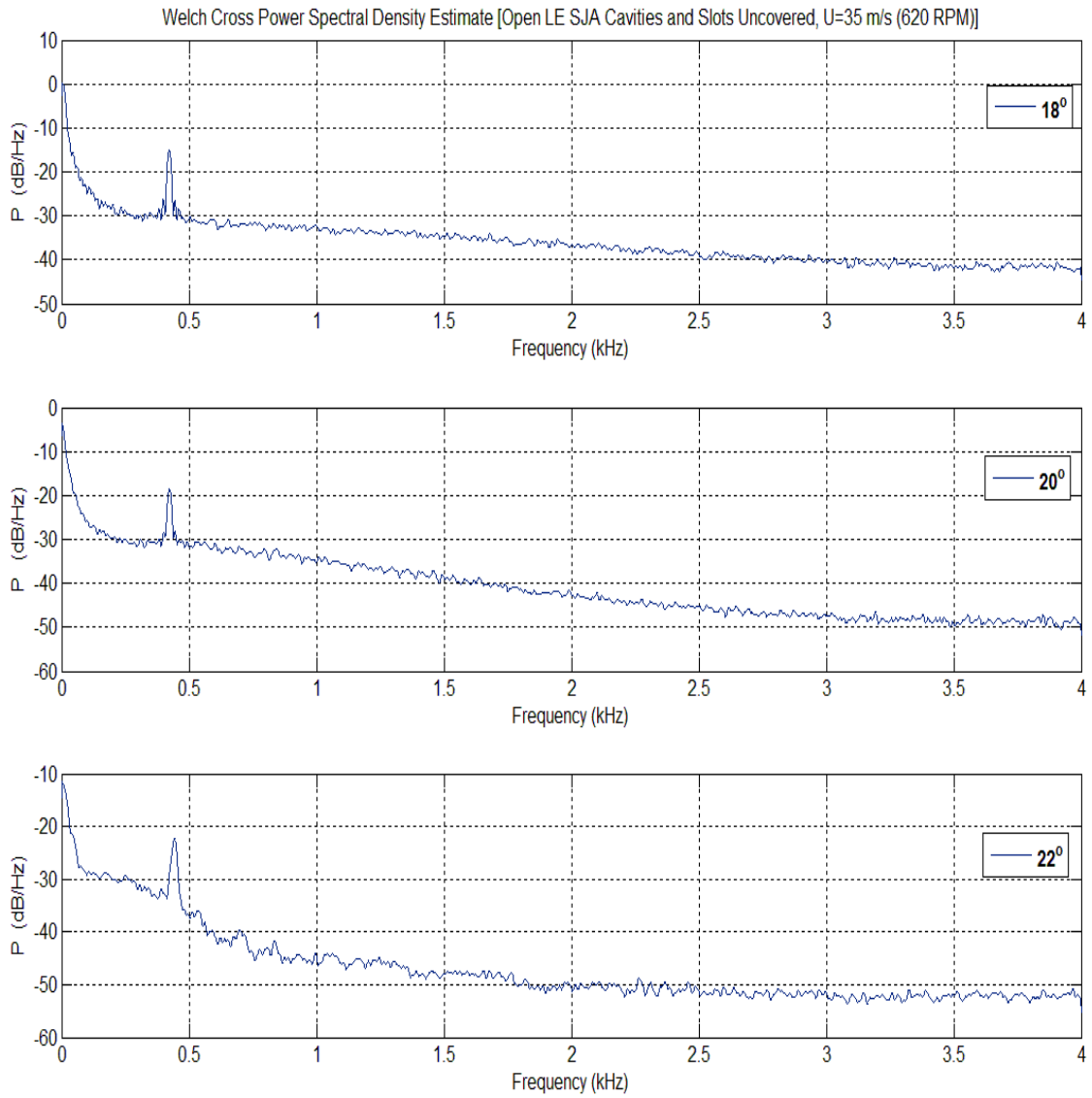


Figure 4.8: Spectra 18-20 degrees AoA

The experiment was repeated with the slots covered. At 4 degrees, it is shown here that the rolling peaks observed in the first experiment are no longer present (Figure 4.9); and at 8 degrees the peak at 715.5 Hz has been removed (Figure 4.10).

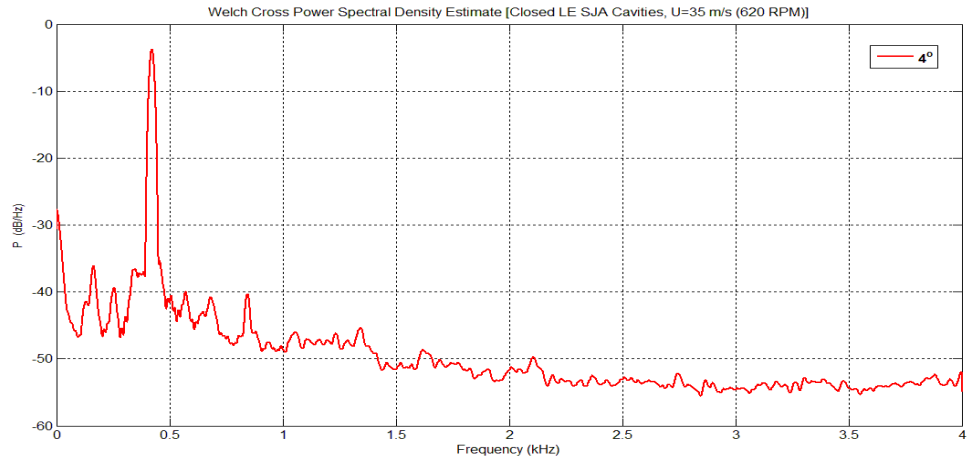


Figure 4.9: Spectra at 4 degrees AoA, Slots Closed

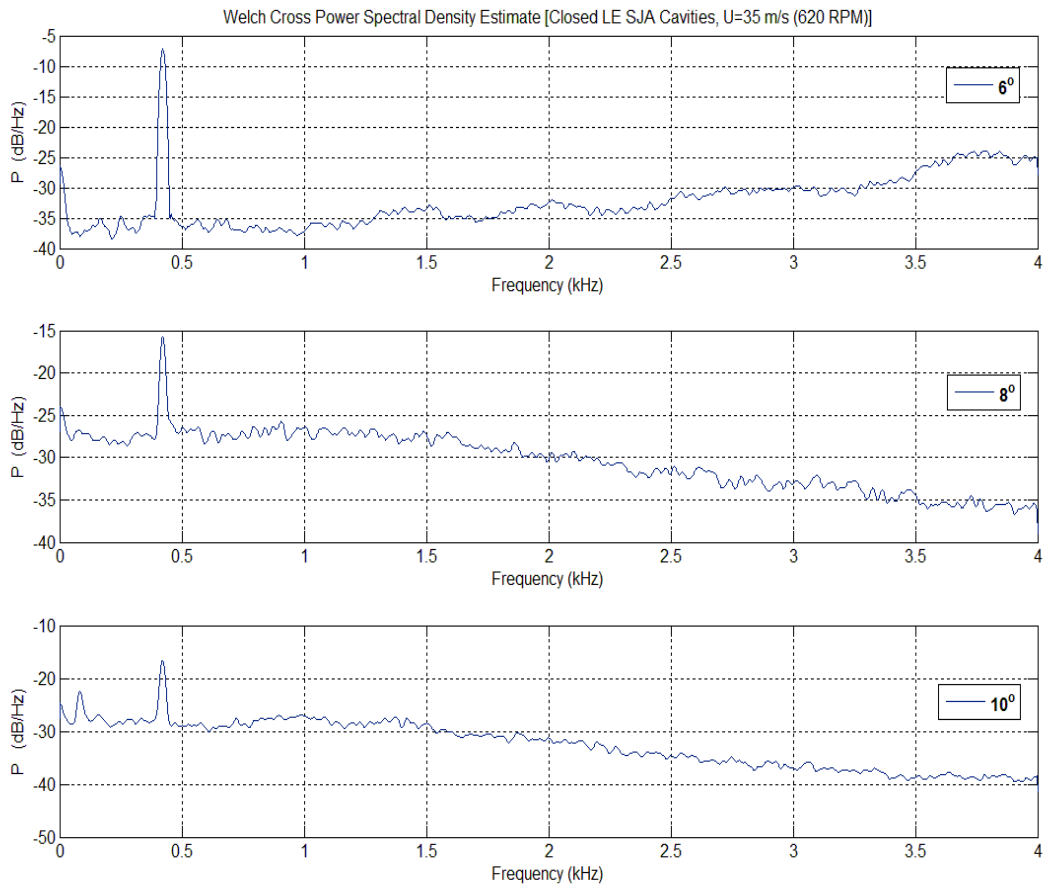


Figure 4.10: Spectra 6-8 degrees AoA, Slots Covered

Let us now revisit the earlier statement about the 423 Hz peak. At first, it was thought that the wind tunnel facility had a Helmholtz frequency, but Helmholtz tones tend to be associated with open cavities. The 423 Hz tone is nearly 3 times that of the blade passage frequency of the lift fan at 165 Hz and is too low to be a shear layer mode. What remains is that this frequency is coming from the wind tunnel test section configuration. Specifically, the test section configuration at Clarkson University is such that each false wall is parallel to the sides of the wind tunnel test section hence the walls form a converging duct; the false walls form a flat plate cascade. In general, a typical rectangular or unstaggered cascade system (Figure 4.11) is defined as an array of parallel or annular plates in the plane of a gas or any compressible fluid, and is generally assumed to be subsonic. The on-coming flow produces a wake at the trailing edge of the false wall cascade which generates an acoustic resonance. These acoustic resonances can interact with the structural resonances of the cascade itself.

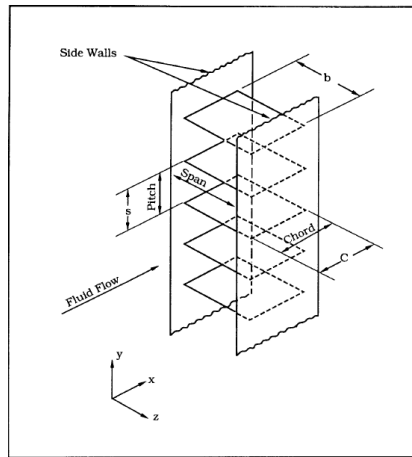


Figure 4.11: Flat Plate Cascade [61]

Runyan et al [62] provide a derivation for an airfoil between solid, reflecting walls using the subsonic integral equation for lifting surface theory. It was noted that the kernel of the

integral equation relating lift pressure to the downwash boundary condition became infinite at frequencies equal to:

$$f_{res} = \frac{a_{\infty}}{2h} \sqrt{1 - M^2} (2n - 1), n = 1, 2, 3 \dots \quad (4.1)$$

where a_{∞} is the speed of sound in air and h is the height of the tunnel. When $n=1$, this is the lowest frequency in the series and it is termed the tunnel resonance frequency. Now the diagram given by Parker (Figure 4.11) schematically represents h as the separation distance between plates; but Runyan indicates that h is the height of the tunnel. In order to clarify this, one has to consult another of Parker's works [63] and [64, NASA CR-4671]. In these references it is indicated that the separation between the plates is the correct parameter to be substituted into equation 4.1. When this is done, the acoustic resonant frequency is 423.107 Hz. The experimental result is 423 Hz at 0 degrees angle of attack.

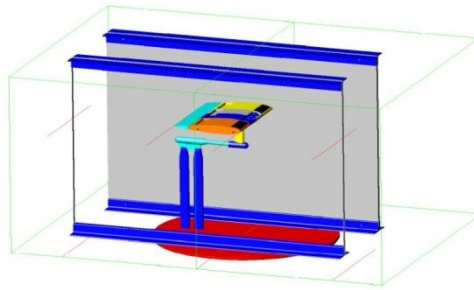


Figure 4.12: Test Section Configuration

In ref [64], it is stated that for certain velocity ranges the vortex shedding frequency from the cascade will become synchronized with the acoustic resonance frequency. For flat plates with a blunt trailing edge (as is the case for our test section configuration) the vortex shedding frequency will lock on to a higher acoustic resonance. If the velocity were to increase further, the cascade vortex shedding frequency may *jump* to the next

highest acoustic resonance frequency. However, the velocity is held constant at 35 m/s but the angle of attack is changing. As the angle of attack is increases the frequency peak tends to exhibit frequency creep to the left and right of 423 Hz in small magnitudes. When the angle of attack becomes greater than 15 degrees, the Parker mode increases from 423 Hz to 425 Hz. At 22 degrees, the frequency jumps to 440Hz (Figure 4.13). It is possible that the bluff body wake is interacting with the cascade wake which causes an amplification of the acoustic mode, hence the variation of the Parker mode with angle of attack, particularly in the post stall regime.

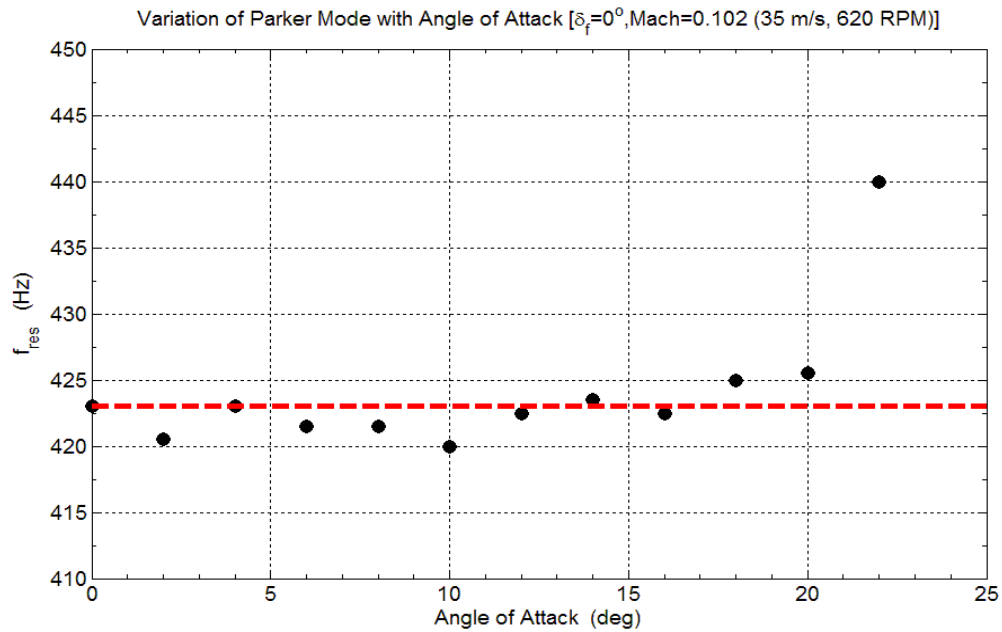


Figure 4.13: Parker Mode Variation with Angle of Attack

As a result of this finding, it is recommended that the wind tunnel testing for AFOSR project refrain from being tested at this velocity or have the trailing edge of the false walls made sharp at the trailing edge. The existence of the Parker Mode acoustically contaminates the experimental data. Further, all subsequent wind tunnel tests will be conducted with the slots covered regardless of whether the synthetic jet have the driver

hardware in the housings or not. The slot will remain covered for the baseline/system identification tests.

4.4 UN-ACTUATED FLOW PHYSICS

For the given configuration (**with actuator slots open**), the pressure fluctuations increase along the chord of the airfoil (See Figure 4.14). The pressure fluctuation profiles are both similar in shape but are slightly shifted due to the flap deflection. The primary reason for the similarity in profile is due to the recirculation region associated with these wing configurations. The increase in pressure fluctuations indicates that the flow is separated from the airfoil. Similar flow behavior i.e. large amplitude pressure fluctuations have been observed in the conduct of flow control experiments on backward facing steps and ramps. Specifically, for the $\delta_f = 0^\circ$ case, the first three pressure transducers show a slight increase in the fluctuation amplitude over the deflected flap configuration. The mid-section pressure fluctuations are only marginally higher due to the flap deflection, but converge to the same fluctuation level at the trailing edge. Figure 4.15 is an excerpt from a 30s data record. The length of the time series was reduced to 0.5s so that the reader may better observe the features of the time series. The time series are arranged in order of location from leading edge to trailing edge. The time series set show the presence of spike trains. Visually there are no significant features in the times series of the $\delta_f = 20^\circ$ flap case and so they will not be presented here. Spike trains or bursting dynamics is the primary mode of electrical activity in a variety of biological systems including the human brain. Spike trains are an indication of phase multi-stability. Phase multi-stability generally assumes that there is a coexistence of two or more synchronous states. As alluded to earlier in the text there is a recirculation and reverse flow region

above the wing in the current configuration. This is confirmed by PIV work completed by Kabiri [65]. Specifically, there is a standing vortex that covers the trailing edge flap; further upstream from the flap but before $x/c=0.2660$, the velocity contours in this region creep upstream and then rapidly change direction. This flow behavior accounts for the large amplitude pressure fluctuations seen in the chordwise direction (Figure 4.14). Figure 4.16 shows a waterfall plot of the power spectral densities along the chord of the wing. If one examines the amplitude of the frequency peaks, in particular the first peak located at an average frequency of approximately 33 Hz, the reader will note that the power increases as one moves from leading edge to trailing edge. It can be observed that here are frequency peaks located at 32.68 Hz, 162.86 Hz, 230.57 Hz, 925.55 Hz and 1092 Hz. The power at these frequencies increase in magnitude as the flow convects downstream of the leading edge. The increase in power at the trailing edge, in particular over the last three pressure transducers is due to the presence of a standing vortex that was mentioned earlier. In addition, the slots of the synthetic jet actuators are uncovered and as such the grazing boundary layer interacts with the open cavities producing self sustained acoustic excitation that generates a sound pressure field that is radiated out into the separated wake. It should be noted that the first mode however is significantly less than both the Helmholtz and natural frequencies (1800 Hz, 1101 Hz).

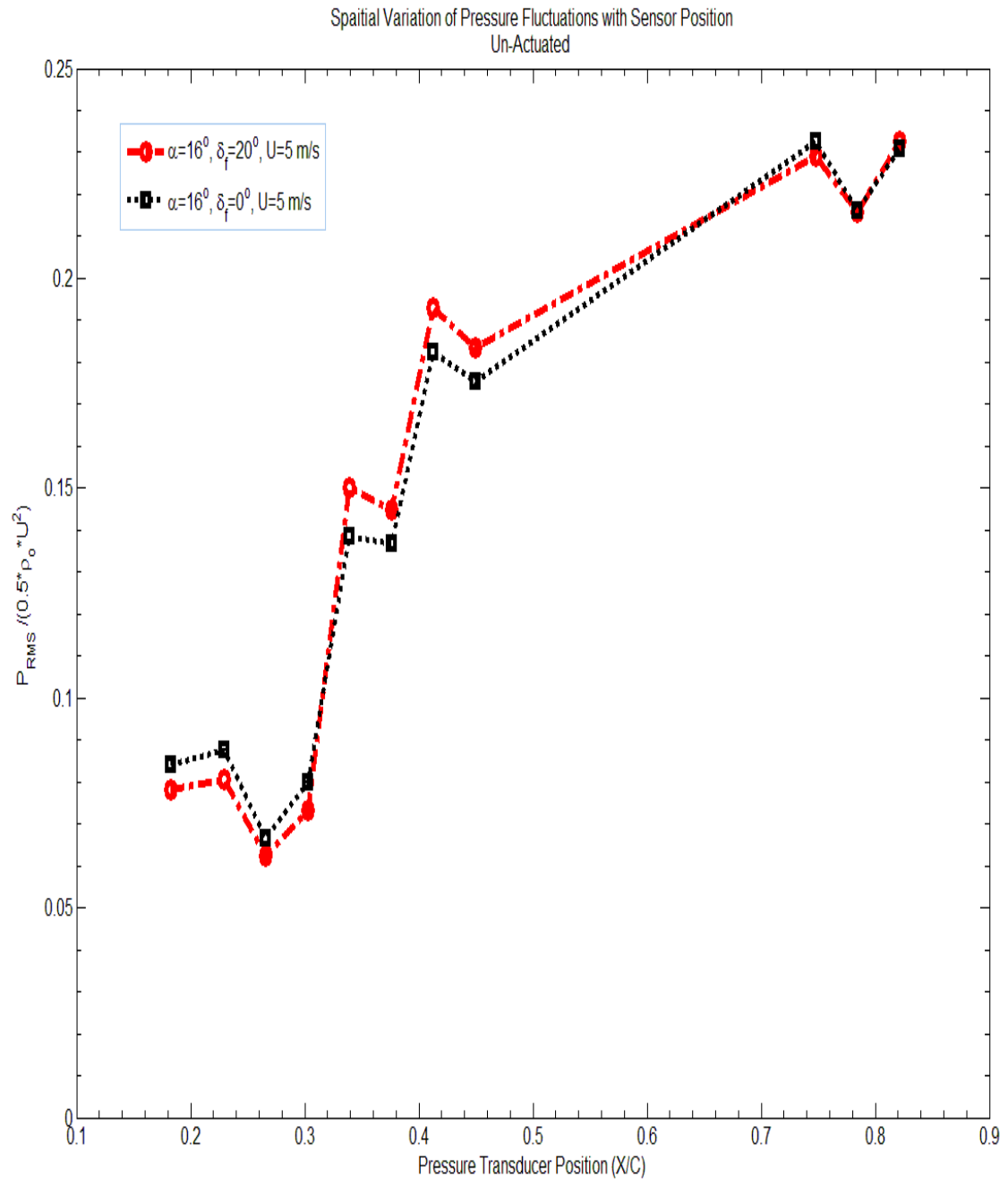


Figure 4.14: RMS Pressure vs. Chordwise Position

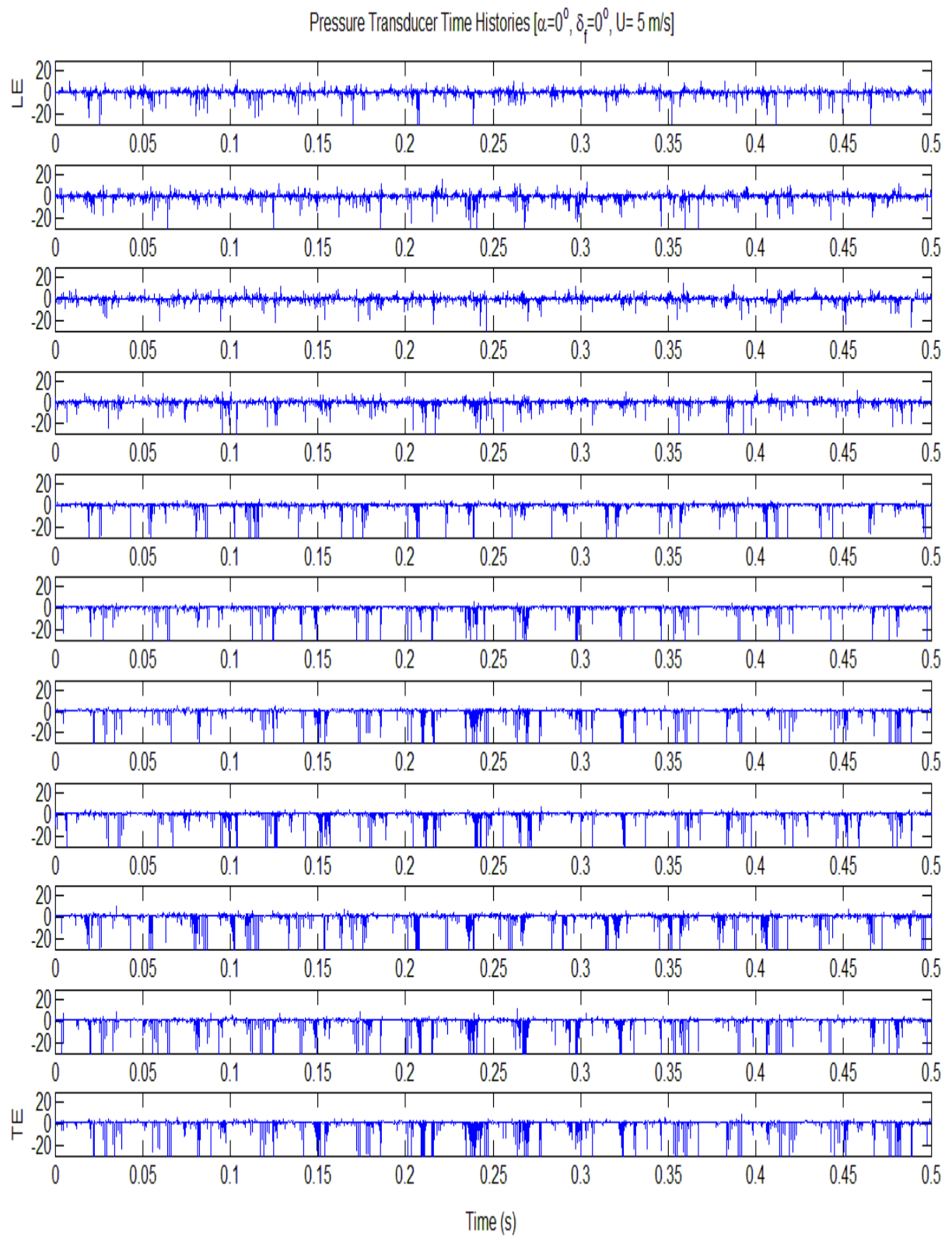


Figure 4.15: Pressure Sensor time series

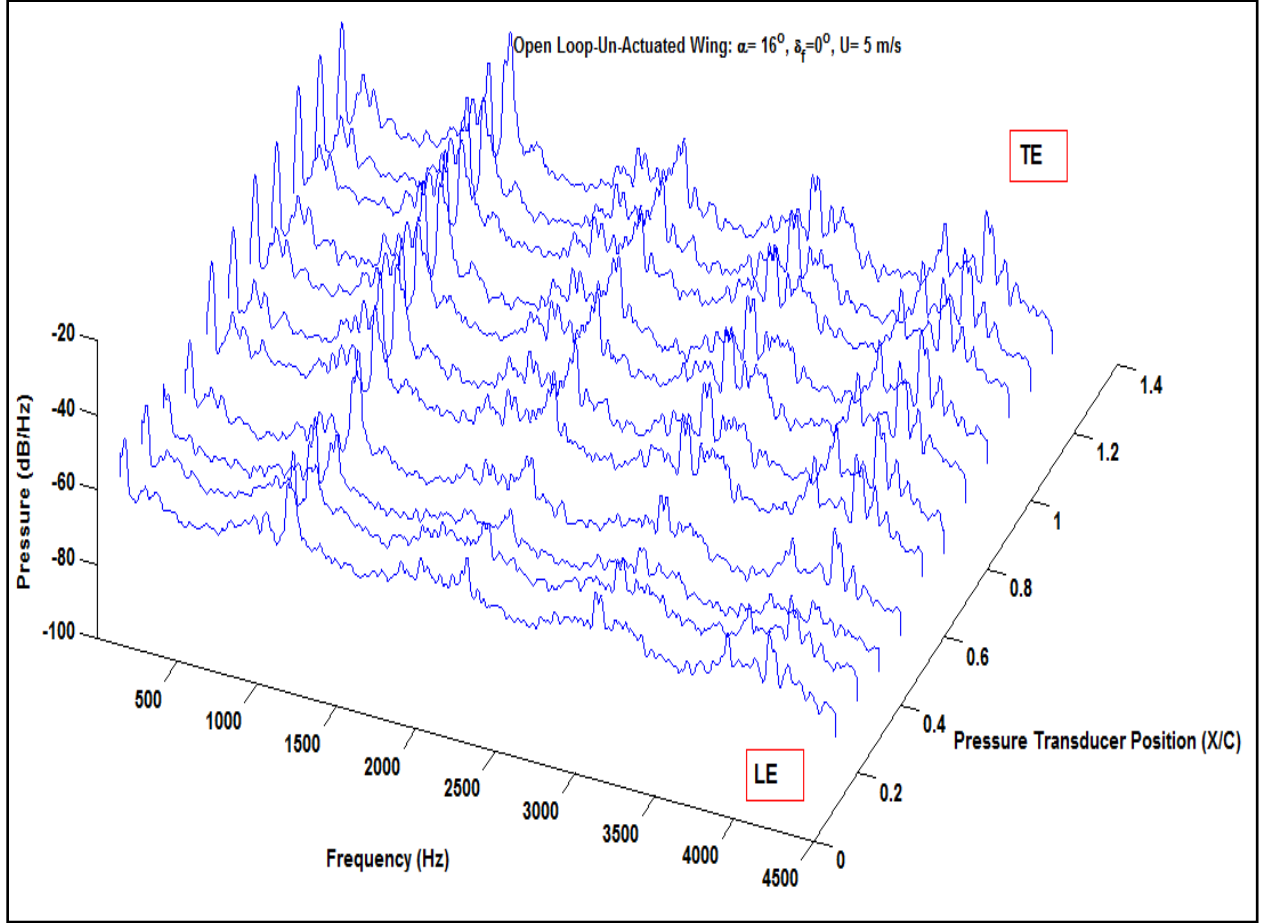


Figure 4.16: Chordwise Power spectra, $\alpha = 16^\circ$, $\delta_f = 0^\circ$, $U = 5$ m/s

Next we present the result of the time frequency analysis (via wavelet transforms) of the measured chordwise pressure fluctuations. There are eleven time frequency maps and they are presented in order of location i.e. from leading edge to trailing edge. At $x/c = 0.1826$ (Figure 4.17), the Morlet scalogram shows a band of low energy centered on 37 Hz with some intermittent higher energy bursts. The low energy events are in fact indications of weak local periodicity in the flow at this chordwise station. The first local periodic event occurs at 93.13 ms at a frequency of 37.84 Hz. The second occurs at 0.9s also at 34.7 Hz. About 0.1s later we observe a burst at 1s at a frequency of 63.64 Hz. In time interval between 1s and 2 s, there is no significant local periodicity, but there are

high energy events that occur at frequencies greater than 50 Hz across the time series. Other events occur at 2.33s, 2.8s, 3.17s, 3.6s and 4.33s with a variation in frequency between 34 Hz and 38 Hz. For the regions in which there is weak periodicity, the corresponding interval on the Mexican Hat scalogram shows large variations in frequency and significant modulation over those time intervals, with lots of activity above 50 Hz. In the Morlet scalogram, there is little activity below 29 Hz. The intermittent finger like patterns above the narrow frequency band indicates that flow is in a chaotic regime.

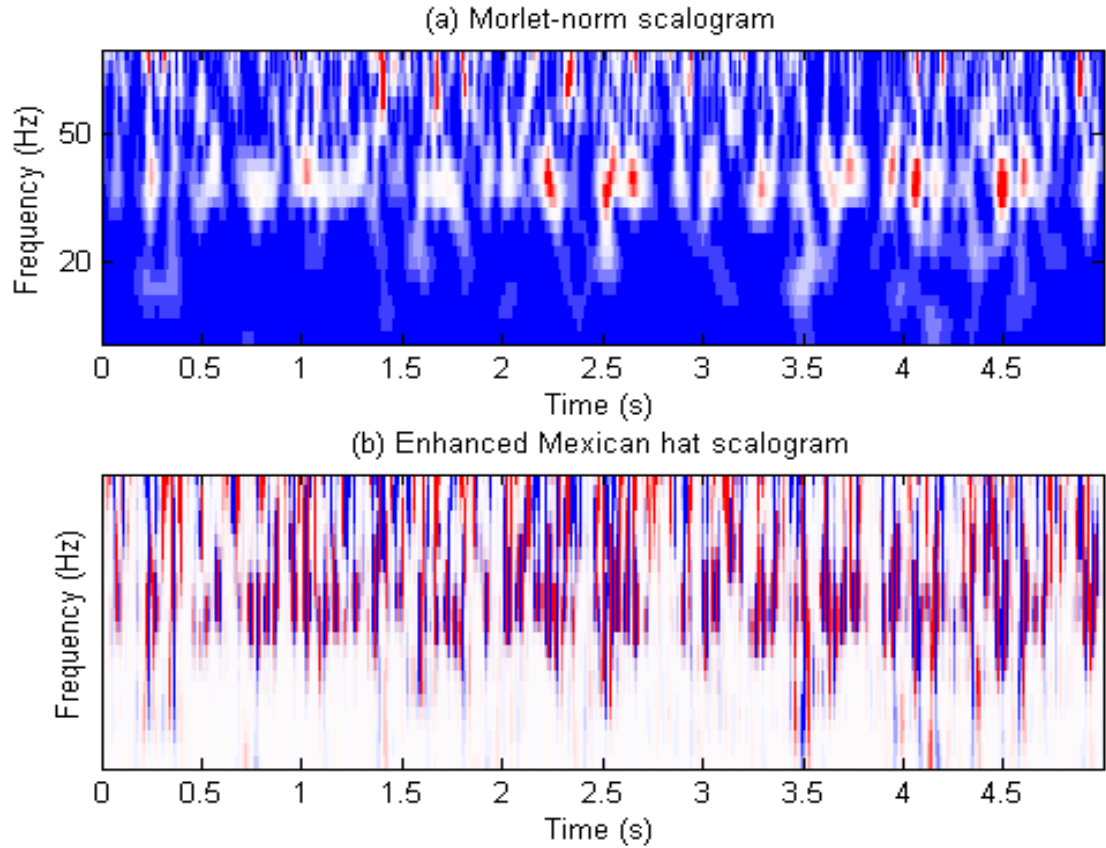


Figure 4.17: Wavelet Map, $x/c=0.1826, \alpha = 16^\circ, \delta_f = 0^\circ, U = 5 \text{ m/s}$

Although the flow is not controlled here, the narrow band seen in the first wavelet map is an indication that there is weak synchronization of the flow at that location even though the periodicity is not that strong. Note also that the root mean square pressure amplitude and power at this location is low (See Figures 4.14 and 4.15). At $x/c= 0.2293$, again we see temporal episodes of weak localized periodicity and that is intermittent. There are high energy events located at 2.228s, 2.53s, 4.1s and 4.5s and range from 34 Hz to 38 Hz. At this location we start to see the appearance of weak periodicity below 29 Hz accompanied by high energy events located above 50 Hz.

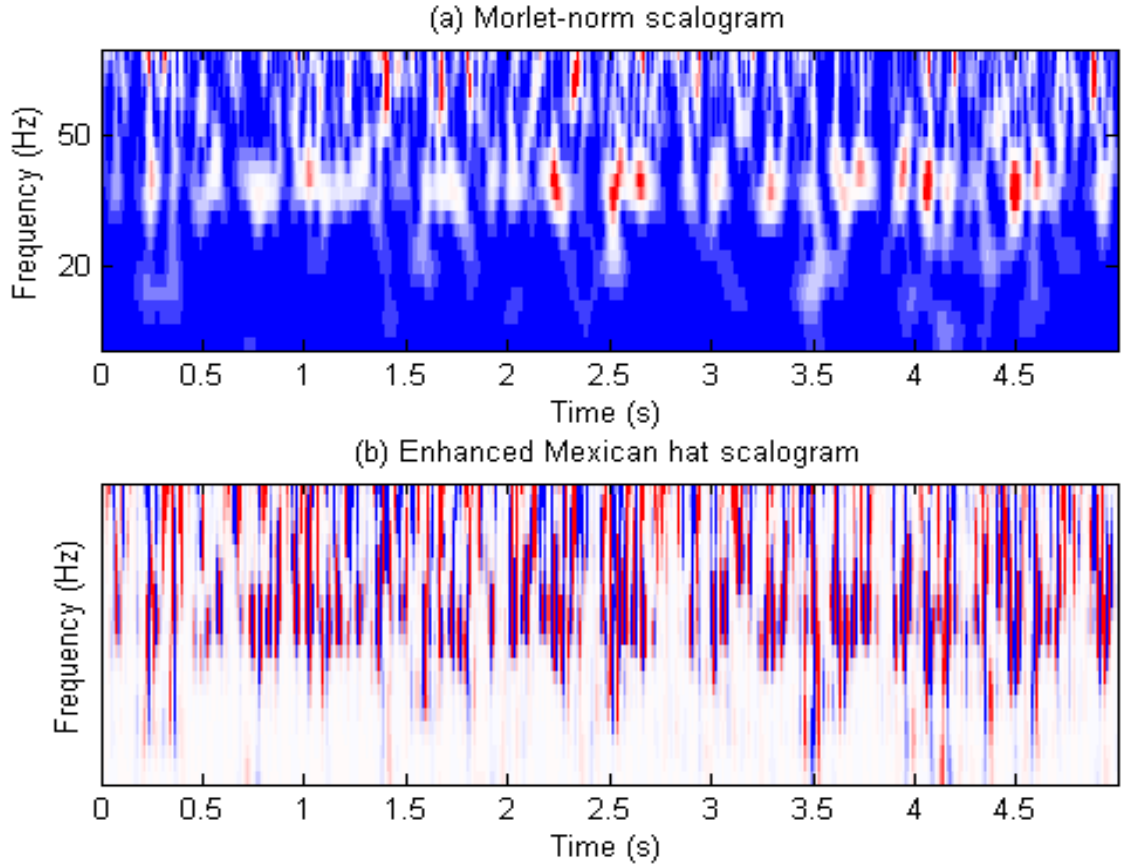


Figure 4.18: Wavelet Map, $x/c=0.2293, \alpha = 16^\circ, \delta_f = 0^\circ, U = 5 \text{ m/s}$

In Figure 4.14, we see that at $x/c=0.2660$, the RMS pressure at this location is significantly lower than the previous two chordwise stations. The Morlet wavelet map (Figure 4.19) at this location shows a significant breakdown in periodicity and coherence. There are four high energy events of very short duration located at 0.46s at 31.82 Hz, 2.44s at 34.7 Hz, 3.47s at 31.82 Hz and at 4.4s also at a frequency of 31.82 Hz. This loss of periodicity and coherence is primarily due to the changes in flow direction as it is located at the upper edge of the recirculation region. The absence of coherence at this location could indicate that the separation line.

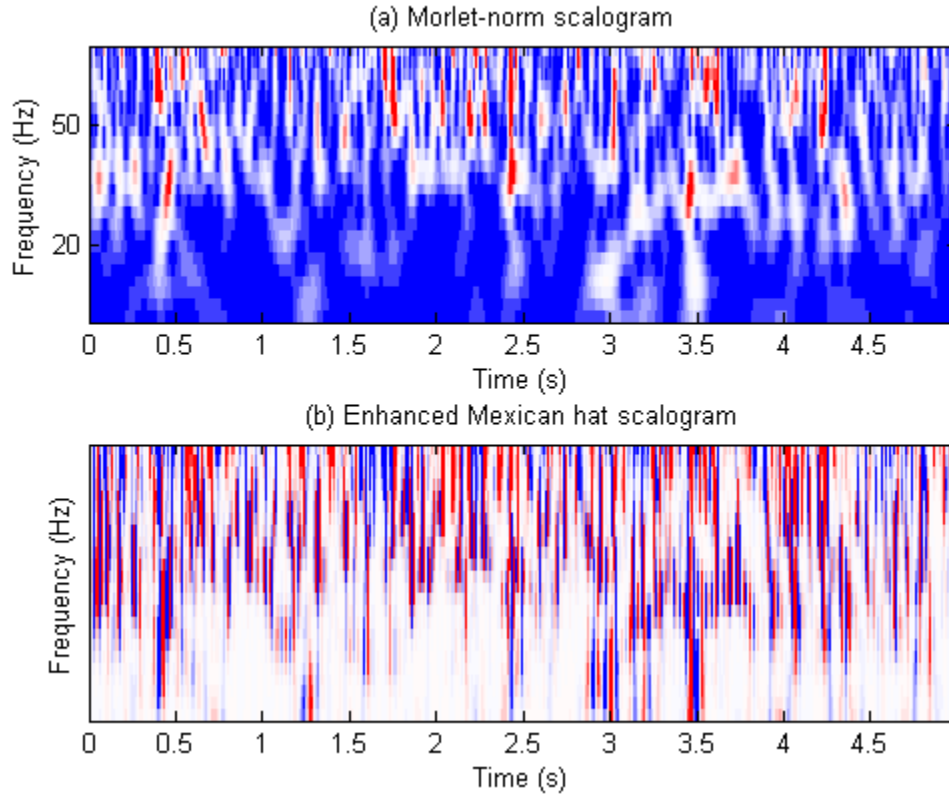


Figure 4.19: Wavelet Map, $x/c=0.2660$, $\alpha = 16^\circ$, $\delta_f = 0^\circ$, $U = 5 \text{ m/s}$

As we start to physically enter the recirculation region, the Morlet wavelet map at $x/c=0.3026$ shows that the synchronization of the flow is more persistent at this

chordwise station. At this location (Figure 4.20) we see that there is a loss of periodicity after 3.5s (see right of black line). Before this time, there are events at 0.22s, 0.69s, 2.24s and 3.48s, all ranging from 34.7 Hz to 41.27 Hz. Again, the Mexican hat wavelet map indicates that events where there is a loss of periodicity, there is still significant modulation of the flow which is accompanied by large changes in the frequency at these instances in time.

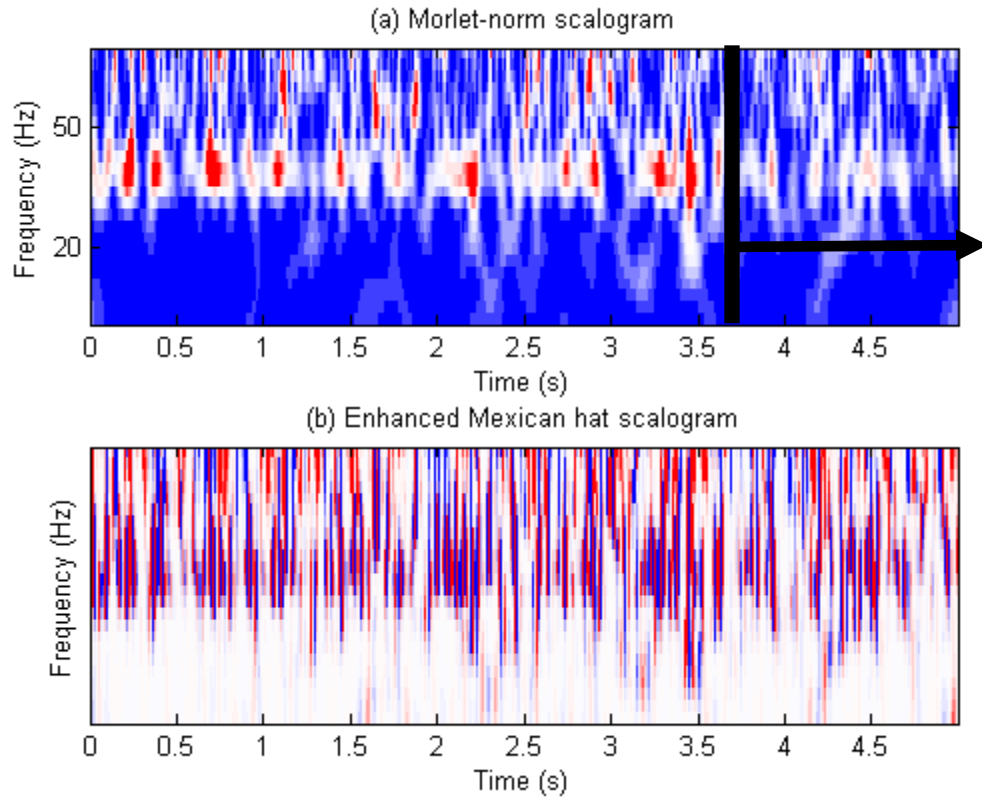


Figure 4.20: Wavelet Maps, $x/c=0.3026$, $\alpha = 16^\circ$, $\delta_f = 0^\circ$, $U = 5 \text{ m/s}$

At station $x/c= 0.3393$ (Figure 4.21), strong periodicity is observed at the time intervals of 0-1s, 2.5s-4s and 4.1s -5s. According to the supporting Mexican Hat scalogram the flow is heavily modulated. In general, the transducers located directly in the recirculation region exhibit increased frequency locking/synchronization. The synchronization is

indicated by a contraction of the time frequency space about a single frequency band. In addition to the contraction we see that there is persistent strong local periodicity. Given the experimental nature of this work, it may be necessary to develop a secondary condition under which we may evaluate frequency locking such as a cross correlations at a given frequency line. There are however, time intervals in the contraction that show a loss of periodicity and coherence. For example, at $x/c=0.3760$, there is a time interval from 0.5s and terminating at 1.5s in which there weak local periodicity. At $x/c=0.4126$, the temporal location of weak periodicity is shifted to the right and starts at 1.2s and terminates at 2s. Again the Mexican hat scalogram indicates that although the periodicity is marginal, the flow is significantly frequency modulated over the 800 millisecond duration. The chordwise station $x/c=0.4493$ is located just before the TE flap hinge. Again weak localized periodicity, yet the flow is still locked in at his location. Before 0.5s, there are three high energy events followed by a temporal region of weak local periodicity starting from 0.75s and terminating at 3.2s. This region is much longer in duration than the previous sensor locations. At locations $x/c=0.7483$, $x/c=0.7846$ and $x/c=0.8210$, there is a marked increase in sustained local periodicity i.e. the high energy periodic events are persistent over the 5s time span. The ‘finger’ structures seen above 50 Hz, are more regular in time and there is very little time frequency activity below 29 Hz at these sensor locations; this likely due to the contraction caused by the flow synchronization. As a first assessment, the flow after $x/c=0.3026$ is passively frequency locked/synchronized by the recirculation region that covers nearly 60% of the chord (which is dominant) and the interaction of the flow with leading array slots.

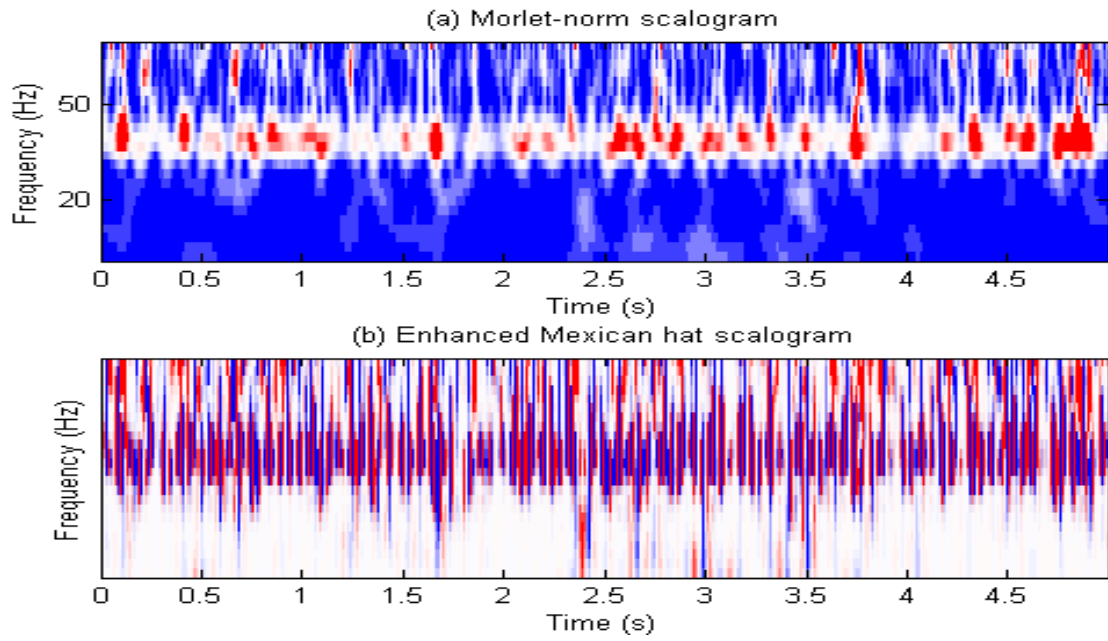


Figure 4.21: Wavelet Maps, $x/c=0.3393$, $\alpha = 16^\circ$, $\delta_f = 0^\circ$, $U = 5 \text{ m/s}$

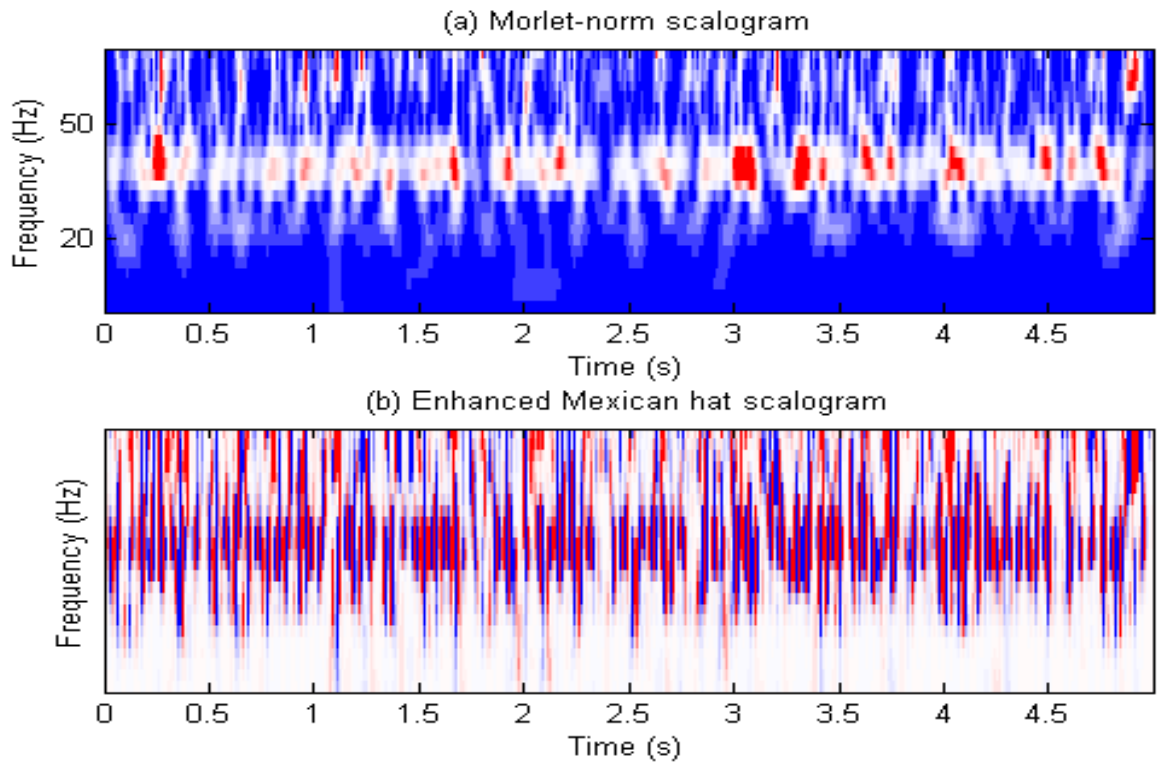


Figure 4.22: Wavelet Maps, $x/c=0.3760$, $\alpha = 16^\circ$, $\delta_f = 0^\circ$, $U = 5 \text{ m/s}$

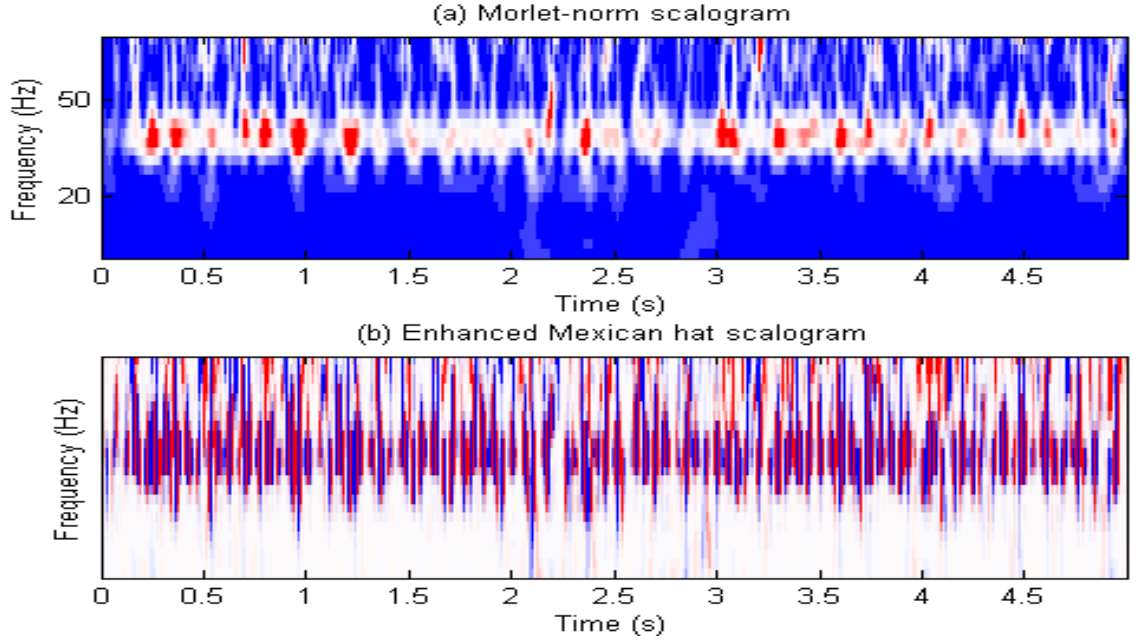


Figure 4.23: Wavelet Maps, $x/c=0.4126$, $\alpha = 16^\circ$, $\delta_f = 0^\circ$, $U = 5 \text{ m/s}$

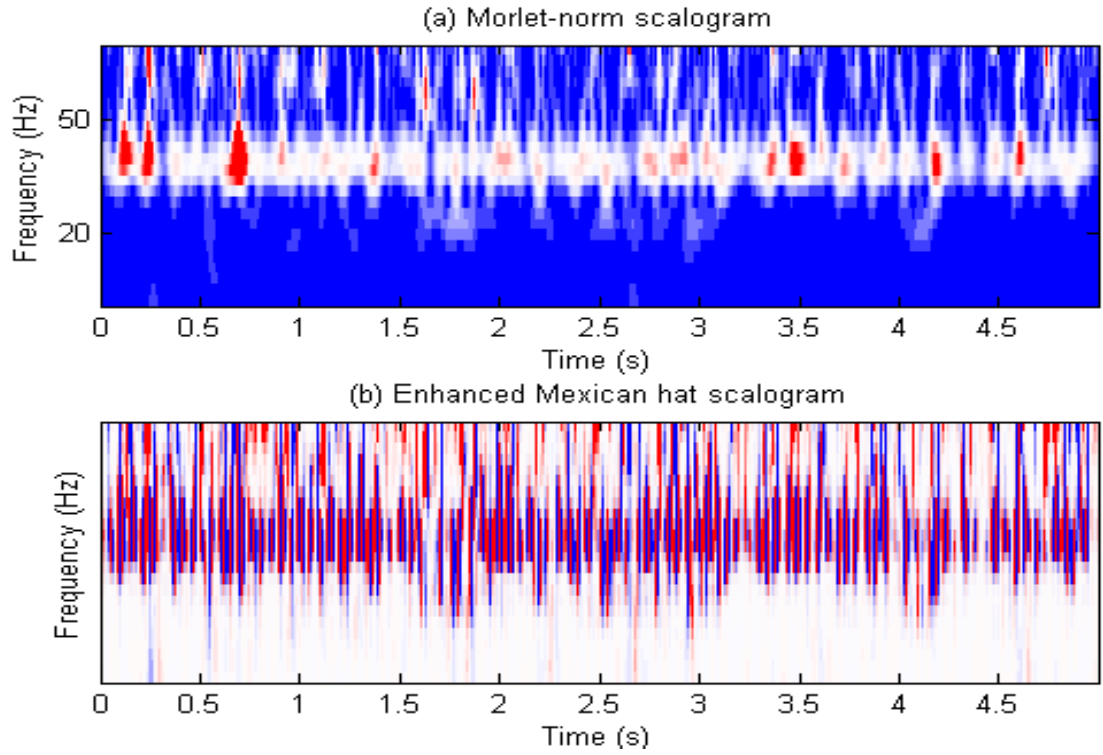


Figure 4.24: Wavelet Maps, $x/c=0.4493$, $\alpha = 16^\circ$, $\delta_f = 0^\circ$, $U = 5 \text{ m/s}$

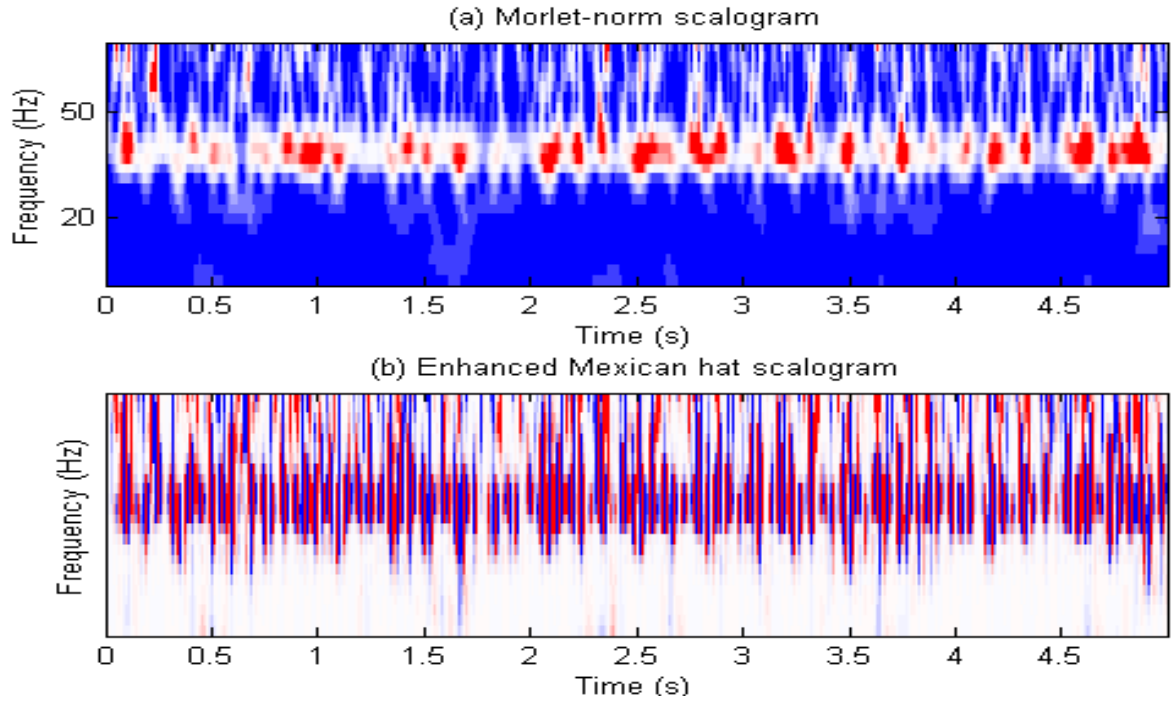


Figure 4.25: Wavelet Maps, $x/c = 0.7483$, $\alpha = 16^\circ$, $\delta_f = 0^\circ$, $U = 5 \text{ m/s}$

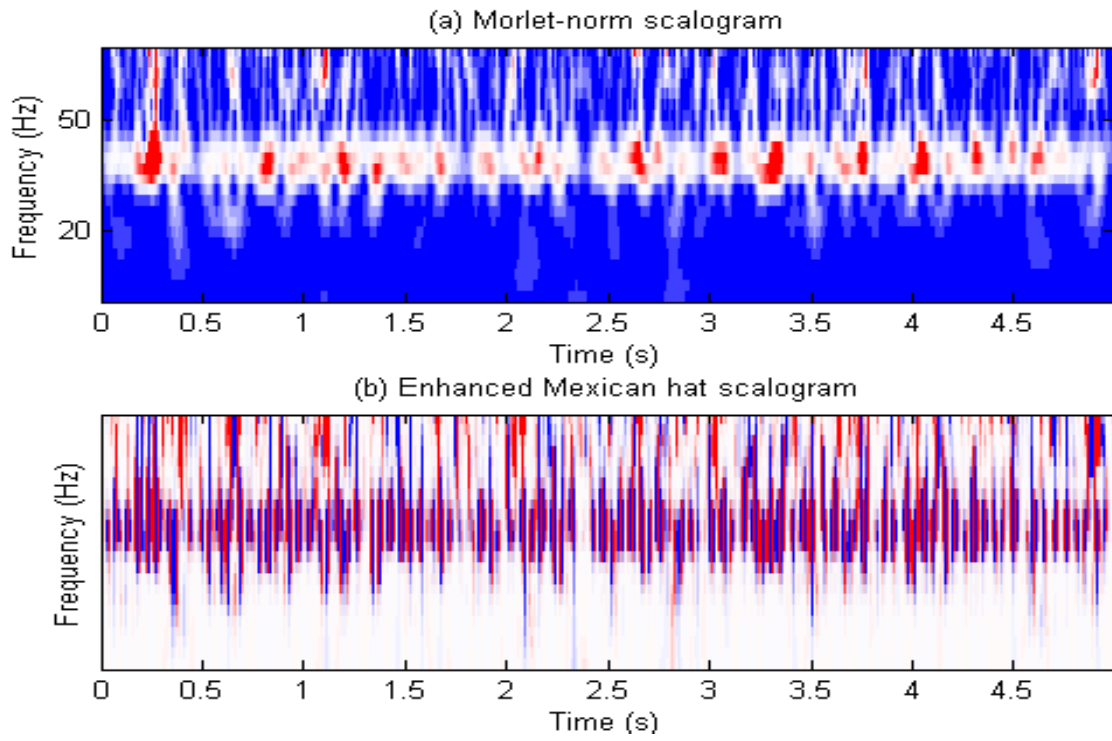


Figure 4.26: Wavelet Maps, $x/c = 0.7846$, $\alpha = 16^\circ$, $\delta_f = 0^\circ$, $U = 5 \text{ m/s}$

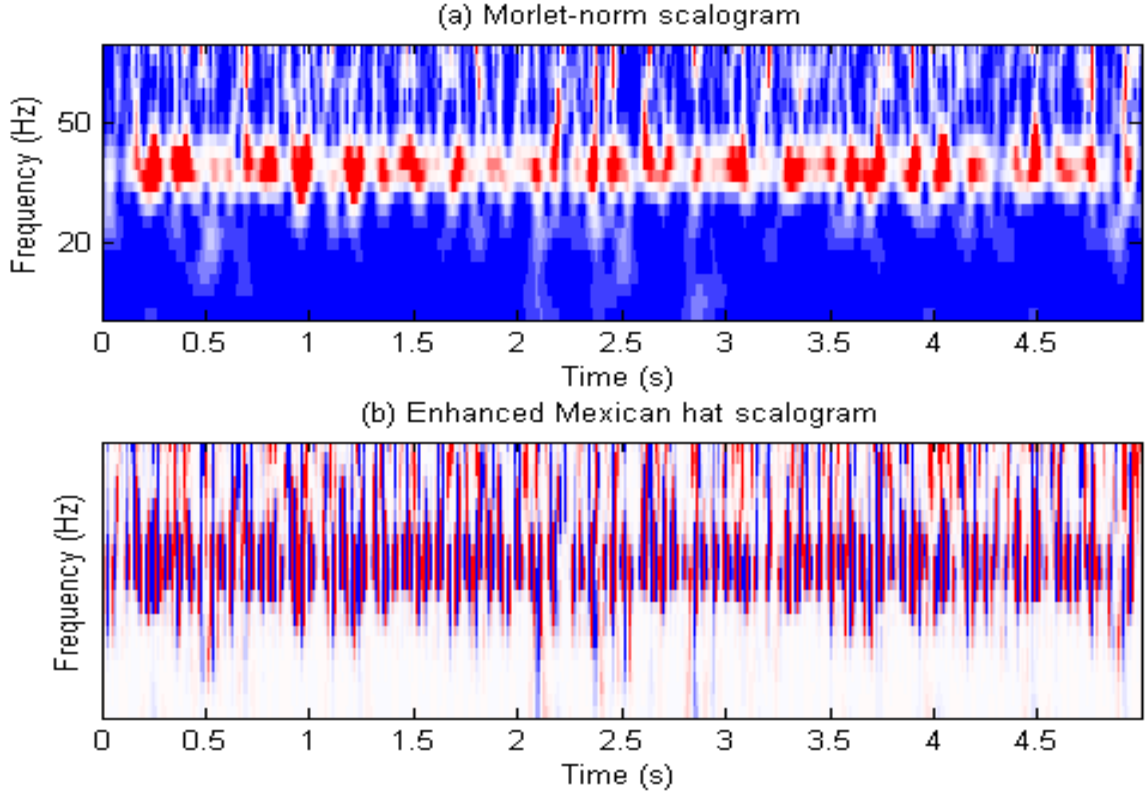


Figure 4.27: Wavelet Maps, $x/c = 0.8120$, $\alpha = 16^\circ$, $\delta_f = 0^\circ$, $U = 5 \text{ m/s}$

Earlier it was pointed out that for the $\delta_f = 0^\circ$ case; the average frequency of the first mode is approximately 33 Hz. For the $\delta_f = 20^\circ$ case the frequency is slightly higher but not by very much at 34.67 Hz. This is due to the sustained 51 Hz recorded by the transducer at $x/c=0.2660$ and the flap deflection. More investigation is required to understand why there is a 51 Hz tone at that location when everywhere else we observe that the frequency is effectively 33 Hz (Figure 4.26). If we were to consider the 51 Hz tone an outlier and remove it from the analysis, then the dominant frequency is still approximately 33 Hz for the flap deflected case. The flap deflection has caused a reduction in the magnitude of the first mode while the second tone located at 132.65 Hz has been amplified and increases in magnitude as a function of distance (Figure 4.27).

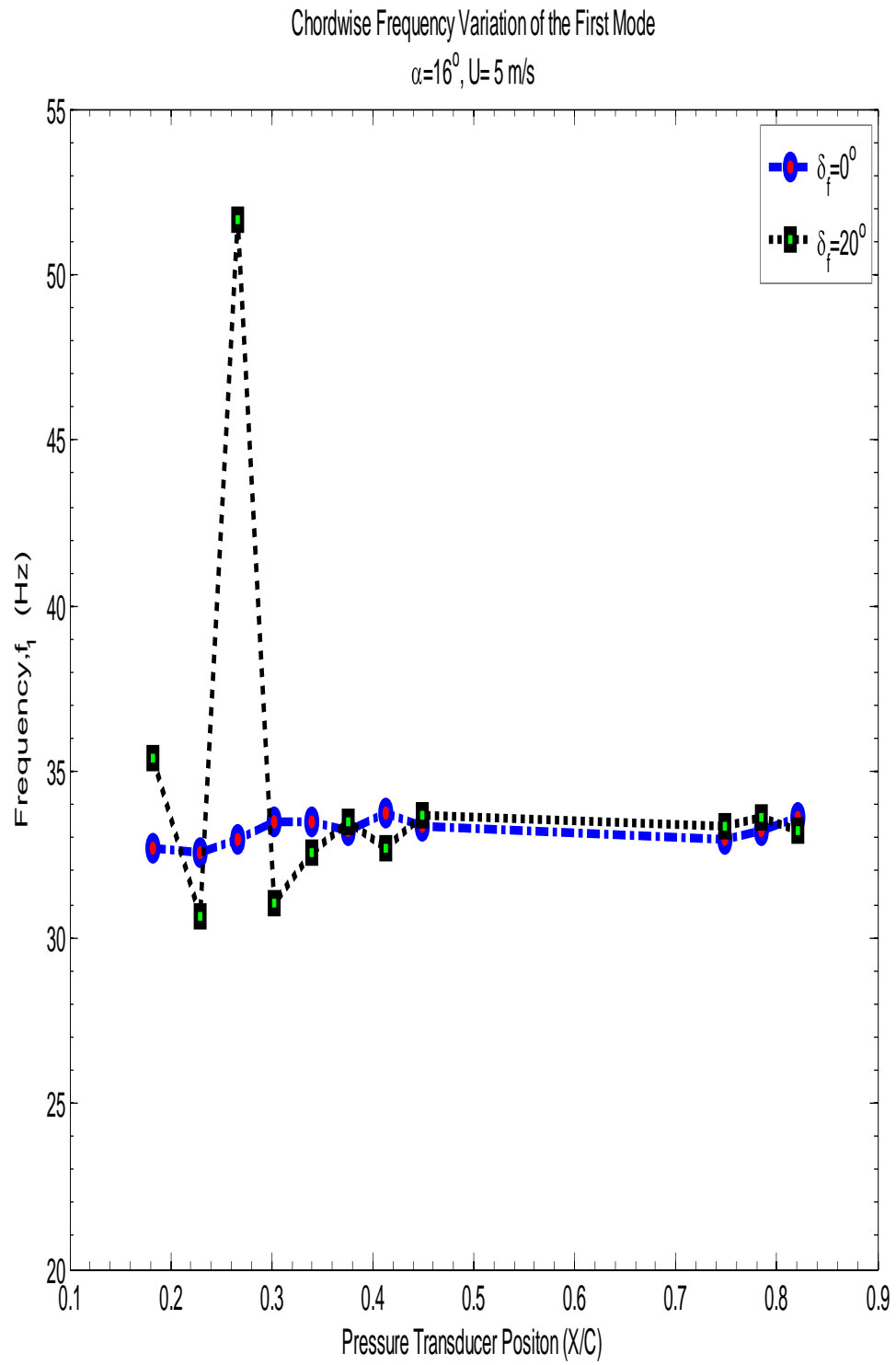


Figure 4.28: Chordwise Variation of Frequency

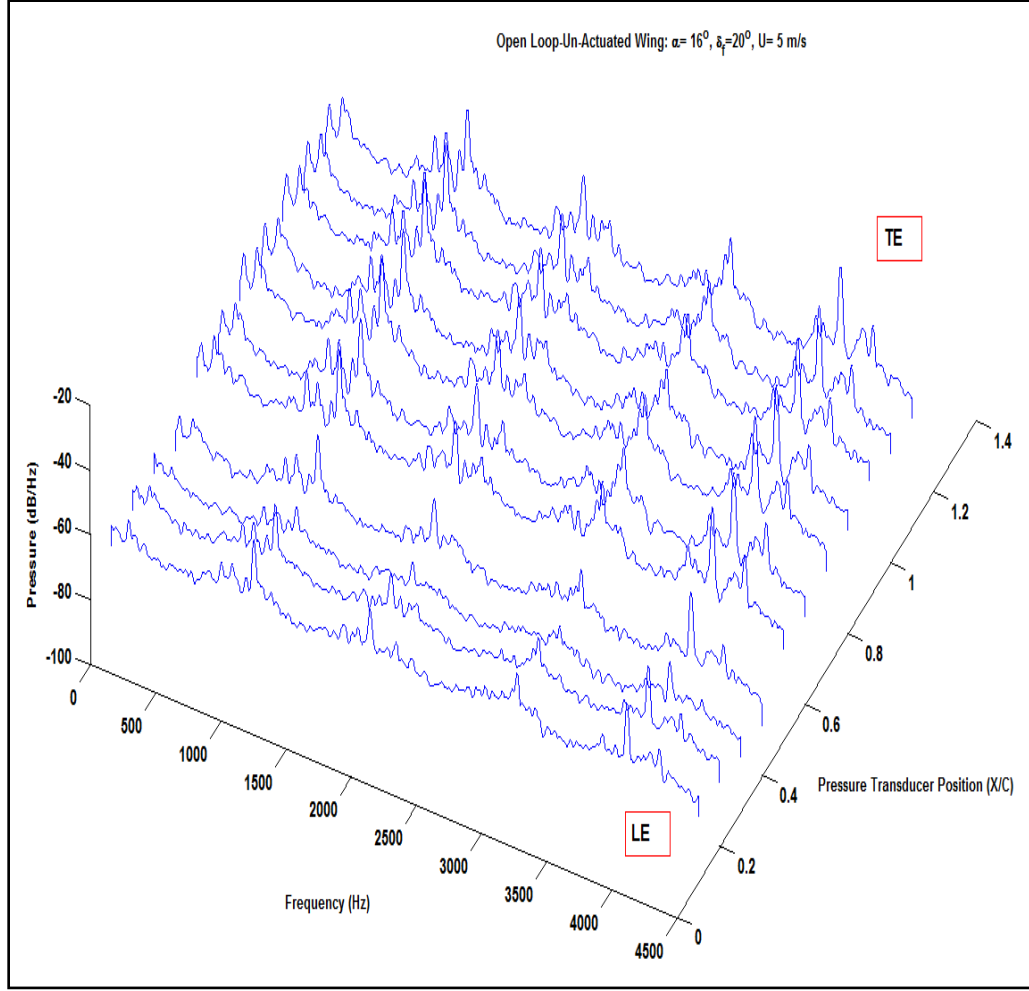


Figure 4.29: Chordwise Power spectra, $\alpha = 16^\circ$, $\delta_f = 20^\circ$, $U = 5 \text{ m/s}$

In a similar manner, the peaks located at 843.43 Hz and 925 Hz show amplification as a function of chordwise distance. The PIV results for a similar configuration show that the recirculation region has shifted toward the trailing edge and within the recirculation region there appears to be two sub-regions; this would account for the increased RMS pressure at the rear of the wing; to clarify a re-distribution of energy between the frequency scales results in the similar RMS pressure profile along the wing, that is most of the energy appears to be transferred to the peak located at 132.65 Hz. The time frequency analysis for the $\delta_f = 20^\circ$ case shows that the global flow condition appears to

be similar to the $\delta_f = 0^\circ$ case. One might have drawn this conclusion based on the results presented in Figures 4.14 and 4.28. As the flow convects downstream of the leading edge with the flap deflected, the local periodicity and flow modulation becomes stronger and sustained; similar to the $\delta_f = 0^\circ$ case as such the time frequency maps for the $\delta_f = 20^\circ$ will not be presented here. Given that the time series show spike trains it might prove useful to examine the pressure traces of the separated flow with the Hilbert Huang Transform (HHT); perhaps by decomposing the signals and then applying the wavelet transforms to the resulting Intrinsic Mode Functions (IMF) we could gain further insight to the time-frequency response of the separated aerodynamic flow. All of the above results hold true for the case where the slots are covered, with the exception of the RMS pressure distributions. A comparison of RMS pressure distributions with slots covered and without (Figure 4.30), reveals that the passive acoustic excitation created by the uncovered slots is able to provide some suppression of the pressure fluctuations between the transducers at $x/c = 0.4493$ and $x/c = 0.7483$. When the slots are covered, the slope of the pressure fluctuations between the transducers located at $x/c = 0.4493$ and $x/c = 0.7483$ is greater than that of the slot uncovered. The frequency of the first mode with the slots covered is still approximately 33 Hz.

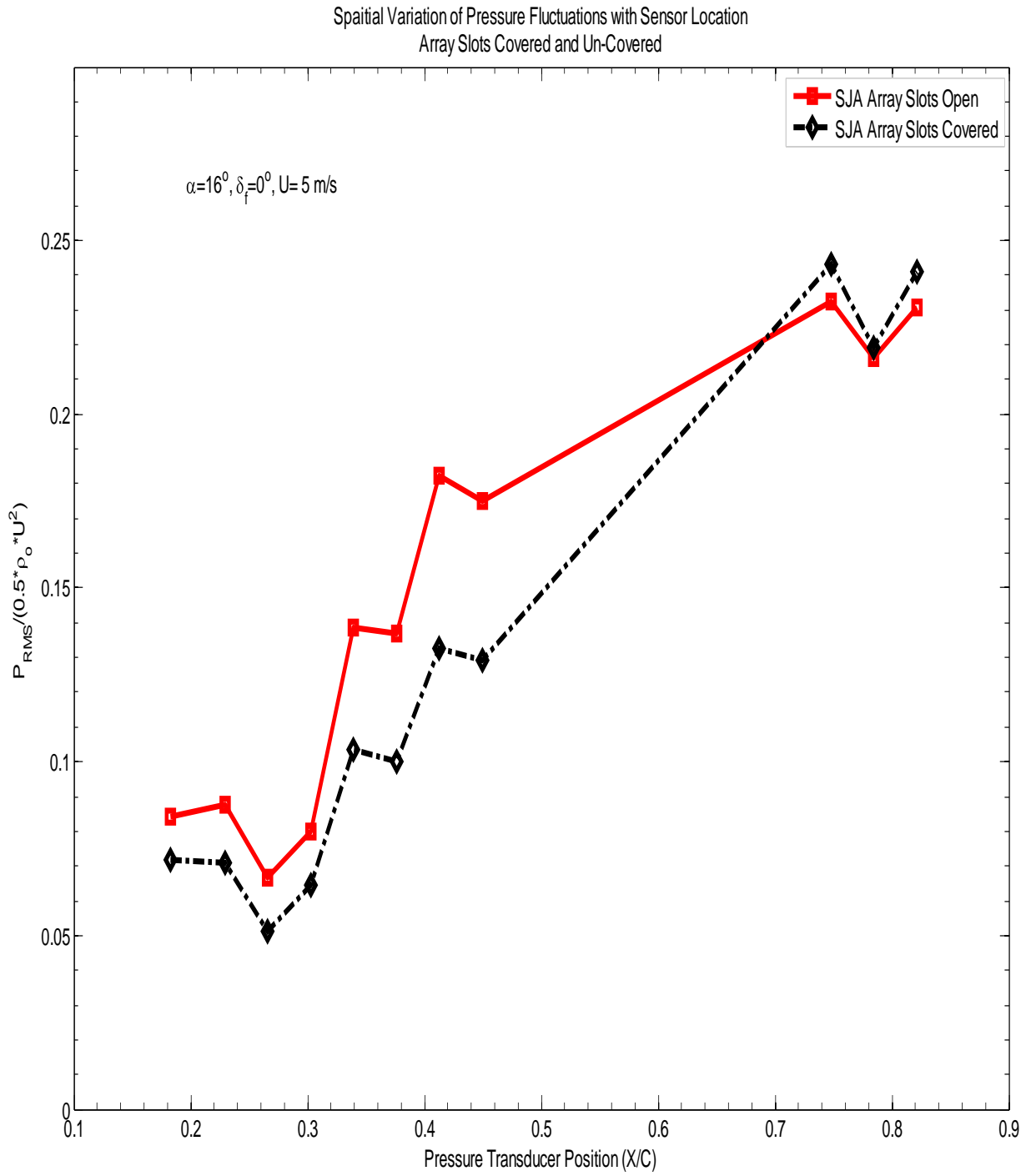


Figure 4.30: Comparison of RMS Pressure distributions

CHAPTER 5.0: ACTIVE CONTROL RESULTS (OPEN & CLOSED LOOP)

5.1 INTRODUCTION

In this chapter we present the results of the active control phase of the project. Three different experiments were conducted; they are amplitude modulated Dual Location Open Loop Control, Adaptive Control with Amplitude Modulation using Direct Sensor Feedback and Adaptive Control with Amplitude Modulation using Extremum Seeking Control. All the closed loop experiments are dual location. The text that follows describes the experimental implementation and results and inferences based on signal analysis. The analysis presented uses the spatial variation of the root mean square pressure fluctuations, power spectral density estimates, Fast Fourier Transforms (FFTs), and time frequency analysis which consists of the application of the Morlet and Mexican Hat wavelets. A description of these methods can be found in Chapter 4 of the thesis.

5.2 DUAL LOCATION OPEN LOOP CONTROL

The open loop control task was conducted using dual location excitation similar to that described by Greenblatt [40]. For our experiment, the feedforward control signal used was an amplitude modulated sinewave given by:

$$V(t) = A_{amp} (\sin \omega_m t) \sin(\omega_{c(LE,TE)} t + \phi_c) [V] \quad (5.1)$$

Note that the directed synthetic jet arrays operated at different carrier frequencies, specifically the leading array operated at 1195 Hz and the trailing edge array at 1197 Hz. The phase angle is used alternate the momentum addition cycles of the synthetic jet arrays with respect to each other. The modulation frequency, which is typically aimed at

exciting the frequency based region of receptivity. For the wing configurations of $\alpha = 0^\circ$ with $\delta_f = 20^\circ$ and 40° , at a tunnel speed of 5 m/s, the modulation frequency was varied from 5 Hz to 245 Hz with the carrier phase angle at zero degrees. Based on the recorded force measurements selected modulation frequencies were chosen to conduct carrier phase angle sweeps. The selected modulation frequencies are 10 Hz, 25 Hz and 200 Hz for carrier phase angles from 0° to 360° . Again, based on the previous experience, for $\delta_f = 40^\circ$, the modulation frequency sweep ranged from 5 Hz to 50 Hz in increments of 5 Hz. This was done so that we could study the response of the flow to open loop control in the frequency range where we believe the vortex shedding frequency to be. This was followed by a post stall wing configuration of $\alpha = 16^\circ$ with $\delta_f = 0^\circ$ and 20° . The modulation frequency was varied from 5 Hz to 100 Hz at a tunnel speed of 5 m/s. In addition to the experiments mentioned above, for the $\delta_f = 0^\circ$ case, the tunnel lift fan was turned off, but the synthetic jet arrays were active. The frequency sweep range is the same as the ‘wind-on’ cases. This test was completed so that we might gain insight into the effect of the boundary layer and wake on the control authority of the actuators in the open and closed loop control configurations. Only the post stall wing configurations will be presented here. We will begin with the RMS pressure distribution (Figure 18) for the clean wing configuration ($\alpha = 16^\circ, \delta_f = 0^\circ$). The RMS pressure distribution shows a marked sensitivity to the changes in modulation/forcing frequency. Superimposed on this plot is the un-actuated RMS pressure distribution. In each case, there are leading edge pressure fluctuations that result from the excitation by the actuators, this result agrees well with work presented in papers Jnl of Aircraft Vol. 29, No. 5 [66] and AIAA Jnl. Vol. 28, No. 8 [67]. There are strong pressure fluctuations at

$x/c=0.2293$; this location is sensitive to changes in modulation/forcing frequency. The same holds true for the secondary location at $x/c= 0.3393$. Initially, for the closely spaced frequencies (5 Hz-45 Hz in steps of 5 Hz) show a tightly spaced RMS pressure amplitudes located at $x/c=0.2293$. For the modulation frequencies of 20 Hz, 25 Hz and 45 Hz are the RMS pressure distributions that have a peak at $x/c=0.2293$. For the modulation frequencies of 40 Hz, 50 Hz, and 60 Hz, the RMS peaks are lower in magnitude. Note that there is no appreciable difference in the RMS pressures at $x/c=0.2293$ for the case where the forcing frequency is 100 Hz and the carrier frequency is both equal and not equal on both channels. The pressure fluctuations in the rear under control are significantly lower than that of the un-actuated case. Note that there is a negative slope associated with the open loop suppression of pressure fluctuations toward the trailing edge of the wing. For the forcing frequency of 90 Hz, there is a uniform amplification of the pressure fluctuations between $x/c= 0.4493$ and $x/c=0.7483$. For the high lift configuration ($\alpha = 16^\circ, \delta_f = 20^\circ$), the RMS pressure distributions (Figure 5.2) reveal that there is a spatial sensitivity to modulation/forcing frequency; particularly at the following chordwise locations $x/c= 0.2293$, $x/c=0.2660$ and $x/c=0.3393$. At $x/c=0.3026$, it is observed that there is very displacement of the pressure amplitude at this location. An assessment of the quiescent (i.e. the lift fan was turned off) acoustic response of the wing revealed that for this location, RMS pressure remained constant until 70 Hz. It stands to reason that even with the flap deflected we are observing similar behavior. More work is required to understand the interaction between the flow and the acoustic properties of the given aerodynamic configuration. For the forcing frequencies of 45 Hz and 90 Hz, the RMS pressure distributions show that there is a shift from $x/c=0.2660$ to

$x/c=0.2293$; the acoustic test indicated that the displacement of the pressure fluctuations occurred at $x/c=0.2293$. So one can infer from that the interaction of the acoustic field and aerodynamic flow causes a chordwise shift in pressure.

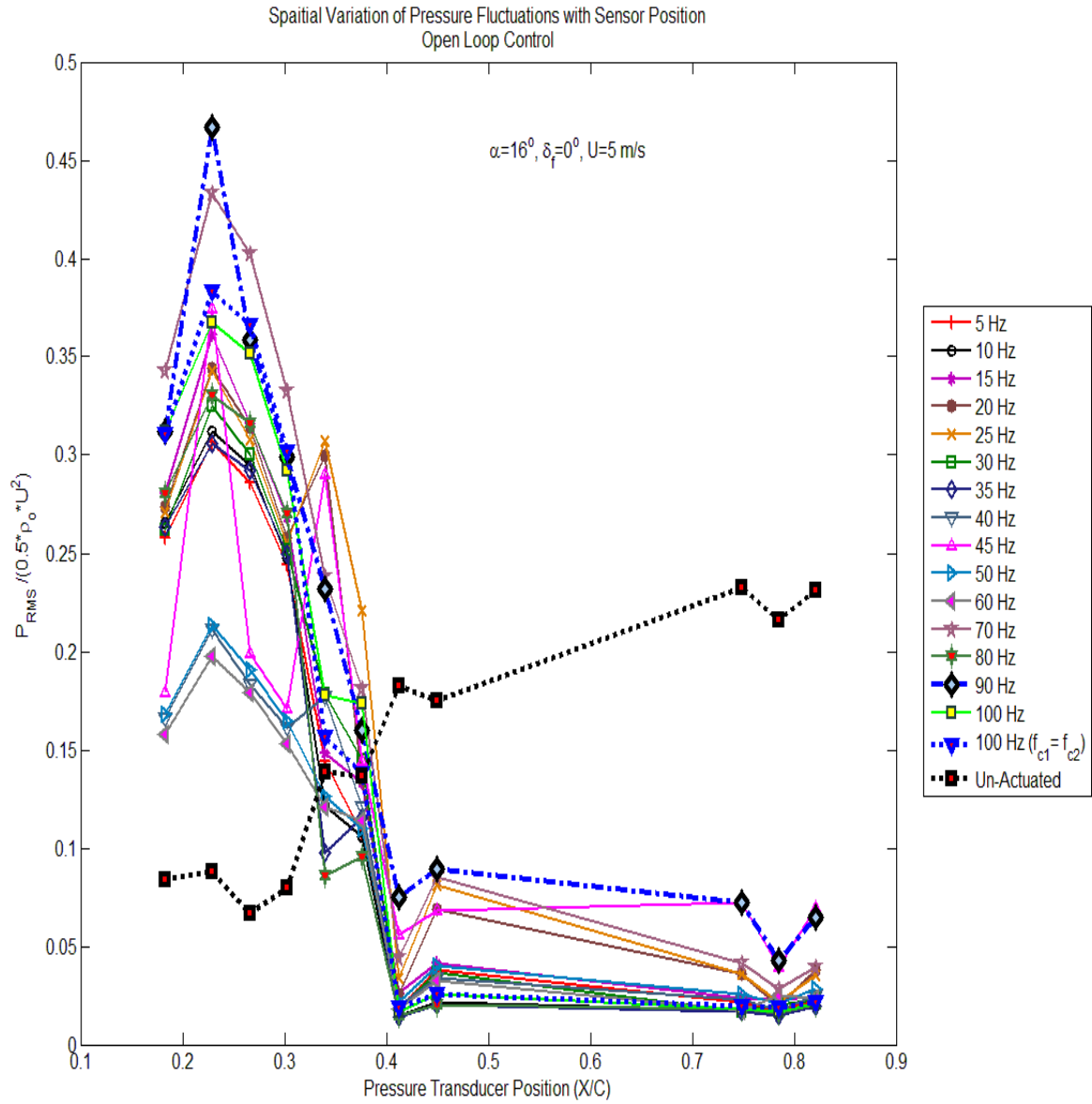


Figure 5.1: RMS Pressure Distributions- Clean Wing Configuration (Frequency Sweep)

For all the frequencies except the 100 Hz case show that the pressure recovery location is around $x/c=0.4126$. For the forcing frequency of 100 Hz, the recovery location has shifted upstream to $x/c=3393$. Chang, Hsiao and Shyu show that for various angles of attack this length scale remains constant but an increase in forcing frequency resulted in the decrease of this length scale. In our case the angle of attack and airspeed were held constant and the forcing frequency was varied, but increases in forcing frequency did not necessarily produce a reduction in the pressure recovery length scale. For example a forcing frequency of 90 Hz did not generate a reduction in the pressure recovery length scale. Again there are complex interactions of aerodynamic flow and acoustic fields that require a detailed experimental investigation in order obtain insight into the effects of these interactions on the control of aerodynamics flows. For both the clean and high-lift configurations we will examine the frequency spectra and the time frequency response of the flow at a forcing frequency of 100 Hz. We have elected to use time averaged FFTs because it provides a more accurate initial assessment of frequency scales that are present in the flow; the power spectral density depending on the windowing selected may ‘smear’ out frequency scales that maybe important. Figure 5.3 shows the un-actuated FFTs in a three dimensional format. In this way we capture the evolution of the coherent structures and energy as one moves from the leading edge to the trailing edge. It is observed that for the un-controlled flow, the amplitude/power of the coherent structure increases as one progresses toward the trailing edge. Again the un-controlled vortex shedding frequency is 33 Hz.

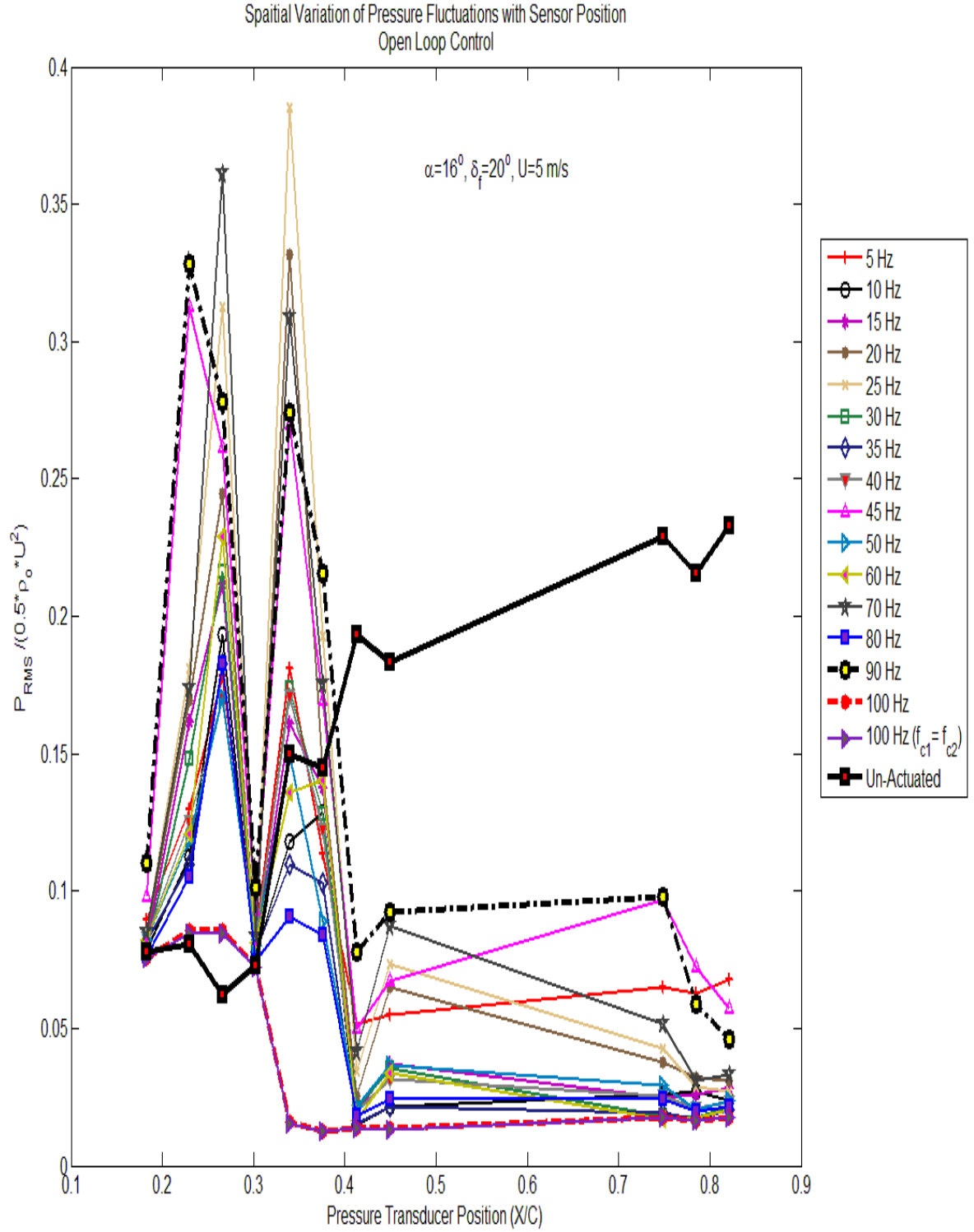


Figure 5.2: RMS Pressure Distributions- High-Lift Wing Configuration (Frequency Sweep)

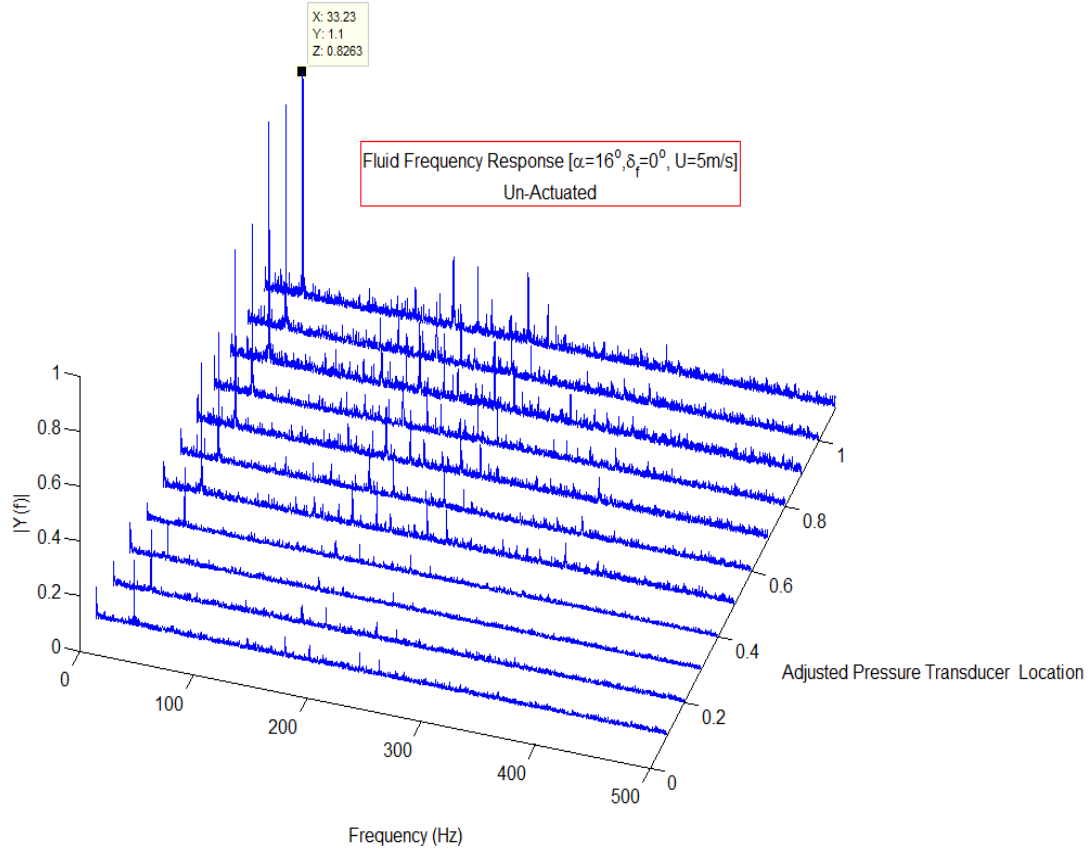


Figure 5.3: Un-Actuated Flow Frequency Spectra (FFT)

Figure 5.4 shows a similar plot for the open loop control of the clean wing configuration. It is observed that the first four pressure transducers show an amplification of the separated flow/wake. After $x/c=0.3026$, we see a marked reduction in the pressure fluctuations, with some persistent chordwise development of coherent structures between 0 and 50 Hz. In Figure 5.1, we see that the slope of the line formed between the pressure transducer located at $x/c=0.7483$ and $x/c=0.7846$ is negative, indicating a further decrease in pressure fluctuations toward the trailing edge. The excitation frequency of 100 Hz has a favorable effect on this post stall flow condition. We will examine in more detail the frequency scales the result from exciting the flow at 100 Hz. To accomplish this, two

dimensional plots of the FFTs will be presented. At $x/c=0.1826$, the frequency scales that present are located at 12.36 Hz, 38.18 Hz, 43.40 Hz and 67.98 Hz. The same frequency scales are seen at $x/c=0.2293$. At $x/c=0.2660$, it is observed that the same frequencies are present but we begin to see the emergence of coherent structures located at 119.90 Hz and 142.40 Hz. On the main element of the airfoil there appear to be two dominant modes of vortex shedding, they are located 43.40 Hz and 200 Hz. These modes coexist together. In addition, at $x/c=0.4126$, we begin to see the evolution of several tones between 0 Hz and 15 Hz located at 7.141 Hz, 9.046 Hz and 297 Hz located at $x/c=0.8210$. From an energy stand point, these modes are weaker in comparison to the modes located further upstream. Note also that the controlled flow toward the trailing edge has energy between 0 Hz and 50 Hz.

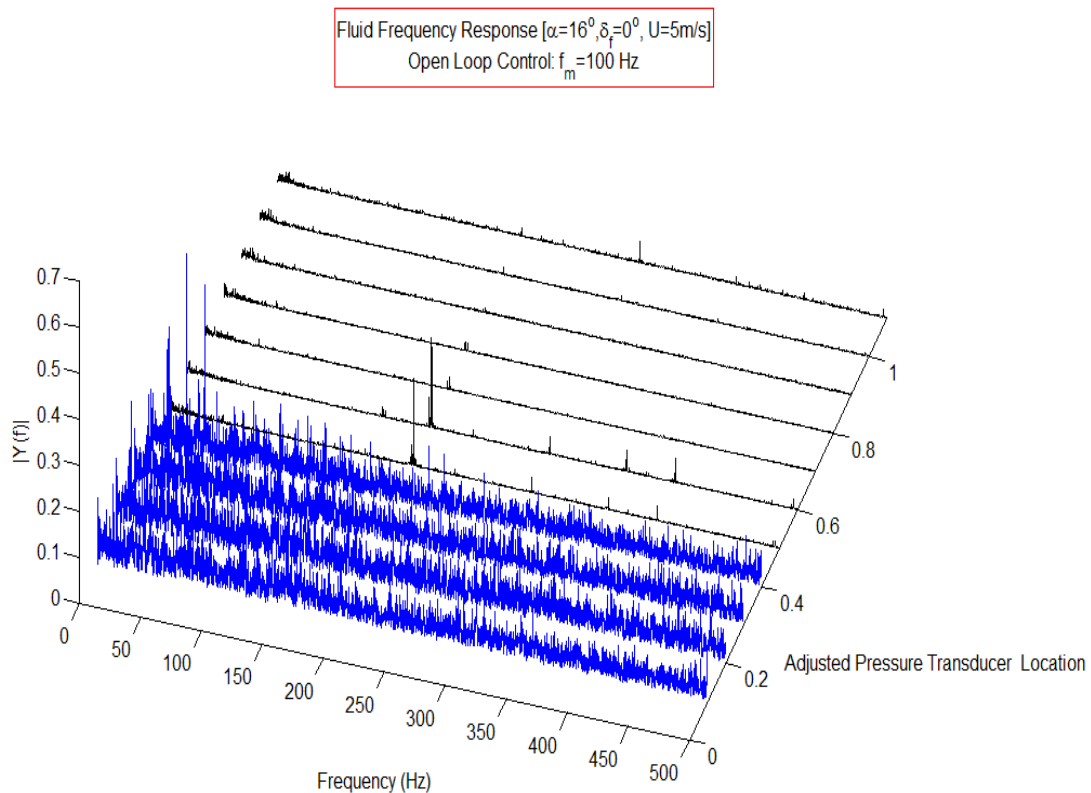


Figure 5.4 Actuated Flow Spectra (FFT): Clean Wing Configuration (Open Loop)

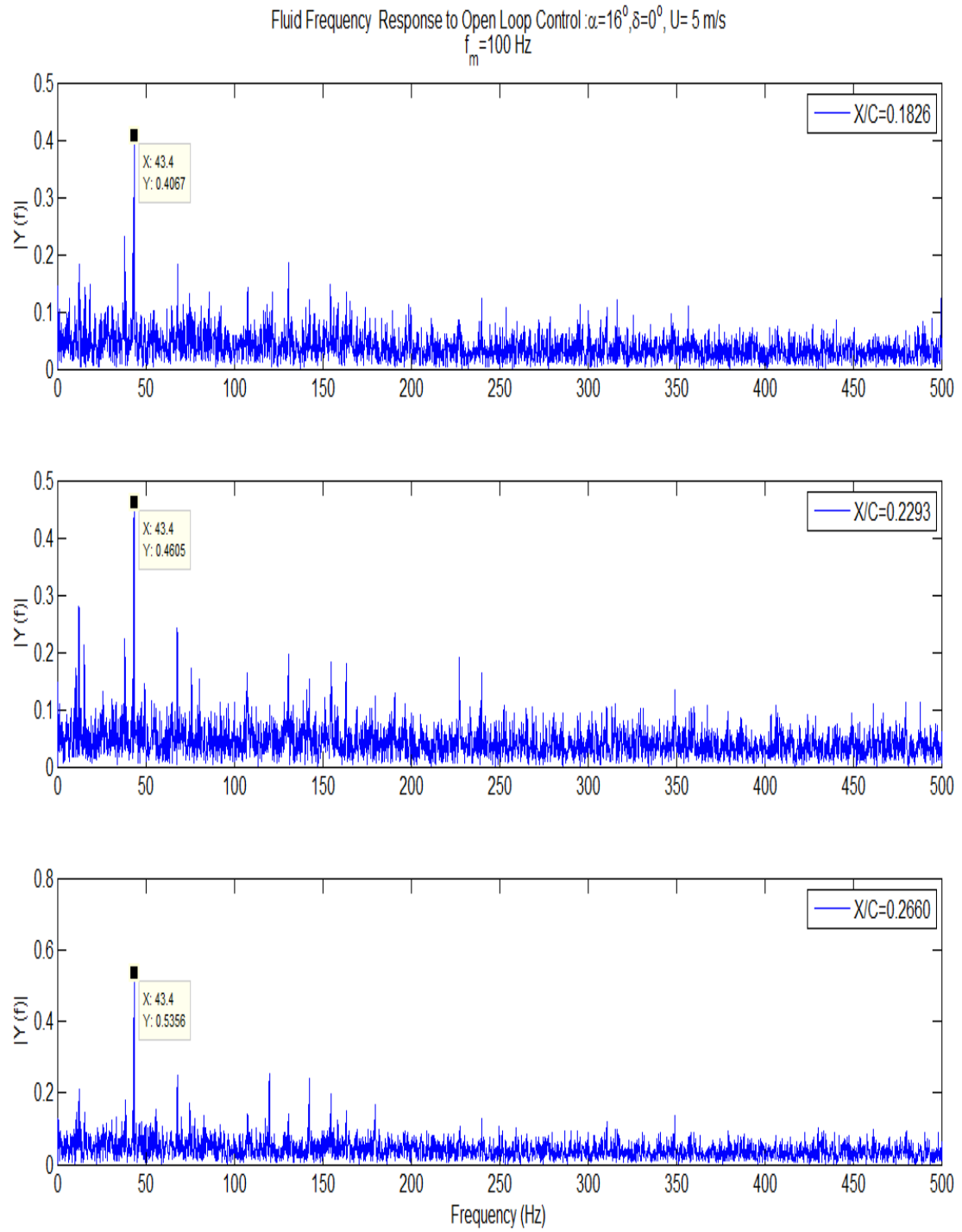


Figure 5.5: Enhanced FFT, Stations 1 to 3 (Open Loop)

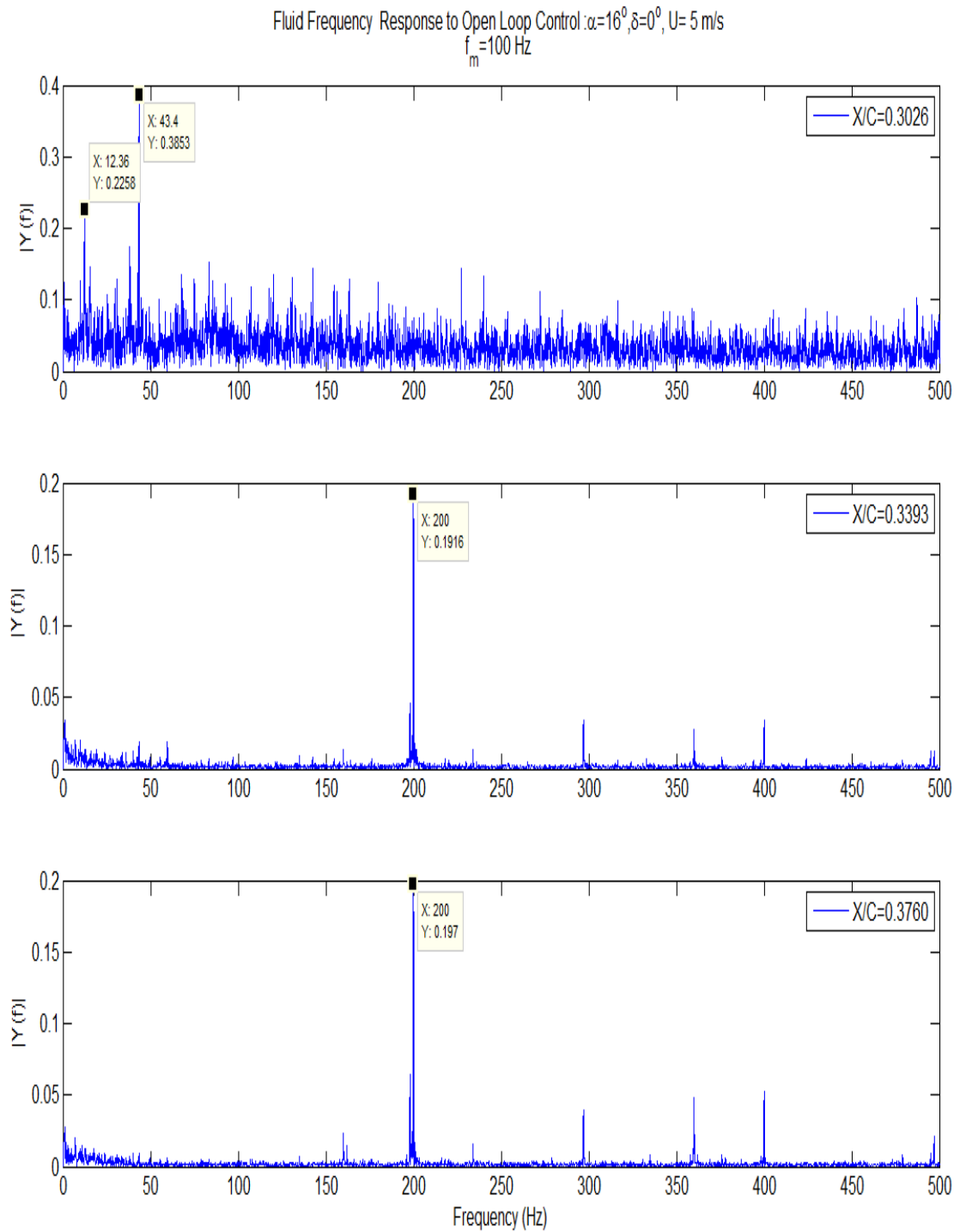


Figure 5.6: Enhanced FFT, Stations 4 to 6 (Open Loop)

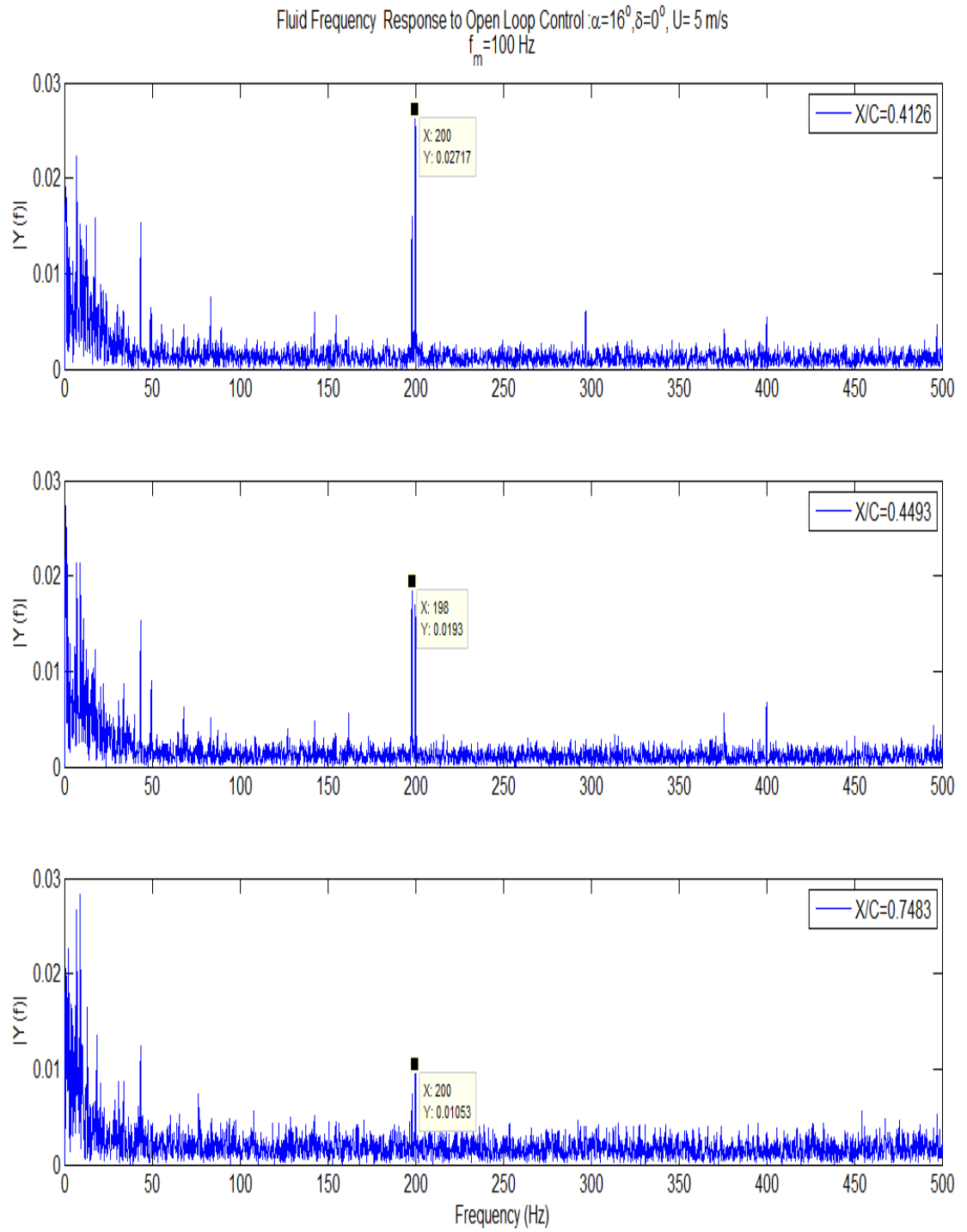


Figure 5.7: Enhanced FFT, Stations 7 to 9 (Open Loop)

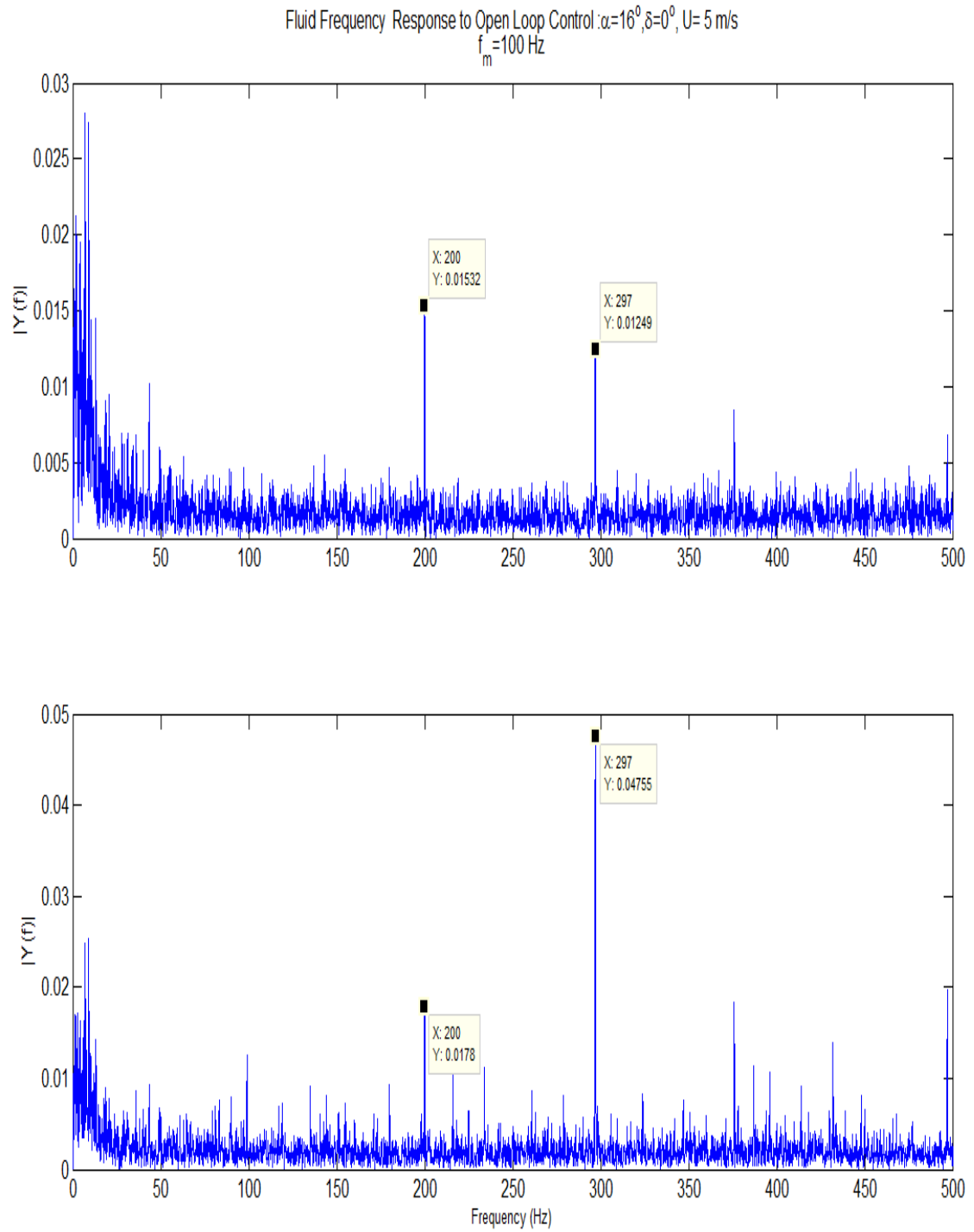


Figure 5.8: Enhanced FFT, Stations 10 & 11(Open Loop)

For the high-lift configuration, again it is observed that the first four pressure transducer stations and amplification of the separated flow/wake are due to internal periodic excitation (Figure 5.9). However the flap deflection produces a slight increase in pressure fluctuations toward the trailing edge. This accounts for the gradual positive slope seen in the RMS pressure distribution in Figure 5.2. Like the clean wing configuration we have detected the same frequency scales with the following exceptions; from $x/c=0.1826$ to $x/c=0.3026$, the dominant frequency is 119.90 Hz at and beyond $x/c=0.3393$, the 119.90 Hz tone disappears and a 43.40 Hz tone appears and persists all the way to the trailing edge. It appears as if the flap deflection has caused ‘swap’ of the coherent structures on the surface of the airfoil in addition to the movement of the pressure recovery/reattachment point.

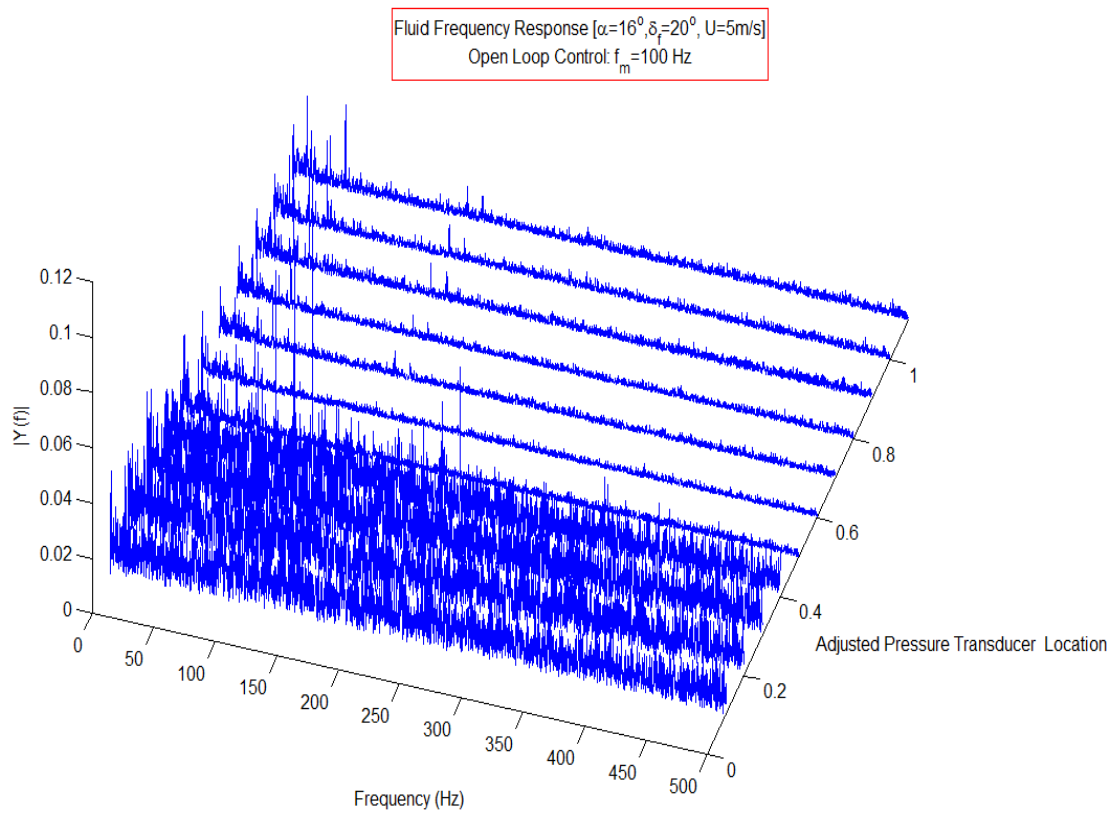


Figure 5.9: Actuated Flow Spectra (FFT): High Lift Configuration

Active flow control ideally is supposed to improve the aerodynamic performance of a lifting surface; however published experimental results show that not every forcing frequency results in a significant improvement in aerodynamic performance [66]. The most obvious feature is that there is a shift in the normal force with flap deflection; this is to be expected. The normal force is plotted as a function of frequency and agrees well with the published results in that we see that for certain forcing frequencies the normal force on the wing does in fact decrease and for others the normal force shows improvement. Specifically, for the clean wing configuration there is an increase in the normal force between the excitation frequencies of 30 to 50 Hz and for the high-lift configuration, 35-60 Hz.

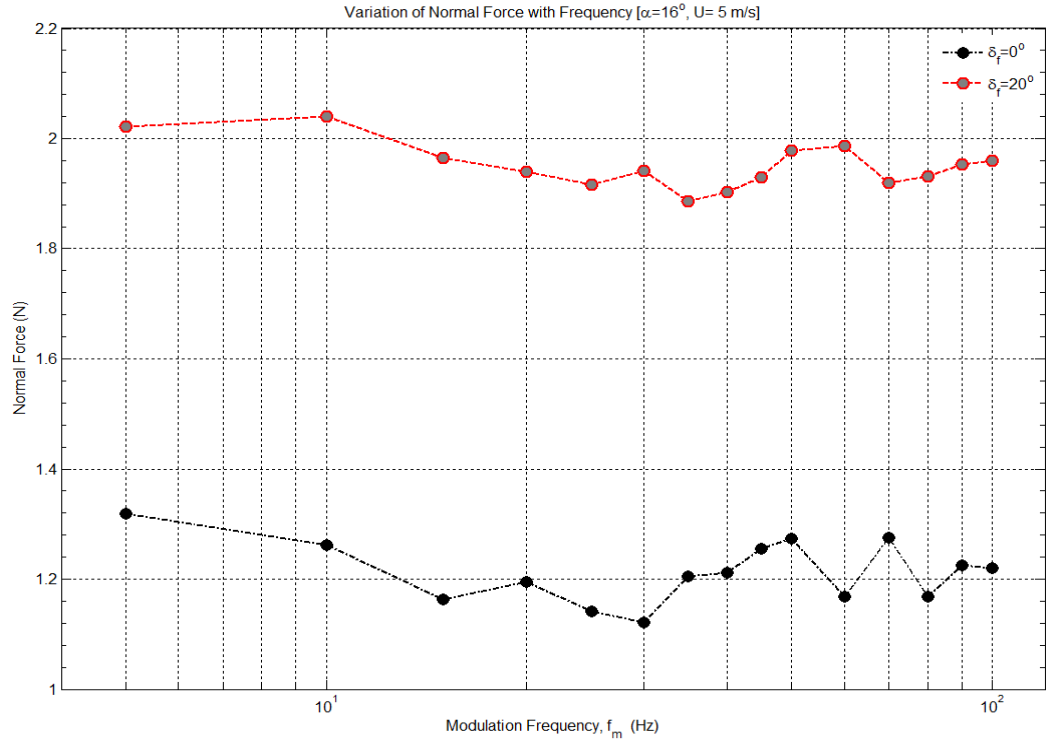


Figure 5.10: Variation of Normal Force with Forcing Frequency

We will focus the time frequency analysis on the high lift configuration only. For a forcing frequency of 100 Hz, it has been observed that there is a significant reduction in the pressure fluctuations at the leading edge and change in the shape of the RMS pressure distribution. At $x/c=0.1826$ (Figure 5.11), we can observe that frequency band about 12 Hz starts to emerge; the corresponding Mexican Hat wavelet window shows that the flow is weakly modulated at this sensor station. At $x/c=0.2293$, there three events with strong periodicity, also centered about 12 Hz. At $x/c=0.2660$, starting at 0s, strong periodic events appear starting at about 30 Hz and then extending down to about 15 Hz and remains this way until 4s. Note that the RMS pressure distribution that corresponds to a forcing frequency of 100 Hz has a smooth transition at the pressure recovery length. Hence the flow has a higher degree of coherence at this location. Note also the periodicity events are consistently above 10 Hz. From $x/c=0.3026$ to $x/c=0.3760$, we see that the flow is weakly modulated. After $x/c=0.3760$, it can be observed that the periodic events are centered on 12 Hz (the FFTs show a tone at 12.36 Hz) get stronger toward the trailing edge as the frequency modulation of the flow. In Figure 5.12 we can see that the controlled vortex shedding frequencies range from 41Hz to 90 Hz with the band being centered at approximately 65.63 Hz (FFTs show a strong peak located at 43.40 Hz). From $x/c=0.1826$ to $x/c=0.3760$, the flow synchronization is weak but strengthens around $x/c=0.4126$, indicating that the resulting coherent structure is pushed toward the trailing edge. It is likely that the sensor stations before $x/c=0.3760$ are actually picking up flow entrainment. In addition, for the sensor located at and after $x/c=0.4126$, we see that there is a secondary frequency band that ranges from 10 Hz to 14 Hz (the 12.36 Hz tone is contained within this range). It is possible that for open loop control, the nonlinear flow

response it is to *switch* between the two stable shedding frequencies. The movement of the flow stability between these stable shedding frequencies is mechanism that underlies the global synchronization this is often discussed in the literature. More investigation is needed (both experimental and mathematical) to determine whether these stable shedding states can be considered stable manifolds and is there a possibility to identify the switching frequency. The next section will discuss the application of Direct Feedback Control.

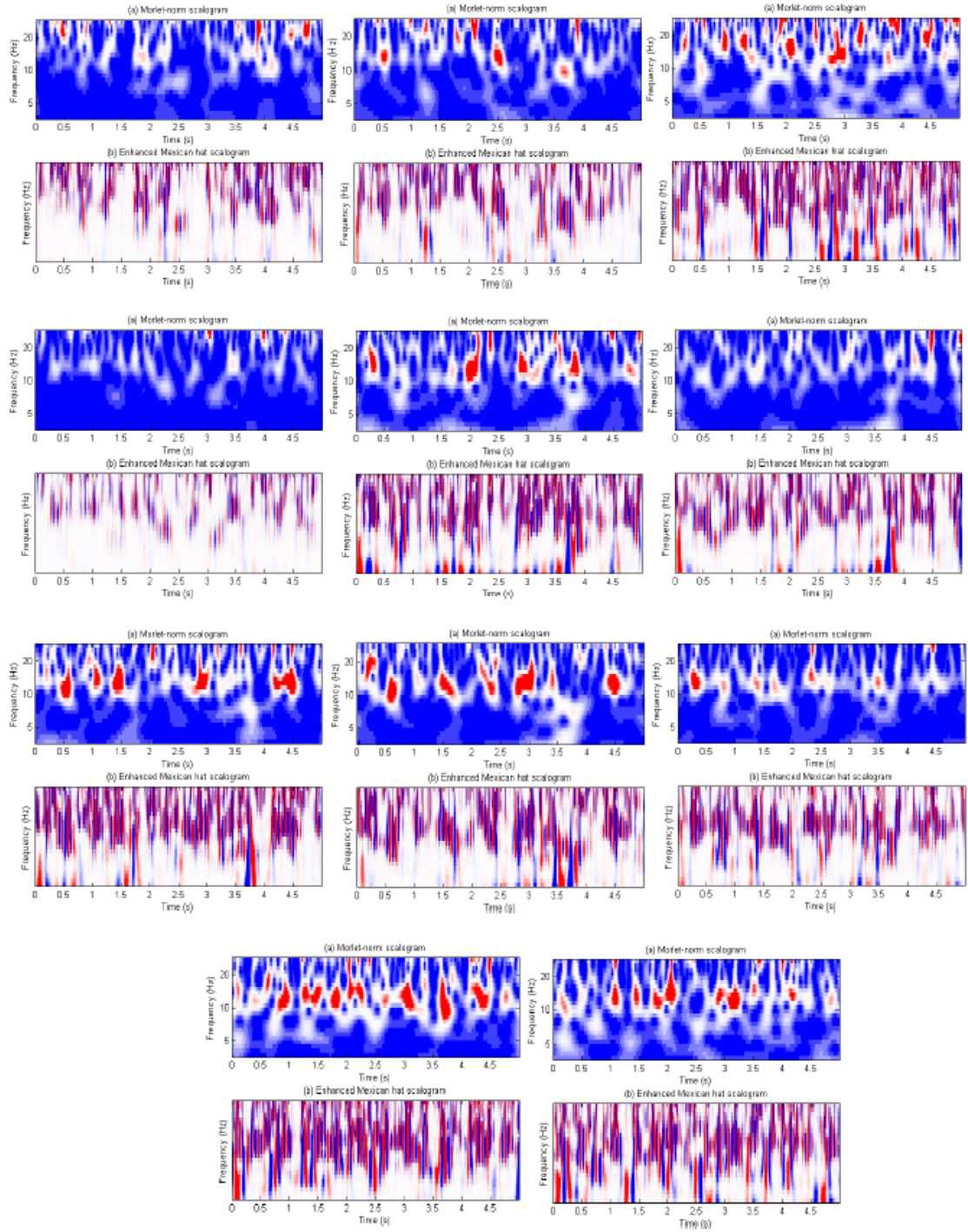


Figure 5.11: Wavelet Map Panel: High Lift Configuration Part 1 ($f_m=100$ Hz)

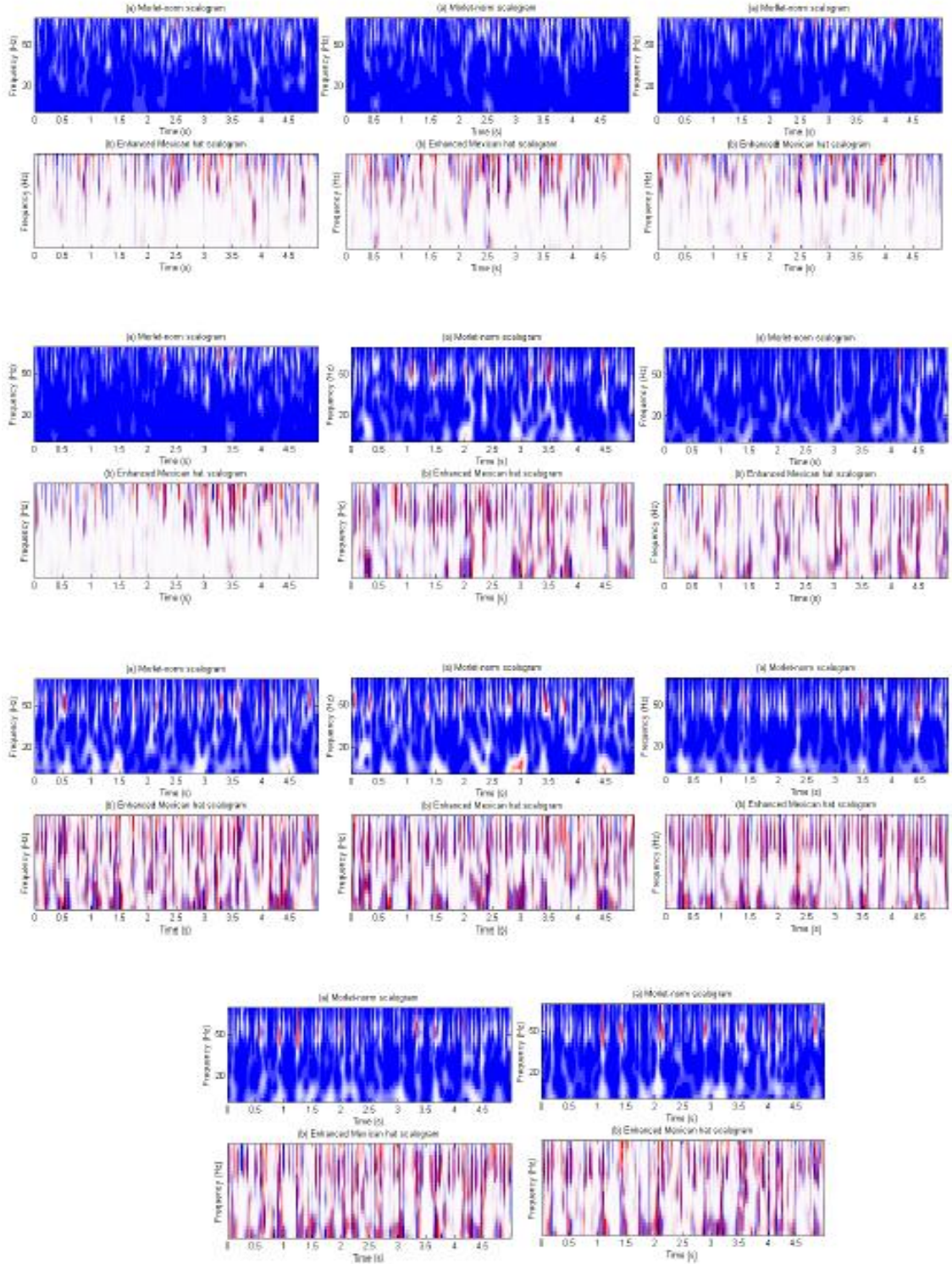


Figure 5.12: Wavelet Map Panel: High Lift Configuration Part 2 ($f_m=100$ Hz)

5.3 ADAPTIVE CONTROL WITH AMPLITUDE MODULATION USING DIRECT SENSOR FEEDBACK (DUAL LOCATION)

The dual location open loop control used discrete or specific frequencies to modulate the carrier sinewave as described by Equation 5.1. In this instance, the pressure transducer signals at 2 different chordwise locations were used as feedback signals. The first feedback signal is located on the main element of the wing located at $x/c=0.4126$ and the second is located at $x/c=0.7846$, this pressure transducer is located on the trailing edge flap. The purpose is to examine the effect of feedback sensor location on the closed loop response of wing aerodynamics. The pressure transducer signals were filtered using a Butterworth filter with a cutoff frequency of 500 and order 125. The control voltage is of the following form:

$$V(t) = A_{amp} P_i(\omega_m, t) \sin(\omega_{c(LE,TE)} t + \phi_c) [V] \quad (5.2)$$

There are 11 dynamic pressure sensors, hence i is from 1 to 11. Similar control voltage configurations have been used by the research group at Syracuse University in which the first POD mode was used at the modulating signal. Bench tests at Clarkson University determined that the peak to peak voltage needed to be centered on 30 Volts, that is the magnitude of the product $A_{amp} P_i(\omega_m, t)$ must be centered on 30 Volts. In reality, the amplifier gain A_{amp} was adjusted such that the voltage oscillated between 30 ± 5 Volts. The closed loop configuration was applied to a wing configuration of $\alpha = 16^\circ$ with $\delta_f = 0^\circ$ and 20° . The wing was tested in these configurations at airspeeds ranging from 5 m/s to 25 m/s in increments of 5 m/s. Phase angle sweeps were conducted for the given wing configurations, the carrier phase angles ranged from 0° to 360° at 5 m/s. Only the cases with phase angle sweep will be presented here.

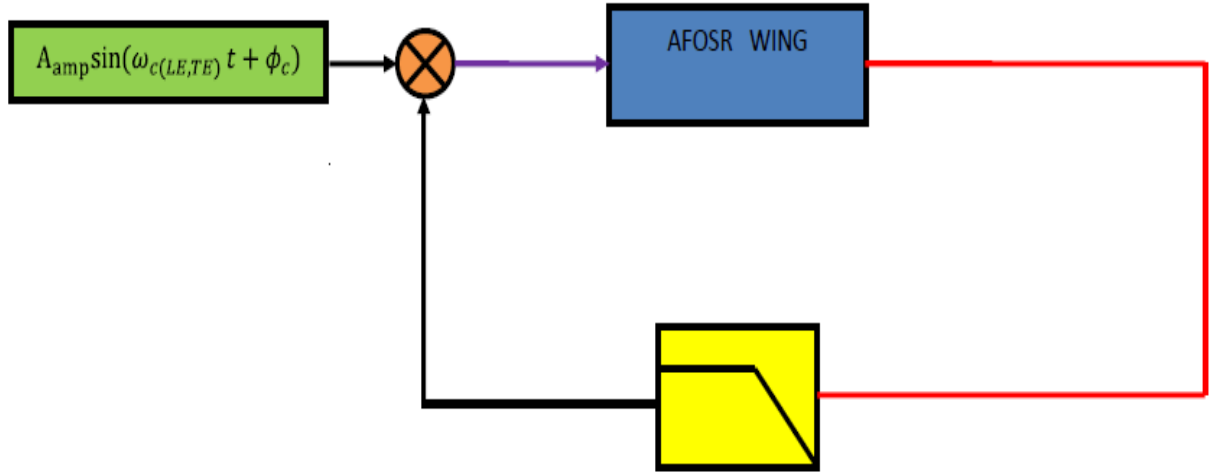


Figure 5.13: Direct Sensor Feedback Adaptive Control

We begin the discussion of the results with an examination of the resulting RMS pressure distributions. For the clean wing configuration with the feedback sensor located at $x/c=0.4126$ (Figure 5.14), we find that there are two peaks located at $x/c=0.2660$ and $x/c=0.3393$. The pressure fluctuations at $x/c=0.3026$ show little no displacement, the same holds true for the fluctuations at $x/c=0.3393$. These locations are possible acoustic nodes, despite the presence of aerodynamic flow. The RMS pressure distribution shows a reduction at and after $x/c=0.3760$. The largest pressure fluctuations are seen at the leading edge at a phase angle of 360 degrees at a magnitude of 0.7. The phase angle setting of 180 degrees, results in a dramatic reduction in pressure fluctuations. From experience, it is likely that the self-excited feedback has amplified a frequency scale for which the flow responds favorably. At $x/c=0.4126$, the location of the feedback sensor, we see that the pressure fluctuations are suppressed. But the information contained at that location influences the response wing at other locations, particularly at $x/c=0.2660$. In Figure 5.15, a comparison of the pressure fluctuations at $x/c=0.2660$ as a function of phase angle for the two feedback sensor locations reveals the following has been constructed. For the

feedback location $x/c=0.4126$, we see that when the phase angle is less than 200 degrees, the RMS pressure decreases to a minimum at 180 degrees. For the feedback location $x/c=0.7846$, the RMS pressure is shifted up, passes through a maximum at 90 degrees and the minimum nearly 90 degrees later (at 195 degrees). For the feedback location $x/c=0.4126$, when the phase angle is greater than 200 degrees, the RMS pressure fluctuations at $x/c=0.2660$ continue to increase. For the feedback location $x/c=0.7846$, when the phase angle is greater than 200 degrees, the pressure fluctuation passes through another maximum at 270 degrees (180 from the previous maximum).

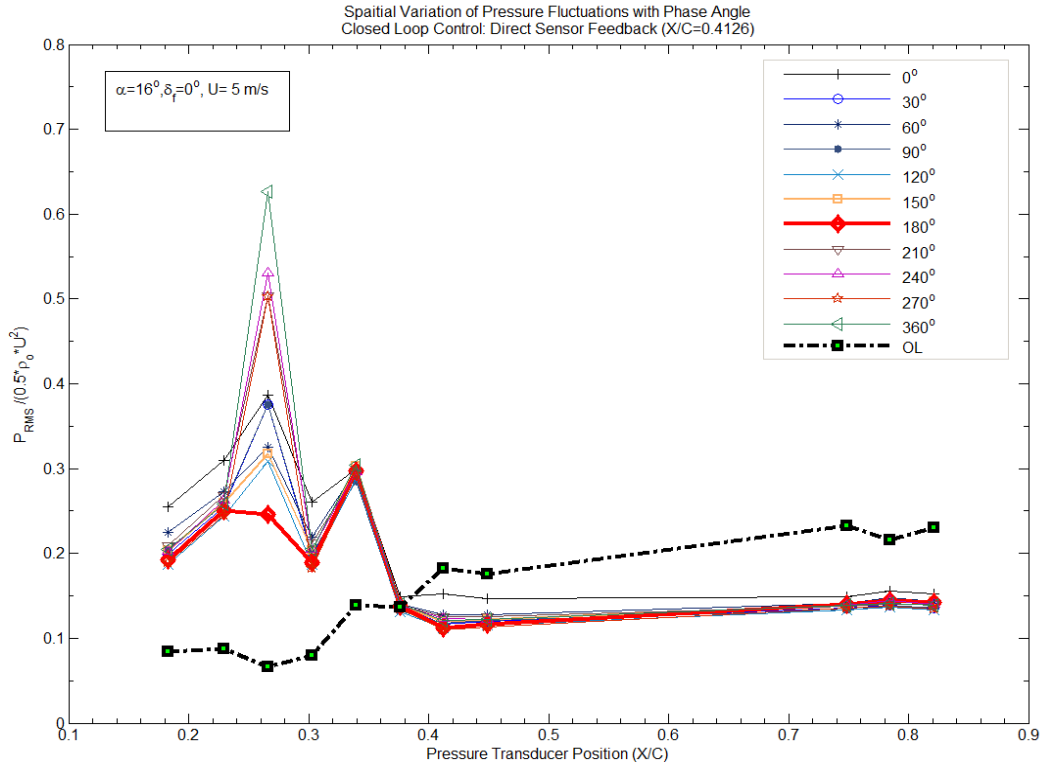


Figure 5.14: RMS Pressure Distribution, Clean Wing configuration ($x/c=0.4126$)

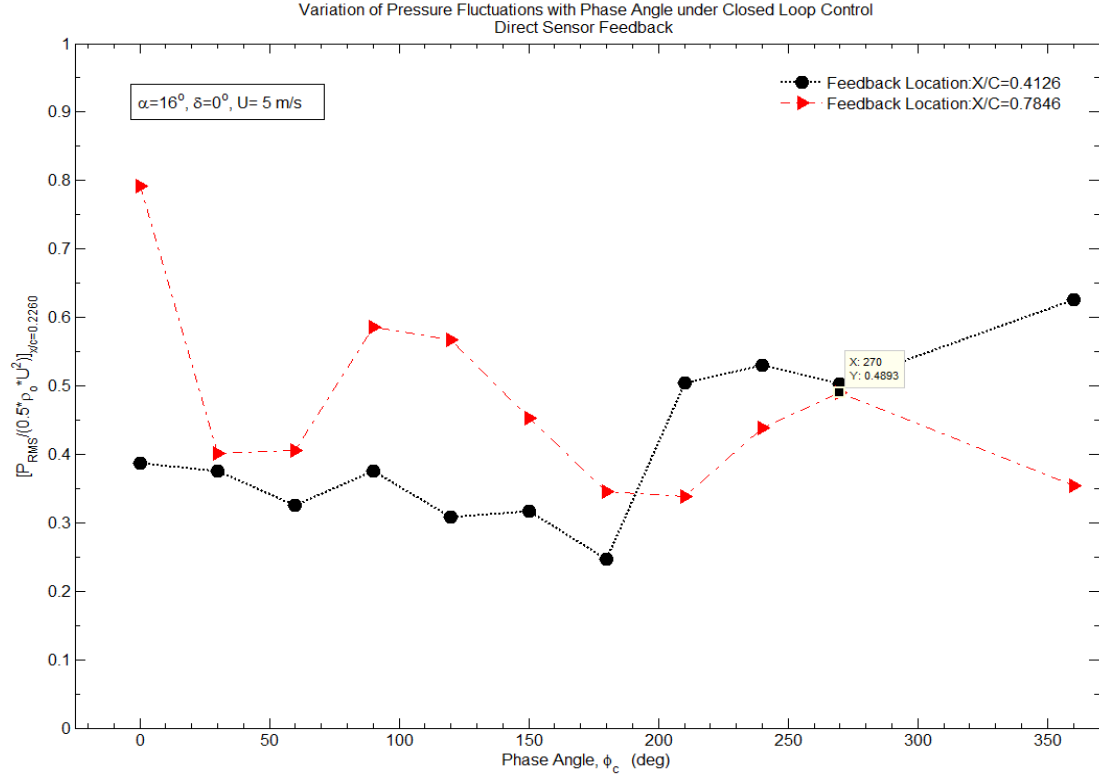


Figure 5.15: Displacement of Fluctuation Level at Sensor Station 3

For the feedback location $x/c=0.7846$, for the clean wing configuration (Figure 5.16) we find that the general ‘shape’ of the RMS pressure distribution has not changed. This is maybe an indication that the phase angle parameter changes only the magnitude of the pressure fluctuations and not the resulting flow frequencies. Specifically we have observed for open loop control at a constant forcing frequency, that the ‘shape’ of the RMS pressure distribution changes. The closed loop experiments with two different feedback sensor locations have no change in the general shape of the RMS pressure distributions indicating that the phasing of the actuator arrays has no effect on the controlled frequency scales in the flow. As a result the normal force remains constant of the range of phase angles.

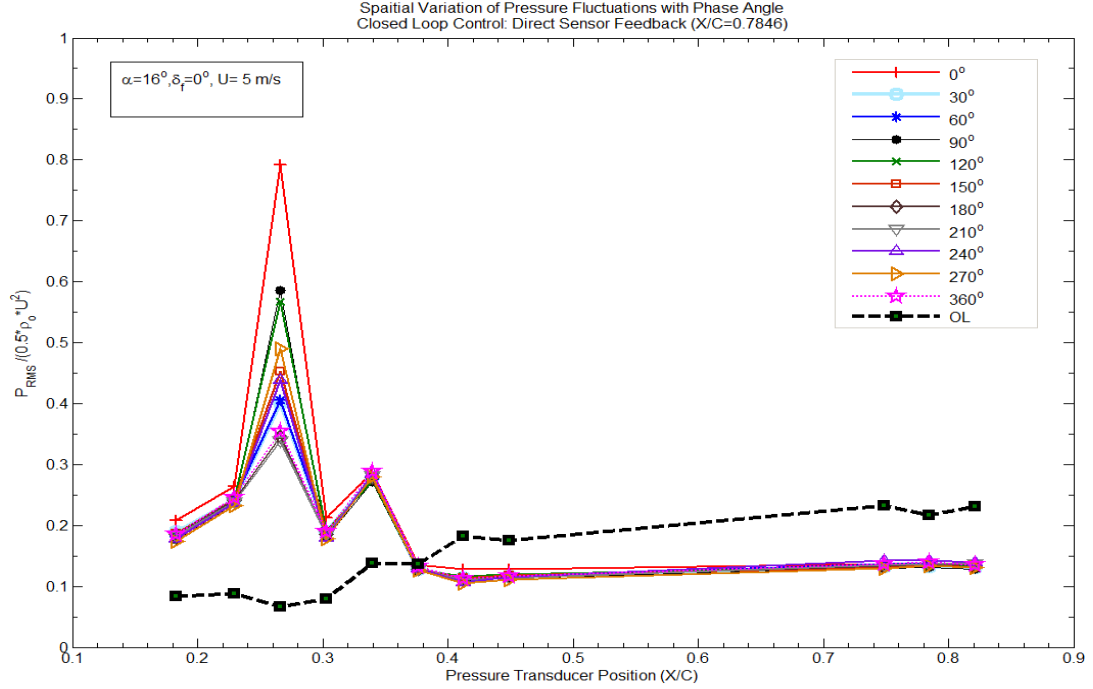


Figure 5.16: RMS Pressure Distribution, Clean Wing configuration ($x/c=0.7846$)

For the high-lift wing configuration, similar results with respect to the shape of the RMS pressure profile; in both Figures 5.17 and 5.18 we see that despite the change in feedback sensor location, the shape remains the same i.e. with pressure fluctuation amplification at $x/c=0.2660$ and $x/c=0.3393$. The main difference between these two high lift cases is the degree of fluctuation amplification at $x/c=0.2660$. At $(x/c, \phi_c) = (0.2660, 360^\circ)$ the pressure fluctuations have a magnitude of 1.278 and at $(x/c, \phi_c) = (0.2660, 150^\circ)$, the magnitude of the pressure fluctuation are 3.474. This is likely caused by the severe flow conditions on the deflected flap (the sensor is located here) which makes the flow ‘noisy’ and so this is noisy flow information is effectively transmitted to actuators which results in the further amplification of the flow state on the main element of the airfoil.

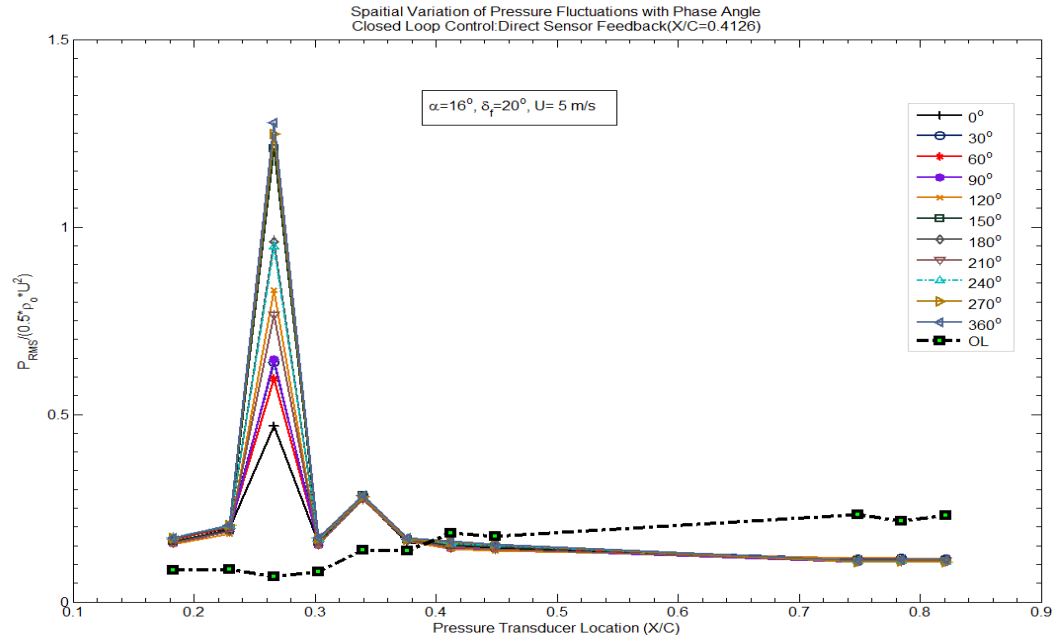


Figure 5.17: RMS Pressure Distribution, High Lift configuration (x/c=0.4126)

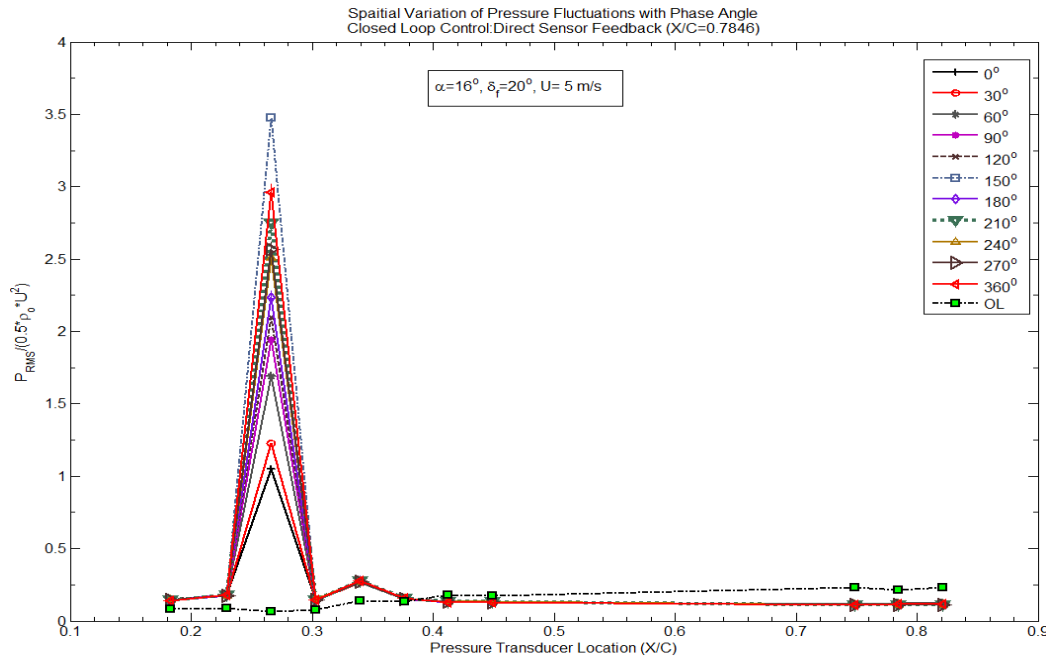


Figure 5.18: RMS Pressure Distribution, High Lift configuration (x/c=0.7846)

For the clean wing configuration, we have seen that at a phase angle of 180 degrees, there was a significant reduction in the pressure fluctuations at the leading edge transducer. We will now examine the flow physics for the given parameter setting. The cascaded FFTs show (Figure 5.19) the following frequency scales: 6.042 Hz, 46.42 Hz, 52.60 Hz and 145.4 Hz. No new frequencies/coherent structures emerge along the chord length. The frequencies presented are invariant. The fact the frequencies don't change correlates well with the consistent shape of the closed loop RMS pressure distributions. The time frequency analysis for aerodynamic configuration at $\phi = 180^\circ$ reveals that all the wavelet maps contain a band that ranges from 5-7 Hz and centered on 6 Hz (Figure 5.20). The FFTs show that there is a large coherent structure at 6.402 Hz. The flow is synchronized about this frequency. From the Mexican Hat window we can see that the flow is strongly modulated throughout the chordwise distance. At $x/c=0.2660$, the synchronization weakens due the exchange of energy between the 6.042 Hz and the frequency scale located at 52.60 Hz; the 52.60 Hz mode receives most of the energy transfer. An inspection of the wavelet maps at all of the sensor stations reveals that there is stable vortex shedding with a frequency range from 45 Hz to 80 Hz (the frequency scales 46.42 Hz and 52.60 Hz fall within this range) which is centered on 63 Hz. At $x/c=0.2660$ (Figure 5.21), we see that there is stable vortex shedding at this location and that there is time-localized periodicity before 1.5s. The periodicity weakens after 1.5s and this correlates with the lost of coherence in the wavelet map at the same location about 6.042 Hz.

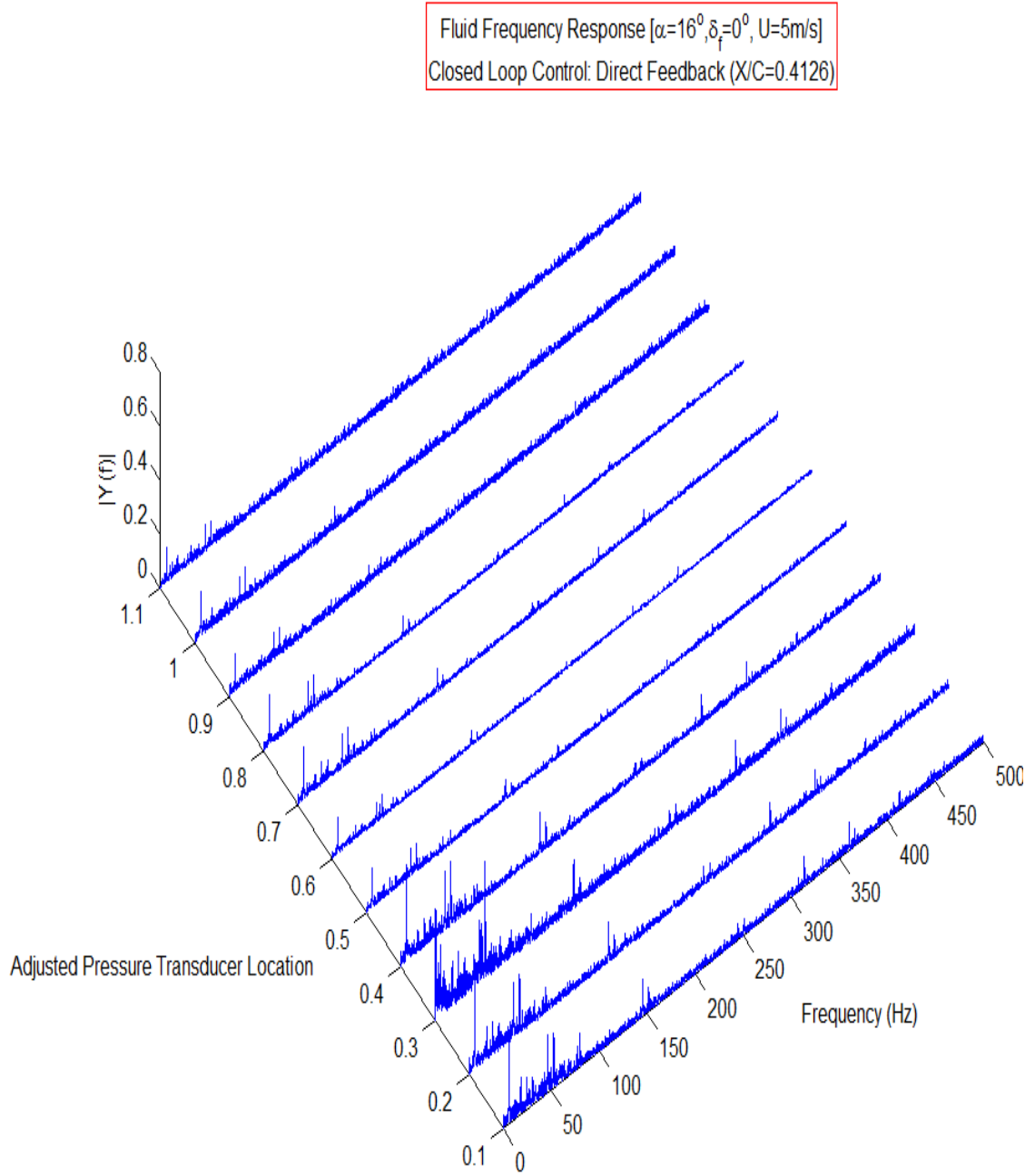


Figure 5.19: Closed Loop Frequency Spectra, Direct Feedback, $\varphi=180^\circ$

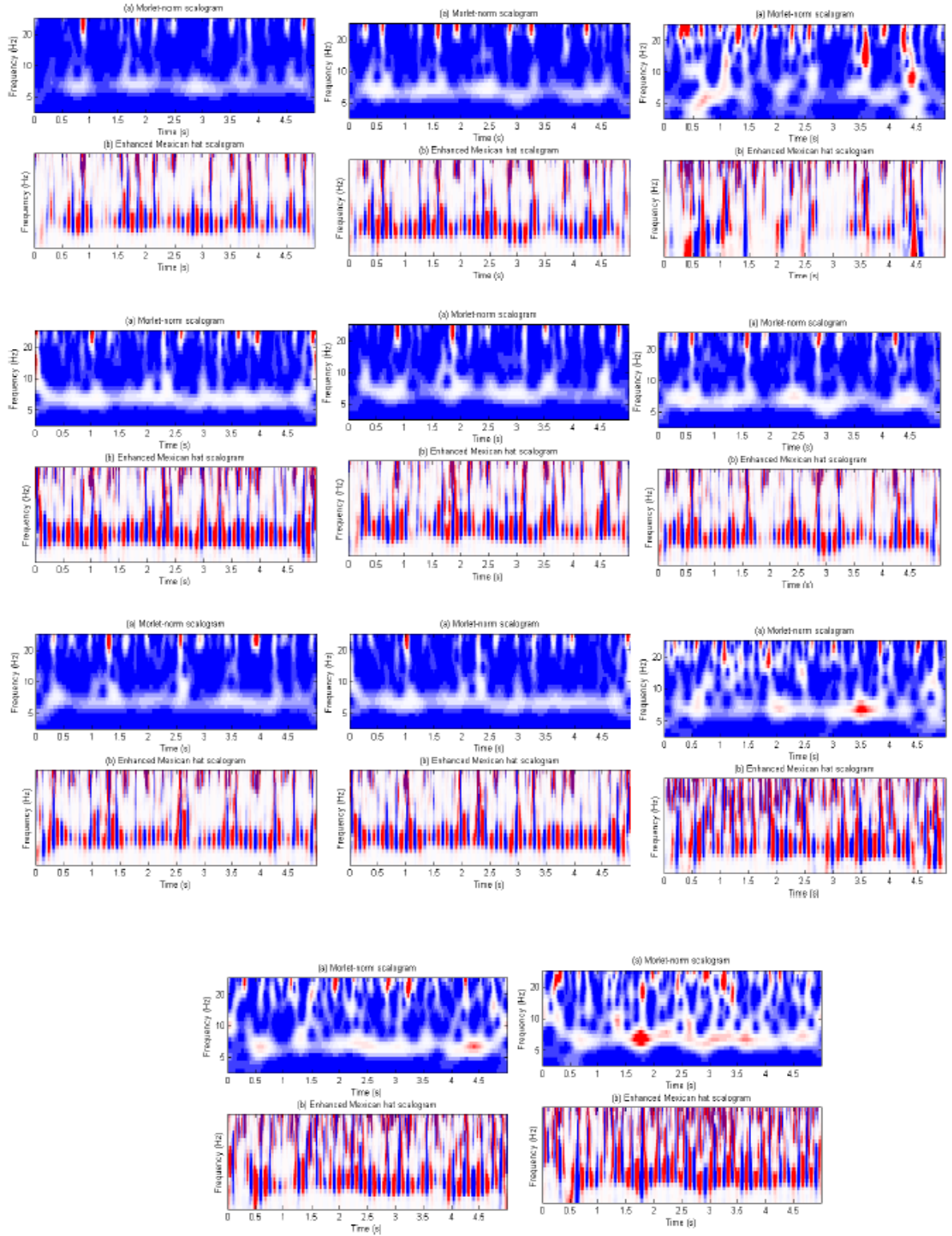


Figure 5.20: Wavelet Map Panel, Clean Wing configuration (DFB Control, $\varphi = 180^\circ$)

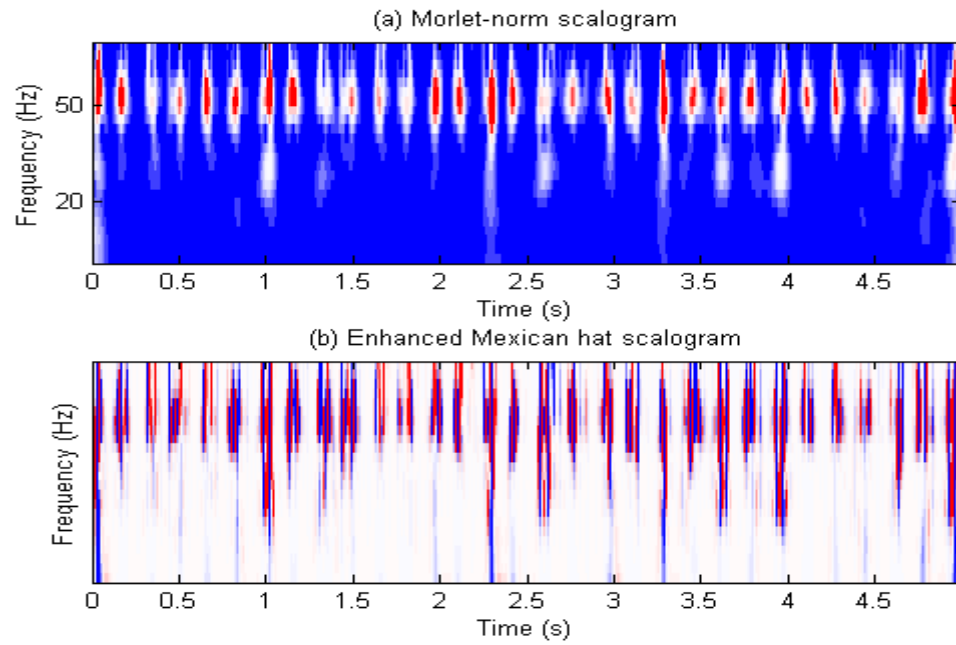


Figure 5.21: Wavelet Map Part 2, $x/c=0.3026$

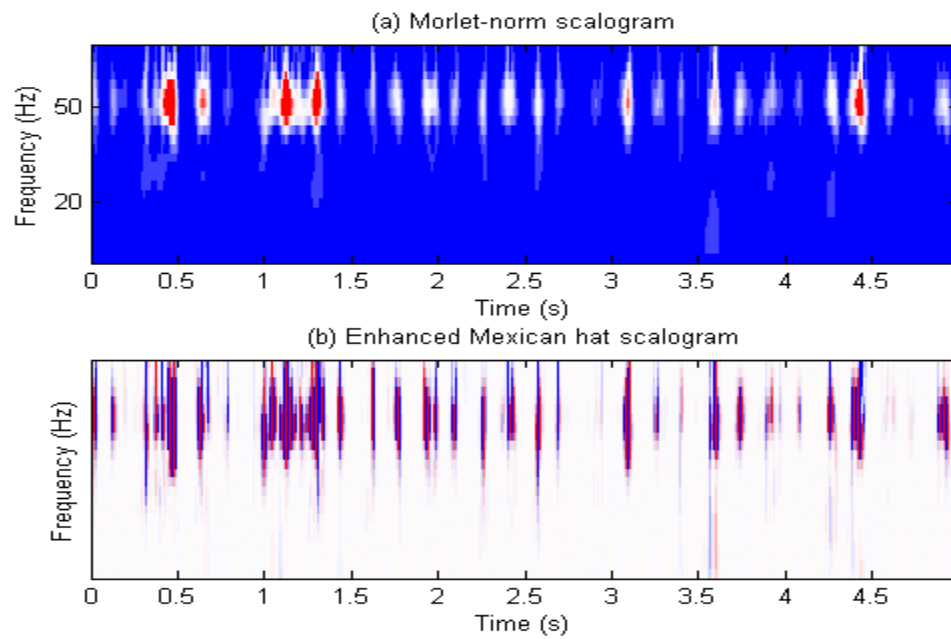


Figure 5.22: Wavelet Map Part 2, $x/c=0.2660$

The direct feedback control scheme is able to suppress the pressure fluctuations in the post stall regime. The closed loop phase angle sweeps revealed that the flow frequencies do not change with phase angle, however for the clean wing configuration at a phase angle setting of 180 degrees we seen that the pressure fluctuations are significantly reduced on the leading portion of the main airfoil element. For all the other phase angle settings, the frequency scale with the most amplification is located at 6.317 Hz except at $\phi = 180^\circ$ where the frequency is 6.042 Hz. This change in frequency correlates with the change in the of the RMS pressure distribution at $\phi = 180^\circ$. The application the Direct Feedback Control scheme results in the latter portion of the RMS pressure distribution having a gradual positive slope between $x/c=0.4493$ and $x/c=0.7483$ for the clean wing configuration and a shallow negative slope for the high-lift configuration. Further investigation is required to understand whether the changes in slope are due to forcing frequency (as in the case of the open loop control results), aerodynamic configuration or method of control. The author believe however, that if the same control method is applied to both aerodynamic configurations, the parameter space is reduced to flow frequency selection in the case of closed loop control, control/forcing frequency selection in the case of open loop control and Reynolds number. The following section will examine the effect of the Extremum Seeking Control scheme on clean and high-lift aerodynamic configurations in post stall.

5.4 ADAPTIVE CONTROL WITH AMPLITUDE MODULATION USING EXTREMUM FEEDBACK CONTROL (DUAL LOCATION)

The wing was configured at an AoA of 16 degrees with flap deflection of 0 and 20 degrees. The wing was subjected to closed loop control using the extremum or peek seeking control scheme documented by Krstic [68]. The final closed loop configuration was configured similar to that demonstrated in axial flow compressor experiment at CalTech [69]. That is the original extremum seeking scheme uses both a low and high pass filter. However, dynamic pressure signals tend to be noisy and this is not considered in the analytical development of the extremum seeking control scheme. So the first order low pass and high pass filters were excluded from the real time controller. Again, a Butterworth filter (low pass) of order 125 with a cutoff frequency of 500 Hz was used to filter the feedback signal before being passed to the ES controller. The purpose of the low pass filter is to enable the controller to operate on the frequency region of receptivity usually between 5 Hz-500Hz. In this way the controller will operate on the resonance frequencies of the actuator arrays. The control voltage is of the following form:

$$V(t) = A_{amp}[P_i(\omega_m, t)]_{ES} \sin(\omega_{c(LE,TE)} t + \phi_c) [V] \quad (5.3)$$

Unlike the Direct Feedback controller configuration, more attention had to be paid to ensuring that was no voltage exceedance for a prolonged period of time. It should be noted that the pressure signals are boosted by an amplification factor to account for any attenuation that might be caused by the filtering process. In some of the publications that discuss the use extremum seeking control for aerodynamic flow control, it is often not clear if the use these filters in the form that they are given in the derivation or whether the

order of the filter is increased; in any case they are presented without any clarification as to their implementation. The closed loop control configuration is given in Figure 5.23. The red line represents the pressure transducer signal used as the feedback signal and the purple line is the complete control signal to the synthetic jet actuator arrays as given in Equation 5.3. The yellow block is the Butterworth filter that has been described earlier in the text. In order to set the parameters of the control loop, the following design constraints need to be considered; the perturbation frequency ω should not be faster than the natural dynamics of the system, the parameter was initially chosen at 3.33 Hz, for a 30 cm chord at 5 m/s, this yields a Strouhal number of 0.2 in keeping with Roshko's findings in 1954 and then it was increased to 5 Hz after a real time bench evaluation of the control signals for each channel. The parameter a was set at 5 V.

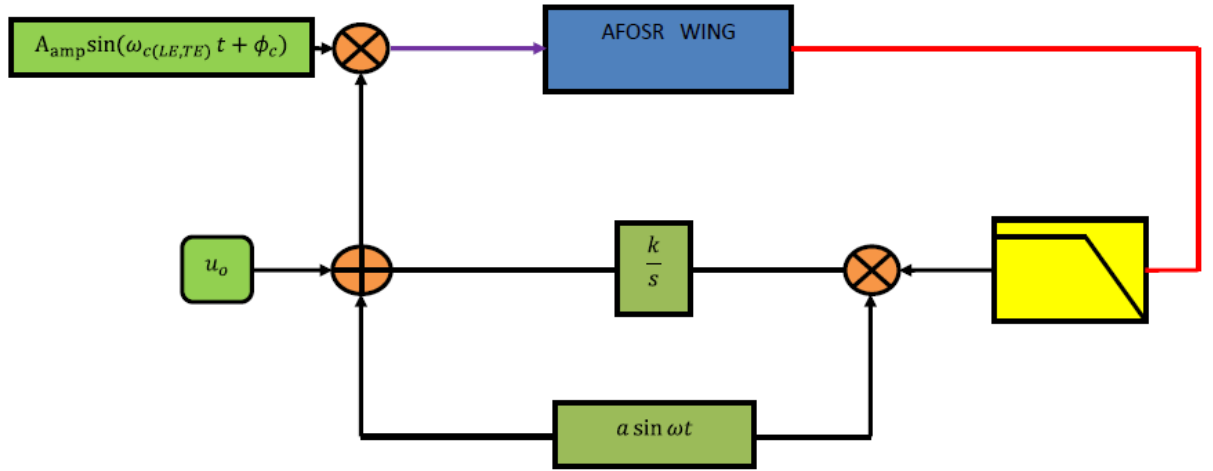


Figure 5.23: Experimental Extremum Seeking Control Loop Configuration

Further, by passing the pressure signal to the extremum seeking controller, the algorithm will optimize the shape of the amplitude modulated waveform such that it locks into one or more vortex shedding frequencies which result in the suppression of pressure

fluctuations along the chord of the wing. A similar waveform optimization approach was used by Joe et al [70]. In this particular study, the controller consisted of a narrow band filter and an Extended Kalman Filter (EKF).

For a flap deflection of 20 degrees, it was noted that at low speeds the gain, K was high and decreased as the airspeed increased. Although the wing is in post stall, at low velocities, the amplitude of the pressure fluctuations are not significant at steady state conditions and may require amplification in order to modulate the perturbation component of the control signal of the extremum seeking controller. Specifically, the control signal is given by:

$$u(t) = u_o + a \sin \omega t + \Delta u(t) \quad (5.4)$$

The gain, K is adjusted such that $\Delta u(t) \gg a \sin \omega t$. The value u_o is set to zero in this case as a safety precaution for the synthetic jet arrays. As the velocity increases, the flow becomes more chaotic and turbulent thus experimental evidence shows that the amplitude of the pressure fluctuations increases, requiring less amplification hence the decrease in the magnitude of the ES gain, K . At higher speeds, the large amplitude pressure fluctuations effectively modulate the perturbation signal. At low speeds with an undeflected flap, requires less amplification, it is also possible that between 5 and 10 m/s, the flow separation is laminar. As the velocity increases to 15 m/s, there is a slight increase in the Es gain, K ; it could be that there is a transition from laminar to turbulent flow. The pressure transducer is SN5419 which is located roughly in the center of the airfoil ($x/c=0.4126$). Perhaps more investigation is needed to understand the increase in the gain K . When the velocity is greater than 15 m/s, the gain drops off and appears to

approach a value of 2; is it possible that this is an asymptotic value that is characteristic of an airfoil at 16 degrees angle of attack? Or is it related to the pressure transducer chosen as the feedback signal? Further experimental investigation is required to confirm this finding, perhaps at 5, 10 and 40 degrees flap deflection would be sufficient to answer this question, for several reasons a) develop a family of curves with the zero flap deflection as the baseline; b) confirm that the ES gain for a wing at 16 degrees AoA does in fact approach the value of 2.

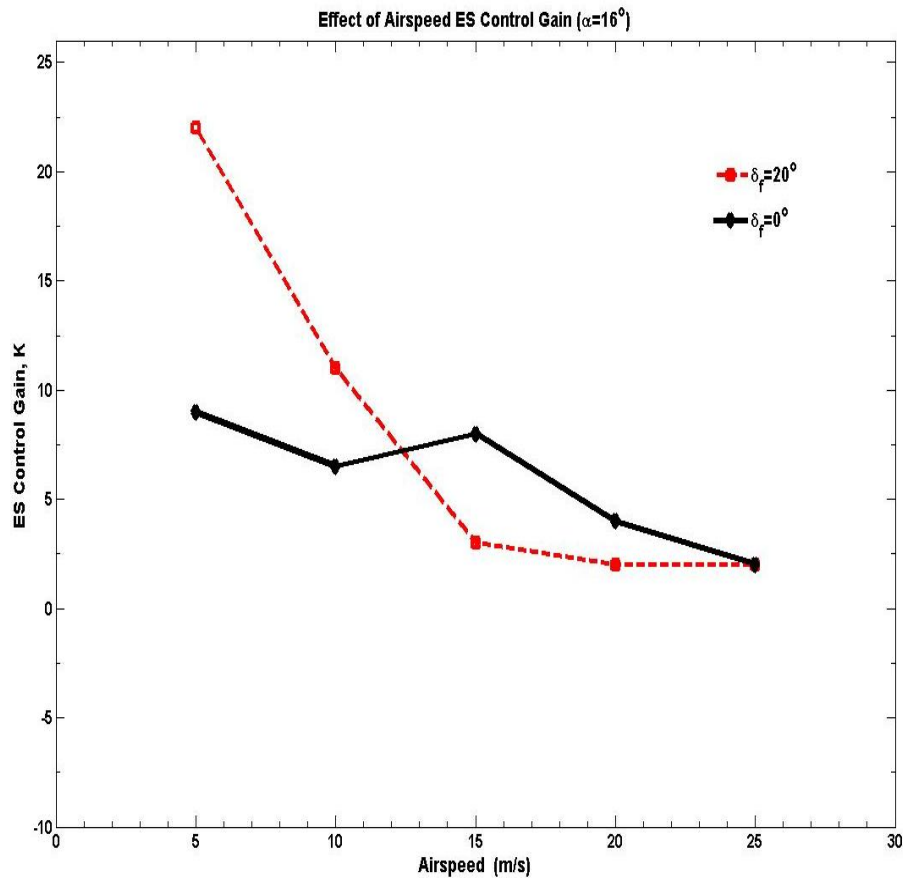


Figure 5.24: Extremum Seeking Controller Gain, K versus Velocity

In Chapter 4, we outlined the channel voltage balancing procedure such that the product of the real time pressure transducer signal and the amplifier gain did not exceed $30V \pm$

5V. The result of this parameter tuning procedure has the following on controller performance; an examination of the frequency response of the resulting control signal reveals that the controller has locked on to a frequency that is possibly contained in the separated flow; that frequency is 6.04 Hz (Figure 5.25). Further examination of the frequency response of the control signal at different tunnel velocities reveals that this frequency is invariant over the range of velocities. By adjusting the controller gain such that the channels were balanced at $30V \pm 5V$, resulted in the displacement of the amplitude at 6.04 Hz ($St \approx 0.1$) for each flow condition and wing configuration (Figure 5.26). When Figure 5.26 is compared to the ES gain vs. Airspeed (See Figure 5.24) we see that the shape of each curve is essentially the same. The use of the extremum seeking controller and voltage constraint forms a constrained optimization problem, specifically; the extremum seeking controller optimizes the pressure signal waveform and selects simultaneously the optimal forcing frequency which is then modulated by the respective primary sinewaves for each channel. The direct feedback control cases show that there is a peak located at 6.04 Hz in FFT and the wavelet maps show lines of persistent periodicity at each chordwise location. The extremum seeking cases also show that there is a peak located at 6.04 Hz except for the 5 m/s wind tunnel run, or at least it does not appear in the FFTs for each sensor location. It is also possible that this frequency is the result of application of closed loop control. The fact that it is not visible in the 5 m/s case does not mean that this frequency is not there. We will show this to be true when the discussion on wavelets is presented. Figure 5.27 shows the control signals at each velocity. Note the slowly modulated control signals; this is the result of multiplying the feedback pressure signal to the perturbation sinewave. The application of empirical mode

decomposition would expose the slowly varying mode that gives the control signals their general shape.

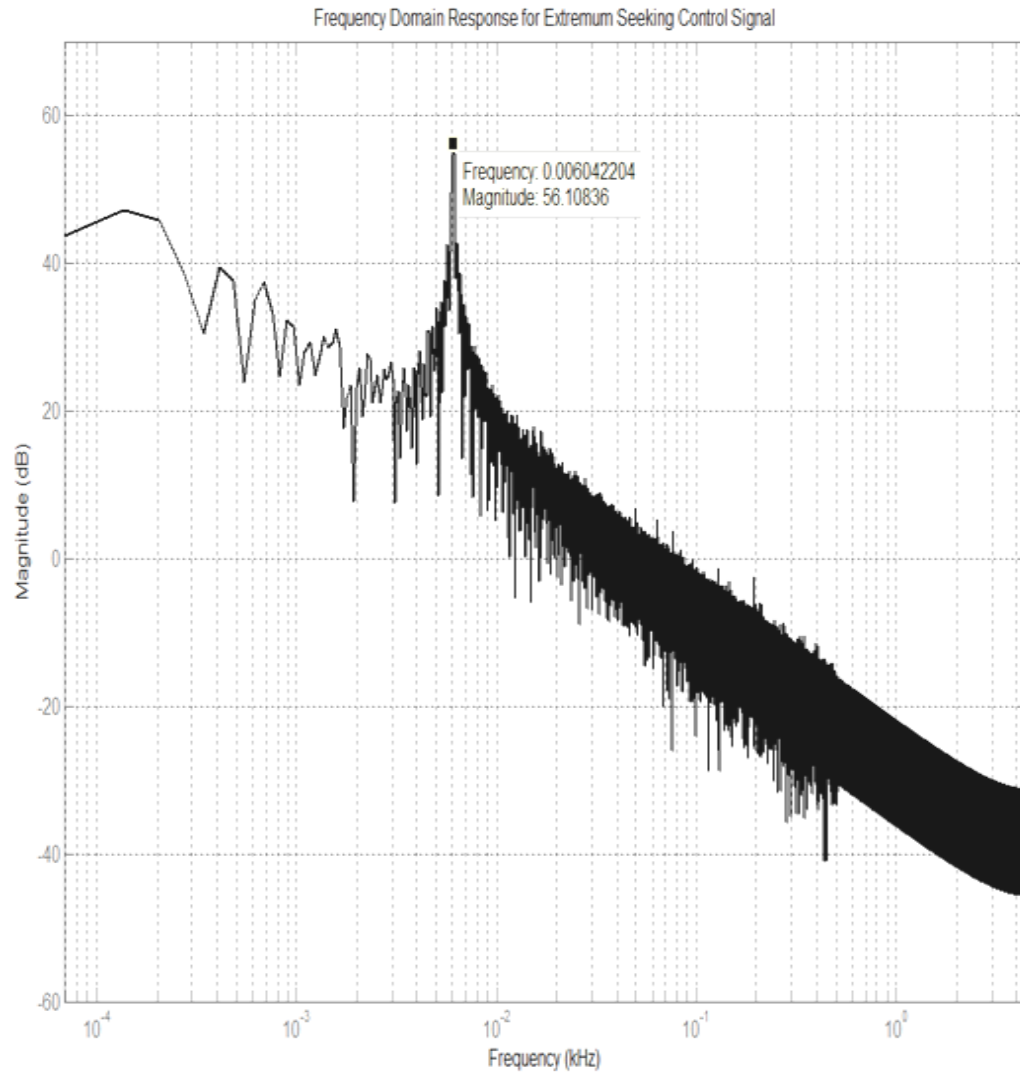


Figure 5.25: Frequency Domain Response of Extremum Seeking Control signal

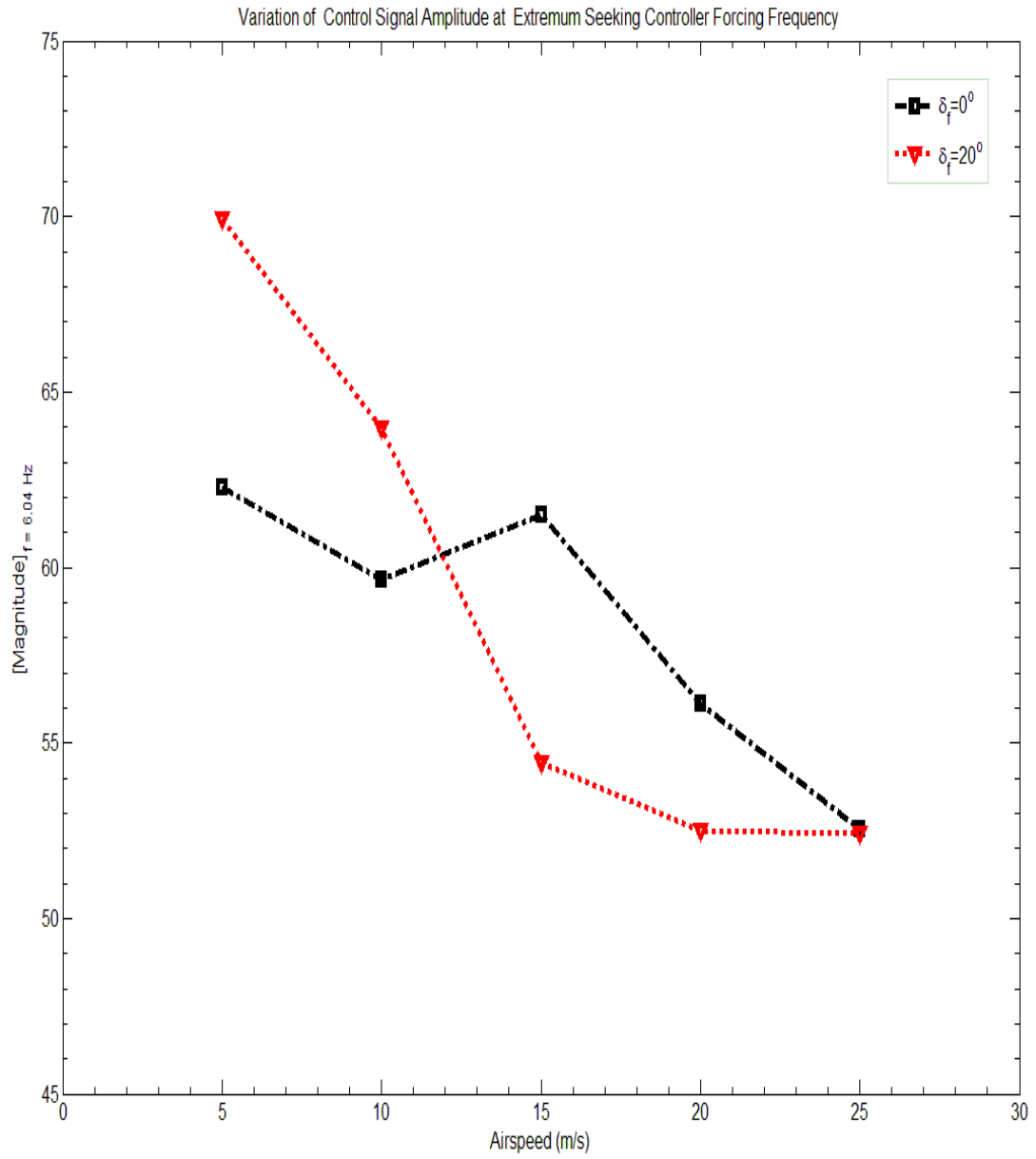


Figure 5.26: Variation of Control Signal Amplitude at ES Control Forcing Frequency

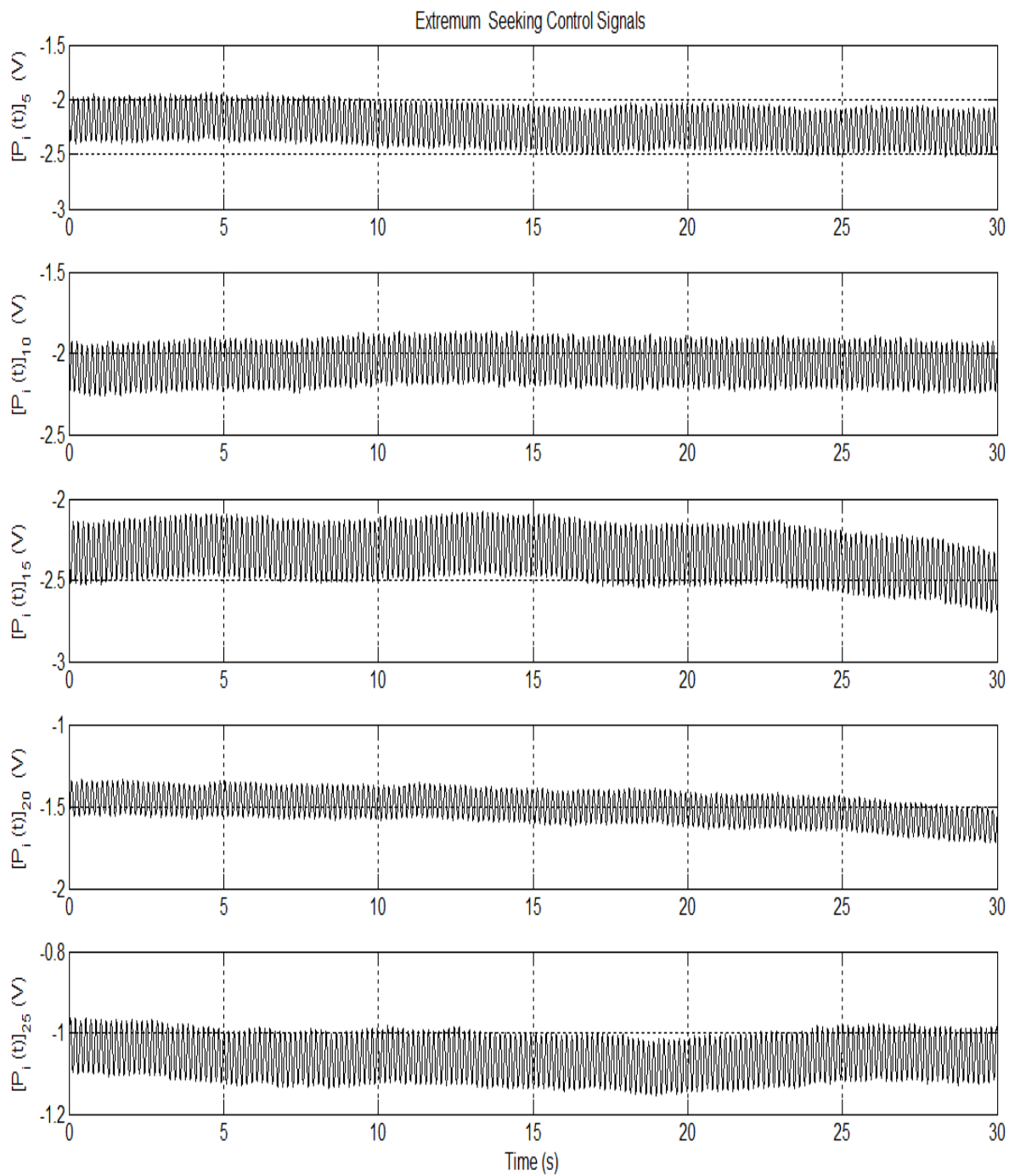


Figure 5.27: Time Series of Extremum Seeking control signals

We will now present the aerodynamic results for the given wing and controller configurations. For $\alpha = 16^\circ, \delta_f = 0^\circ$, Figure 5.28 shows the resulting RMS pressure distribution. The reference airspeed is 5 m/s. The RMS pressure shows a sensitivity to airspeed at the following at $x/c=0.2660$ and $x/c= 0.3393$. At $x/c= 0.3026$ we note that there is very little displacement of the pressure fluctuations. At 15 m/s and 10 m/s, the pressure fluctuations are less than that of the 5 m/s, 20 m/s and the 25 m/s cases. For the 15 m/s case, the peak pressure fluctuation has shifted forward to $x/c=0.2293$. It is likely that the sensitivity at the aforementioned transducer locations are responding not only to the change in airspeed but the different closed loop frequency scales that are being imparted to the flow. Specifically we see that for some lower airspeeds, the magnitude of the pressure fluctuations are significantly reduced toward the leading edge and while other airspeeds result in RMS pressure spikes at certain chordwise stations. The pressure fluctuations appear to be suppressed significantly after $x/c=0.3760$ (or 11.28 cm). Chang, Hsiao and Shyu presented results on a length scale called the asymptotic pressure recovery point. It is defined as the distance from the leading edge where the surface pressure reaches its base pressure. For our configuration, the results presented here would be the dynamic counterpart to that length scale parameter. Experimental results show that for forcing frequencies between 0 and 100 Hz, the pressure recovery point ranges from $x/c=0.3$ to 0.6, with the post stall region beginning at 18 degrees (NACA 63₃-018). The results presented in the RMS pressure distribution shows the pressure recovery point falls within the range stated above.

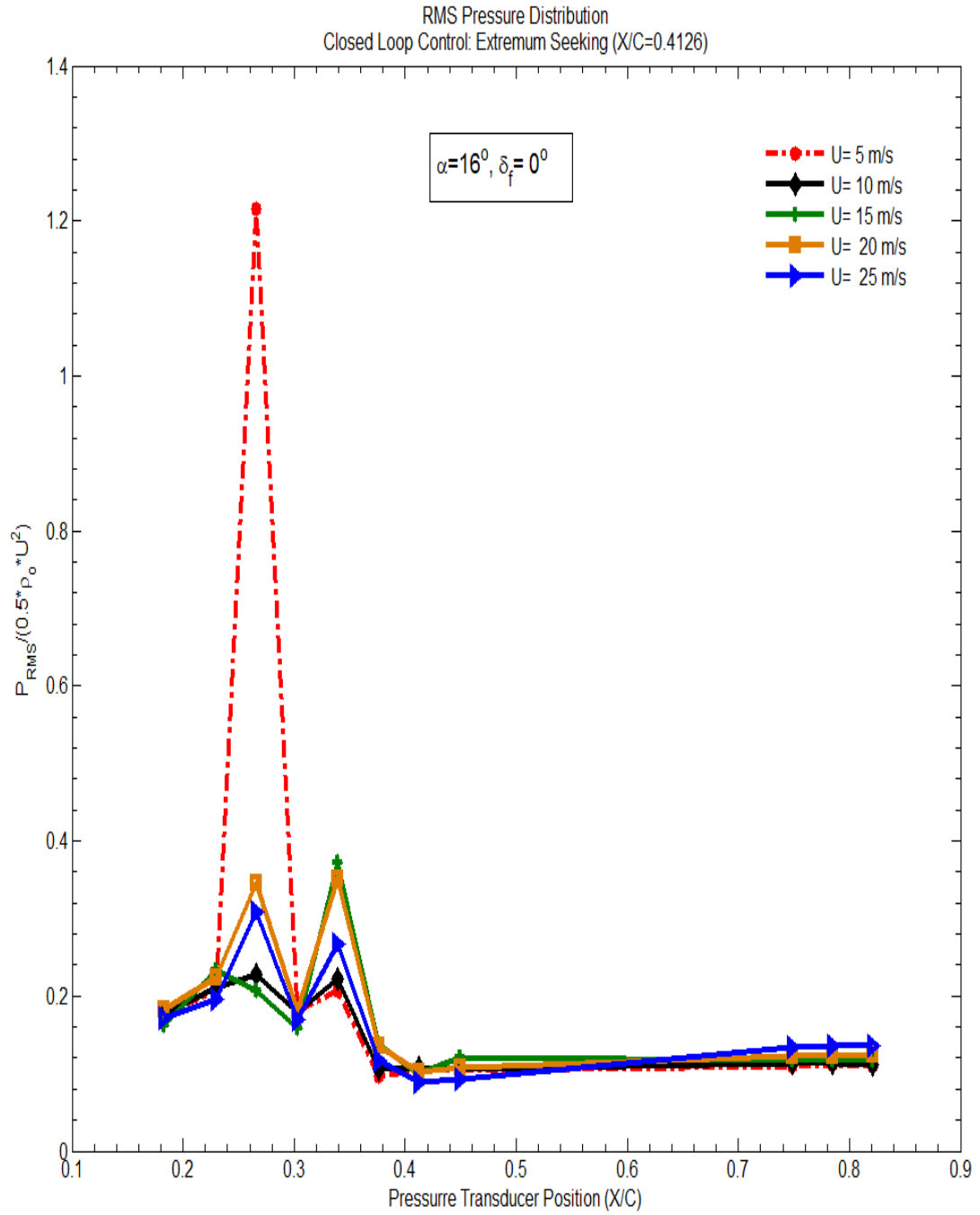


Figure 5.28: RMS pressure distribution for wing under Extremum Seeking Control

When observing the closed loop time series, we see that the broadband excitation adds coherence to the pressure waveforms. Visually we see that this changes with chordwise

distance and the spike trains seen in the open loop un-actuated response are reduced and amplitude as well as the number of clusters. At $x/c=0.2660$, it is observed that the pressure waveform at this location ceases to be coherent. This is confirmed visually by looking at the irregularity in the waveform and the spike in RMS pressure seen in Figure 5.28 At $x/c=0.3393$, we see that the waveform is periodic and free of spike trains. A similar observation can be made of the pressure waveform at $x/c=0.3760$, except the amplitude of the pressure fluctuation is reduced; again this is confirmed by the RMS pressure distribution at the given location. For our configuration the experimental results show that this length scale is about 0.4. An examination of the time averaged Fast Fourier Transforms (FFT) for each chordwise stations show the following frequency scales are present at all of the sensor locations except $x/c=0.2660$. They are 8.789 Hz, 19.36 Hz, 30.08 Hz, 45.04 Hz, 53.83 Hz, 62.76 Hz, 79.65 Hz, 143.90 Hz and 153 Hz. At $x/c=0.2660$ we see following frequency scales; 41.89 Hz, 47.79 Hz and 53.97 Hz. The frequency scales that are not present at $x/c=0.2660$ are 8.789 Hz, 19.36 Hz and 30.08 Hz. Note that at $x/c=0.3026$, these frequency scales re-appear. It could be conjectured that the absence of listed frequency scales is an indication that there is a strong flow nonlinearity at $x/c=0.2660$; it also shows that there is a loss of periodicity at this sensor location as confirmed by the lack of coherence in the time series at $x/c=0.2660$. Further, this loss of waveform coherence and periodicity coincides with the large increase in RMS pressure at $x/c=0.2660$. Note that the lowest frequency scale at 8.789 Hz comes from the application of the closed loop controller. Lastly, the new vortex shedding frequency resulting from closed loop control is 45.04 Hz.

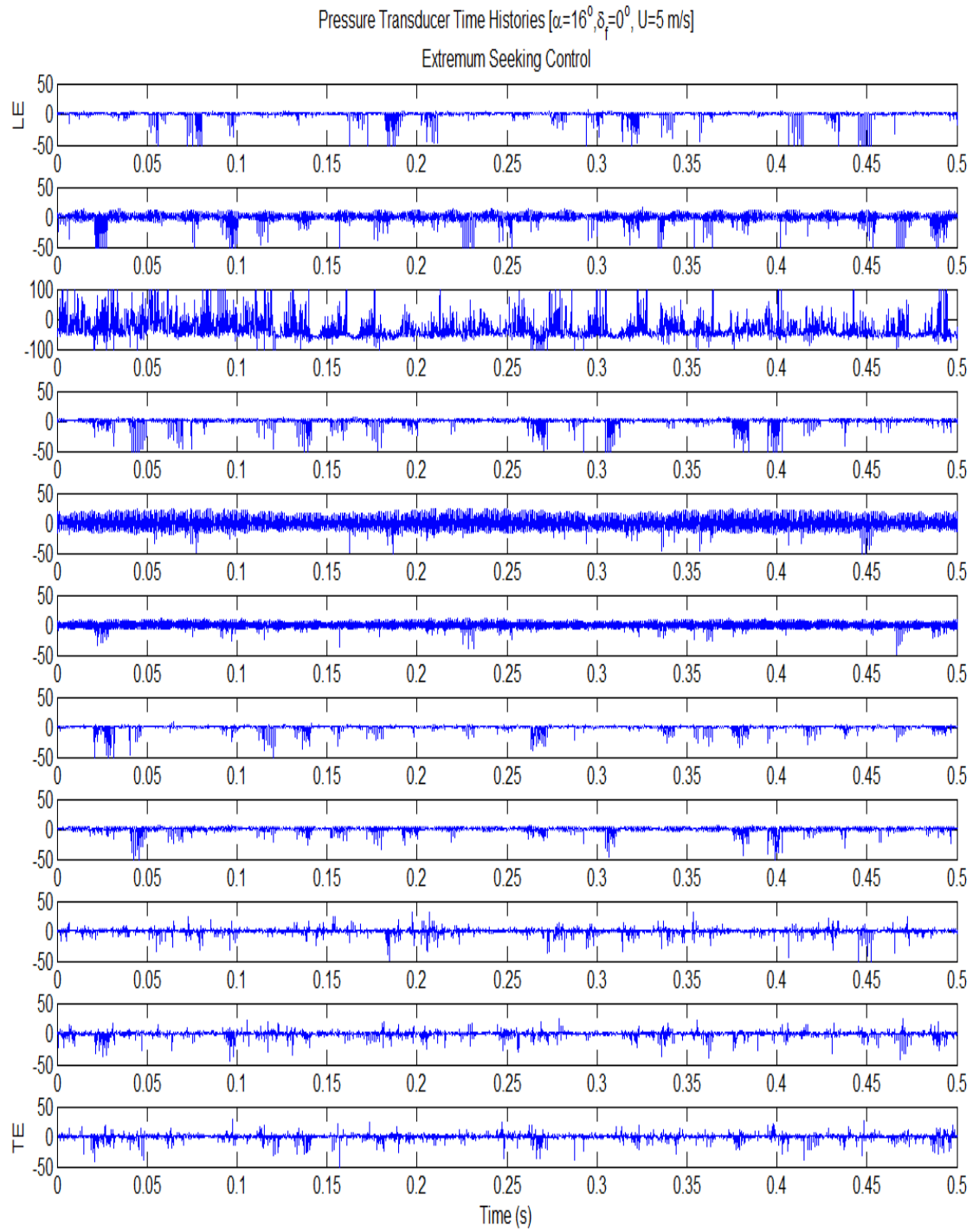


Figure 5.29: Extremum Seeking Control Times Series, Clean Wing configuration

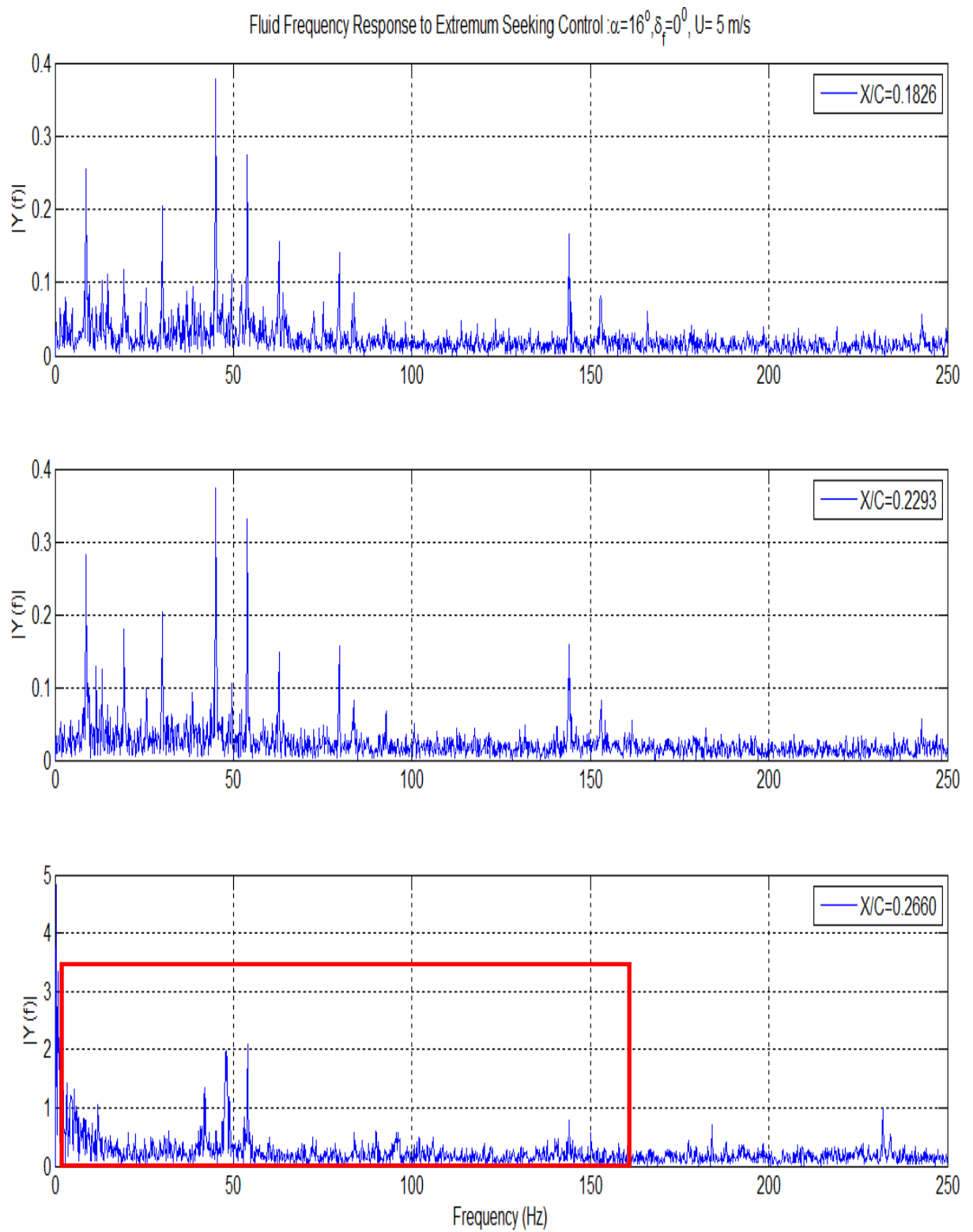


Figure 5.30: Enhanced FFT, Stations 1 to 3 (Extremum Seeking)

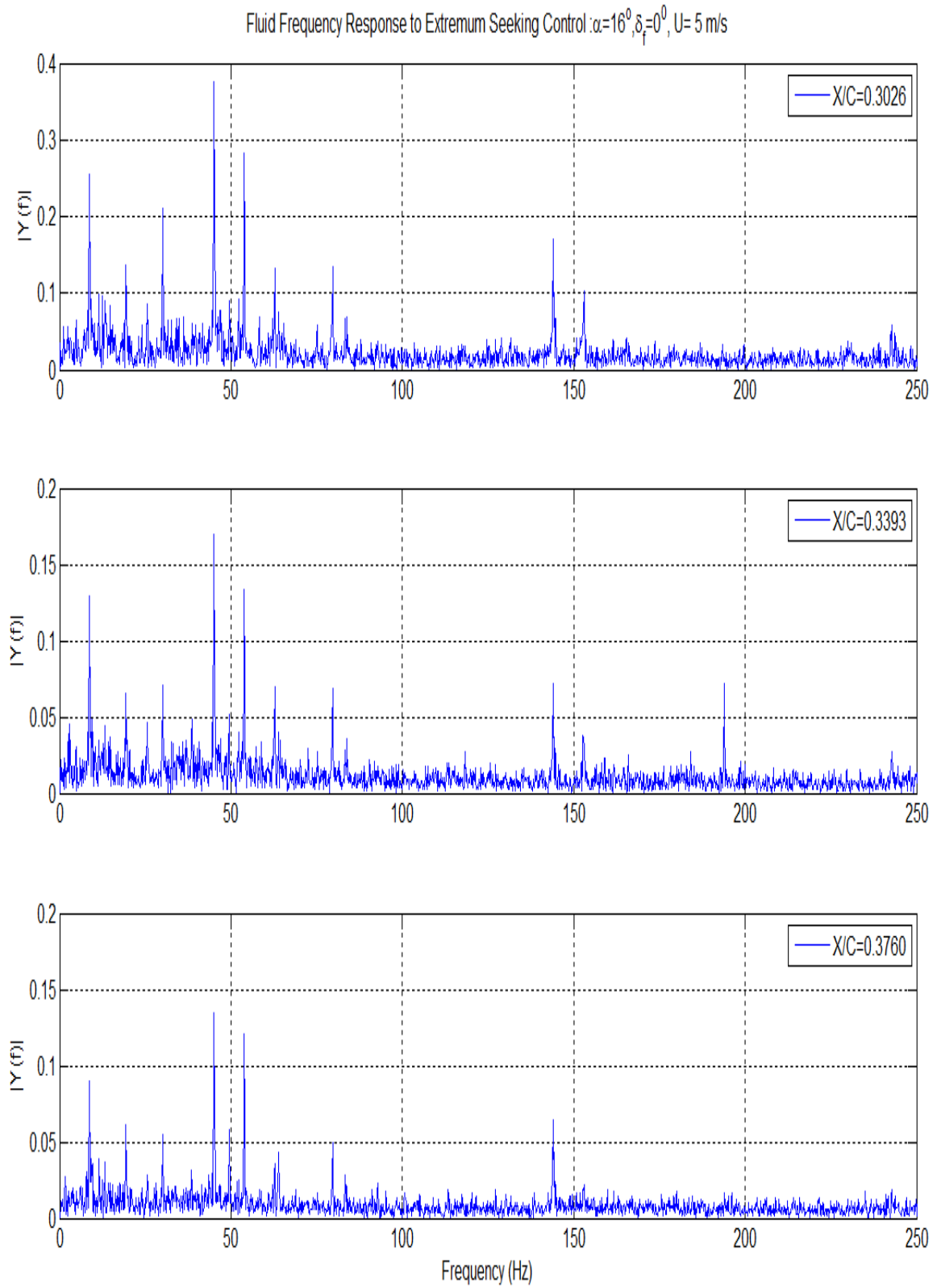


Figure 5.31: Enhanced FFT, Stations 4 to 6 (Extremum Seeking)

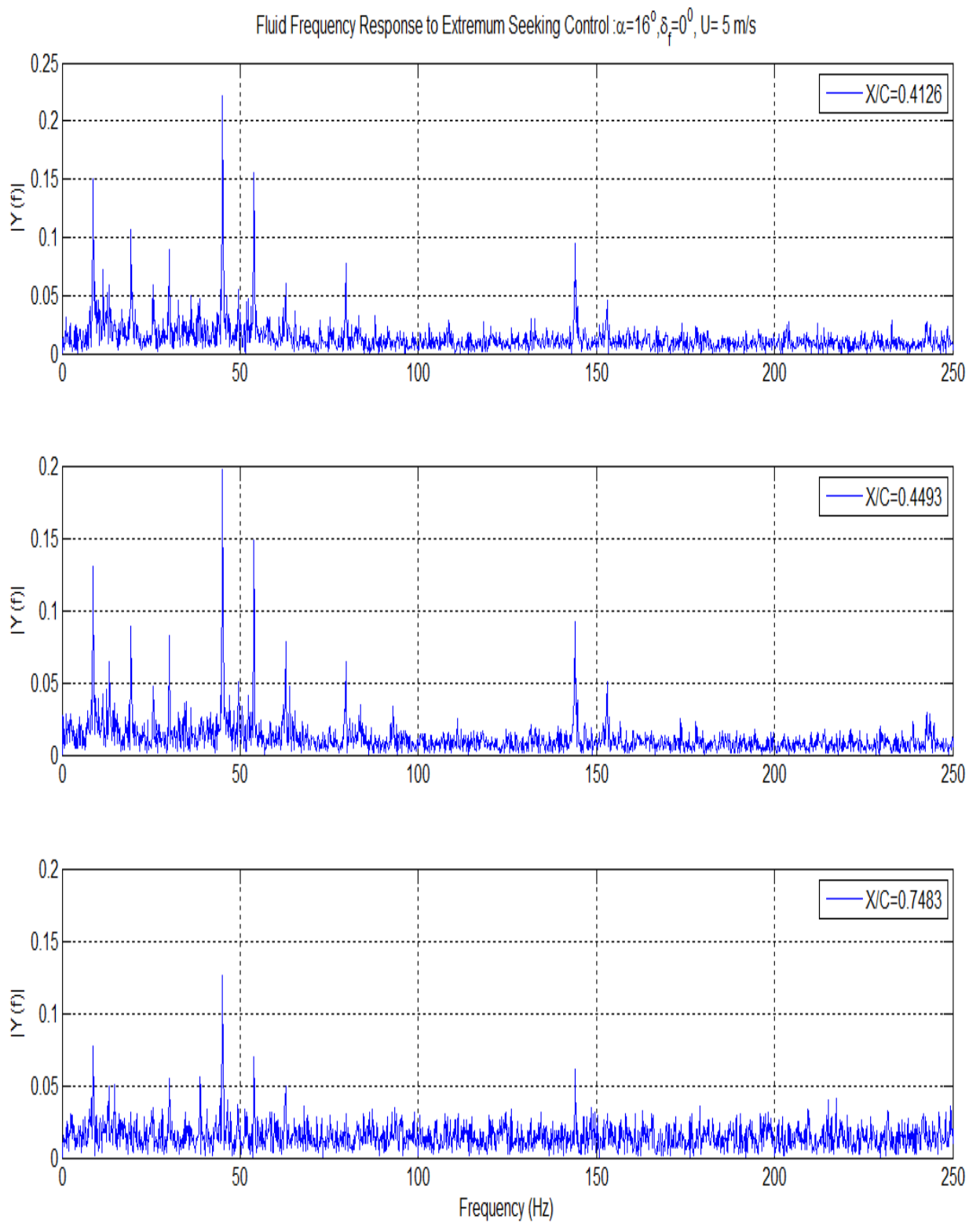


Figure 5.32: Enhanced FFT, Stations 7 to 9 (Extremum Seeking)

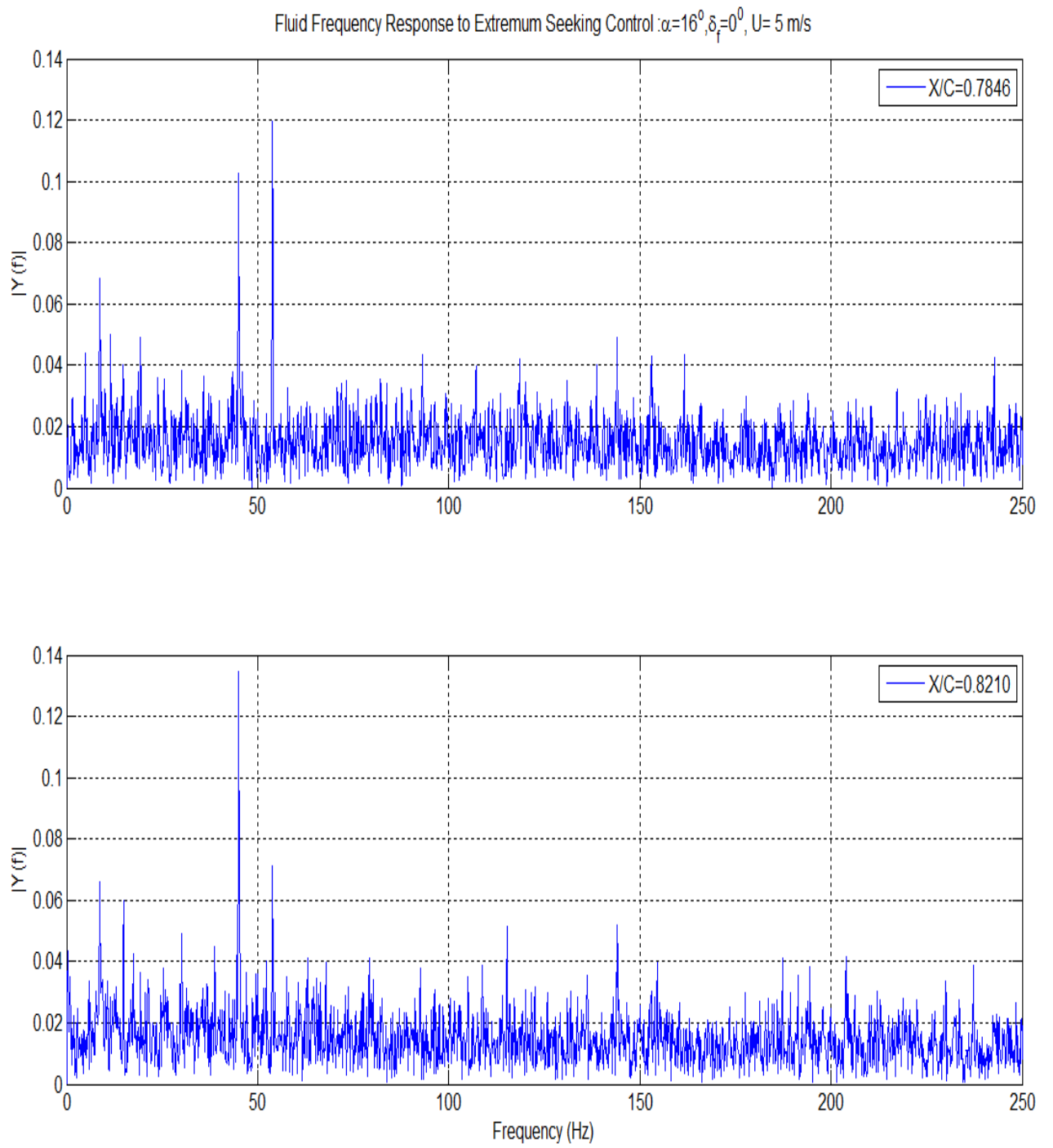


Figure 5.33: Enhanced FFT, Stations 1 to 3 (Extremum Seeking)

Figure 5.34 is the wavelet map panel for the wing configuration of $\alpha = 16^\circ$, $\delta_f = 0^\circ$ at $U = 5$ m/s. The panel is organized as follows; the wavelet tile in the upper most left corner is the time-frequency representation for $x/c=0.1826$, the second is to the right of it and so on. Visual inspection of the wavelet panels reveals that the frequency line ranges from 8 Hz to 11 Hz, with the center of mass at approximately 9.227 Hz. This time-frequency result agrees with the FFTs previously presented in that 8.789 Hz falls within the frequency band shown in the wavelet maps. The controller generates a frequency of 6.042 Hz, yet the flow appears to be locked in about 9.227 Hz. Perhaps the 9.227 Hz tone is a super harmonic of the controller frequency for which the flow accepts this tone as admissible in a dynamical systems sense. An examination of the Mexican Hat portion of the wavelet maps show that the flow is strongly modulated at this frequency throughout the chordwise distance; in addition the wavelet packets tend to be longer in the frequency axis and show some regularity. We see that there are what appear to be shedding events that are on average 1.5s seconds apart. The frequency scales contained in a nonlinear system will naturally exchange energy. This finger- like structures seen in the Morlet wavelet maps energy exchanges with other dominant frequency scales embedded in the flow. Of particular interest in the time-frequency response at $x/c=0.2660$. Specifically, we observe that there are three very pronounced aerodynamic with strong periodicity between 2.5s and 3s, at 3.5s and again at 4s to 4.5s. The flow appears to lose coherence (indicated by the absence of certain frequencies See Figure 5.34) at this location and correlates with the large amplitude pressure fluctuations recorded at this location as well as the loss of periodicity in the recorded times series at this location. The transducer that immediate after $x/c=0.2660$, returns to a locked in condition. The

response at $x/c=0.2660$ has to do with the shape of the airfoil and how the shape and augmented aerodynamic flow interact with the acoustic field. More experimental investigation is needed to study this conjecture.

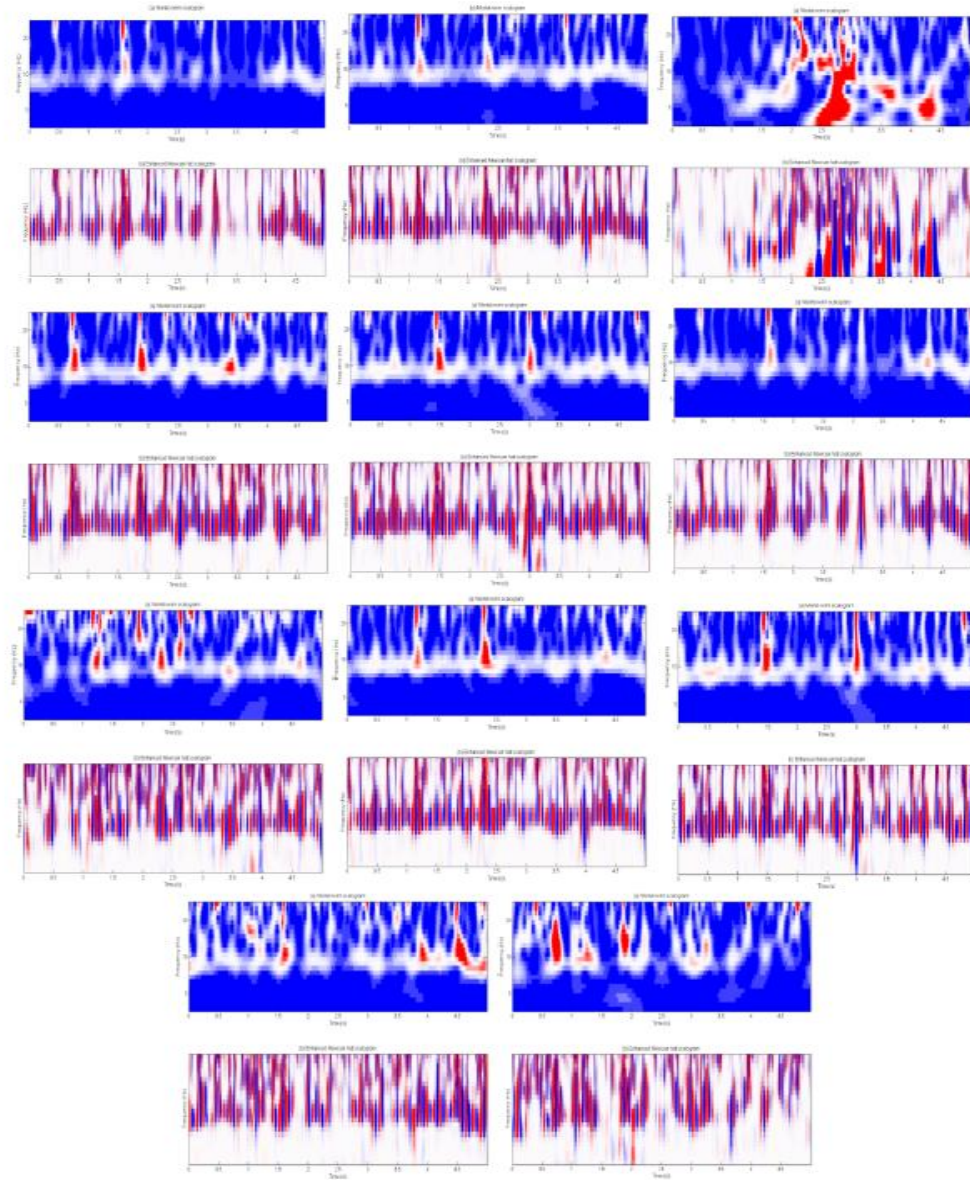


Figure 5.34: Wavelet Map Panel, Clean Wing configuration (Extremum Seeking)

An examination of the wavelet maps at a higher frequency range reveals a band of periodicity (Figure 5.35) centered on 50 Hz. The remaining wavelet maps are similar and will not be shown here. Further the reader will note that there is similar time-frequency behavior for the high-lift configuration; this is expected as we have already shown that the RMS pressure distributions are similar. Of particular interest for the clean configuration in this frequency range at $x/c=0.2660$ is the activity at 2 s for a duration of 1.5 s, we see that there is periodicity/vortex shedding that is stable and controlled. The vortex shedding begins again just after 4s. The energy exchange is transient at this chordwise station.

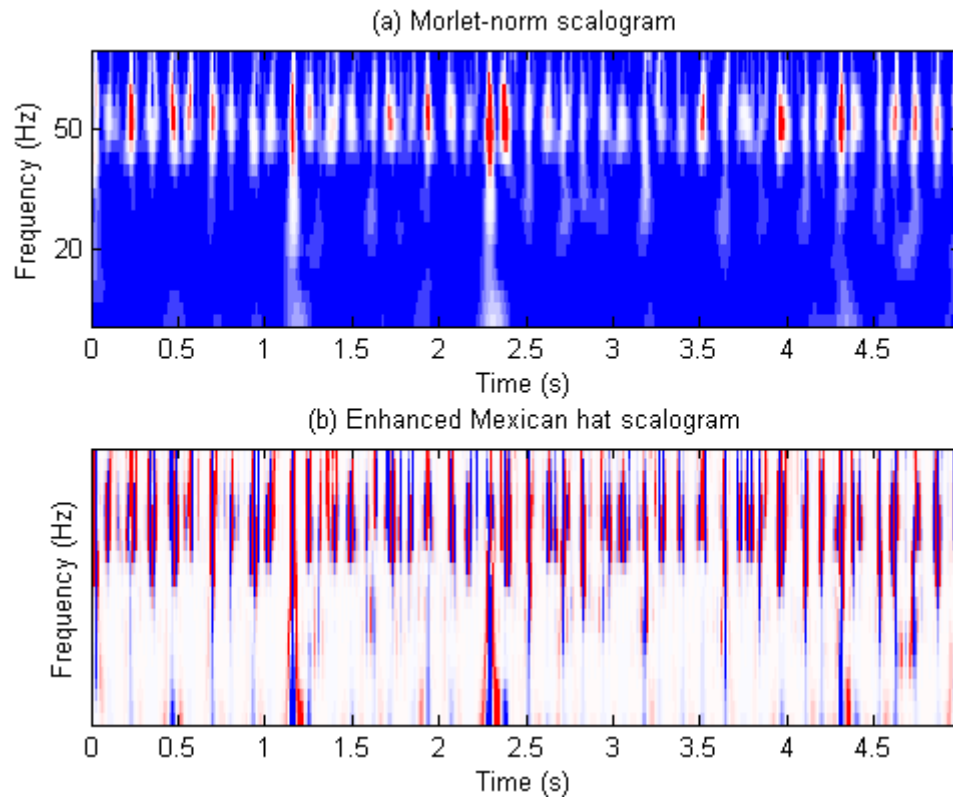


Figure 5.35: Wavelet Map Part 2, Clean Wing configuration (Extremum Seeking)

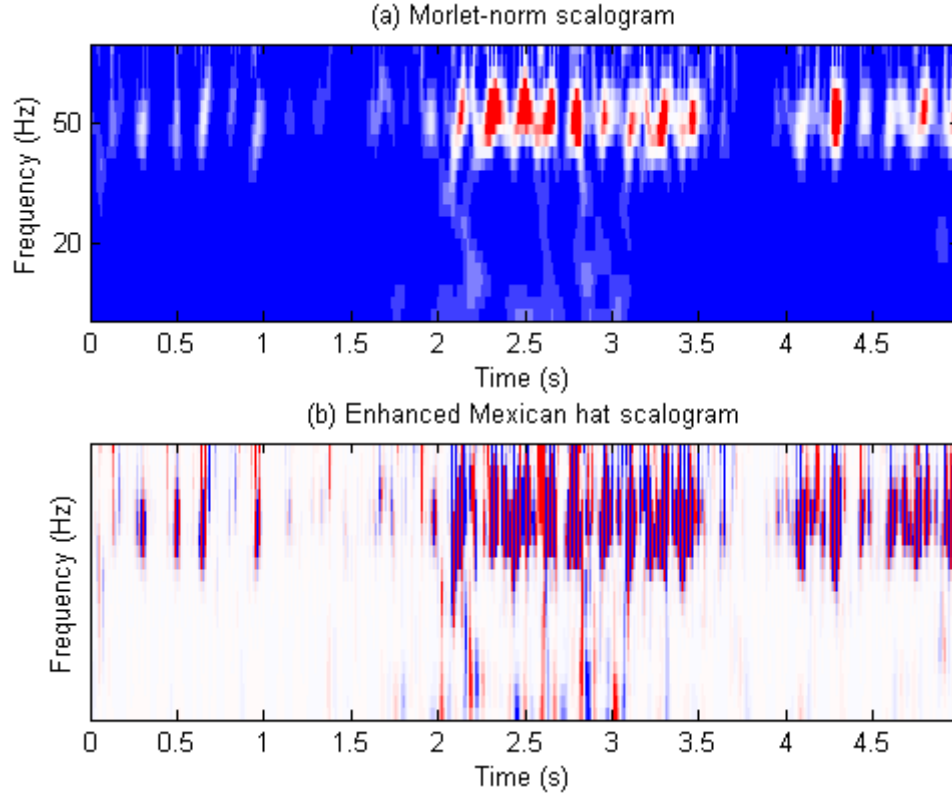


Figure 5.36: Wavelet Map Part 2 ($x/c=0.2660$), $\delta_f = 0^\circ$ (Extremum Seeking)

For the $\alpha = 16^\circ$, $\delta_f = 20^\circ$ we present the RMS pressure distribution (Figure 5.37). It is observed that there excitation peaks located at $x/c=0.2660$ and $x/c=0.3393$. From previous results, we know that the certain locations on the wing are sensitive to excitation frequency; but because the excitation is broadband it might be difficult to understand what frequency the flow is responding to at these locations; further investigation is required to answer this question. The reader will observe that at these locations are also sensitive to change in airspeed. The RMS pressure at the above mentioned locations are significantly higher than that of the un-deflected flap case, this a direct result of the flap being deflected. At 25 m/s, notice that that neither there is no RMS pressure peak at $x/c=0.2660$; it is possible that controller is producing frequencies in the flow that create a

velocity based receptivity. A visual inspection of the time series (Figure 5.38) reveals that there is significant aerodynamic activity at the first six sensor locations which can be correlated with the RMS pressure distribution; similar behavior is observed when the flap is not deflected. However for the configuration with flap deflection, there appears to be a marked amplification of certain frequency scales in the flow/wake. For example, at $x/c=0.2293$ we see that there lobes that approximately 165 milliseconds apart. At $x/c=0.2660$, there are spike train clusters that are also 165 milliseconds apart; when one converts this to a frequency, we arrive at approximately 6 Hz. Similar features are observed at $x/c=0.4493$ and $x/c=0.7483$. This result will be further explained with the examination of the pressure transducer FFTs. Again, as we move toward the trailing edge, the RMS pressure fluctuations appear to be suppressed.

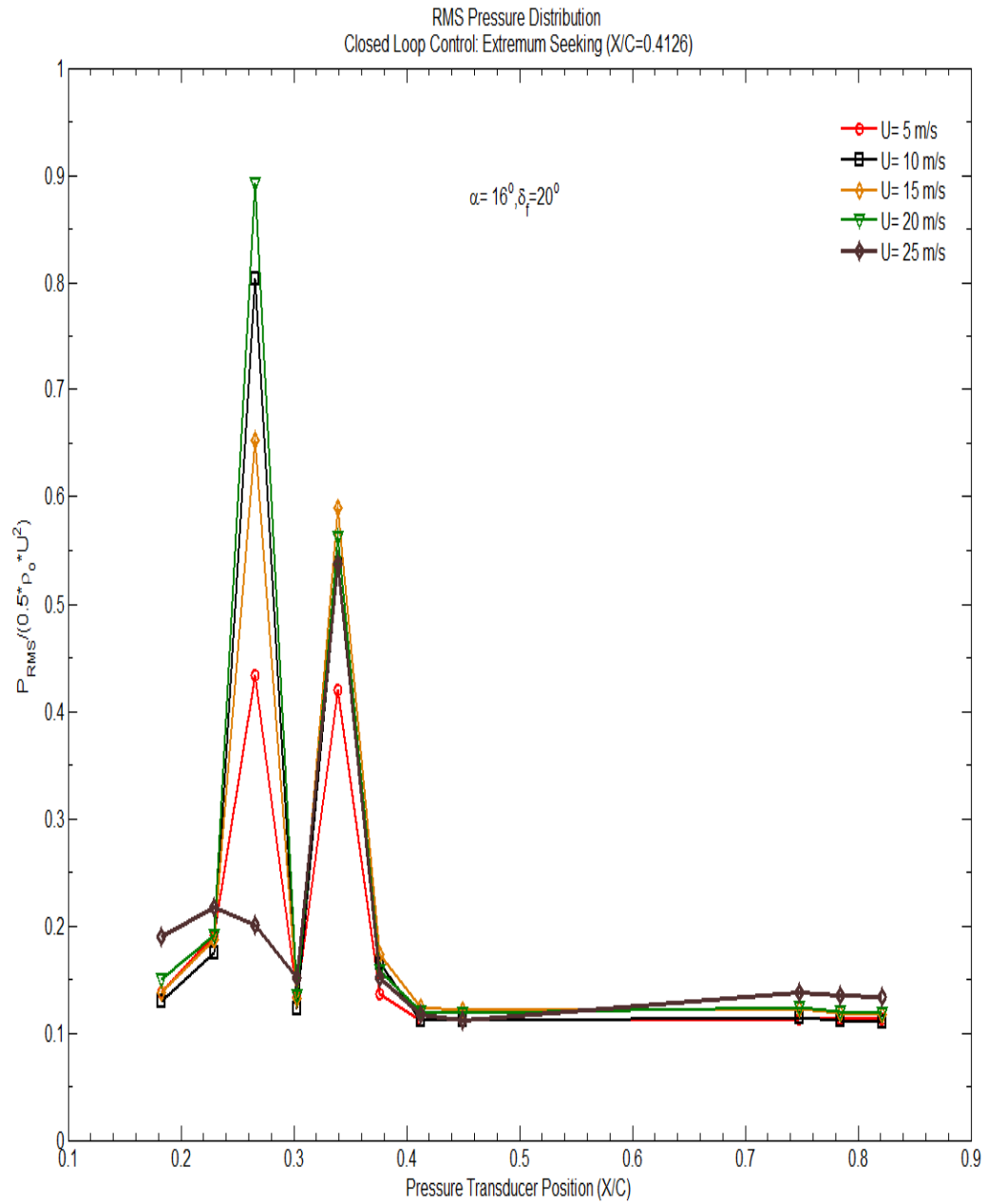


Figure 5.37: RMS Pressure Distribution, High Lift Configuration (Extremum Seeking)

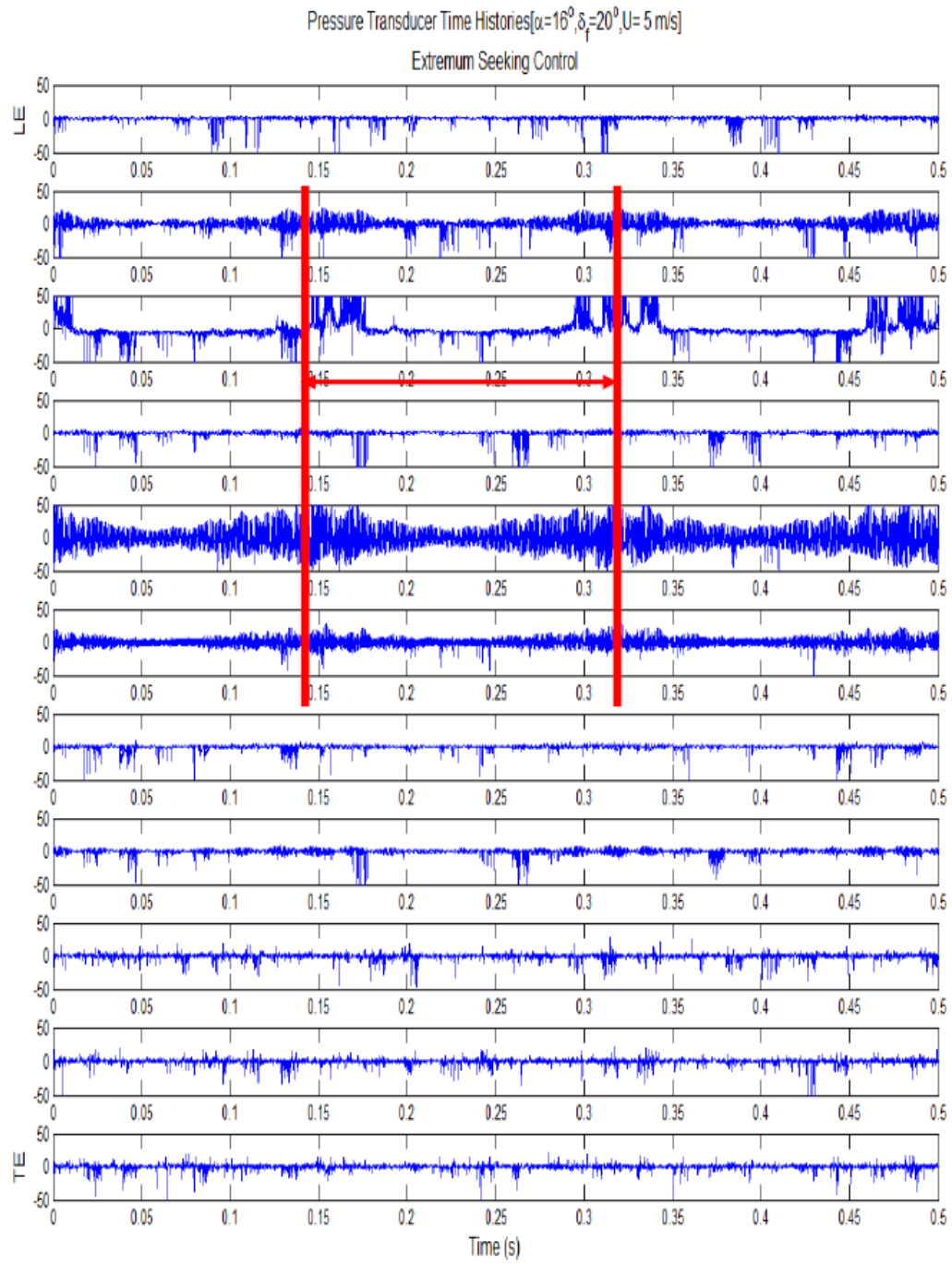


Figure 5.38: Time Series, High Lift configuration (Extremum Seeking)

An examination of the Fast Fourier Transforms (Figures 5.39-5.42) reveals that the following frequency scales are present in the flow; they are as follows, 8.789 Hz, 45.32 Hz, 53.97 Hz, 79.65 Hz and 152.8 Hz. At $x/c=0.2660$, we begin to see a frequency scale located at 6.042 Hz ($St= 0.099$) evolve alongside 8.789 Hz. At the preceding sensor locations it is observed that the magnitude of the 8.789 Hz frequency scale remains above 0.2. At $x/c=0.2660$, it is observed that there is a significant energy exchange between the modes in the flow. We see that while the other flow structures have received energy, the frequency scale located at 6.042 Hz ($St= 0.099$) has received most of the energy. The frequency peak located at 8.789 Hz has shifted to 12.08 ($St=0.199$) and has about a quarter of the energy that 6.042 Hz modes does. For nonlinear systems that are under periodic closed loop control experience a re-distribution of frequencies such that these frequencies align themselves with a perturbation frequency; in this way we say the system is *synchronized* or *frequency locked*. Notice that the magnitude at both frequency locations increase indicating that there is an exchange of energy between these modes. Such behavior is typical of nonlinear dynamical systems. At sensor locations $x/c=0.3393$ and $x/c=0.3760$, the 6.042 Hz tone again has evolved over the two sensor stations, at both these stations, it is observed that the magnitude decreases with the appearance of the secondary tone at 6.042 Hz. For the clean wing configuration we see that the flow is locked in at 8.789 Hz (and 9.227 Hz from Morlet wavelet map) but with the flap deflection, we observe the evolution and increase in the strength of the periodicity at 6.042 Hz at $x/c=0.2660$. The reader will further observe that there is a frequency scale located at 53.97 Hz ($St=0.89$). This frequency is the new vortex shedding frequency that results when the closed loop control is applied. Note that the un-actuated vortex

shedding frequency (unstable) of 33 Hz does not appear in the anywhere in the spectra, indicating that this frequency scale has been suppressed. The magnitude at 53.97 Hz is increases to a magnitude of 1 at $x/c=0.2660$ when there is an exchange of energy between frequency scales at low end of the spectra and then decreases after $x/c=0.2660$ (Figure 5.39)

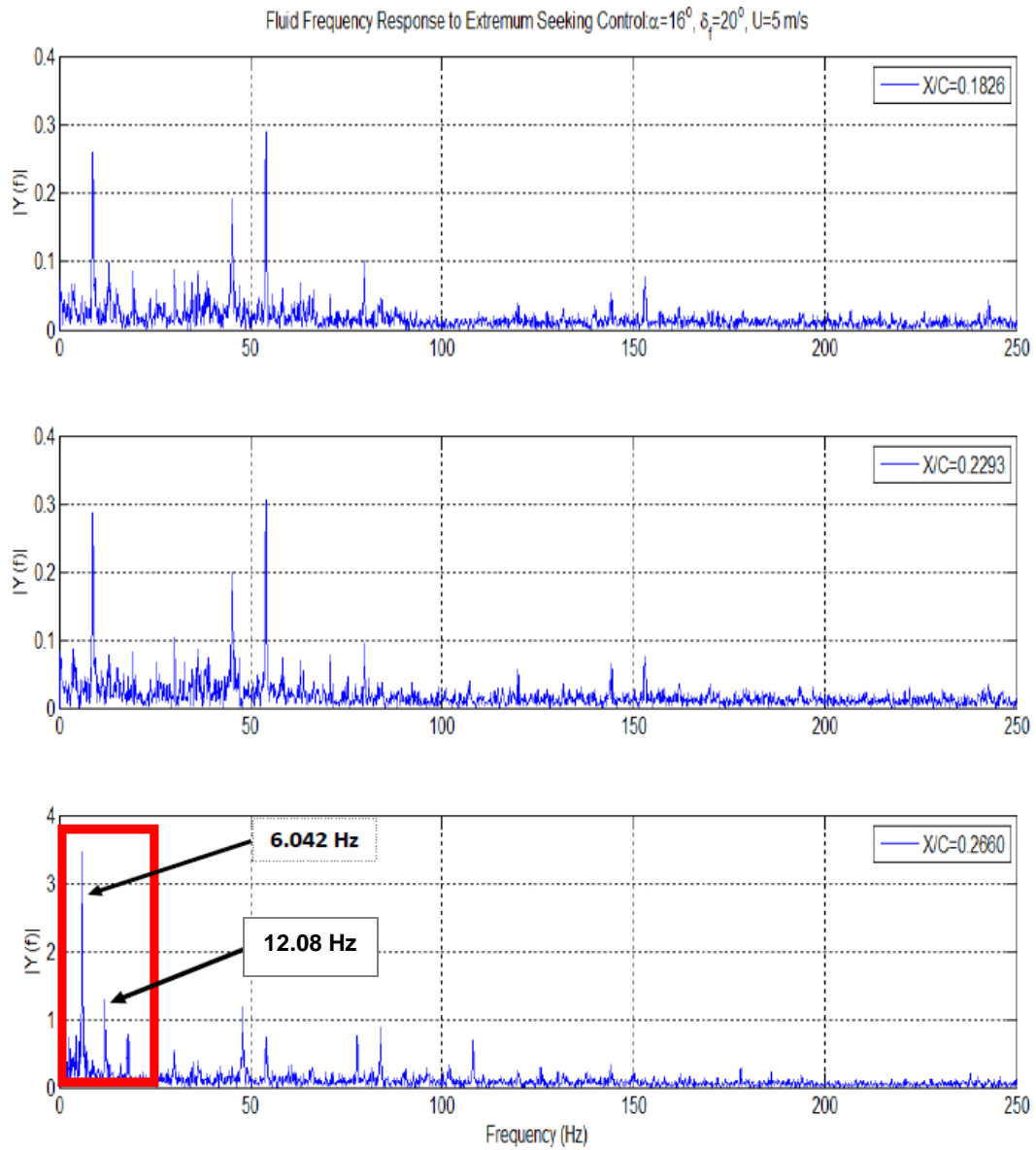


Figure 5.39: Enhanced FFT, Stations 1 to 3 (High Lift, Extremum Seeking)

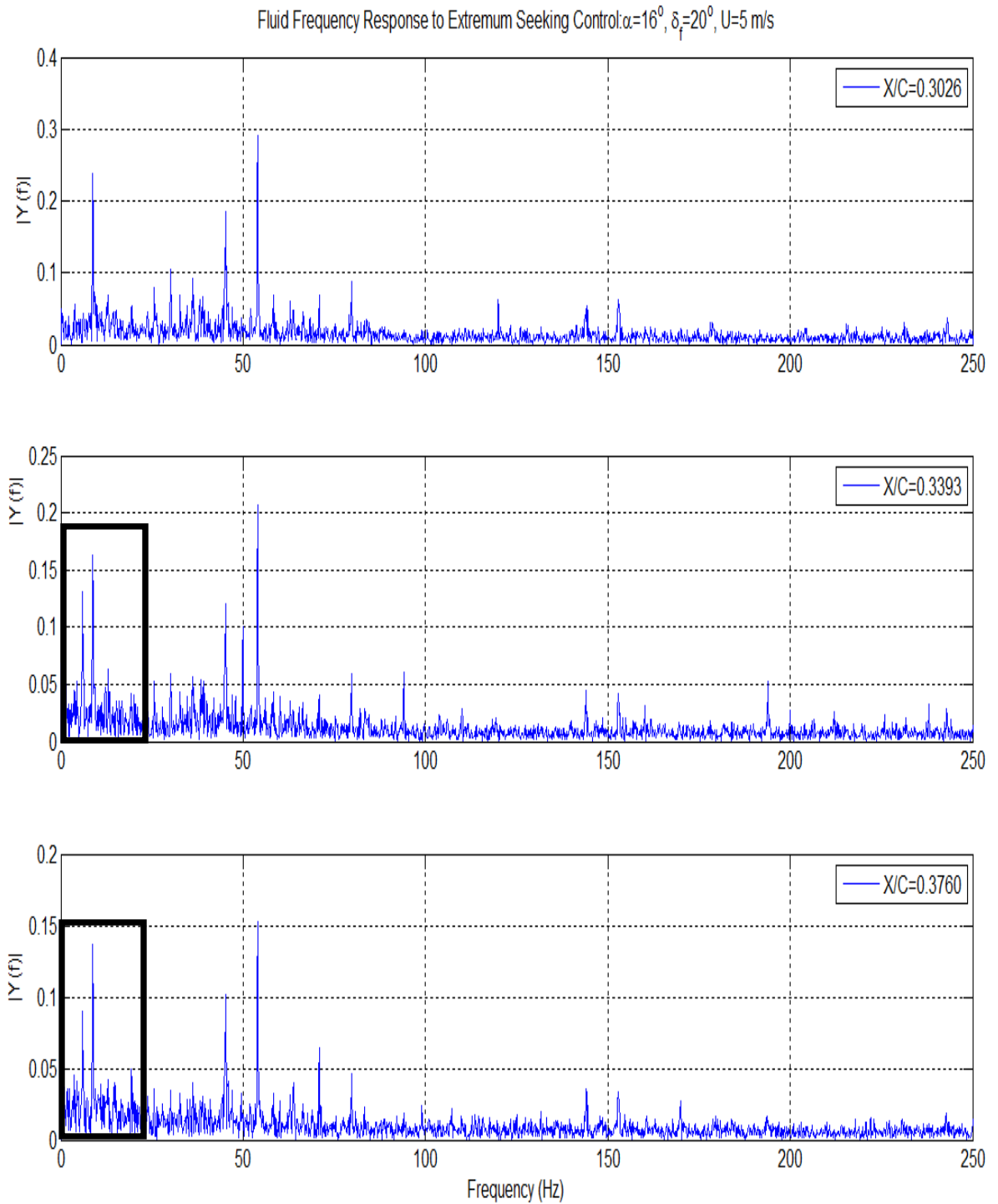


Figure 5.40: Enhanced FFT, Stations 4 to 6 (High Lift, Extremum Seeking)

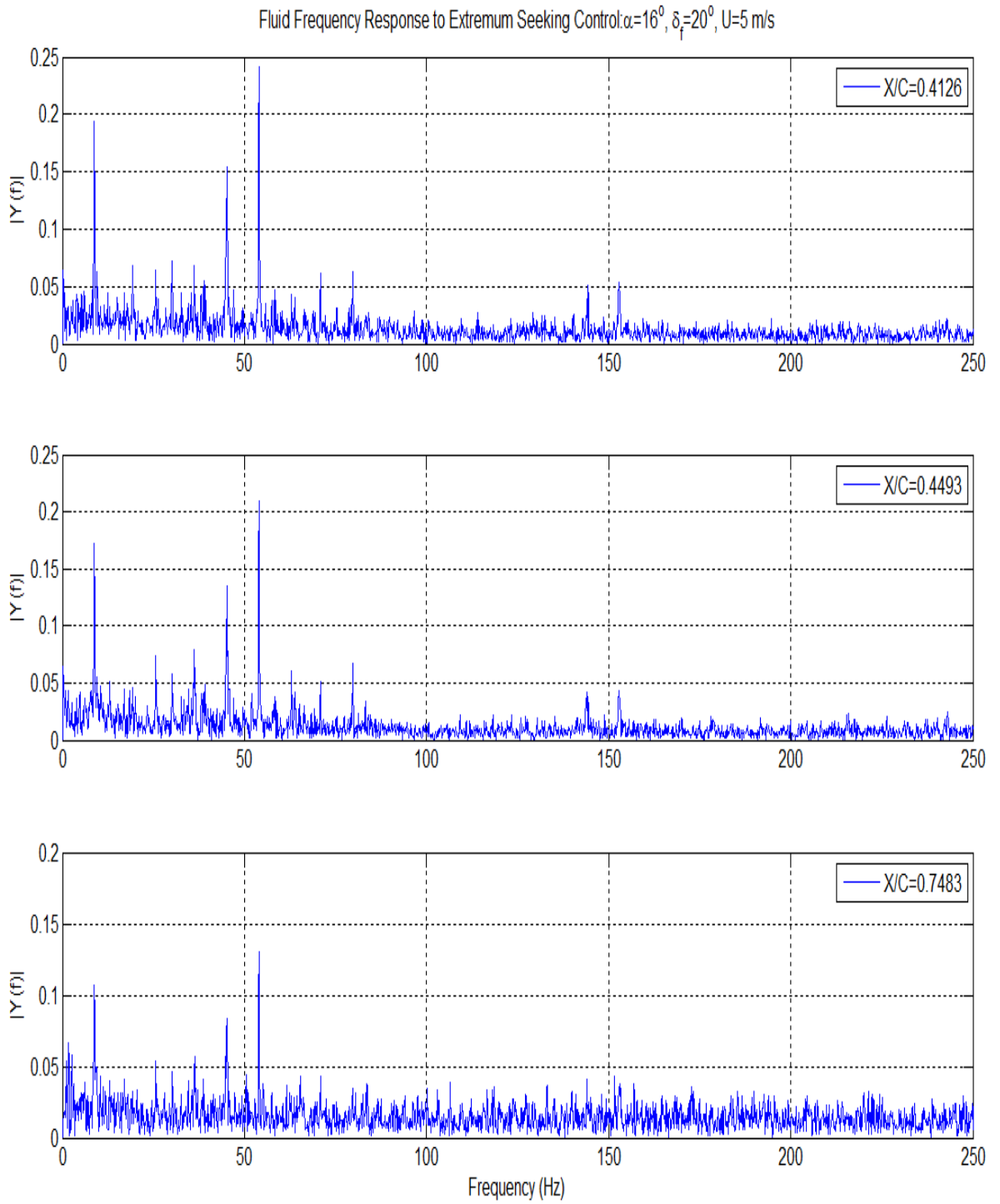


Figure 5.41: Enhanced FFT, Stations 7 to 9 (High Lift, Extremum Seeking)

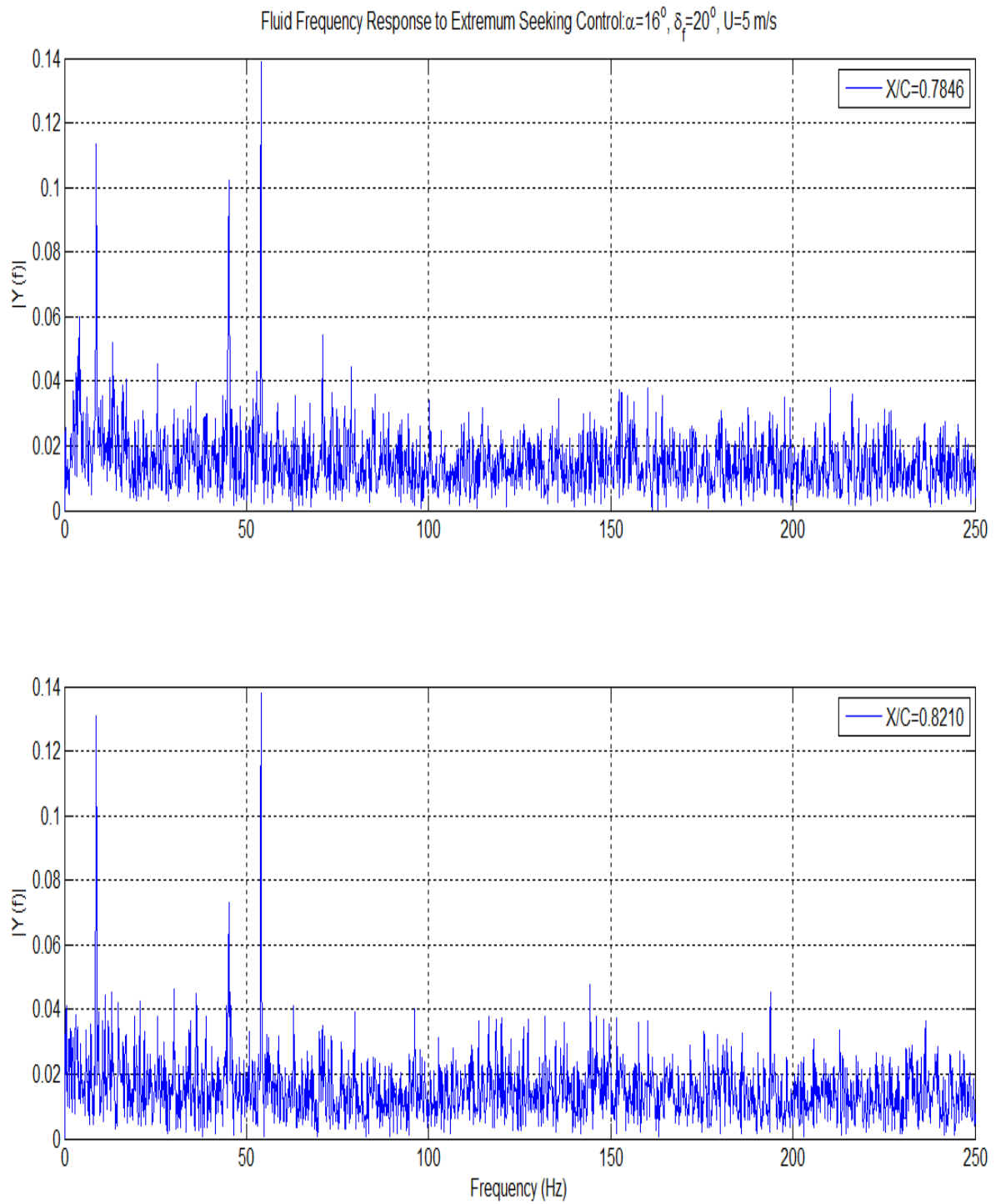


Figure 5.42: Enhanced FFT, Stations 10 to 11 (High Lift, Extremum Seeking)

The time frequency analysis (Figures 5.43 and 5.44) shows that the flow is frequency locked at about 9.227 Hz, the 8.789 Hz falls within the frequency band seen in the wavelet maps. It is also observed that there are finger-structures seen in the wavelet maps that appear to have some regularity. Of significance is the activity in the time-frequency space at $x/c=0.2660$, $x/c=0.3393$ and $x/c=0.3760$. Specifically, at $x/c=0.2660$, it is observed that there is very strong local periodicity (indicated by the red tones) at 6.042 Hz. The finger-like structures seen in the other wavelet maps are much sharper and have ‘countable’ regularity; also, we see that there is a secondary frequency band at about 11-13 Hz (the 12.08 Hz tone identified in the FFTs falls within this band). The secondary tone in the Mexican hat wavelet window shows that the flow although partially synchronized at this frequency is not heavily modulated and is clearly exchanging energy with the tone located at 6.042 Hz. What we are observing is flow synchronization at 6.042 Hz; the frequencies in this experimental system are re-distributing themselves in a highly structured fashion in order to lock in with the forcing frequency. We see that there is similar behavior at $x/c=0.3393$, but with more significant inter-modulation (See $x/c=0.3393$ Mexican Hat Window). At $x/c=0.3760$, the inter-modulation weakens and the flow reverts back to synchronization about 9.227 Hz. In addition, we believe that the finger-like structures seen above the frequency bands at $x/c=0.2660$ indicate an energy exchange between modes located at higher frequencies. In general, there is global inter-modulation along the upper surface of the wing. The next set of wavelet maps (Figure 5.44) range capture the higher frequencies not seen in the previous array. The time frequency analysis shows that there are new vortex shedding frequencies in the flow due to the application of adaptive control. The frequency band is centered about 50 Hz. The

vortex shedding is stable; this is indicated by the highly periodic vertical bands seen in the Morlet wavelet windows. At $x/c=0.2660$, we observe that there are two bands, the one centered about 50 Hz and the other a lower frequency. Note that the vertical bands of the tone centered about 50 Hz are much shorter in time duration i.e. they are thinner, indicating that the energy is being transferred to the lower frequency scales as previously identified. The strength of the vortex shedding seen in the wavelet maps correlates well with the persistent large amplitude 53.97 Hz ($St=0.89$) tone seen in the FFTs presented earlier. A NACA 0012 airfoil has a shedding frequency at 50 Hz for a tunnel speed of 5 m/s [63].

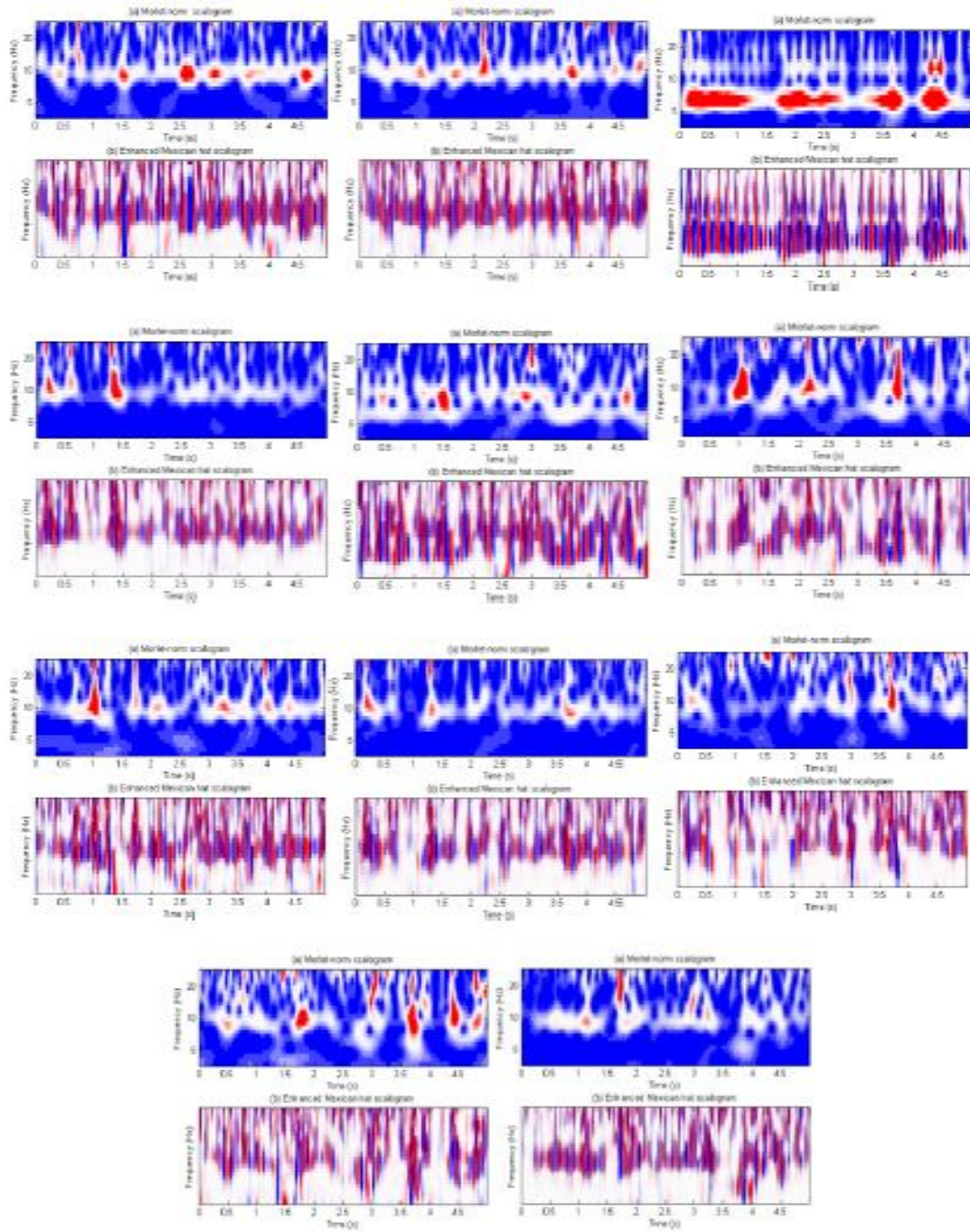


Figure 5.43: Wavelet Map Panel Part 1, High Lift configuration (Extremum Seeking)

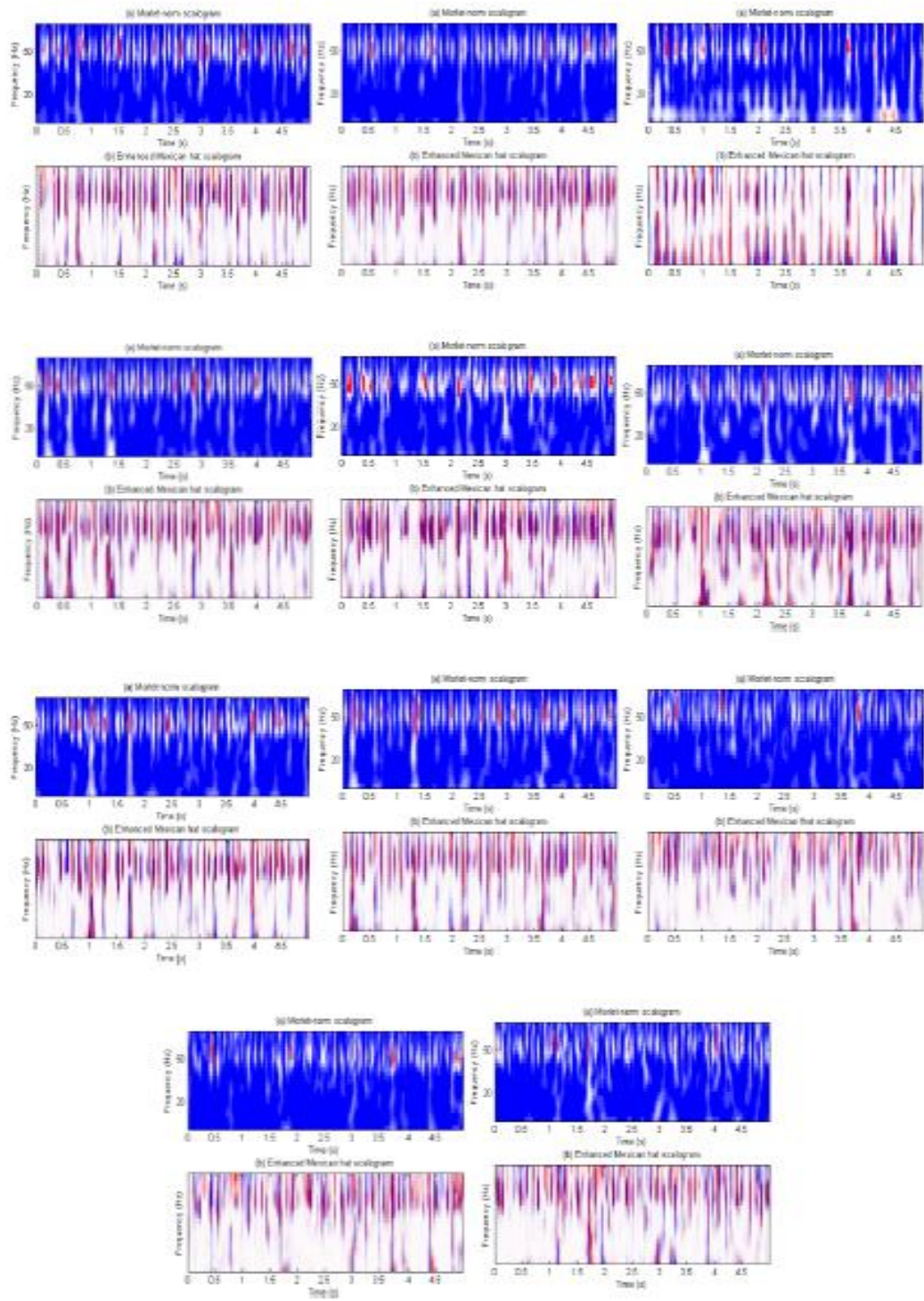


Figure 5.44: Wavelet Map Panel Part 2, High Lift configuration (Extremum Seeking)

For the application of extremum seeking control we have observed the following results; for the clean wing configuration, the controlled vortex shedding frequency is 45.04 Hz and for the high lift configuration, the controlled vortex shedding frequency is 53.97 Hz. Note that both of these frequency scales were present in the flow for both configurations but the flap deflection at high angle of attack produced an amplification of 53.97 Hz tone. Both of these frequencies are less than 100 Hz and are representative of what can be expected for vortex shedding on a symmetric airfoil. Further, these results agree with the real-time optimization and control work (for a NACA 0025 airfoil) presented by Cattafesta and Tian in that their modulation frequency always converged to a value less than 100 Hz. The implication is that this is the new controlled shedding frequency the NACA 0025 airfoil. The original vortex shedding frequency has been suppressed/inhibited by the application of the controller. Such behavior agrees well with the simulations presented in Chapter 2. Broadband excitation of a separated wake produces a closed loop aerodynamic flow that can be frequency locked at multiple frequencies, all of which are admissible in the dynamical systems sense. With respect to the controller performance, we have seen that the extremum seeking controller gain decreases with increasing velocity for both the clean wing and high-lift configuration. By holding the voltage constant combined with closed loop broadband excitation resulted in the controller selecting a frequency of 6.042 Hz which remained invariant with changes in airspeed. We have seen that at $x/c=0.2660$, there is a transient energy exchange after which the RMS pressure distributions show that there is a reduction in pressure fluctuations. A reduction in pressure fluctuations means that there is pressure recovery and an improvement in lift. Also, it was believed that the effectiveness of the synthetic jet

actuator monotonically decreases with increase in speed, but with closed loop control, one can exploit the acoustic properties of the actuator as shown by some of the velocity runs in this experiment. Note that there is a Strouhal number effect at certain velocities. It would be of interest to investigate further the effects of Reynolds number/tunnel speed on the performance of the extremum seeking controller. A comparison of the un-actuated RMS pressure distribution with the closed loop RMS pressure distribution (Figure 5.45) show that the application of extremum seeking control reduces the pressure fluctuations significantly and there is a zero slope on the latter portion of the airfoil i.e. from $x/c=0.4126$ to $x/c=0.8210$

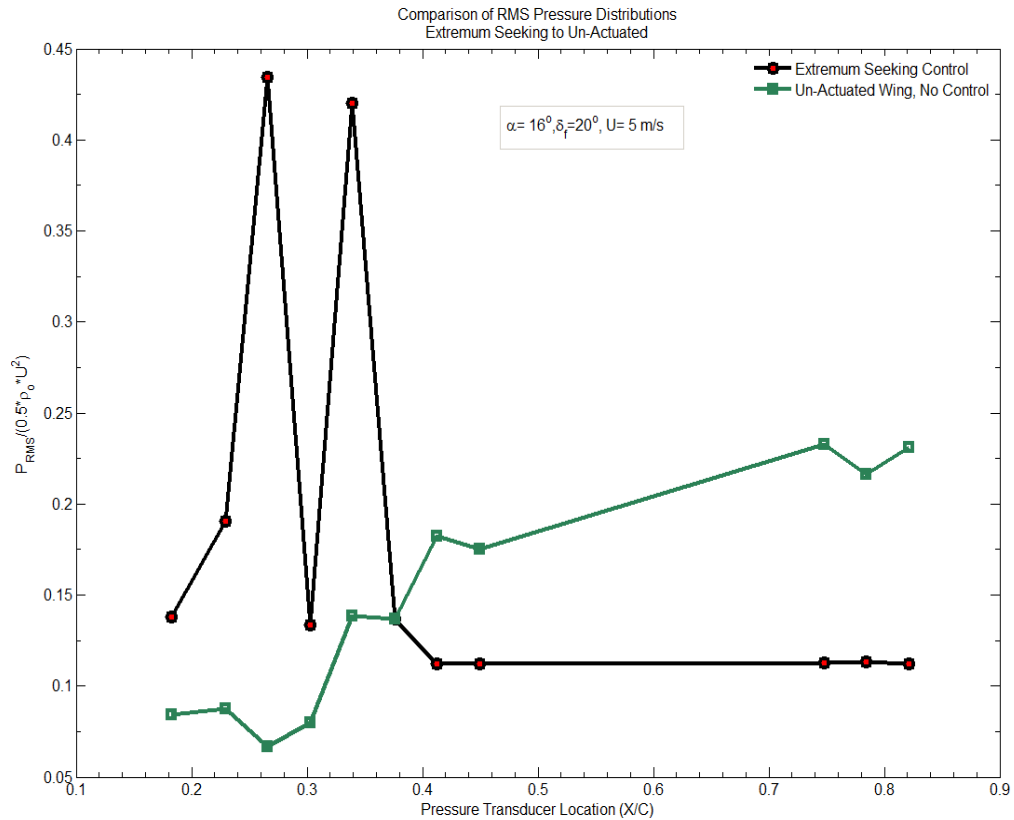


Figure 5.45: Comparison of RMS Pressure Distributions

A waterfall plot shows (Figure 5.46) that the application of adaptive control is effective in suppressing the pressure fluctuations, both at the leading edge and at the trailing edge of the airfoil. In Figure 5.46, the third sensor station has been highlighted in red because of the significant energy exchange between frequency scales. The amount energy transferred causes the amplitude to be raised to 5, if we want to see the details; the FFT for the third station has to be removed. When this done, we observe that distribution of the fluctuations is uneven at best especially at the mid chord sensor stations. One can again conjecture that this is to be expected as the control scheme does not prescribe a discrete forcing/modulation frequency (Figure 5.47). For the high-lift configuration the waterfall FFTs look the same. They differ because of the evolving frequency scales about $x/c=0.2660$.

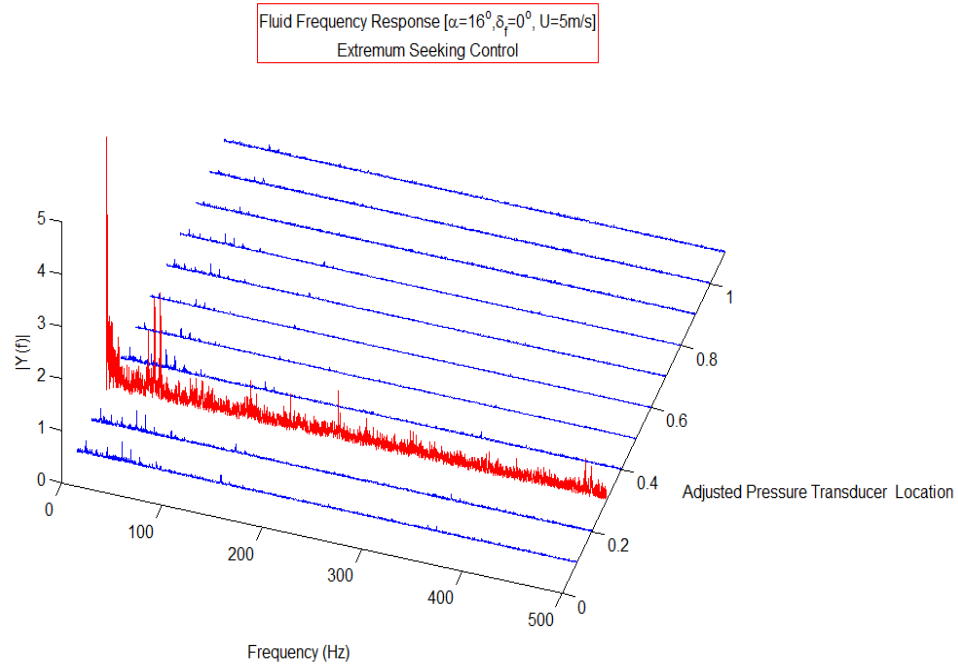


Figure 5.46: Closed Loop Frequency Spectra (Clean, Extremum Seeking)

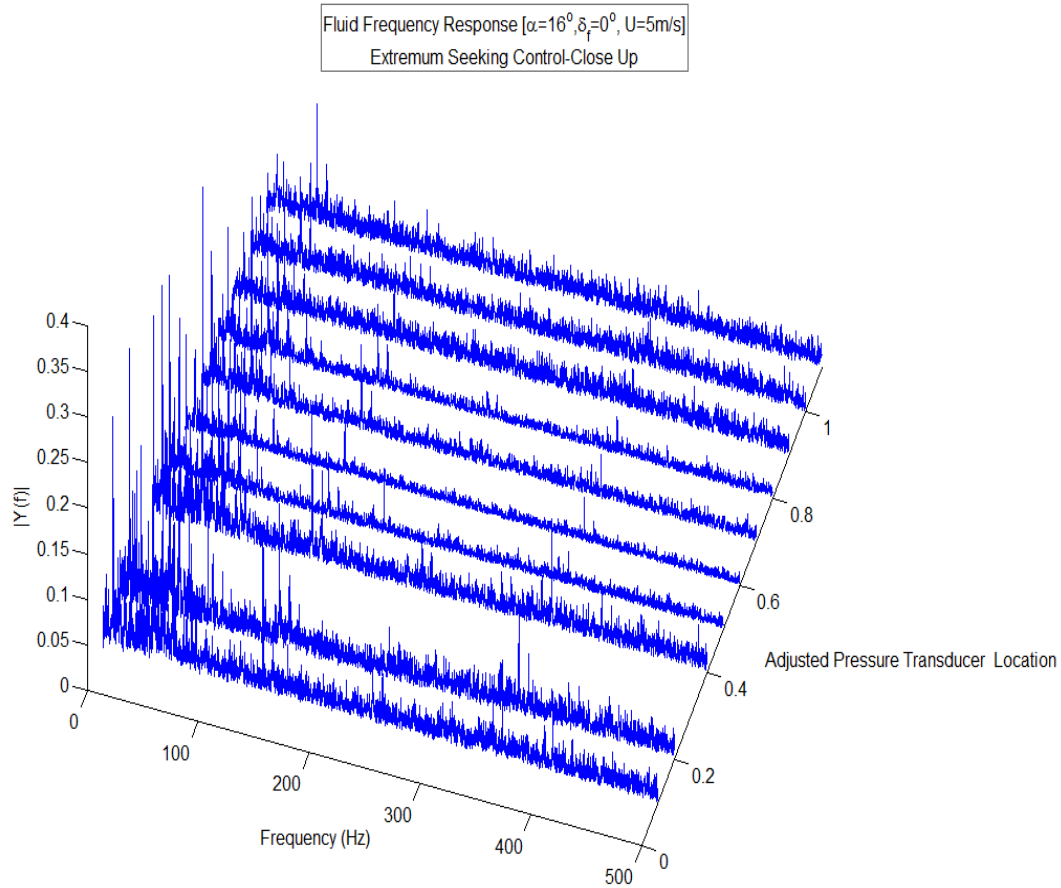


Figure 5.47: Closed Loop Frequency Spectra, Magnified (Clean, Extremum Seeking)

The first thing that was noticed in Figures 5.48 and 5.49 is that the pressure fluctuations fall below a fluctuation level of 0.2. A comparison of closed loop control methods for the clean wing configuration reveals that the extremum seeking controller performs slightly better in suppressing the pressure (fluctuation level is 0.1096) at 5 m/s. There is sensitivity to where the feedback sensor is located. When the feedback sensor is located deeper into the recirculation it seems to amplify the pressure fluctuations on the leading edge. In addition the slope between $x/c=0.4493$ and $x/c=0.7483$ is nearly flat as compared to the high lift cases under direct feedback control show a shallow negative slope

between the aforementioned sensor locations. The double peaks seen for the high lift cases still remain severe, but this is due to the flap deflection. The fluctuation level for the closed loop high lift cases is 0.1107. The open loop control cases both for the clean and high lift configurations at certain constant forcing frequencies, the pressure fluctuations fell below 0.05. It may be worthwhile to explore experimentally the application of a hybrid controller. Specifically, the hybrid controller would consist of two terms, the first is a constant frequency term and the second is an adaptive term. More will be said on this topic in Chapter 6.

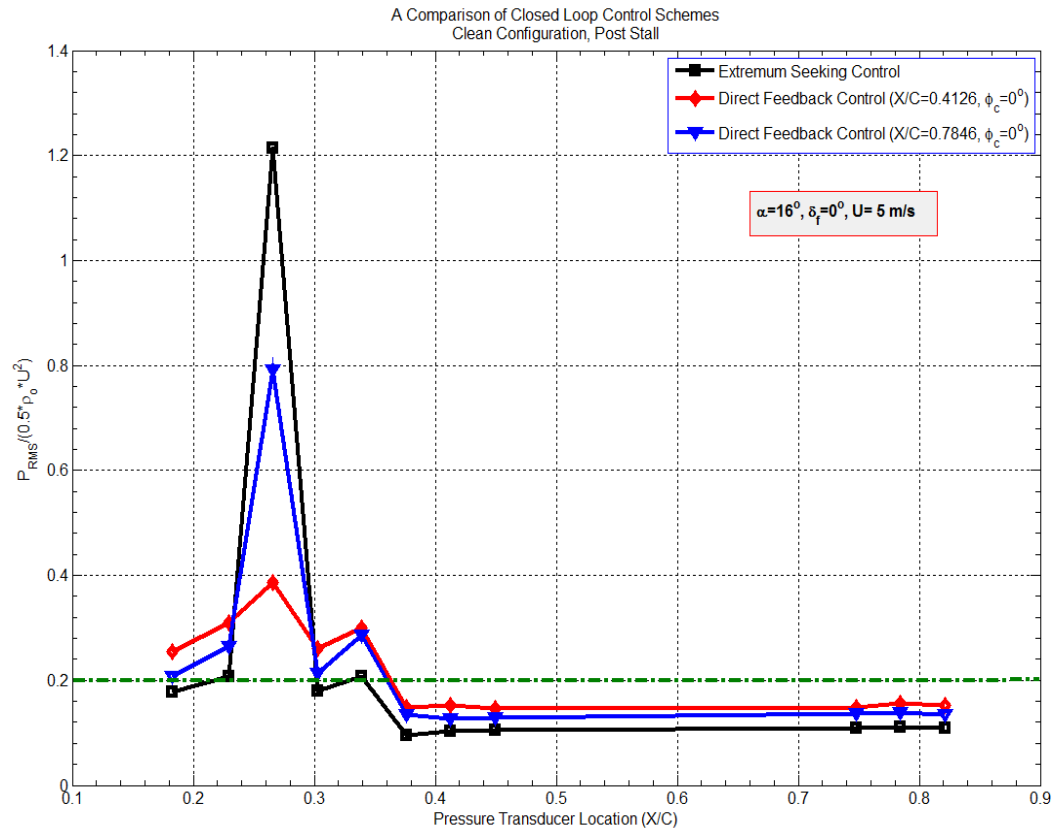


Figure 5.48: Comparison of adaptive controllers (Clean configuration)

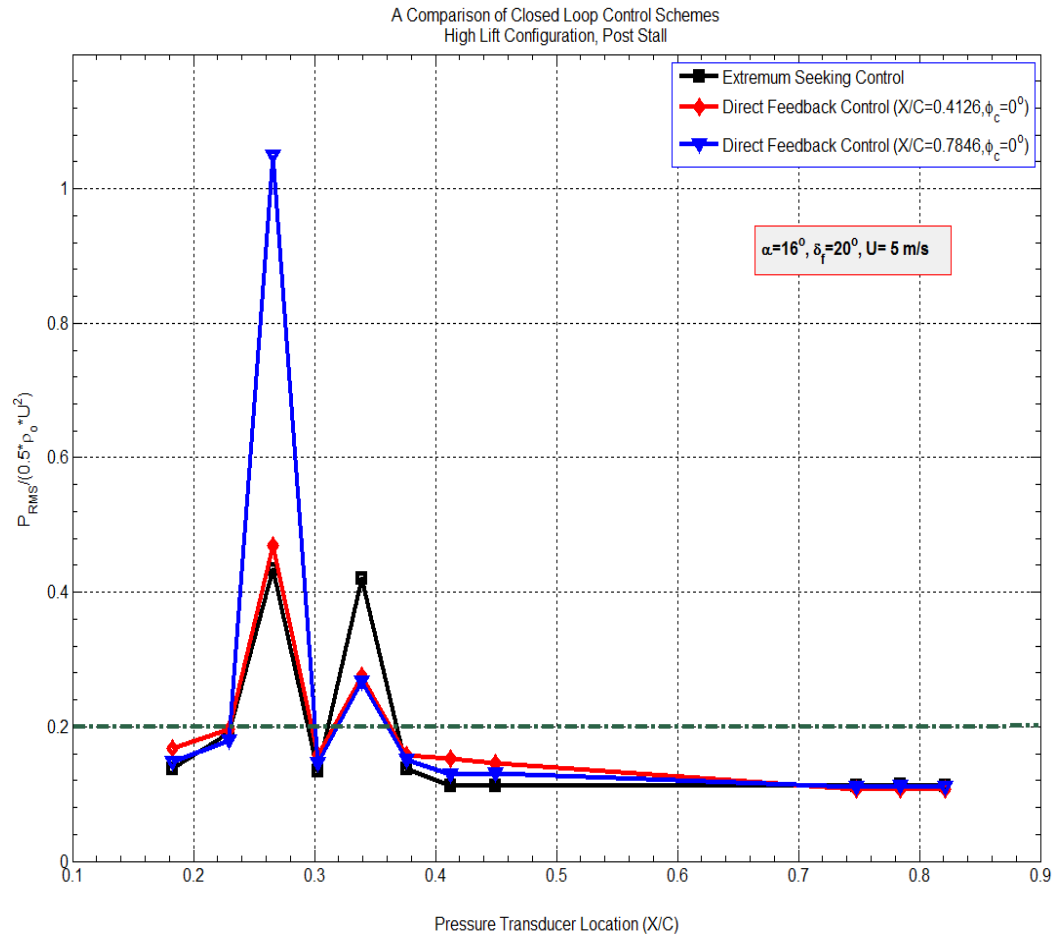


Figure 5.49: Comparison of adaptive controllers (High Lift configuration)

CHAPTER 6.0: CONCLUSIONS AND FUTURE WORK

6.1 CONCLUSIONS

For the open loop control experiments it has been demonstrated that the RMS pressure distributions are sensitive to changes in the forcing frequency. Specifically, we have seen that the shape of the distribution changes. Under open loop control the flow develops multiple stable states and it is conjectured (based on the wavelet analysis) the switching between these stable states that synchronizes the flow. The normal force varies with forcing frequency. This agrees well with the published literature on internal acoustic forcing. The forcing frequency of 100 Hz for the high lift configuration resulted in a significant reduction in the pressure fluctuations and the pressure recovery length scale. The pressure fluctuation level for open loop control is below 0.05. The open loop control time frequency analysis reveals that the flow is stabilized about more than one frequency. The original vortex shedding frequency of 33 Hz is not present in the resulting spectra presented and pressure fluctuations have been reduced. The application of closed loop broadband excitation has proven to be effective in reducing the pressure fluctuations and size of a separated wake of a wing in a post stall flight condition. It has been observed that a separated wake under closed loop control *selects* the frequency it locks into. This frequency is usually less than 100 Hz. Specifically, for the Direct Feedback Control application the controlled vortex shedding 52.60 Hz with a secondary locking frequency at 6.042 Hz. The variation of phase angle affects the level of pressure fluctuations at the leading edge. Once the flow is frequency locked (under closed loop control) the change in phase angle does not affect the frequencies in the flow. For the application of extremum seeking control, the flow responds with a controlled shedding frequency of 50

Hz with secondary frequency at 9.227 Hz for the clean wing configuration and for the high lift configuration a controlled shedding frequency of 53.97 Hz with a secondary frequency at 6.042 Hz.

6.2 FUTURE WORK

- The signature of frequency locking or synchronization in the time-frequency space shows up as a narrow band of frequencies for duration of time. In our case we have utilized the Morlet scalogram. This signature will appear when closed loop flow control is applied to an aerodynamic system such as ours; however it is limited in control authority once the flow selects a frequency to lock into. In this way the controller could be considered saturated. As such, it may prove to be beneficial to explore the application of a hybrid controller. The hybrid controller will have an amplitude modulated (that is if the researcher insists on using piezoceramic discs) fixed frequency term and an adaptive term in which either the frequency is actively tracked or a broadband excitation signal is used i.e. like the control signal generated by the LMS algorithm. From experimental experience obtained during the course of this research, the fixed frequency open loop control resulted in shape changes in the RMS pressure distribution and lower fluctuation levels on the latter portion of the airfoil. The open loop control term excites other frequency scales in the flow as we have seen from the spectra and the time frequency analysis. However, there are other frequency scales that are not controlled. By combining the adaptive control term with the open loop feed-forward term, the two control terms will interact positively to enhance the robustness of the controller. Specifically, the modes that cannot be accessed by

the fixed frequency term can be successfully addressed using the additional closed loop broadband excitation. The two terms may further reduce the pressure fluctuations and ‘pin’ the aerodynamic system to a set of stable states which will result in a robust frequency locked flow condition. The use of specially designed voice coils/subwoofers would improve the performance of the controller as these devices have a wide, flat bandwidth.

- A test was conducted in which the synthetic jet arrays were energized in the open loop configuration and the tunnel lift fan was shut off. The data obtained from this experiment needs to be examined as it may provide some insight into how the acoustic environment in the test section interacts with the presence of an external aerodynamic flow.
- The design and optimization for directed synthetic jet actuators (use voice coils/or subwoofer electromechanical configurations) should include the following steps:
 1. Aerodynamic Design: Select geometry and match components;
 2. Treat cavity and slot as acoustic devices and employ frequency design methods;
 3. Check aerodynamic design with CFD;
 4. Cycle through Steps 2 and 3 until the acoustic frequency response and the aerodynamic characteristics satisfy design criteria;
 5. Experimental testing (Hotwire and Omni-Directional Microphone)
 6. Repeat should the experimental results not satisfy design specifications
- Apply advance flow visualization techniques and include a hotwire anemometer in the wake during initial aerodynamic system identification tunnel runs and flow control tunnel runs.

REFERENCES

- [1] Schubauer, G.B., Skramstad, H.K., 'Laminar boundary layer oscillations and transition on a flat plate', NACA Report 909, 1948.
- [2] Roos, Frederick, W., Kegelman, Jerome, T., 'Control of coherent structures in reattaching laminar and turbulent shear layers', AIAA Journal, Vol. 24, No. 12, 1986, pp. 1956-1963
- [3] Viets, Hermann, Piatts, Micheal, Ball, Mont, 'Boundary layer control by unsteady vortex generation', Journal of Wind Engineering and Industrial Aerodynamics, Vol. 7, No. 2, March 1981, pp. 135-144.
- [4] Flow Control and Aeroelasticity Portfolio, Broad Area Announcement, AFOSR Wright-Patterson AFB, Dayton OH, 2008.
- [5] Cattafesta, Louis N, Sheplak, Mark, 'Actuators for Active Flow Control', Annual Review of Fluid Mechanics, Vol. 43, January 2011, pp. 247-272.
- [6] Holman, R., Yogen, U., Mittal, R., Smith, Barton L., Cattafesta, Louis, 'Formation Criterion For Synthetic Jets', AIAA Journal, Vol. 43, No. 10, October 2005.
- [7] Gallas, Quentin, 'On the Modeling and Design of Zero-Net Mass Flux Actuators', Ph.D. Thesis, Department of Mechanical and Aerospace Engineering, University of Florida, USA, 2005.
- [8] Kotapati, Rupesh B., Mittal, Rajat, Marxen, Olaf, Ham, Frank, Donghyun, You, Cattafesta Louis N., 'Nonlinear Dynamics and synthetic-jet-based control of a canonical flow', Journal of Fluid Mechanics, Vol. 654, pp. 65-97
- [9] Gallas, Q., Guiqin, W., Melih, P., Sheplak, M., Cattafesta, L., 'Optimization of Synthetic Jet Actuators', 41st Aerospace Sciences Meeting & Exhibit, January 6-9, 2003, Reno NV. AIAA-2003-0635
- [10] Oyarzun, Matias A., Cattafesta, Louis, 'Design and Optimization of Piezoceramic Zero-Net Mass-Flux Actuators', 5th Flow Control Conference, June 28- July 1st, 2010, Chicago IL., AIAA-2010-4414
- [11] Arunajatesan, S., Oyarzun, M., Palavicini, M., Cattafesta, L., 'Modeling of Zero-Net Mass-Flux Actuators for Feedback Flow Control', 47th AIAA Aerospace Sciences Meeting, Orlando FL, January 2009, AIAA-2009-743.

- [12] Holman, Ryan Jay, 'An Experimental Investigation of Flows from Zero-Net Mass-Flux Actuators', Ph.D Thesis, Department of Mechanical and Aerospace Engineering, University of Florida, 2006.
- [13] Gilarranz, J.L., Traub, L.W., Rediniotis, O.K., 'A New Class of Synthetic Jet Actuators- Part 1: Design, Fabrication and Bench Top Characterization', ASME Journal of Fluids Engineering, Vol. 127, March 2005.
- [14] Nagib, M., Kiedaish, John W., Wygnanski, Israel J., Stalker, Aaron D., Wood, Tom, McVeigh, Micheal, 'First-In-Flight Full-Scale Application of Active Flow Control: The XV-15 Tiltrotor Download Reduction', NATO-RTO Report, RTO-MP-AVT- 111
- [15] Nishri, B., Wygnanski, I., 'Effects of Periodic Excitation on Turbulent Separation from a Flap', AIAA Journal, Vol. 36, No. 4, 1998
- [16] Narayanan, Satish, Banaszuk, Andrzej, 'Experimental Study of a Novel Active Separation Control Approach', 41st Aerospace Sciences Meeting and Exhibit, January 6-9, 2003, Reno NV, AIAA-2003-60.
- [17] Pyragas, K., 'Continuous control of chaos by self-controlling feedback', Physics Letters A 170 (1992), pp. 421-428
- [18] Wiltse, J., and Glezer, A., 'Manipulation of Free Shear Flows Using Piezoelectric Actuators', Journal of Fluid Mechanics, Vol. 249, pp. 261-285, 1993
- [19] Rowley, Clarence W., 'Modeling, Simulation, and Control of Cavity Flow Oscillations' Ph.D Thesis, Department of Mechanical Engineering, CalTech, 2001
- [20] Cattafesta, Louis, Williams, David, Rowley, Clancy, Alvi, Farrukh, 'Review of ActiveControl of Flow-Induced Cavity Resonance', 33rd AIAA Fluid Dynamics Conference ,June 23-26, 2003, Orlando FL, AIAA-2003-3567
- [21] Rowley, Clarence W., Batten, Belinda A., 'Dynamic and Closed Loop Control', Chapter 5, Fundamentals and Applications of Modern Flow Control, Vol. 231, Progress in Aeronautics and Astronautics, AIAA, 2009
- [22] Greenblatt, David, Wygnanski, Israel, J., 'The Control of Flow Separation by Periodic Excitation', Progress in Aerospace Sciences Vol. 36, 2000, pp. 487-545
- [23] Gad-el-Hak, M., 'Modern Developments in Flow Control', Applied Mechanics Reviews Vol. 49, pp. 365-379, 1996.
- [24] Takahashi, H., Liu, F., Palavicini, M., Oyarzun, M., Griffin, J., Ukeiley, L., Cattafesta, L., 'Experimental Study of Adaptive Control of High Speed Flow Induced Cavity Oscillations', Journal of Fluid Science and Technology, Vol. 6, No. 5, 2011

- [25] Debiasi, M., Samimy, M., 'Logic Based Active Control of Subsonic Cavity Flow Resonance', AIAA Journal, Vol. 42, No. 9, September 2004.
- [26] Caraballo, E., Samimy, M., DeBonis, J., 'Low Dimensional Modeling of Flow for Closed Loop Flow Control', 41st Aerospace Sciences Meeting and Exhibit, January 6-9, 2003, Reno NV, AIAA-2003-59.
- [27] Takahashi, H., Liu, F., Palavicini, M., Oyarzun, M., Griffin, J., Ukeiley, L., Cattafesta, L., 'Progress on Active Control of Open Cavities', 49th AIAA Aerospace Sciences Meeting, January 4-7, 2011, Orlando FL, AIAA-2011-1221
- [28] Breuer, Kenneth, and Kevin Wu. 'Control of Turbulent Boundary Layers using FXLMS Feedforward Architectures', 3rd AIAA Flow Control Conference, June 5-8, 2006 San Francisco, CA, AIAA-2006-3022
- [29] Haykin, Simon S., *Adaptive Filter Theory Fourth Edition*, Prentice Hall, 2002
- [30] Rathnasingham, Ruben, and Kenneth S. Breuer. "Active control of turbulent boundary layers." *Journal of Fluid Mechanics* 495 (2003): 209-233.
- [31] Tian, Ye, Qi Song, and Louis Cattafesta. "Adaptive Feedback Control of Flow Separation." 3rd AIAA Flow Control Conference, June 5-8, 2006, San Francisco CA, AIAA-2006-3016
- [32] Tain, Ye, 'Adaptive Control of Separated Flow', Ph.D Thesis, Department of Mechanical and Aerospace Engineering, University of Florida, 2007
- [33] Banaszuk, Andrzej, Narayanan, Satish, Zhang, Youping, 'Adaptive Control of Flow Separation in a Planar Diffuser', 41st Aerospace Sciences Meeting and Exhibit, January 6-9, Reno NV, AIAA-2003-617.
- [34] Garwon, M., Urzunicok, F., Darmadi, L. H., Bärwolff, G., & King, R., 'Adaptive Control Separated Flows', Proceeding of the European Control Conference, 2003
- [35] Kim, K., Kasnakoglu, C., Serrani, A., & Samimy, M., 'Extremum seeking control of Subsonic cavity flow', AIAA Journal, Vol. 47, No. 1, January 2009.
- [36] Ralf Becker, Rudibert King, Ralf Petz, and Wolfgang Nitsche., 'Adaptive Closed-Loop Control on a High Lift Configuration Using Extremum Seeking', AIAA Journal, Vol. 45, No. 6, June 2007.
- [37] Pastoor, Mark, Lars Henning, Bernd R. Noack, Rudibert King, and Gilead Tadmor, 'Feedback shear layer control for bluff body drag reduction', *Journal of Fluid Mechanics* Vol. 608, No. 1 (2008), pp. 161-196

- [38] Lovato, Julie Anne, 'Active Control of the Separation Region on a Two-Dimensional Airfoil', Ph.D Thesis, Department of Mechanical & Materials Engineering, Washington State University, May 1992.
- [39] Pack Melton, LaTunia, Schaeffler, Norman W., Lin, John C., 'High-Lift System for a Supercritical Airfoil: Simplified by Active Flow Control', 45th Aerospace Sciences Meeting and Exhibit, January 8-11, Reno NV, 2007, AIAA-2007-707
- [40] Greenblatt, David, 'Dual Location Separation Control on a Semi-Span Wing', 23rd AIAA Applied Aerodynamics Conference, June 6-9, 2005, Toronto, Ontario Canada, AIAA-2005-5085
- [41] Nagib, Hassan, Kiedaisch, John, Reinhard, Paul, Demanett, Brian, 'Active Flow Control for High Lift Airfoils: Separation versus Circulation Control', 45th Aerospace Sciences Meeting and Exhibit, January 8-11, Reno NV, 2007, AIAA-2007-1119
- [42] Pack Melton, LaTunia, Hannon, Judith, Yao, Chung-Sheng, Harris, Jerome, 'Active Control at Low Reynolds Numbers on a NACA 0015 Airfoil', 26th AIAA Applied Aerodynamics Conference, August 8-11, 2008, Honolulu, HI, AIAA-2008-6407
- [43] Pikovsky, A.S., Rosenblum, M.G., Osipov. G.V., Kurths, J., 'Phase Synchronization of chaotic oscillators by external driving', *Physica D* 104 (1997), 219-238
- [44] Seifert, A., Darabi, A., & Wygnanski, I., 'Delay of Airfoil Stall by Periodic Excitation', *Journal of Aircraft*, Vol 33, No. 4, August 1996
- [45] Joe, W., Taira, K., Colonius, T., MacMynowski, D., Tadmor, G., 'Closed Loop Control of Vortex Shedding on a Two-Dimensional Flat-Plate Airfoil at a Low Reynolds Number', 46th Aerospace Sciences Meeting and Exhibit, Reno NV, January 7-10, 2008, AIAA-2008- 0634
- [46] Taira, K., Rowley, C. W., & Colonius, T., 'Feedback Control of High-Lift State for A Low Aspect Ratio Wing', 48th AIAA Aerospace Sciences Meeting, Orlando FL, January 2010, AIAA-2010-0357.
- [47] Holmes, Philip, Lumley, John L. and Berkooz, Gal. *Turbulence, Coherent Structures, Dynamical Systems and Symmetry*, Cambridge University Press, 1998
- [48] Cohen, Leon. *Time Frequency analysis*. Prentice Hall, 1995
- [49] Garwon, M., King, R., 'A multivariable adaptive control strategy to regulate the separated flow behind a backward-facing step', Proceedings of the 16th IFAC World Congress, 2005 Czech Republic.

- [50] Lin, Feng, Brandt, Robert D., Saikalis, George, 'Self-Tuning of PID Controllers by Adaptive Interaction', Proceedings of the American Control Conference, Chicago IL June 2000
- [51] Krstic, M., Wang, H., 'Stability of extremum seeking feedback for general nonlinear dynamic systems', Automatica, Vol. 26, 2000, pp. 595-601.
- [52] McCormick, Duane C., Lozyniak, Steven A., MacMartin, Douglas G., Lorber, Peter F., 'Compact, High-Power Boundary Layer Separation Control Actuation Development' 2001 ASME Fluids Engineering Division Summer Meeting, New Orleans Louisiana, 2001
- [53] William, D.R. and Fabris, D., 'Closed-loop control in cavities with unsteady bleed forcing', AIAA- 2000-0470
- [54] Cocanower, Alfred Benjamin, 'A Unified Method for Predicting the Performance of Subsonic Diffusers of Several Geometries', Ph.D Thesis, Department of Mechanical Engineering, Stanford University, 1965.
- [55] Dixon, S.L., *Fluid Mechanics, Thermodynamics of Turbomachinery*. Butterworth & Heinemann, Fourth Edition, 1998
- [56] Mossi, K., Castro, N.D., Bryant, R., Mane, P., 'Boundary Condition Effects on Piezo- Synthetic Jets', Integrated Ferroelectrics, Vol. 71, pp. 257-266, 2005
- [57] Gallas, Quentin, 'Lumped Element Modeling of Piezoelectric-Driven Synthetic Jet Actuators for Flow Control', Master's Thesis, Department of Mechanical and Aerospace Engineering, University of Florida, 2002
- [58] Huang, Rong F., Lin, Chih L., 'Vortex Shedding and Shear-Layer Instability of a Wing at Low- Reynolds Numbers', AIAA Journal, Vol. 33, No. 8, pp. 1398-1403, August 1995
- [59] Zaman, K.B.M.Q., McKinzie, D.J., Rumsey, C.L., 'A natural low-frequency oscillation of the flow over an airfoil near stalling conditions', Journal of Fluid Mechanics, Vol. 202, pp. 403-442, 1989
- [60] Yarusevych, S., Kawall, J.G., Sullivan, P. E., 'Unsteady Separated Flow Characterization on Airfoils Using Time-Resolved Surface Pressure Measurements', AIAA Journal, Vol. 46, No. 2, pp. 508-516. February 2008.
- [61] Parker, R., 'Resonance Effects in Wake Shedding from Parallel Plates: Calculation of Resonant Frequencies', Journal of Sound and Vibration, Vol. 5, No. 2 pp. 330-343, 1967.

- [62] Runyan, H.L., Woolston, D.S., Rainey, A.G., 'Theoretical and Experimental Investigation of the Effect of Tunnel Walls on the Forces on an Oscillating Airfoil in Two-Dimensional Subsonic Compressible Flow', NACA Report 1262, 1956.
- [63] Parker, R., 'A Note on Frequency Ratios for Acoustic Resonances of Flat Plate Cascades with Plate Spacing Less than Half the Longitudinal Wavelength', Journal of Sound and Vibration, Vol. 86, No. 4, pp. 594-596.
- [64] Lucas, M. J.; Noreen, R.; Southerland, L. D.; Cole, J., III; Junger, M., 'The Acoustic Characteristics of Turbomachinery Cavities', NASA-CR-4671, 1995
- [65] Kabiri, Pooya, 'Active Flow Control Over a NACA 0015 Airfoil by Using Synthetic Jet Actuators', Ph.D Thesis, Department of Mechanical and Aeronautical Engineering, Clarkson University, 2012
- [66] Chang, R.C., Hsiao, F.B., Shyu, J.N., 'Forcing Level Effects of Internal Acoustic Excitation on the Improvement of Airfoil Lift Performance', Journal of Aircraft, Vol. 29, No. 5, Sept-Oct, 1992
- [67] Hsiao, F.B., Shyu, J.N., Liu, C., 'Control of Wall-Separated Flow by Internal Acoustic Excitation', AIAA Journal, Vol. 28, No. 8, 1990.
- [68] Ariyur, Kartik B., Krstic, Miroslav. *Real-Time Optimization by Extremum Seeking Feedback*. Wiley, 2003
- [69] Wang, H-H., Yeung, S. Krstic, M., 'Experimental Application of Extremum Seeking on an Axial Flow Compressor', IEEE Transactions on Control Systems Technology, Vol. 8, No. 2, March 2000
- [70] Joe, W.T., Colonius, T., MacMynowski, D.G., 'Optimized Waveforms for Feedback Control of Vortex Shedding', Notes on Numerical Fluid Mechanics and Multidisciplinary Design, Vol. 108, 2010, pp. 391-404